

DAMAGE DETECTION  
IN STRUCTURES USING  
FREQUENCY RESPONSE FUNCTION  
(FRF) DATA AND FINITE ELEMENT  
MODELLING

DUNG HUYNH

MASTER OF ENGINEERING  
(RESEARCH)

VICTORIA UNIVERSITY OF TECHNOLOGY



3 0001 00790 7845

2003



**DAMAGE DETECTION  
IN STRUCTURES USING  
FREQUENCY RESPONSE FUNCTION  
(FRF) DATA AND FINITE ELEMENT  
MODELLING**

by  
Dung Huynh



A thesis submitted in fulfilment of the requirement  
of the Degree of Master of Engineering (Research)  
to Victoria University of Technology

**SCHOOL OF ARCHITECTURAL, CIVIL AND MECHANICAL ENGINEERING**

**VICTORIA UNIVERSITY OF TECHNOLOGY**

**MELBOURNE, AUSTRALIA**

**NOVEMBER 2003**

FTS THESIS

624.171 HUY

30001007907845

Huynh, Dung

Damage detection in  
structures using frequency  
response function (FRF) data

## **ACKNOWLEDGEMENT**

I would like to express my sincere gratitude to Dr. Danh Tran and Dr. Jimin He for their untiring supervision, advice and guidance throughout this Masters thesis, which have greatly contributed to the success of this thesis. I wish also to thank Victoria University of Technology and the School of Architectural, Civil and Mechanical Engineering for making available the resources that allowed me to complete this thesis.

---

---

## ABSTRACT

This thesis presents a method to detect structural damage using frequency response function (FRF) data obtained from non-destructive vibration tests. The method is used to study cases of early structural damage in which there is no appreciable change in mass and damping. The resulting change in structural stiffness matrix is reflected in changes of FRF which can be exemplified by the evaluation of the damage location vector. This requires the dynamic stiffness matrix of the original undamaged structure and the frequency response curve of the currently damaged structure. In this thesis, the former is obtained from a finite element model of the virgin structure and the latter are obtained from an impact hammer test. The Damage Detection Algorithm will be used to detect simulated damage FRF data applied to a simple mass spring system, space truss structure and a plate structure and effects of noise. Both numerically simulated and experimentally measured noises are investigated. Experimental FRF data were obtained for a plate structure and used for detection of physical damage and comparisons made with the simulated data. Results show that the Damage Detection Algorithm can be used to successfully detect structure damage in situations where coordinate incompatibility and noise exists.

---

# NOMENCLATURE

The following lists below are symbols and abbreviations that are used within this thesis.

|                        |  |
|------------------------|--|
| [C]                    | - Viscous damping matrix of a structure  |
| E                      | - Young's modulus (GPa)  |
| [H]                    | - Hysteric damping matrix of a structure   |
| [I]                    | - Identity matrix  |
| [K]                    | - Stiffness matrix of a structure  |
| [M]                    | - Mass matrix of a structure   |
| $n_d$                  | - Number of averages   |
| [T]                    | - Linear transformation matrix   |
| t                      | - Thickness (m)  |
| {x}                    | - Vector of displacement   |
| $\{\ddot{x}\}$         | - Second derivative of displacement with respect to time, acceleration vector    |
| {d( $\Omega$ )}        | - Damage location vector   |
| [Z( $\Omega$ )]        | - Dynamic stiffness matrix   |
| { $\alpha(\Omega)$ }   | - Receptance frequency response function   |
| [ $\Delta Z(\Omega)$ ] | - Difference between dynamics stiffness matrix of damage and undamaged structure |
| $\epsilon_r$           | - Normalised error   |
| $\gamma^2(f)$          | - Coherence function at a frequency  |
| $\rho$                 | - Density (kg/m <sup>3</sup> )   |
| $\nu$                  | - Poisson's ratio  |
| $\Omega$               | - Frequency of the system (Hz)   |

## Operators and Symbols

|                  |  |
|------------------|--|
| $\Sigma$         | - Summation  |
| $\{ \}^T, [ ]^T$ | - Transpose  |
| $\otimes$        | - Matrix multiplication element by element operation |
| $[ ]^{-1}$       | - Standard matrix inverse                            |
| $[ ]_D$          | - Subscript D represents damaged structure           |
| $[ ]_{UD}$       | - Subscript UD represents undamaged structure        |
| $\{ \}^{mc}$     | - Superscript mc refers to measured coordinate       |
| $\{ \}^{uc}$     | - Superscript uc refers to unmeasured coordinate     |

## Abbreviations

|         |   |
|---------|---|
| CDLV    | - Cumulative Damage Location Vector                   |
| COMAC   | - Coordinate Modal Assurance Criterion                |
| DEM     | - Dynamic Expansion Method                            |
| DLV     | - Damage Location Vector                              |
| DOFs    | - Degrees of Freedom                                  |
| EOM     | - Equation of Motion                                  |
| FE      | - Finite element                                      |
| FEM     | - Finite element model                                |
| FRF     | - Frequency response function                         |
| MAC     | - Modal assurance criterion                           |
| MDOF    | - Multiple degree of freedom                          |
| RFRF    | - Receptance frequency response function              |
| SEREP   | - System equivalent reduction expansion process       |
| Plate9  | - Thin cantilever plate with 9 nodes and 4 elements   |
| Plate28 | - Thin cantilever plate with 28 nodes and 18 elements |

---

# TABLE OF CONTENTS

|  |     |
|--|-----|
| Title  | i   |
| Acknowledgement  | ii  |
| Abstract   | iii |
| Nomenclature   | iv  |
| Table of Contents  | vi  |
| List of Figures  | ix  |
| List of Tables   | xiv |
|  |     |
| 1. Introduction .....  | 1   |
| 1.1 Review of Previous Work.....   | 3   |
| 1.2 Damage Detection Techniques Based on Experimental Data.....                              | 3   |
| 1.3 Damage Detection Techniques Based on Modal Data and Finite Element<br>Analysis Data..... | 4   |
| 1.3.1 Optimal Matrix Method.....   | 6   |
| 1.3.2 Eigen-Structure Assignment.....  | 8   |
| 1.3.3 Sensitivity Analysis.....  | 8   |
| 1.4 Methods to Overcome Coordinate Incompatibility.....                                      | 9   |
| 1.4.1 Reducing the Analytical Data.....  | 9   |
| 1.4.2 Expanding the Measurement Data.....  | 9   |
| 1.5 Scope of Present Work.....   | 10  |
| 1.6 Assumptions of This Study.....   | 12  |
|  |     |
| 2. Damage Detection Using Frequency Response Function Data.....                              | 14  |
| 2.1 Damage Location Vector.....  | 14  |
| 2.2 Damage Detection with Coordinate Incompatibility.....                                    | 19  |
| 2.3 Dynamic Expansion Method A (D.E. A).....   | 21  |
| 2.4 Normalised Random Errors.....  | 23  |
| 2.5 Damage Detection Algorithm Written in Matlab™.....                                       | 24  |

---

---

|  |    |
|--|----|
| 3. Damage Detection in a Simple Mass Spring System.....                        | 27 |
| 3.1 Damage Detection without Coordinate Incompatibility and No Noise.....      | 31 |
| 3.2 Damage Detection without Coordinate Incompatibility and with 5% Noise..... | 32 |
| 3.3 Damage Detection with Coordinate Incompatibility and No Noise.....         | 34 |
| 3.3.1 Six Measured Coordinate Supplied.....                                    | 35 |
| 3.3.2 Eight Measured Coordinate Supplied.....                                  | 37 |
| 3.3.3 Ten Measured Coordinate Supplied.....                                    | 38 |
| 3.4 Damage Detection with Coordinate Incompatibility and with 5% Noise.....    | 40 |
| 3.5 Discussion.....  | 42 |
| 4. Damage Detection in Truss Structures.....                                   | 43 |
| 4.1 Description of the Structure.....  | 43 |
| 4.2 Case of Non Damaged Structure.....   | 47 |
| 4.3 Damage Cases.....  | 51 |
| 4.3.1 Damage Case A.....   | 51 |
| 4.3.2 Damage Case B.....   | 53 |
| 4.3.3 Damage Case C.....   | 55 |
| 4.4 Damage Detection without Coordinate Incompatibility and No Noise.....      | 57 |
| 4.5 Damage Detection without Coordinate Incompatibility and with 5% Noise..... | 62 |
| 4.6 Damage Detection with Coordinate Incompatibility and with 5% Noise.....    | 67 |
| 4.7 Discussion.....  | 72 |
| 5. Damage Detection in Plate Structures.....                                   | 73 |
| 5.1 Basic Thin Plate Theory.....   | 73 |
| 5.2 Validation of Mass and Stiffness Matrices.....                             | 75 |
| 5.2.1 Finite Element Analysis of Plate9.....                                   | 76 |
| 5.2.2 Theoretical Calculations Using Matlab™.....                              | 79 |
| 5.2.3 Comparison of Theoretical Results with Finite Element.....               | 80 |
| 5.3 Simulation of Damage.....  | 81 |
| 5.4 Description of the Plate Structure.....                                    | 82 |
| 5.5 Undamaged Case.....  | 86 |
| 5.6 Damage Case A.....   | 89 |

---

---

|  |     |
|--|-----|
| 5.7 Damage Case B.....   | 93  |
| 5.8 Damage Case C.....   | 98  |
| 5.9 Coordinate Incompatibility.....                                  | 101 |
| 5.10 Discussion.....   | 107 |
| <br>   |     |
| 6. Experimental Studies: Damage Detection of a Cantilever Plate..... | 108 |
| 6.1 Basic Modal Analysis.....  | 108 |
| 6.1.1 Transducers.....   | 109 |
| 6.1.2 Excitation Mechanism.....                                      | 110 |
| 6.1.3 Frequency Analyser.....  | 110 |
| 6.2 Experimental Setup.....  | 111 |
| 6.3 Experimental Test Piece.....                                     | 113 |
| 6.4 Calibration.....   | 114 |
| 6.5 Structure Setup.....   | 117 |
| 6.6 Simulation of Damage.....  | 117 |
| 6.7 Obtaining Experimental Frequency Response Function Data.....     | 117 |
| 6.8 ICATS & Circle Fit Method.....                                   | 118 |
| 6.9 Undamaged Case.....  | 119 |
| 6.10 Damage Case A.....  | 124 |
| 6.11 Damage Case B.....  | 130 |
| 6.12 Damage Case C.....  | 136 |
| 6.13 Discussion.....   | 143 |
| <br>   |     |
| 7. Conclusions.....  | 144 |
| <br>   |     |
| References.....  | 147 |
| <br>   |     |
| Appendices.....  | 151 |

---

# LIST OF FIGURES

## Chapter 1:

|   |   |
|---|---|
| Figure 1.1a: Difference between Two Models resulting in Modelling Errors..... | 5 |
| Figure 1.1b: Difference between Two Models resulting in Damage.....           | 5 |

## Chapter 2:

|   |    |
|---|----|
| Figure 2.1a: An Example of a 3D DLV Plot of a 12 DOFs Mass Spring System without Noise.....   | 17 |
| Figure 2.1b: An Example of a 2D CDLV Plot for a 12 DOFs Mass Spring System without Noise..... | 18 |
| Figure 2.2: All Nodes are Measured, No Incompatibility Exists.....                            | 19 |
| Figure 2.3: Not All Nodes are Measured, Coordinate Incompatibility Exists.....                | 20 |
| Figure 2.4: Damage Detection Algorithm Logic.....   | 26 |

## Chapter 3:

|  |    |
|--|----|
| Figure 3.1: Simple 12 DOFs Mass Spring System.....   | 28 |
| Figure 3.2: Receptance FRF Plot at $\alpha(1, 1)$ for Before and After Damage for the Simple 12 DOFs Mass Spring System.....                       | 30 |
| Figure 3.3a: 3D DLV Plot of the 12 DOFs Mass Spring System without Coordinate Incompatibility and No Noise Interference.....                       | 31 |
| Figure 3.3b: 2D CDLV Plot of the 12 DOFs Mass Spring System without Coordinate Incompatibility and No Noise Interference.....                      | 32 |
| Figure 3.4a: 3D DLV Plot of the 12 DOFs Mass Spring System without Coordinate Incompatibility and with 5% Noise Interference.....                  | 33 |
| Figure 3.4b: 2D CDLV Plot of the 12 DOFs Mass Spring System without Coordinate Incompatibility and with 5% Noise Interference.....                 | 34 |
| Figure 3.5a: 3D DLV Plot of the 12 DOFs Mass Spring System with 6 Measured Coordinates and 6 Expanded Coordinates and No Noise Interference.....   | 35 |
| Figure 3.5b: 2D CDLV Plot of the 12 DOFs Mass Spring System with 6 Measured Coordinates and 6 Expanded Coordinates and No Noise Interference.....  | 36 |
| Figure 3.6a: 3D DLV Plot of the 12 DOFs Mass Spring System with 8 Measured Coordinates and 4 Expanded Coordinates and No Noise Interference.....   | 37 |
| Figure 3.6b: 2D CDLV Plot of the 12 DOFs Mass Spring System with 8 Measured Coordinates and 4 Expanded Coordinates and No Noise Interference.....  | 38 |
| Figure 3.7a: 3D DLV Plot of the 12 DOFs Mass Spring System with 10 Measured Coordinates and 2 Expanded Coordinates and No Noise Interference.....  | 39 |
| Figure 3.7b: 2D CDLV Plot of the 12 DOFs Mass Spring System with 10 Measured Coordinates and 2 Expanded Coordinates and No Noise Interference..... | 40 |
| Figure 3.8a: 3D DLV Plot of the 12 DOFs Mass Spring System with 10 Measured Coordinates and 2 Expanded Coordinates and 5% Noise Interference.....  | 41 |
| Figure 3.8b: 2D CDLV Plot of the 12 DOFs Mass Spring System with 10 Measured Coordinates and 2 Expanded Coordinates and 5% Noise Interference..... | 41 |

---

**Chapter 4:**

|  |    |
|--|----|
| Figure 4.1: NASA Eight Bay Truss Structure.....  | 44 |
| Figure 4.2: Section of Eight Bay Truss Lattice Structure.....                                      | 45 |
| Figure 4.3: Receptance FRF Plot of $\alpha(1, 1)$ for Undamage Case.....                           | 49 |
| Figure 4.4a: 3D DLV Plot for Undamage Case without Coordinate Incompatibility<br>nor noise.....    | 50 |
| Figure 4.4b: 2D CDLV Plot for Undamage Case without Coordinate Incompatibility<br>nor noise.....   | 50 |
| Figure 4.5: Receptance FRF Plot of $\alpha(1, 1)$ for Damage Case A.....                           | 53 |
| Figure 4.6: Receptance FRF Plot of $\alpha(1, 1)$ for Damage Case B.....                           | 55 |
| Figure 4.7: Receptance FRF Plot of $\alpha(1, 1)$ for Damage Case C.....                           | 56 |
| Figure 4.8a: 3D DLV Plot for Damage Case A without Coordinate Incompatibility<br>nor noise.....    | 57 |
| Figure 4.8b: 2D CDLV Plot for Damage Case A without Coordinate Incompatibility<br>nor noise.....   | 58 |
| Figure 4.9a: 3D DLV Plot for Damage Case B without Coordinate Incompatibility<br>nor noise.....    | 59 |
| Figure 4.9b: 2D CDLV Plot for Damage Case B without Coordinate Incompatibility<br>nor noise.....   | 60 |
| Figure 4.10a: 3D DLV Plot for Damage Case C without Coordinate Incompatibility<br>nor noise.....   | 61 |
| Figure 4.10b: 2D CDLV Plot for Damage Case C without Coordinate Incompatibility<br>nor noise.....  | 62 |
| Figure 4.11a: 3D DLV Plot for Damage Case A without Coordinate Incompatibility<br>(2% Noise).....  | 63 |
| Figure 4.11b: 2D CDLV Plot for Damage Case A without Coordinate Incompatibility<br>(5% Noise)..... | 63 |
| Figure 4.12a: 3D DLV Plot for Damage Case B without Coordinate Incompatibility<br>(5% Noise).....  | 64 |
| Figure 4.12b: 2D CDLV Plot for Damage Case B without Coordinate Incompatibility<br>(5% Noise)..... | 65 |
| Figure 4.13a: 3D DLV Plot for Damage Case C without Coordinate Incompatibility<br>(5% Noise).....  | 66 |
| Figure 4.13b: 2D CDLV Plot for Damage Case C without Coordinate Incompatibility<br>(5% Noise)..... | 66 |
| Figure 4.14a: 3D DLV Plot for Damage Case A with Coordinate Incompatibility<br>(5% Noise).....     | 67 |
| Figure 4.14b: 2D CDLV Plot for Damage Case A with Coordinate Incompatibility<br>(5% Noise).....    | 68 |
| Figure 4.15a: 3D DLV Plot for Damage Case B with Coordinate Incompatibility<br>(5% Noise).....     | 69 |
| Figure 4.15b: 2D CDLV Plot for Damage Case B with Coordinate Incompatibility<br>(5% Noise).....    | 70 |
| Figure 4.16a: 3D DLV Plot for Damage Case A with Coordinate Incompatibility<br>(5% Noise).....     | 71 |

---

|   |     |
|---|-----|
| Figure 4.16b: 2D CDLV Plot for Damage Case A with Coordinate Incompatibility<br>(5% Noise).....                         | 72  |
| <b>Chapter 5:</b>   |     |
| Figure 5.1: A Single Rectangular Thin Flat Plate Element.....   | 74  |
| Figure 5.2: Thin Flat Plate Structure with 4 Smaller Elements also Known as Plate9.....                                 | 76  |
| Figure 5.3: The Plate9 Example Modelled in ANSYS™.....  | 77  |
| Figure 5.4: Mode Shape No.1 – Isometric and Side View of Plate9 Example.....  | 78  |
| Figure 5.5: Mode Shape No.2 – Isometric and Side View of Plate9 Example.....  | 78  |
| Figure 5.6: Mode Shape No.3 – Isometric and Side View of Plate9 Example.....  | 79  |
| Figure 5.7a: Damage between Nodes.....  | 81  |
| Figure 5.7b: Damage of One Whole Element.....   | 81  |
| Figure 5.7c: Partial Damage of One Element Affecting Only the Nodes.....  | 82  |
| Figure 5.7d: Damage at the Fixing Point.....  | 82  |
| Figure 5.8a: Nodes and Elements Configuration for Plate28 Example.....  | 83  |
| Figure 5.8b: Nodes and Elements Configuration for Plate28 Example Illustrating<br>Damage Case A.....                    | 83  |
| Figure 5.8c: Nodes and Elements Configuration for Plate28 Example Illustrating<br>Damage Case B.....                    | 84  |
| Figure 5.8d: Nodes and Elements Configuration for Plate28 Example Illustrating<br>Damage Case C.....                    | 84  |
| Figure 5.9: Point Receptance Plot at $\alpha(1, 1)$ for Undamage Case.....  | 88  |
| Figure 5.10: Receptance FRF Plot at $\alpha(1, 1)$ for Damage Case A.....   | 90  |
| Figure 5.11a: 3D DLV Plot for Damage Case A without Coordinate Incompatibility<br>(5% Noise).....                       | 91  |
| Figure 5.11b: 2D CDLV Plot for Damage Case A without Coordinate Incompatibility<br>(5% Noise).....                      | 92  |
| Figure 5.12: Receptance FRF Plot at $\alpha(1, 1)$ for Damage Case B.....   | 95  |
| Figure 5.13a: 3D DLV Plot for Damage Case B without Coordinate Incompatibility<br>(5% Noise).....                       | 96  |
| Figure 5.13b: 2D CDLV Plot for Damage Case B without Coordinate Incompatibility<br>(5% Noise).....                      | 96  |
| Figure 5.14: Receptance FRF Plot at $\alpha(1, 1)$ for Damage Case C.....   | 99  |
| Figure 5.15a: 3D CDLV Plot for Damage Case C without Coordinate Incompatibility<br>(5% Noise).....                      | 100 |
| Figure 5.15b: 2D CDLV Plot for Damage Case C without Coordinate Incompatibility<br>(5% Noise).....                      | 101 |
| Figure 5.16a: 3D DLV Plot for Damage Case A with 48 Measured Coordinates and<br>24 Expanded Coordinates (5% Noise)..... | 103 |

|  |     |
|--|-----|
| Figure 5.16b: 2D CDLV Plot for Damage Case A with 48 Measured Coordinate and 24 Expanded Coordinates (5% Noise).....                 | 103 |
| Figure 5.17: Node Map of Possible Damage Area for Damage Case A.....   | 104 |
| Figure 5.18a: 3D DLV Plot for Damage Case A with 60 Measured Coordinates and 12 Expanded Coordinates (5% Noise).....                 | 105 |
| Figure 5.18b: 2D CDLV Plot for Damage Case A with 60 Measured Coordinates and 12 Expanded Coordinates (5% Noise).....                | 106 |
| Figure 5.19: Node Map of Possible Damage Area.....   | 106 |
| <br><b>Chapter 6:</b>  |     |
| Figure 6.1: Limitation of Frequency Response Range.....  | 109 |
| Figure 6.2: Sketch of Experimental Setup.....  | 112 |
| Figure 6.3: Experimental Test Piece.....   | 113 |
| Figure 6.4: Free-Free Known Mass Structure.....  | 115 |
| Figure 6.5: Accelerance and Coherence Plot for Calibration of Known Mass.....  | 116 |
| Figure 6.6: Experimental Setup of Plate28 without Damage.....  | 119 |
| Figure 6.7: ICATS Identification of Mode Shapes.....   | 120 |
| Figure 6.8: Comparison of Experimental against Theoretical Receptance FRF at $\alpha(1, 1)$ for the Undamage Cantilevered Plate..... | 121 |
| Figure 6.9a: 3D DLV Plot for Undamage Case.....  | 123 |
| Figure 6.9b: 2D CDLV Plot for Undamage Case.....   | 123 |
| Figure 6.10: Experimental Setup of Plate28 for Damage Case A.....  | 124 |
| Figure 6.11: Comparison of Experimental against Theoretical Receptance FRF at $\alpha(1, 1)$ for Damage Case A.....                  | 126 |
| Figure 6.12a: 3D DLV Plot for Damage Case A.....   | 128 |
| Figure 6.12b: 2D CDLV Plot for Damage Case A.....  | 128 |
| Figure 6.13: Configuration of Lower Magnitude DOFs for Damage Case A.....  | 130 |
| Figure 6.14: Experimental Setup for Plate28 for Damage Case B.....   | 131 |
| Figure 6.15: Comparison of Experimental against Theoretical Receptance FRF at $\alpha(1, 1)$ for Damage Case B.....                  | 132 |
| Figure 6.16a: 3D DLV Plot for Damage Case B.....   | 134 |
| Figure 6.16b: 2D CDLV Plot for Damage Case B.....  | 134 |
| Figure 6.17: Configuration of Lower Magnitude DOFs for Damage Case B.....  | 136 |
| Figure 6.18: Experimental Setup for Damage Case C.....   | 137 |
| Figure 6.19: Comparison of Experimental against Theoretical Receptance FRF at $\alpha(1, 1)$ for Damage Case C.....                  | 139 |
| Figure 6.20a: 3D DLV Plot for Damage Case C.....   | 140 |

---

|   |     |
|---|-----|
| Figure 6.20b: 2D CDLV Plot for Damage Case C.....                         | 141 |
| Figure 6.21: Configuration of Lower Magnitude DOFs for Damage Case C..... | 143 |

---

# LIST OF TABLES

## Chapter 1:

No Table Used

## Chapter 2:

No Table Used

## Chapter 3:

|   |    |
|---|----|
| Table 3.1: Stiffness Matrix of the Undamaged Structure for the 12 DOFs Mass Spring System.....      | 27 |
| Table 3.2: Stiffness Matrix of the Damaged Structure for the 12 DOFs Mass Spring System.....        | 29 |
| Table 3.3: Mass Matrix for the Undamaged/Damaged 12 DOF Mass Spring System.....                     | 29 |
| Table 3.4: Natural Frequency Before and After Damage for the Simple 12 DOFs Mass Spring System..... | 29 |
| Table 3.5: Measured Coordinates Index.....  | 35 |

## Chapter 4:

|   |    |
|---|----|
| Table 4.1: Mass Configuration.....  | 45 |
| Table 4.2: Summary of Damage Cases.....   | 46 |
| Table 4.3: Corresponding DOFs for Damage Cases.....   | 46 |
| Table 4.4: Diagonal Undamage Stiffness Values at DOF Locations.....                             | 47 |
| Table 4.5: Comparison of Natural Frequencies between Matlab™ and ANSYS™ for Undamage Case.....  | 48 |
| Table 4.6: Comparison of Delta K Values for Damage Case A.....                                  | 51 |
| Table 4.7: Comparison of Natural Frequencies between Matlab™ and ANSYS™ for Damage Case A.....  | 52 |
| Table 4.8: Comparison of Delta K Values for Damage Case B.....                                  | 54 |
| Table 4.9: Comparison of Natural Frequencies between Matlab™ and ANSYS™ for Damage Case B.....  | 54 |
| Table 4.10: Comparison of Natural Frequencies between Matlab™ and ANSYS™ for Damage Case C..... | 56 |

## Chapter 5:

|   |    |
|---|----|
| Table 5.1: DOFs with Respect to Node Numbers for a Single Plate Element.....                    | 74 |
| Table 5.2: First Six Natural Frequencies and Mode Shape for Plate9 Example from ANSYS™.....     | 77 |
| Table 5.3: Comparison of Results for Non-Compatible and Compatible Theories against ANSYS™..... | 80 |

|   |    |
|---|----|
| Table 5.4: Summary of Simulated Damage Cases for Plate28 Example.....                           | 85 |
| Table 5.5: Corresponding DOFs for Damage Cases.....   | 86 |
| Table 5.6: Comparison of Natural Frequencies between Matlab™ and ANSYS™ for Undamage Case.....  | 87 |
| Table 5.7: Diagonal Undamaged Stiffness Value at DOF Locations.....                             | 87 |
| Table 5.8: Comparison of Natural Frequencies between Matlab™ and ANSYS™ for Damage Case A.....  | 89 |
| Table 5.9: Comparison of Natural Frequencies between Undamaged and Damage Case A.....           | 90 |
| Table 5.10: Damage Extent Corresponding to DOFs for Damage Case A.....                          | 93 |
| Table 5.11: Comparison of Natural Frequencies between Matlab™ and ANSYS™ for Damage Case B..... | 94 |
| Table 5.12: Comparison of Natural Frequencies between Undamaged and Damage Case B.....          | 94 |
| Table 5.13: Damage Extent Corresponding to DOFs for Damage Case B.....                          | 97 |
| Table 5.14: Comparison of Natural Frequencies between Matlab™ and ANSYS™ for Damage Case C..... | 98 |
| Table 5.15: Comparison of Natural Frequencies between Undamaged and Damage Case C.....          | 99 |

## Chapter 6:

|   |     |
|---|-----|
| Table 6.1: Comparison of Natural Frequencies for the Cantilever Plate Undamage.....                   | 121 |
| Table 6.2: Natural Frequency of the Cantilever Plate Obtained from Experiment for Damage Case A.....  | 125 |
| Table 6.3: Change from Experimental Undamage Natural Frequency for Damage Case A.....                 | 125 |
| Table 6.4: Change in Stiffness for Damage Case A.....   | 129 |
| Table 6.5: Summary of Lower Magnitude DOFs for Damage Case A.....                                     | 129 |
| Table 6.6: Natural Frequency of the Cantilever Plate Obtained from Experiment for Damage Case B.....  | 131 |
| Table 6.7: Change from Experimental Undamage Natural Frequency for Damage Case B.....                 | 132 |
| Table 6.8: Change in Stiffness for Damage Case B.....   | 135 |
| Table 6.9: Summary of Lower Magnitude DOFs for Damage Case B.....                                     | 135 |
| Table 6.10: Natural Frequency of the Cantilever Plate Obtained from Experiment for Damage Case C..... | 138 |
| Table 6.11: Change from Experimental Undamage Natural Frequency for Damage Case C.....                | 138 |
| Table 6.12: Rank of DOFs from the 2D CDLV Plot for Damage Case C.....                                 | 141 |

## Chapter 7:

No Tables Used

# CHAPTER 1

## INTRODUCTION

In recent years, structural damage detection has become a major research focus in the area of structural dynamics. Advancements in material science have made it possible to build larger and more complex structures that are much lighter in weight. It is therefore essential to periodically monitor these structures to ensure that a catastrophic failure does not occur.

Despite existing non-destructive testing methods such as ultrasound, X-ray, dye penetrant, magnetic particles and acoustic emissions, sporadic failures that have disastrous consequences in terms of human life and resources still occur. This is largely due to the fact that existing non-destructive testing methods are often limited to observations in a limited area and rely on a presumption of the likely area of damage. Often it may be difficult to observe visually any damage that may have occurred within a structure due to material degradation, since the surface appearance may remain unchanged. It is therefore desirable to devise a method that can be used to evaluate the integrity of a structure as a whole. Such a technique that can successfully detect damage within a structure would greatly aid in ensuring the integral safety of a structural system.

Ideally, a method that can successfully detect damage must be able to address the following criteria:

1. Assess that structural damage has occurred
  2. Determine the location of the damage
  3. Quantify the severity of the damage
  4. Predict the remaining service life of the damaged structure
-

In most cases, if the first three criteria are achieved, then the fourth criterion is obtainable.

Aside from successfully addressing the essential criteria for a successful damage detection technique, the method must also be able to deal with the major barriers that have been hindering successful damage detection.

In structural damage detection there are two major barriers that must be overcome, these are:

1. Noisy measurement data
2. Coordinate Incompatibility

It is relatively simple to determine damage from measurements that are free from errors. However, in reality, measurements are always contaminated by various random errors or noise. The amount of noise present in the measurement data ultimately affects the quality of the data and the accuracy of the detected damage. An inability to cope with data that may be contaminated by noise would lead to inaccurate damage detection.

Coordinate incompatibility is caused by the inability to adequately capture and describe the characteristic behaviour of a structure. This is largely due to the fact that a real life structure has an infinite number of degrees of freedom (DOFs), and in reality not all DOFs may be measured on a structure. This leads to a coordinate incompatibility between the data obtained from the spatial model of the structure and the data obtained from measurement. Methods to overcome coordinate incompatibility will be discussed later in this chapter.

---

## 1.1 REVIEW OF PREVIOUS WORK

At present structural damage detection is still in its infancy. In spite of the multitude of techniques that have been developed, not many techniques are able to address all the criteria for a successful damage detection technique.

To date, existing damage detection techniques can be categorized into two main areas of study.

There are as follows:

1. Damage detection techniques based on experimental data
2. Damage detection techniques based on modal data and finite element data

## 1.2 DAMAGE DETECTION TECHNIQUES BASED ON EXPERIMENTAL DATA

In the past, early structural damage detection techniques were very crude and inaccurate, as they relied on visual or acoustic methods to determine damage. A common practice used by early locomotive drivers in the 19<sup>th</sup> and 20<sup>th</sup> Century to detect the presence of damage was to hammer each wheel of their locomotive to determine if there was any difference in the acoustic responses. A difference in the norm would indicate the presence of damage. This was highly inaccurate as it relied on the driver's acoustic experiences. It was also difficult to produce the same consistent impact each time.

Early damage detection techniques during the 19<sup>th</sup> Century involved determining frequency shifts of resonant frequencies of a structure. It was found that changes in the stiffness of a structure often indicated the presence of damage. It was also found that a change in the stiffness of a structure was also linked to changes in natural frequencies of the same structure. Cawley and Adams (1979) suggested that if one set of natural frequency was measured before the structure was put into service, subsequent natural frequency measurements could be used to determine

---

whether the structure was still sound by comparing the measured frequency with the original natural frequency. Furthermore, by measuring the natural frequencies of a structure at different stages of its life, it is possible to observe the frequency shifts as the damage propagates through the structure.

A similar damage detection technique based on frequency used statistical methods to predict the most likely damage location (Friswell et al. 1994). It was assumed that sets of frequencies were measured before the structure was put into service, which represented the undamaged structure. From these, frequency shifts of the first several modes for all possible damage scenarios were calculated mathematically. Measurements of natural frequencies of the structure at different stages of its life would then be fitted against the postulated damage scenarios. The quality of the fit to each postulated damage scenario indicated the existence of damage.

The method proposed by Cawley and Adams (1979) did not give any indication with regards to the accuracy of their predictions. Their method would still locate damage from slight changes in the natural frequencies due to temperature effects or measurement noise, even though no damage actually exists. Statistical methods proposed by Friswell et al. (1994) postulating damage scenarios were found to be impractical, as a lot of unnecessary calculations were required.

### **1.3 DAMAGE DETECTION TECHNIQUES BASED ON MODAL DATA AND FINITE ELEMENT ANALYSIS DATA**

Considerable advancements in Modal Analysis in the field categorised as “Model Updating” were also applied to structural damage detection. It was possible to borrow techniques developed for model updating because by nature damage detection and model updating are intrinsically linked. Both aim to determine the differences between two models.

---

The objective of model updating is to determine the difference between measured experimental data and finite element model (FEM) data. Here, it is assumed that the measured experimental data is correct and that the difference between the FEM data represents the modelling errors as shown in Figure 1.1a.

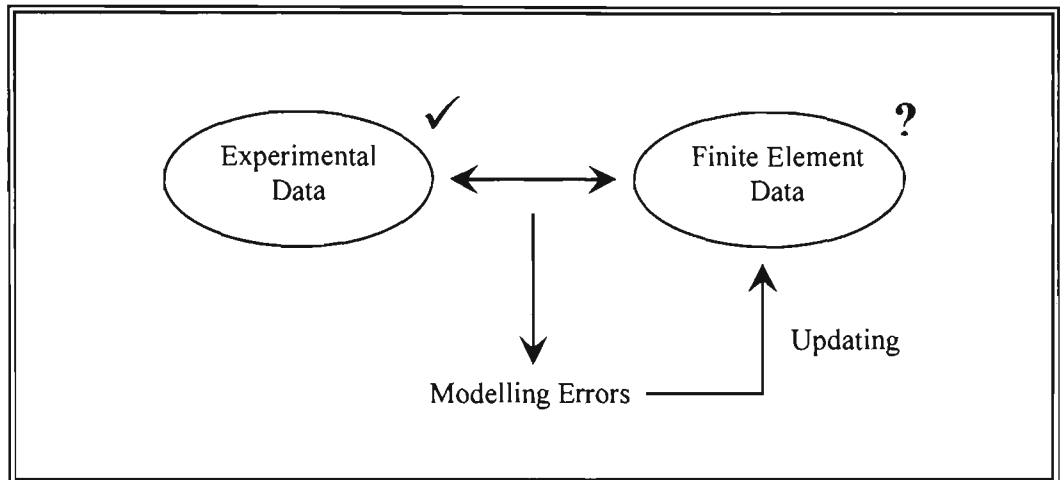


**Figure 1.1a: Difference between Two Models resulting in Modelling Errors**

For damage detection, the objective is to determine the difference between the undamaged structure and the damaged structure. Here the data from the damaged structure is usually obtained from experimental methods, while data from the undamaged structure is usually obtained from a finite element model. The difference between the two models represents damage as shown in Figure 1.1b.

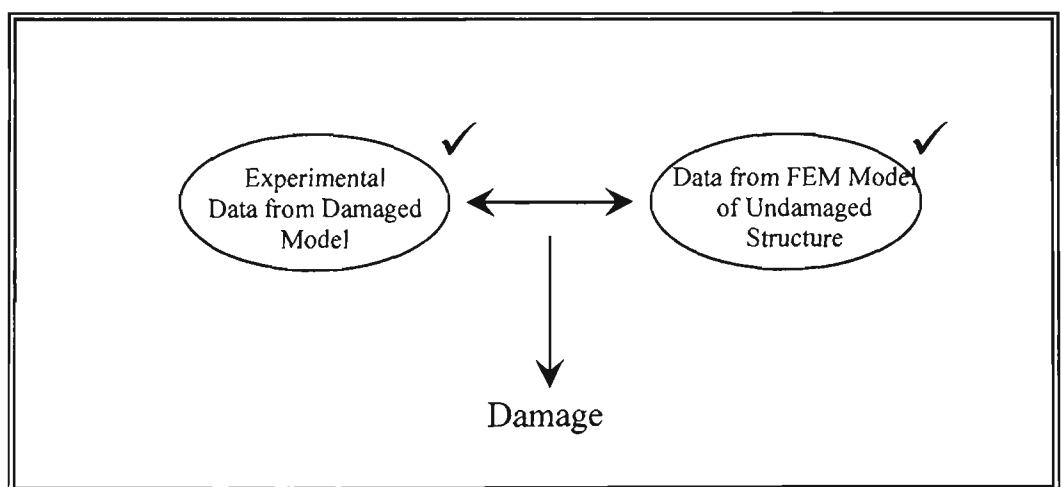


**Figure 1.1b: Difference between Two Models resulting in Damage**

The relevant techniques of model updating that can be used for structural damage detection can be broadly categorised into three fields and they are as follows:

1. Optimal Matrix Method
2. Eigen-structure Assignment
3. Sensitivity Analysis

### **1.3.1 OPTIMAL MATRIX METHOD**

The goal of Optimal Matrix Method is to find an updated system matrix which is closest to the original matrix that produces the measured natural frequencies and mode shapes. Rodden (1967) was the first to use this optimal matrix approach. He used vibrational test data to determine the influence coefficients of a structure. Brock (1968) postulated that since the data was determined experimentally that errors might have been introduced. Hence, in order to determine the optimal matrix, the matrix must satisfy a set of measurements, as well as meeting the requirements of symmetry and positive definiteness. Berman and Flannely (1971) addressed the possibility of deriving an optimal system matrix with incomplete vibration data (when the number of degrees of freedom (DOFs) and the number of modes do not coincide). Baruch and Bar Itzack (1978) developed a method that involved the minimisation of Euclidean norm subjected to the orthogonality requirements. Berman and Ngay (1983) also adopted a similar approach, but were able to improve on the mass and stiffness matrices, producing more refined mass and stiffness matrices that conform to the orthogonality requirements. However, in order to achieve the orthogonality requirement, the physical connectivity of the structure was not preserved. Hence, it would not be possible to determine the location of damage within the structure. Kabe (1985) showed that a more accurate stiffness matrix would be achieved if the structural connectivity could be preserved. He proposed that this could be accomplished by insisting that all coefficients with values of zero in the original stiffness matrix should also have zero values in the adjusted stiffness matrix. Although the result was an adjusted stiffness matrix that predicted the measured

---

mode data accurately and also preserved the connectivity of the original stiffness matrix, the mathematical solution of the method required large eigen solutions that would not be practical for large space structure problems that may have thousands of degrees of freedom. In order to avoid the eigen solution requirements without losing the advantage of Kabe's (1985) method, Krammer (1988) utilised the projector matrix theory and the Moore-Penrose generalised theory to produce a more computationally efficient solution. Zimmerman et al. (1998) also explored the possibilities if using Linear Matrix Inequality (LMI) to provide an improved optimal matrix update and parameter update methods for model refinements and damage detection in structures. This was highly advantageous, since LMI optimisation problem have low computational complexities and can be solved very efficiently.

Another type of approach that can be classified as an optimal matrix method involves minimisation of the rank of the perturbation matrix, rather than the norm of the perturbation matrix. This approach is based on the assumption that the damage will tend to be concentrated in a few structural members, rather than be distributed throughout a large number of structural members. Zimmerman and Kauok (1994) presented the basic minimum rank perturbation theory (MRPT) algorithm to estimate the mass, stiffness and proportional damping perturbation matrices simultaneously. A nonzero entry in the damage vector is interpreted as an indication of the location of damage. The resulting perturbation matrices have the same rank as the numbers of modes used to compute the model force errors.

Lim and Kashagaki (1994) used the concept of best achievable eigen-vectors, a method developed by which measured modes and frequencies can be used to determine both the location and magnitude of damage within the structure. Instead of identifying matrix coefficient changes, this method identifies damaged structural elements directly, thus the additional step of identifying damaged members from the matrix coefficient changes is avoided.

---

### 1.3.2 EIGEN-STRUCTURE ASSIGNMENT

Eigen-structure assignment is another approach that may be used for structural damage detection. This technique is used in engineering to dictate the force response of a structure. For structural damage detection, eigen-structure assignment can be used to determine a pseudo-control value that would be required to produce the measured modal properties with the initial finite element model (FEM). This pseudo-control component is then translated into a matrix adjustment, which can be applied to the initial FEM. Zimmerman and Widengren (1990) used a symmetric eigen-structure assignment technique to produce the adjusted finite element model which incorporated information regarding eigen parameters of the damaged structure.

### 1.3.3 SENSITIVITY ANALYSIS

Sensitivity Analysis is another approach that may be used for structural damage detection. This method relies on the sensitivity analysis of the modal parameters with respect to the physical variables and is based on the solution of the first order Taylor series that minimises an error function of the matrix perturbations. Haug and Choi (1984) calculated the first and second order derivatives from measured structural responses with respect to design variables using the generalised global stiffness and mass matrices formulation of structural equation. The variations in the stiffness and mass matrices were shown to be accurate, thus avoiding the requirements for explicit reduction of matrices as seen in other methods. However this method was only successful for simple structures, since the sensitivity analysis was based on the derivatives of the first and second order Taylor series meant that the method would be unable to deal with 'large' physical variable changes that may be present in larger and more complex structures.

---

## **1.4 METHODS TO OVERCOME COORDINATE INCOMPATIBILITY**

In reality, coordinate incompatibility exists and must be addressed. Any successful damage detection technique must address this problem. The existing methods that address the problem of coordinate incompatibility can be broadly categorised as follows:

1. Reducing the analytical data
2. Expanding the measured data

### **1.4.1 REDUCING THE ANALYTICAL DATA**

There are a number of reduction techniques developed in recent year. The most commonly used reduction technique is Guyan Reduction (1965). However, it is not a preferred technique used for damage detection since the original connectivity among the DOFs may be distorted after the reduction. As a result, it becomes impossible to locate accurately where the damage occurs (Tran and He, 1998). For such reasons, many researchers have not utilised model reduction techniques, since the structural connectivity is an important element required for the location of damage.

The System Equivalent Reduction Expansion Process (SEREP) developed by O'Callahan, Aitavale and Riemer (1989) allows the exact mapping of large analytical models down to much smaller equivalent reduced models. Unlike other reduction processes, SEREP produces a reduced model whose frequencies and mode shapes are exactly the same as the full model for the selected modes of interest.

### **1.4.2 EXPANDING THE MEASURED DATA**

The objective of these methods is to expand the DOFs of the measured FRF data to match the DOFs of the analytical model. Choudhury (1996) devised a method referred to as the Dynamic

---

Expansion Method A (D.E. A) that is based on Kidder's (1973) approach, in which the unmeasured FRF data can be related to the measured FRF data by a linear transformation. The result is a complete set of FRF data made up with measured and expanded FRF data. This complete FRF data has equal numbers of coordinates to that of the analytical FE model. Choudhury and He (1993) have also used interpolation techniques based on an inverse reduction procedure to also overcome coordinate incompatibility. The FE model data and experimental receptance data were used to interpolate the receptance data corresponding to the unmeasured coordinates. This also produced a complete set of FRF data that has an equal number of coordinates to that of the analytical FE model. However, this technique was found to be successful only under certain ideal conditions.

## **1.5 SCOPE OF PRESENT WORK**

Damage detection methods using measured frequency response function (FRF) data has been found to be a promising method that can address the criteria required for a successful damage detection technique. It has been proposed by Choudhury (1996) to use measured FRF data and finite element (FE) data, instead of modal data for damage detection, since using measured FRF data for damage detection offers advantages over the traditional methods that utilises modal data.

Firstly, any numerical errors inherent in the modal analysis results caused by inaccurate curve fitting are avoided. Secondly, no more effort is required to process measured FRF data in order to derive modal data. Ultimately, the most significant advantage of using measured FRF data over derived modal analysis data lies in the fact that FRF data provides an abundant amount of information on the dynamic behaviour of a structure compared to modal data. Modal data provides information on resonant frequencies, corresponding mode shapes and damping ratios only. Hence modal data offers only limited information about the dynamic behaviour of a

---

structure because much of the information is lost during numerical processes to obtain the modal data. For this reason, it has been found that modal data cannot provide sufficient information needed to describe the dynamic behaviour of the structure if it is contaminated with noise.

Frequency response function data on the other hand contains a greater number of elements, of which each element contains information on the dynamic behaviour of the structure over a large number of discrete frequencies. If one part of the FRF data is contaminated by noise, then the other parts can be referred to since there is an abundant amount of information available.

The research program presented in this thesis will be concerned with the further development and testing of the damage detection algorithm developed by Choudhury (1996). A detailed study into the robustness of the Damage Detection Algorithm will be carried out. The content covered in this thesis is outlined as follows:

Chapter 2: Introduces the theories involved in the developed Damage Detection Algorithm. Components of the “Damage Location Vector (DLV)”, the “Damage Location Vector Plot (DLV Plot)” and the “Cumulative Damage Location Vector Plot (CDLV Plot)”, which make up the Damage Detection Algorithm will be discussed in details. How normalised random error (noise) can be simulated and its effects on the developed algorithm will also be investigated.

Chapter 3: Theories discussed in Chapter 2 will be applied to a simple 12-DOFs mass spring system to assess the effectiveness and robustness of the developed damage detection algorithm in all types of situations. The simplicity of such an example will allow detailed explanation of the Damage Detection Algorithm process.

---

- Chapter 4: A large three dimensional NASA eight bay space truss structure will be investigated theoretically. Simulated damage will be introduced to various locations on the eight bay truss structure. The damage detection algorithm will firstly be used to detect the simulated damage in conditions where no coordinate incompatibility exists. Coordinate incompatibility and noise interference will then be introduced into the structure. The success of the damage detection algorithm under various conditions will be assessed.
- Chapter 5: The robustness of the Damage Detection Algorithm will then be tested on a cantilevered plate structure using simulated damage at various locations. The success of the Damage Detection Algorithm under various conditions will be assessed.
- Chapter 6: Experimental FRF data will be obtained for the cantilevered plate used in Chapter 5. This experimental FRF data will be inputted into the Damage Detection Algorithm and its success in determining the physical damage will be assessed. Basic modal analysis techniques will also be covered.
- Chapter 7: Discussions and conclusion will be presented in this chapter. A proposal for further investigation will also be raised.

## **1.6 ASSUMPTIONS OF THIS STUDY**

Throughout this thesis, certain assumptions have been made to enable computations to be more efficient. These assumptions have been made after an extensive literature review of the existing

---

---

methods for structural damage detection and are consistent with the assumptions used in other existing methods for structural damage detection. These assumptions are:

- Damage in the structure is seen as a change in the structural stiffness of the structure and not changes in the mass of the structure. Therefore any damage present in the structure will reflect changes in the stiffness matrix only. Any changes in the mass matrix are considered to be small and can be neglected.
  - Structural damping in the structure is considered to be small and can be neglected.
  - Structures are assumed to exhibit linear behaviour. This means that the response of a structure to a combination of forces applied simultaneously is the summation of the responses to each individual force.
-

# CHAPTER 2

## DAMAGE DETECTION USING FREQUENCY RESPONSE FUNCTION DATA

Measured frequency response function (FRF) data are usually the most compact form of data obtained from vibration tests of structures. Unlike modal data, they can be retrieved without further numerical processing and hence without the associated errors. The FRF data provides an abundance of information on the structure's dynamic behaviour, much of which would have been lost in using modal analysis data, due to the necessary numerical process to extract them.

A damage detection technique using measured frequency response function (FRF) data has been found to be a promising method that can successfully address the criteria required for successful damage detection (Choudhury, 1996).

### 2.1 DAMAGE LOCATION VECTOR

Frequency response function data can be derived from the characteristics of the structural system or the equation of motion. Its main characteristics are contained in its mass  $[M]$ , stiffness  $[K]$  and damping  $[C]$  or hysteric damping  $[H]$  matrices. Since damping and hysteretic effects will not be considered in this thesis, the equation of motion of an undamped system without excitation can be described as follows:

$$[M]_{UD} \{\ddot{x}\} + [K]_{UD} \{x\} = \{0\} \quad (2.1)$$

---

where  $[M]$  and  $[K]$  are the  $N \times N$  analytical mass and stiffness matrices of the structure, and  $\{x\}$  is an  $N \times 1$  vector of displacement. The subscript symbol UD has been introduced to indicate that the structure is undamaged.

Similarly, the system with structural damage is described by:

$$[M]_D \{\ddot{x}\} + [K]_D \{x\} = \{0\} \quad (2.2)$$

where the subscript D indicates that the structure is damaged.

Damage in this thesis will be considered to be a reduction in the stiffness of a structure rather than the loss of mass, since a loss of mass would mean the likelihood of a catastrophic failure. Therefore, the mass matrix of the damage structure can be assumed to be equal to the mass matrix of the undamaged structure. Hence:

$$[M]_{UD} = [M]_D \quad (2.3)$$

If a single column of receptance frequency response function (RFRF) at a particular frequency  $\Omega$  is given by  $\{\alpha(\Omega)\}$  then:

$$([K]_D - \Omega^2 [M]_D) \{\alpha_D(\Omega)\} = ([K]_{UD} - \Omega^2 [M]_{UD}) \{\alpha_{UD}(\Omega)\} \quad (2.4)$$

The dynamic stiffness matrix before and after damage can be related as follows:

$$([Z(\Omega)]_D) \{\alpha_D(\Omega)\} = ([Z(\Omega)]_{UD}) \{\alpha_{UD}(\Omega)\} \quad (2.5)$$

$$\text{Let: } [Z(\Omega)]_D = [Z(\Omega)]_{UD} - [\Delta Z(\Omega)] \quad (2.6)$$

where  $[Z(\Omega)]_D$  represents the dynamic stiffness matrix of the damaged RFRF at a particular frequency  $\Omega$ .  $[Z(\Omega)]_{UD}$  represents that of the undamaged RFRF.  $[\Delta Z(\Omega)]$  represents the difference in RFRFs between the damaged and undamaged structure at a frequency  $\Omega$ .

Equation (2.5) can also be rewritten as:

$$[Z(\Omega)]_{UD} \{\alpha_{UD}(\Omega)\} = ([Z(\Omega)]_{UD} - [\Delta Z(\Omega)])\{\alpha_D(\Omega)\} \quad (2.7)$$

$$\text{or, } [Z(\Omega)]_{UD} (\{\alpha_D(\Omega)\} - \{\alpha_{UD}(\Omega)\}) = [\Delta Z(\Omega)]\{\alpha_D(\Omega)\} \quad (2.8)$$

$$\text{Let: } \{d(\Omega)\} = [\Delta Z(\Omega)]\{\alpha_D(\Omega)\} \quad (2.9)$$

$$\text{Thus by (2.8) } \{d(\Omega)\} = [Z(\Omega)]_{UD} \{\Delta\alpha(\Omega)\} \quad (2.10)$$

where the vector  $\{\Delta\alpha(\Omega)\}$  represents the difference between RFRFs of the damaged and the undamaged structure at a frequency  $\Omega$ . A straight multiplication of the undamaged dynamic stiffness matrix and the vector  $\{\Delta\alpha(\Omega)\}$  would generate the corresponding vector  $\{d(\Omega)\}$ . This  $\{d(\Omega)\}$  is an  $N \times 1$  vector containing non-zero values for DOFs that contain damage and zero values for undamaged DOFs and is also referred to as “Damage Location Vector” (DLV).

The DLV can be shown in a 3D graph to locate damage. Figure 2.1a is an example of a 3D DLV plot of a 12 DOFs mass spring system that will be studied in chapter 3 of this thesis. The first axis of the graph represents the Degrees of Freedoms (DOFs) in the “Damage Location Vector”. The second axis represents the frequency ranges for which the damage location algorithm is applied and the third axis represents the absolute value obtained for the elements in the “Damage

Location Vector”. Elements in the DLV whose value is due only to the effects of noise will follow a random pattern with insignificant amplitudes when plotted over a certain frequency range. The value of elements that are truly affected by damage will follow a more distinctive pattern and occur with greater amplitude. It can be seen in Figure 2.1a that damage exists between DOF 6 and DOF 9. All other peaks and ripples that occur outside of DOF6 and DOF 9 are due to noise.

A two dimensional representation of the DLV can be obtained by adding the values of each DLV for each frequency to each other to obtain a resultant vector called a “Cumulative Damage Location Vector” or (CDLV). This CDLV when plotted produces a 2D graph and can be seen in Figure 2.1b. The first axis corresponds to the DOFs and the second axis represents the cumulative amplitude of the DLV over a frequency range. Since the elements in the DLV due to damage will be mostly bigger than those due to noise, the CDLV would magnify any presence of damage greatly, making it easier to isolate the location of damage.

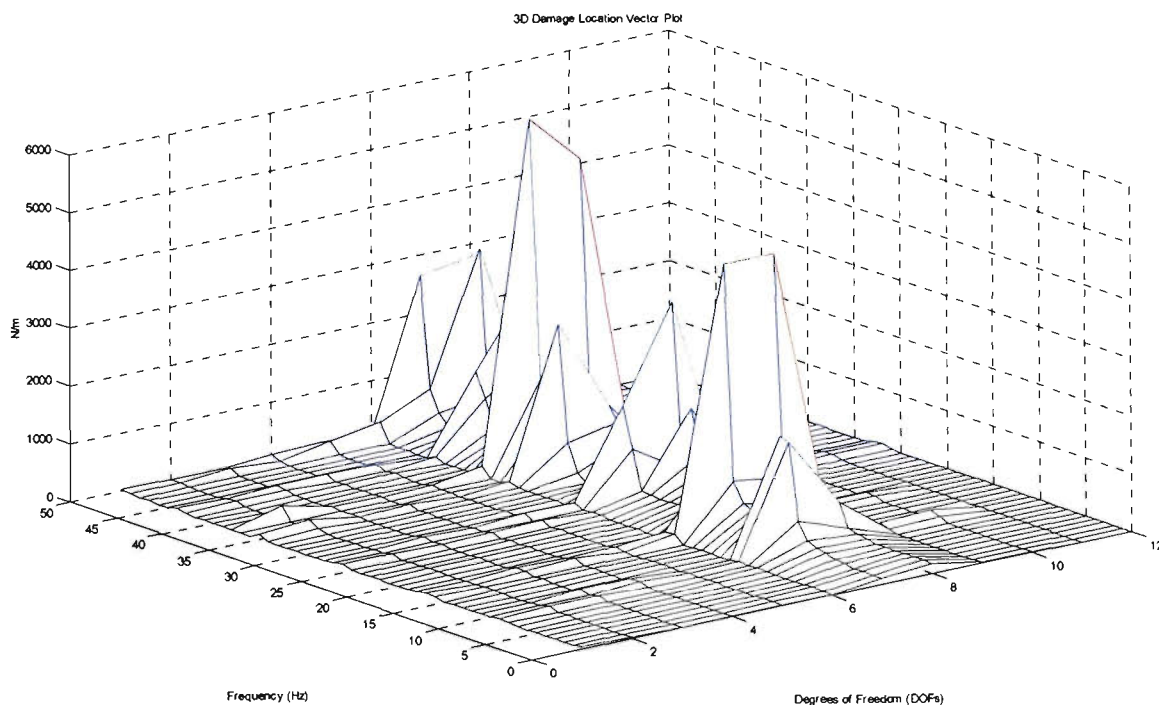


**Figure 2.1a: An Example of a 3D DLV Plot of a 12 DOFs Mass Spring System without Noise**

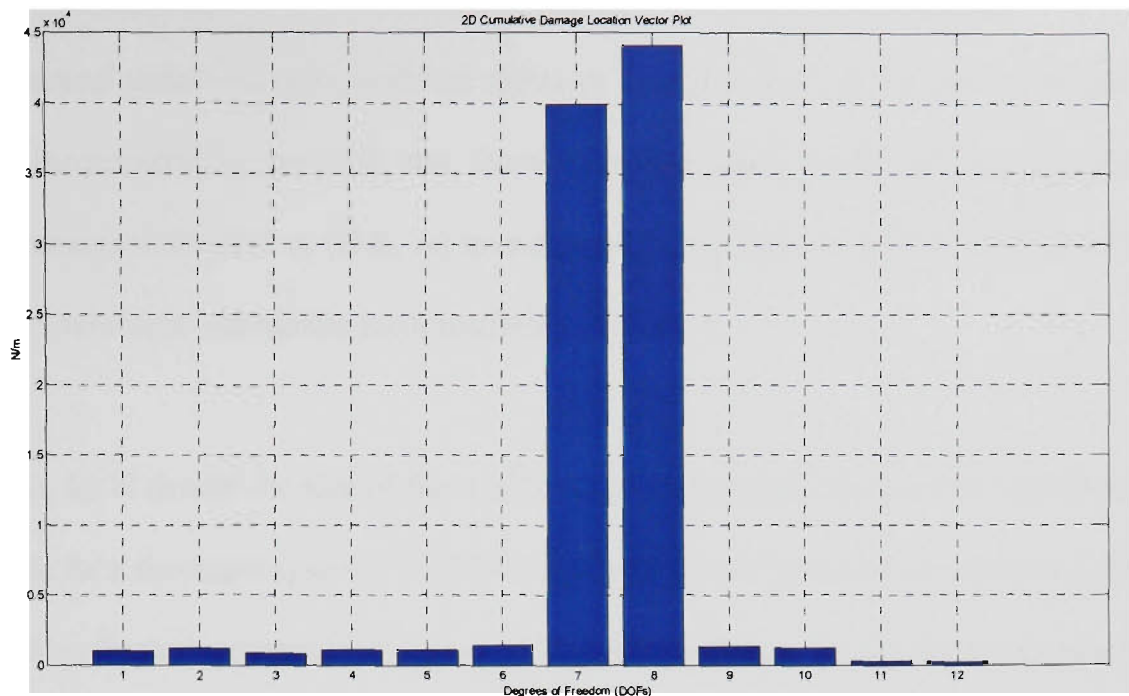


**Figure 2.1b: An Example of a 2D CDLV Plot for a 12 DOFs Mass Spring System without Noise**

It can be clearly seen in Figure 2.1b that the damage is located at an element connected to DOF 7 and DOF 8 since their cumulative values are much greater than all the other remaining DOFs. It must be noted that since the CDLV is a cumulative quantity based on the frequency ranges of the DLV, the magnitude indicated on the 2D graph is not a static quantity and would change according to the number of frequencies and frequency resolution.

By referring to the 3D DLV plot and the 2D CDLV plot, it is possible to determine the location of damage and estimate the extent of damage when all the coordinates of the system are known. It becomes more difficult to apply the 3D DLV plot and the 2D CDLV plot in systems where coordinate incompatibility exists. In such a situation, a preliminary step is required to either expand or reduce the systems to the same equivalent size before applying the 3D DLV plot and the 2D CDLV plot.

## 2.2 DAMAGE DETECTION WITH COORDINATE INCOMPATIBILITY

There are several reduction and expansion methods available that can be used to overcome this coordinate incompatibility problem and these were presented in the previous chapter. The Dynamic Expansion method A (D.E. A) investigated by Choudhury (1996) will be used within this thesis to overcome coordinate incompatibility problems.

For example, let  $N$  denote the size of the matrix for an undamaged system and  $M$  denote the size of the matrix for a damaged system. If all DOFs of a particular structure are measured, then there will be no coordinate incompatibility between both the systems. This is further explained using Figure 2.2.

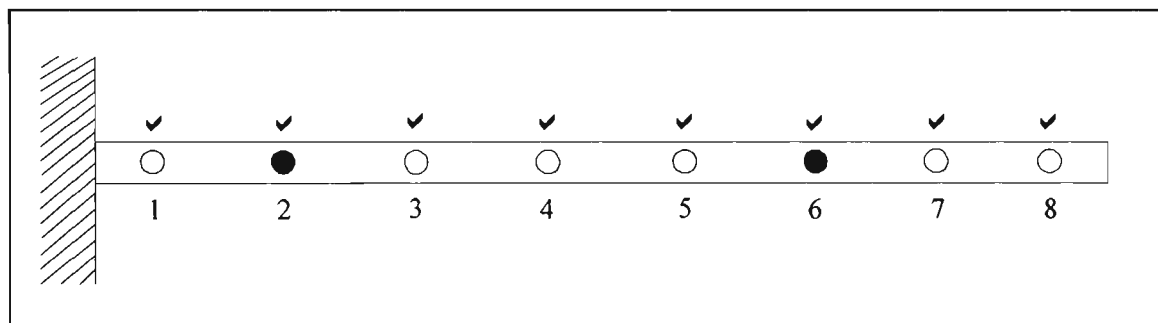


**Figure 2.2: All Nodes are Measured, No Incompatibility Exists**

In Figure 2.2 damage has been introduced into node no. 2 and node no. 6. If all the nodes are measured then no coordinate incompatibility exists and the damage can be easily found. (Note ✓ represents the measured coordinates and ● represents damage present in the structure).

Let  $\otimes$  represent the change in  $Z(w)$  due to damage, then if the matrix operation represented by equation (2.10) is carried out, the effect of such change would be present only in the damage location vector elements corresponding to such change. The change in  $\{d(w)\}$  is denoted by  $\oplus$  and is illustrated in the following diagram:

$$\begin{bmatrix} 1 & & & & & & & \\ & \otimes & & & & & & \\ & & 3 & & & & & \\ & & & 4 & & & & \\ & & & & 5 & & & \\ & & & & & \otimes & & \\ & & & & & & 7 & \\ & & & & & & & 8 \end{bmatrix} \begin{Bmatrix} \checkmark \\ \checkmark \end{Bmatrix} = \begin{Bmatrix} \checkmark \\ \oplus \\ \checkmark \\ \checkmark \\ \checkmark \\ \oplus \\ \checkmark \\ \checkmark \end{Bmatrix} \begin{matrix} 1 \\ 2 \\ 3 \\ 4 \\ 5 \\ 6 \\ 7 \\ 8 \end{matrix} \quad (2.11)$$

From (2.11) it is clear that damage affects DOF no. 2 and DOF no. 6.

However in the following example as shown in Figure 2.3, not all the DOFs are measured. In this example only 4 DOFs are measured (at nodes 1, 3, 5 and 6), thus the  $M \times M$  matrix would yield a  $4 \times 4$  matrix, whereas the  $N \times N$  matrix would yield an  $8 \times 8$  Matrix. It can be seen in this example that damage at DOF no. 6 can be detected, whilst damage at DOF no. 2 will not be detected with pinpoint accuracy.

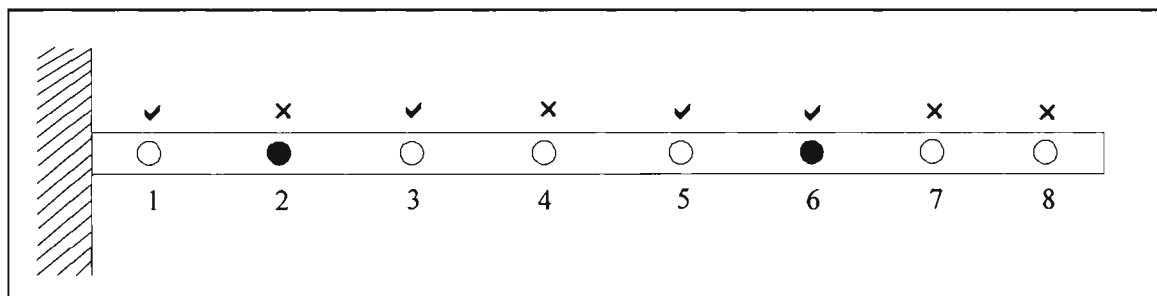


Figure 2.3: Not All Nodes are Measured, Coordinate Incompatibility Exists

Hence the damage (denoted by  $\oplus$ ) can be found for only the measured coordinate as follows:

$$\begin{bmatrix} 1 & & & & & & & \\ & & 3 & & & & & \\ & & & & & & & \\ & & & & 5 & & & \\ & & & & & \otimes & & \end{bmatrix} \begin{Bmatrix} \checkmark \\ \checkmark \\ \checkmark \\ \checkmark \\ \checkmark \end{Bmatrix} = \begin{Bmatrix} \checkmark \\ \checkmark \\ \checkmark \\ \checkmark \\ \oplus \end{Bmatrix} \begin{matrix} 1 \\ 3 \\ 5 \\ 6 \end{matrix} \quad (2.12)$$

From (2.12), the connectivity between the structures is lost and not all the damage can be located. Only damage present within the measured coordinates appears. By applying a method referred to as the Dynamic Expansion Method A (D.E. A), developed by Choudhury (1996) it becomes possible to overcome this coordinate incompatibility.

### 2.3 DYNAMIC EXPANSION METHOD A (D.E. A)

The Dynamic Expansion Method A (D.E. A) relates the unmeasured FRF data to that of the measured FRF data by a linear transformation [T]. Let's consider the unmeasured FRF data in a vector denotes as  $\{\alpha_D^{UC}(\omega)\}$  and the measured subset denoted as  $\{\alpha_D^{MC}(\omega)\}$ , where superscript UC denotes unmeasured coordinates and superscript MC denotes measured coordinate. Hence the main aim of the Dynamic Expansion Method A is to derive a suitable transformation matrix [T] that relates the unmeasured coordinates to the measured coordinates as illustrated by equation (2.13).

$$\{\alpha_D^{UC}(\omega)\} = [T]\{\alpha_D^{MC}(\omega)\} \quad (2.13)$$

The dynamic stiffness matrix can then be re-arranged and partitioned into terms of measured and unmeasured DOFs. Hence this becomes:

$$\begin{bmatrix} [Z_{11}(\Omega)] & [Z_{12}(\Omega)] \\ [Z_{21}(\Omega)] & [Z_{22}(\Omega)] \end{bmatrix}_{UD} \begin{Bmatrix} \alpha_{UD}^{MC}(\Omega) - \alpha_D^{MC}(\Omega) \\ \alpha_{UD}^{UC}(\Omega) - \alpha_D^{UC}(\Omega) \end{Bmatrix} = [\Delta Z(\Omega)] \begin{Bmatrix} \alpha_D^{MC}(\Omega) \\ \alpha_D^{UC}(\Omega) \end{Bmatrix} \quad (2.14)$$

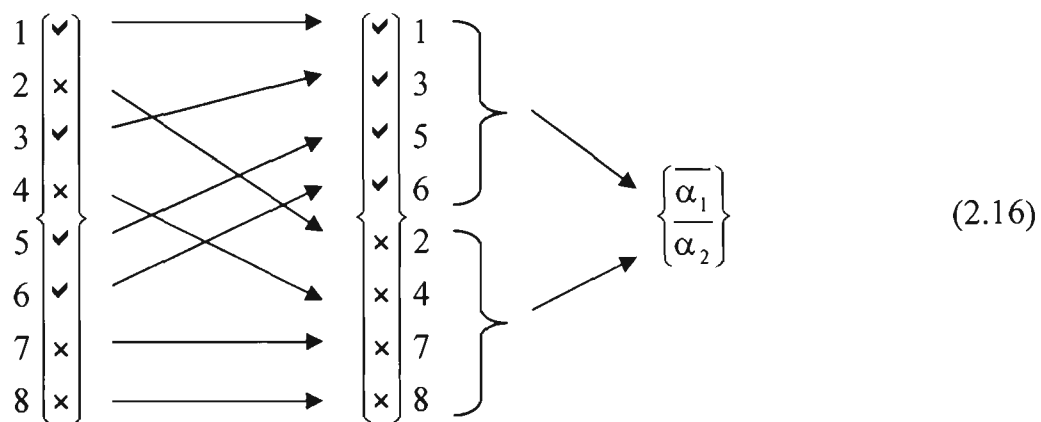
Without knowing matrix  $[\Delta Z(\Omega)]$  it is quite impossible to expand the measured FRF data to that of the unmeasured coordinates. However, it is possible to assume that matrix  $[\Delta Z(\Omega)]$  is a null matrix. By doing so, it becomes possible to calculate the sub-vector  $\{\alpha_D^{UC}(\Omega)\}$  from  $\{\alpha_D^{MC}(\Omega)\}$  using equation (2.14). From this an expanded vector  $\{\alpha_D(\Omega)\}$  is obtained with full coordinates, which may then be used for damage detection.

In this method the transformation matrix is calculated by the inverse of the partitioned dynamic stiffness matrix corresponding to the unmeasured DOFs. The transformation matrix becomes:

$$[TR] = -[[K_{22}]_{UD} - \Omega^2[M_{22}]_{UD}]^{-1}[[K_{21}]_{UD} - \Omega^2[M_{21}]_{UD}] \quad (2.15)$$

Here the partitioned dynamic stiffness matrix corresponding to unmeasured DOFs is a square matrix and has a dimension of  $(N-M) \times (N-M)$ , where “N” is the number of DOFs for the structure, and “M” is the number of measured DOFs. Here the subscript 21 corresponds to the partitioned matrix that contains measured coordinates and subscript 22 corresponds to the partitioned matrix that contains unmeasured coordinates.

Thus from the previous example using the D.E. A it becomes:



Where ✓ represents the measured coordinates and × represents the unmeasured coordinate against the degree of freedom of the structure. This is carried out by grouping all the measured coordinates before the unmeasured coordinates. All measured coordinates can be represented by  $\overline{\alpha_1}$  and all unmeasured coordinates are represented by  $\overline{\alpha_2}$ . Thus an expanded vector  $\{\alpha\}$  with full coordinates is obtained. This vector can be used in equation (2.9) to obtain the DLV and subsequently the CDLV.

## 2.4 NORMALISED RANDOM ERRORS

It is relatively simple to determine damage from measurements that are free from errors. However, in reality, measurements are always contaminated by various random errors from noise and/or measurement. It has been found that using FRF data over conventional modal analysis data offers a distinct advantage that is capable of dealing with data contaminated with noise (Choudhury, 1986). This is because errors such as noise would follow a random pattern, becoming negligible at certain frequency points and becoming noticeable at others (Choudhury, 1986).

The random error in a typical FRF measurement can be quantified by the coherence function (Ewins, 1984). Coherence gives a measure of the degree of linear dependence between two signals, as a function of frequency (Ewins, 1984).

Theoretical randomised errors can be introduced into the FRF data in two different forms:

1. Random Number between  $\pm 0.05 \times \text{FRF} + \text{Original FRF}$
2. Random Number between  $0.95 - 1.05 \times \text{FRF}$

It was found that the first instance was computationally better, since the first instance meant that it was also possible to optionally include randomised errors without much trouble, by resetting the randomised number generated back to a zero value.

Even though randomised errors are usually associated with the time domain. It is possible to introduce the randomised errors in the frequency domain (Ewins, 1984). The randomly generated errors can be simply added to the FRFs.

---

## 2.5 DAMAGE DETECTION ALGORITHM WRITTEN IN MATLAB™

An algorithm was written in Matlab™ to calculate the Damage Location Vector, the Cumulative Damage Location Vector and the Dynamic Expansion Method A when required. From this point forward this algorithm shall be referred to as the “Damage Detection Algorithm” or “DDA”. Using the same damage detection algorithm, it was also possible to simulate normalised random errors in the calculations. Natural frequencies and mode shapes can also be calculated using the same Damage Detection Algorithm. Figure 2.4 outlines the Damage Detection Algorithm logic used in writing the Matlab™ program. The Damage Detection Algorithm codes written in Matlab™ can be found in Appendix 1.

- **Damage Detection Algorithm Logic in Matlab™ for scenarios without Coordinate Incompatibility**

1. Is there coordinate incompatibility involved? **NO**
2. Do you want to simulate random noise? If **YES** proceed to 3. If **NO** proceed to 4.
3. User Input is required. Here the user is asked to input the percentage of normal random errors to generate. This is then stored for later usage in the DLV.
4. User Input is required. Here the user is asked to input the following:
  - Frequency Range
  - Number of Measured Coordinates
  - $[K]_{UD}$  Is represented by files with extension (\*.USM)
  - $[M]$  Is represented by files with extension (\*.MAS)
  - $[K]_D$  Is represented by files with extension (\*.DSM)
5. The DLV and CDLV is calculated and the 3D DLV and 2D CDLV Plot are outputted.

- **Damage Detection Algorithm Logic in Matlab™ for scenarios with Coordinate Incompatibility**

1. Is there coordinate incompatibility involved? **YES**
2. Do you want to simulate random noise? If **YES** proceed to 3. If **NO** proceed to 4.
3. User Input is required. Here the user is asked to input the percentage of normal random errors to generate. This is then stored for later usage in the DLV.
4. User Input is required. Here the user is asked to input the following:
  - Frequency Range
  - Number of Measured Coordinates
  - $[K]_{UD}$  Is represented by files with extension (\*.USM)
  - $[M]$  Is represented by files with extension (\*.MAS)
  - $[K]_D$  Is represented by files with extension (\*.DSM)
  - Vector  $\{\alpha\}$  Is represented by files with extension (\*.AIM)
5. The unmeasured coordinates are expanded using Dynamic Expansion Method A (D.E. A)
6. The DLV and CDLV is calculated and the 3D DLV and 2D CDLV Plot are outputted.

Having briefly discussed the theories involved in the Damage Detection Algorithm, it is time to apply the developed algorithm to a simple structure to study effectiveness of the algorithm. The next chapter will see the Damage Detection Algorithm (DDA) applied to a relatively simple mass spring structure that has only 12 translational DOFs. The performance of the DDA will be assessed. It will then be used to investigate simulated damage in the NASA eight bay space truss structure and finally in a thin flat cantilevered plate.

---

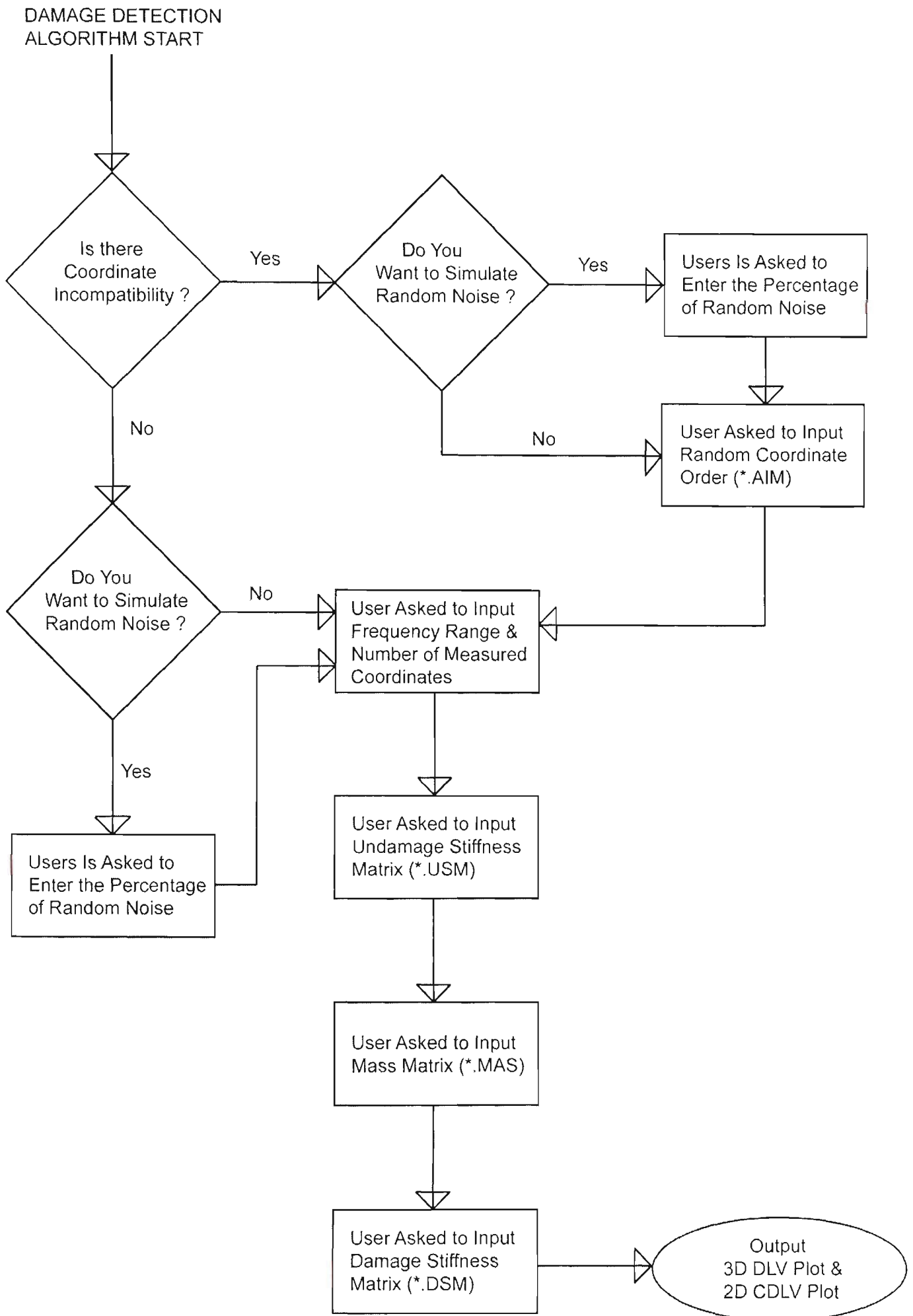


Figure 2.4: Damage Detection Algorithm Logic

# CHAPTER 3

## DAMAGE DETECTION

### IN A SIMPLE MASS SPRING SYSTEM

Let's consider a 12 DOFs simple undamaged mass spring system as shown in Figure 3.1, which was studied by Choudhury (1996) using constrained minimisation damage quantification (CMDQ) method. The stiffness matrix for the undamaged and damage system is presented in Table 3.1 and Table 3.2 respectively. The mass matrix is presented in Table 3.3. For both cases it is assumed that the mass matrix is unaffected by the introduction of damage. The natural frequency for the 12 DOFs system before and after damage is presented in Table 3.4.

Damage was simulated by reducing the stiffness in the spring member that was located between mass No.5 and mass No.6 from 6000 N/m to 5200 N/m, a reduction of 800 N/m. The Damage Detection Algorithms and resultant Damage Location Vector (DLV) plot and Cumulative Damage Location Vector (CDLV) plot were computed in Matlab™.

|       |       |       |       |       |       |       |       |       |       |       |       |
|-------|-------|-------|-------|-------|-------|-------|-------|-------|-------|-------|-------|
| 6000  | -2000 | 0     | 0     | 0     | 0     | -2000 | 0     | 0     | 0     | 0     | 0     |
| -2000 | 6000  | -2000 | 0     | 0     | 0     | 0     | -2000 | 0     | 0     | 0     | 0     |
| 0     | -2000 | 6000  | -2000 | 0     | 0     | 0     | 0     | -2000 | 0     | 0     | 0     |
| 0     | 0     | -2000 | 6000  | -2000 | 0     | 0     | 0     | 0     | -2000 | 0     | 0     |
| 0     | 0     | 0     | -2000 | 6000  | -2000 | 0     | 0     | 0     | 0     | -2000 | 0     |
| 0     | 0     | 0     | 0     | -2000 | 6000  | -2000 | 0     | 0     | 0     | 0     | -2000 |
| -2000 | 0     | 0     | 0     | 0     | -2000 | 6000  | -2000 | 0     | 0     | 0     | 0     |
| 0     | -2000 | 0     | 0     | 0     | 0     | -2000 | 6000  | -2000 | 0     | 0     | 0     |
| 0     | 0     | -2000 | 0     | 0     | 0     | 0     | -2000 | 6000  | -2000 | 0     | 0     |
| 0     | 0     | 0     | -2000 | 0     | 0     | 0     | 0     | -2000 | 6000  | -2000 | 0     |
| 0     | 0     | 0     | 0     | -2000 | 0     | 0     | 0     | 0     | -2000 | 6000  | -2000 |
| 0     | 0     | 0     | 0     | 0     | -2000 | 0     | 0     | 0     | 0     | -2000 | 6000  |

**Table 3.1: Stiffness Matrix of the Undamaged Structure for the 12 DOFs Mass Spring System (N/m)**

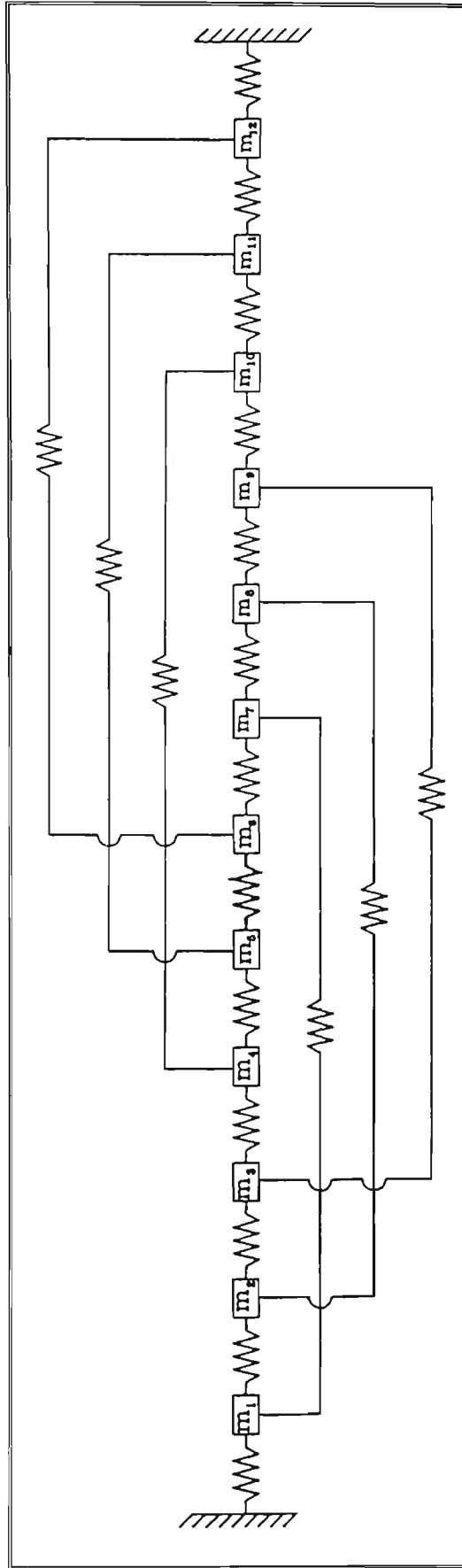


Figure 3.1: Simple 12 DOFs Mass Spring System

|       |       |       |       |              |              |       |       |       |       |       |       |
|-------|-------|-------|-------|--------------|--------------|-------|-------|-------|-------|-------|-------|
| 6000  | -2000 | 0     | 0     | 0            | 0            | -2000 | 0     | 0     | 0     | 0     | 0     |
| -2000 | 6000  | -2000 | 0     | 0            | 0            | 0     | -2000 | 0     | 0     | 0     | 0     |
| 0     | -2000 | 6000  | -2000 | 0            | 0            | 0     | 0     | -2000 | 0     | 0     | 0     |
| 0     | 0     | -2000 | 6000  | -2000        | 0            | 0     | 0     | 0     | -2000 | 0     | 0     |
| 0     | 0     | 0     | -2000 | <b>5200</b>  | <b>-1200</b> | 0     | 0     | 0     | 0     | -2000 | 0     |
| 0     | 0     | 0     | 0     | <b>-1200</b> | <b>5200</b>  | -2000 | 0     | 0     | 0     | 0     | -2000 |
| -2000 | 0     | 0     | 0     | 0            | -2000        | 6000  | -2000 | 0     | 0     | 0     | 0     |
| 0     | -2000 | 0     | 0     | 0            | 0            | -2000 | 6000  | -2000 | 0     | 0     | 0     |
| 0     | 0     | -2000 | 0     | 0            | 0            | 0     | -2000 | 6000  | -2000 | 0     | 0     |
| 0     | 0     | 0     | -2000 | 0            | 0            | 0     | 0     | -2000 | 6000  | -2000 | 0     |
| 0     | 0     | 0     | 0     | -2000        | 0            | 0     | 0     | 0     | -2000 | 6000  | -2000 |
| 0     | 0     | 0     | 0     | 0            | -2000        | 0     | 0     | 0     | 0     | -2000 | 6000  |

Table 3.2: Stiffness Matrix of the Damaged Structure for the 12 DOFs Mass Spring System (N/m)

|   |   |   |   |   |   |   |   |   |    |    |    |
|---|---|---|---|---|---|---|---|---|----|----|----|
| 1 | 0 | 0 | 0 | 0 | 0 | 0 | 0 | 0 | 0  | 0  | 0  |
| 0 | 2 | 0 | 0 | 0 | 0 | 0 | 0 | 0 | 0  | 0  | 0  |
| 0 | 0 | 3 | 0 | 0 | 0 | 0 | 0 | 0 | 0  | 0  | 0  |
| 0 | 0 | 0 | 4 | 0 | 0 | 0 | 0 | 0 | 0  | 0  | 0  |
| 0 | 0 | 0 | 0 | 5 | 0 | 0 | 0 | 0 | 0  | 0  | 0  |
| 0 | 0 | 0 | 0 | 0 | 6 | 0 | 0 | 0 | 0  | 0  | 0  |
| 0 | 0 | 0 | 0 | 0 | 0 | 7 | 0 | 0 | 0  | 0  | 0  |
| 0 | 0 | 0 | 0 | 0 | 0 | 0 | 8 | 0 | 0  | 0  | 0  |
| 0 | 0 | 0 | 0 | 0 | 0 | 0 | 0 | 9 | 0  | 0  | 0  |
| 0 | 0 | 0 | 0 | 0 | 0 | 0 | 0 | 0 | 10 | 0  | 0  |
| 0 | 0 | 0 | 0 | 0 | 0 | 0 | 0 | 0 | 0  | 11 | 0  |
| 0 | 0 | 0 | 0 | 0 | 0 | 0 | 0 | 0 | 0  | 0  | 12 |

Table 3.3: Mass Matrix for the Undamaged/Damaged 12 DOFs Mass Spring System (kg)

| Natural Frequency No. | Before Damage (Hz) | After Damage (Hz) | % Change from Undamaged |
|-----------------------|--------------------|-------------------|-------------------------|
| 1                     | 0.92               | 0.92              | 0                       |
| 2                     | 2.50               | 2.50              | 0                       |
| 3                     | 2.94               | 2.84              | 3.4                     |
| 4                     | 3.96               | 3.94              | 0.5                     |
| 5                     | 4.28               | 4.26              | 0.5                     |
| 6                     | 4.60               | 4.53              | 1.5                     |
| 7                     | 5.06               | 4.98              | 1.6                     |
| 8                     | 5.56               | 5.53              | 0.5                     |
| 9                     | 6.38               | 6.06              | 5.0                     |
| 10                    | 7.32               | 7.27              | 0.7                     |
| 11                    | 8.98               | 8.98              | 0                       |
| 12                    | 13.00              | 13.00             | 0                       |

Table 3.4: Natural Frequency Before and After Damage for the Simple 12 DOFs Mass Spring System

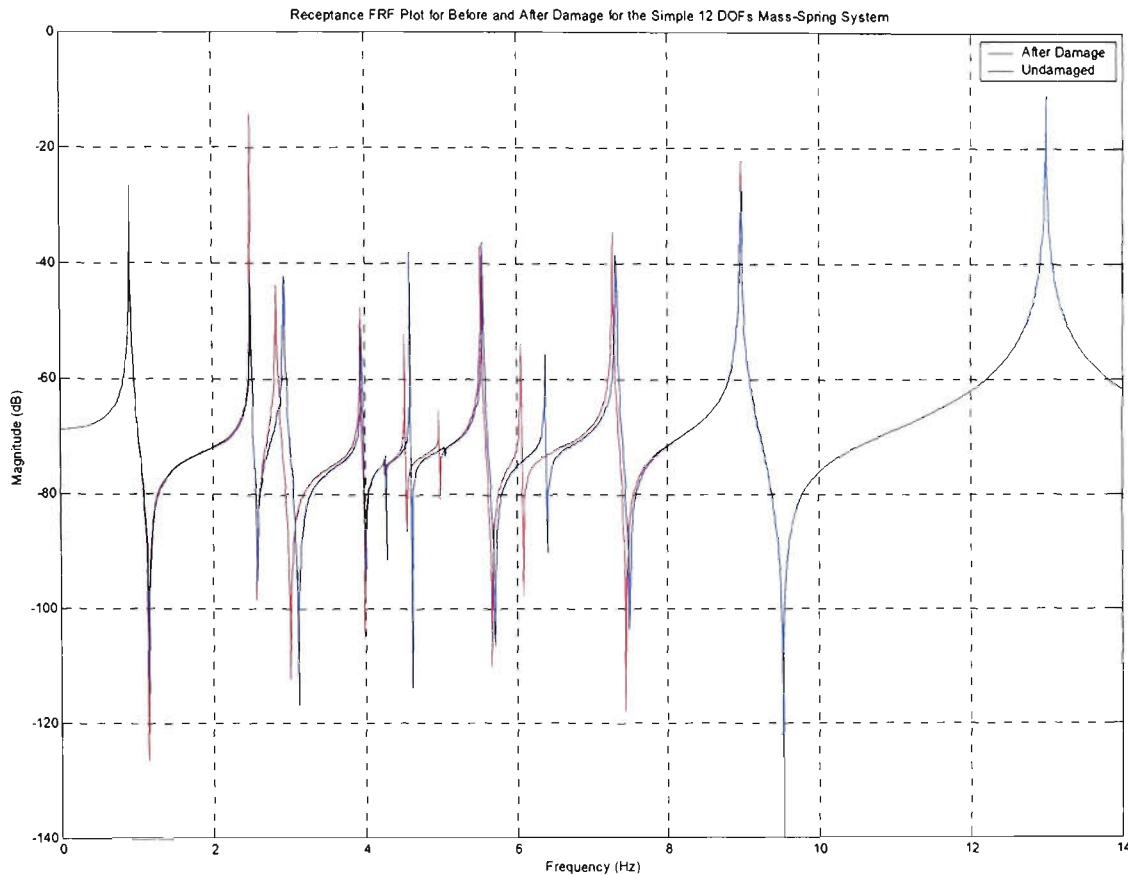


**Figure 3.2: Receptance FRF Plot at  $\alpha(1, 1)$  for Before and After Damage for the Simple 12 DOFs Mass Spring System**

Shown in Figure 3.2 is the computed receptance FRF plot exhibited by the simple mass spring system before and after damage at  $\alpha(1, 1)$ . It must be noted that these receptance FRFs are simulated results obtained from Matlab™ and that  $\alpha(1, 1)$  would correspond to having the accelerometer located on mass no. 1 while also exciting mass no. 1 in a real experiment. A comparison of the receptance FRFs plot for the undamaged and the damaged condition shows frequency shifts. The frequency trace corresponding to the system after damage can be seen to be shifted lower at some frequencies compared to the undamaged frequency trace.

### 3.1 DAMAGE DETECTION WITHOUT COORDINATE INCOMPATIBILITY AND NO NOISE

The Damage Detection Algorithm which was written in Matlab™ and has been discussed in Chapter 2 was first applied to data corresponding to the 12 DOFs mass spring system that was free from any noise interference or numerical errors. All data points were also available, thus no coordinate incompatibility exists. A frequency range of 0 – 14 Hz covering the 12 modes of vibration for the system was chosen. A frequency resolution of 0.32Hz was found to be the best sampling rate to adequately describe the structure.

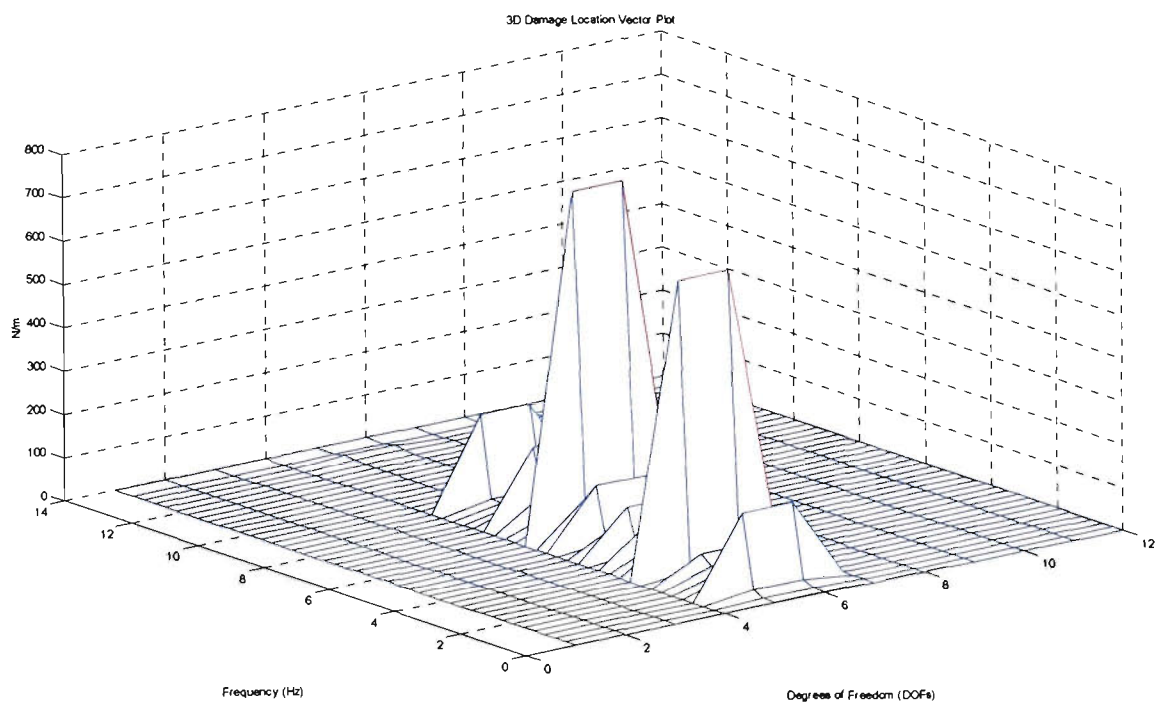


**Figure 3.3a: 3D DLV Plot of the 12 DOFs Mass Spring System without Coordinate Incompatibility and No Noise Interference**

Figure 3.3a is the 3D Damage Location Vector (DLV) plot for the 12 DOF mass spring system without any coordinate incompatibility and no noise interference. Peaks can be observed to occur between DOF 5 and DOF 6. These peaks are the non-zero entry in the Damage Location Vector and relate to damage present within the structure. The damage can be observed to occur consistently throughout the frequency range of the structure. Reading from the vertical axis of the 3D DLV plot the maximum damage can be estimated to be 800 N/m. Figure 3.3b is the

corresponding 2D Cumulative Damage Location Vector (CDLV) plot and confirms that the damage is indeed located between DOF 5 and DOF 6.

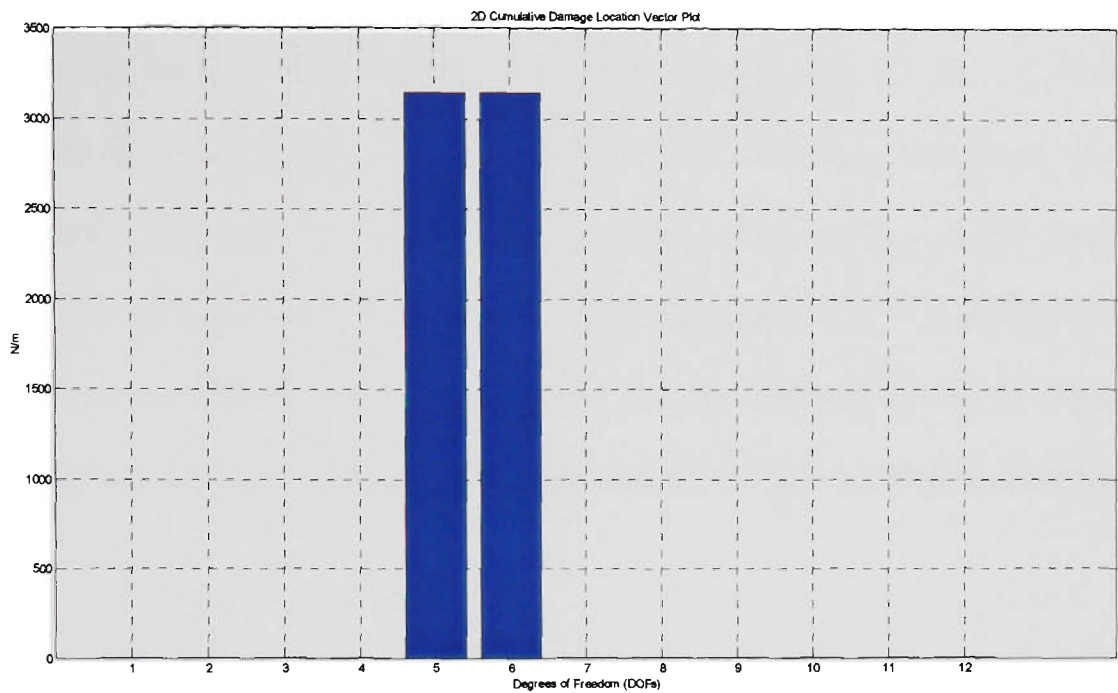


**Figure 3.3b: 2D CDLV Plot of the 12 DOFs Mass Spring System without Coordinate Incompatibility and No Noise Interference**

It should be noted the CDLV plot accentuate the damage but the magnitudes thus found are not as relevant as those in the 3D DLV.

### **3.2 DAMAGE DETECTION WITHOUT COORDINATE INCOMPATIBILITY AND WITH 5% NOISE**

Since the Damage Detection Algorithm was successful in locating the damage for error-free data, 5% noise will be introduced to the structure in the form of normalised random errors using the method discussed in Chapter 2. The purpose of introducing 5% normalised random errors is to simulate a noisy environment and to represent any measurement errors that may be observed on a real structure.

Figure 3.4a and Figure 3.4b show the 3D DLV Plot and the 2D CDLV Plot respectively for the 12 DOFs mass spring system with 5% normalised random errors introduced. When normalised random errors have been introduced all elements of the DLV are non-zero. The DOFs associated with damage can be observed to be much larger than those that are due to random errors throughout the frequency range. It is also interesting to note that randomised errors can be observed to affect the system at certain frequency ranges, while leaving other frequency ranges unaffected. The 2D CDLV plot show the cumulative values for DOF 5 and DOF 6 to be much larger than the other DOFs. This demonstrates that the Damage Detection Algorithm can successfully detect damage with data that is contaminated with 5% normalised random errors.

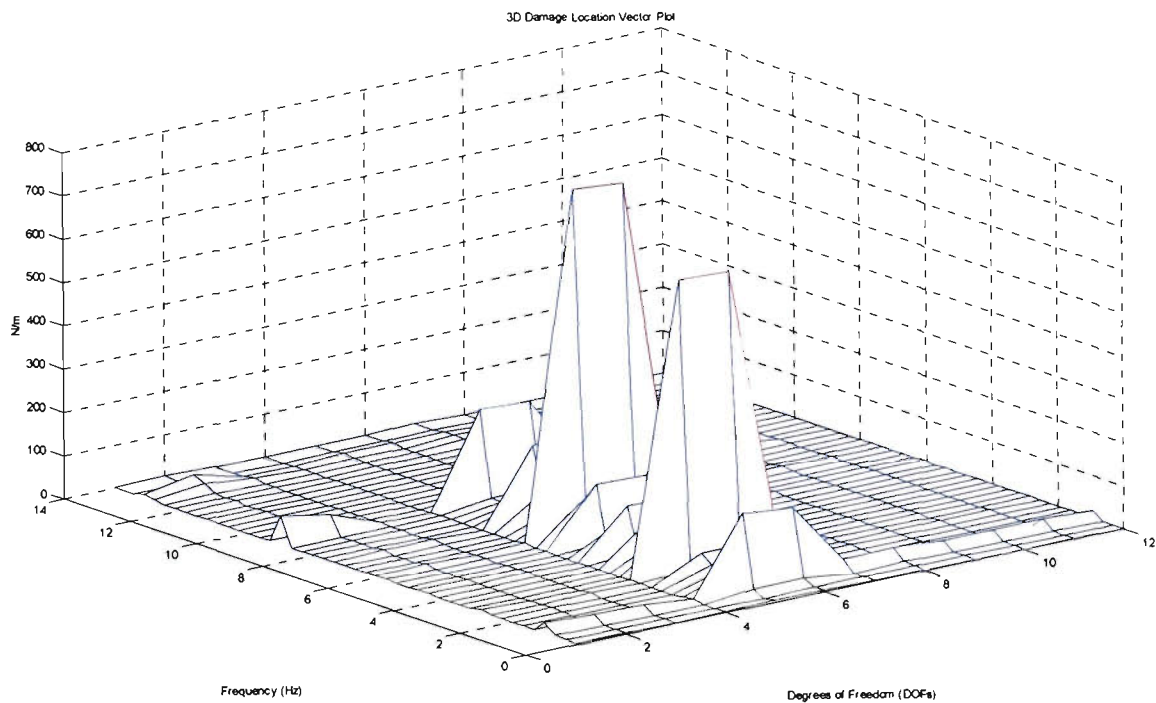


**Figure 3.4a: 3D DLV Plot of the 12 DOFs Mass Spring System without Coordinate Incompatibility and with 5% Noise Interference**

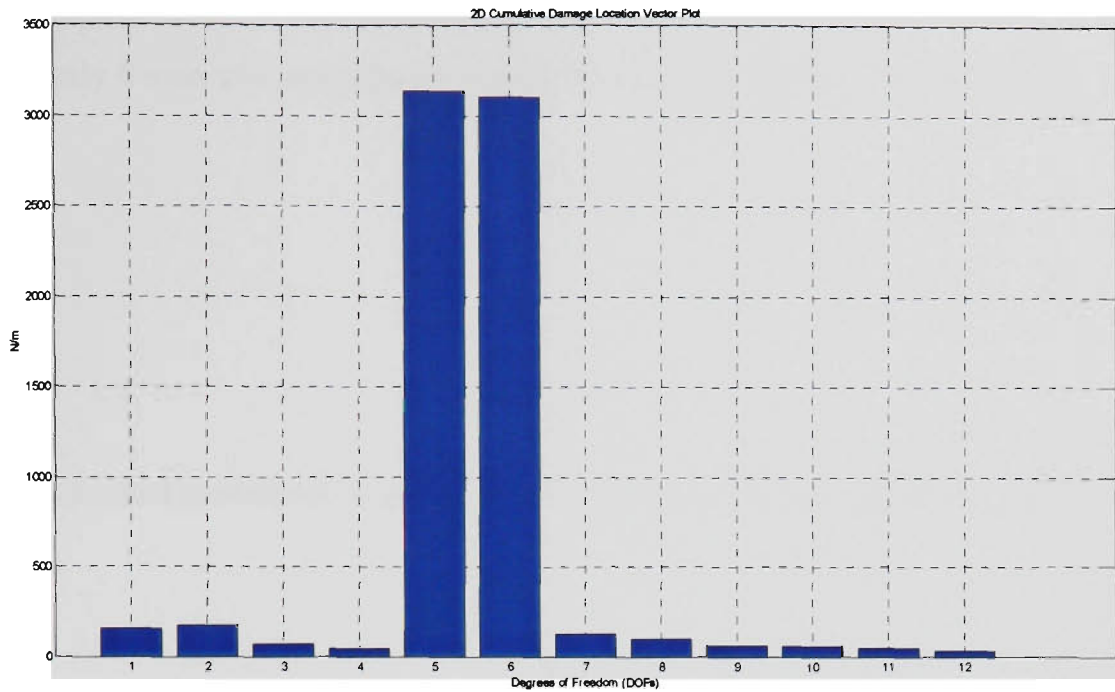


**Figure 3.4b: 2D CDLV Plot of the 12 DOFs Mass Spring System without Coordinate Incompatibility and with 5% Noise Interference**

### 3.3 DAMAGE DETECTION WITH COORDINATE INCOMPATIBILITY AND NO NOISE

In a real life experiment, it may not always be possible to measure the entire coordinate system on the structure. Ideally, one full column or one full row of data is required to adequately describe the structure. The accuracy is increased if more than one full column or one full row is available. However, what would happen if it were not possible to have one full row or one full column of data? A coordinate incompatibility would occur and the Dynamic Expansion Method A (D.E. A) discussed in Chapter 2 would be required to firstly expand the data. Consequently, the Damage Detection Algorithm was then applied to the same mass spring system when only 6 measured coordinates were supplied. This meant that the remaining 6 unsupplied coordinates were required to be expanded using the D.E. A. The 6 measured coordinate were randomly chosen from the possible 12 DOFs. The randomly chosen measured coordinates are indicated in Table 3.5.

Let us consider three cases:

### 3.3.1 SIX MEASURED COORDINATE SUPPLIED

In this case only 6 measured coordinates are chosen from the random set. They are:

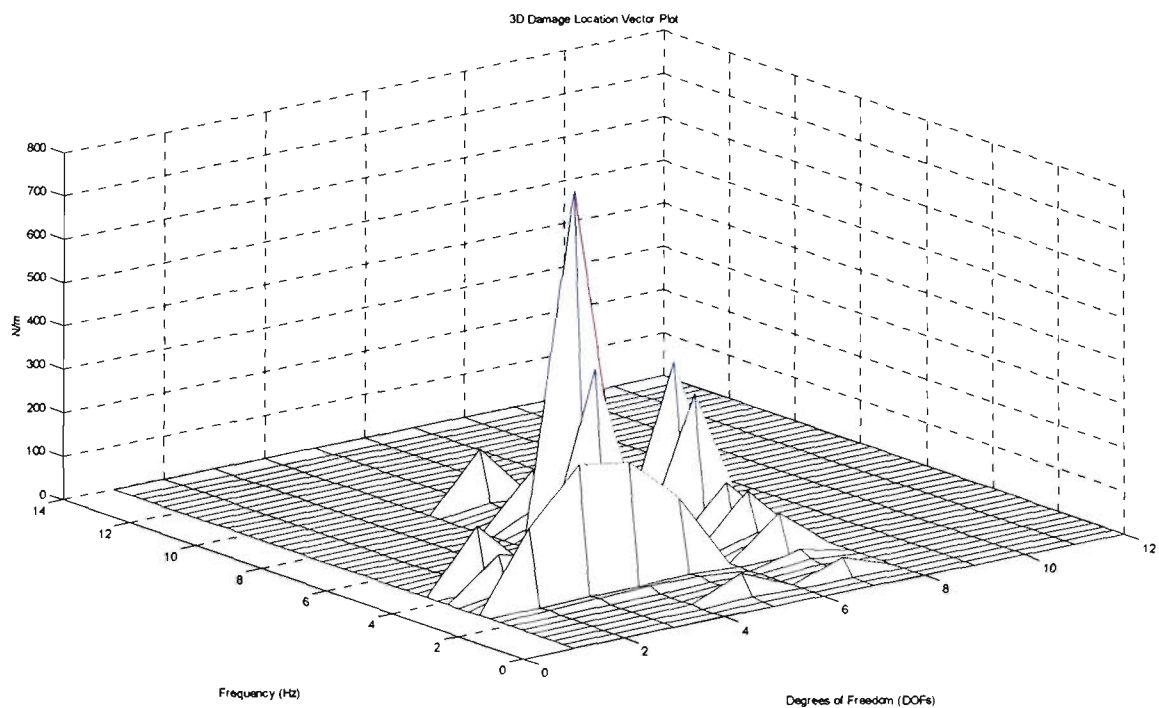
$$\{\bar{\alpha}\}_{mc} = \begin{Bmatrix} 2 \\ 4 \\ 7 \\ 1 \\ 3 \\ 5 \end{Bmatrix}$$

And the unmeasured coordinate would be the remaining coordinates and are as follows:

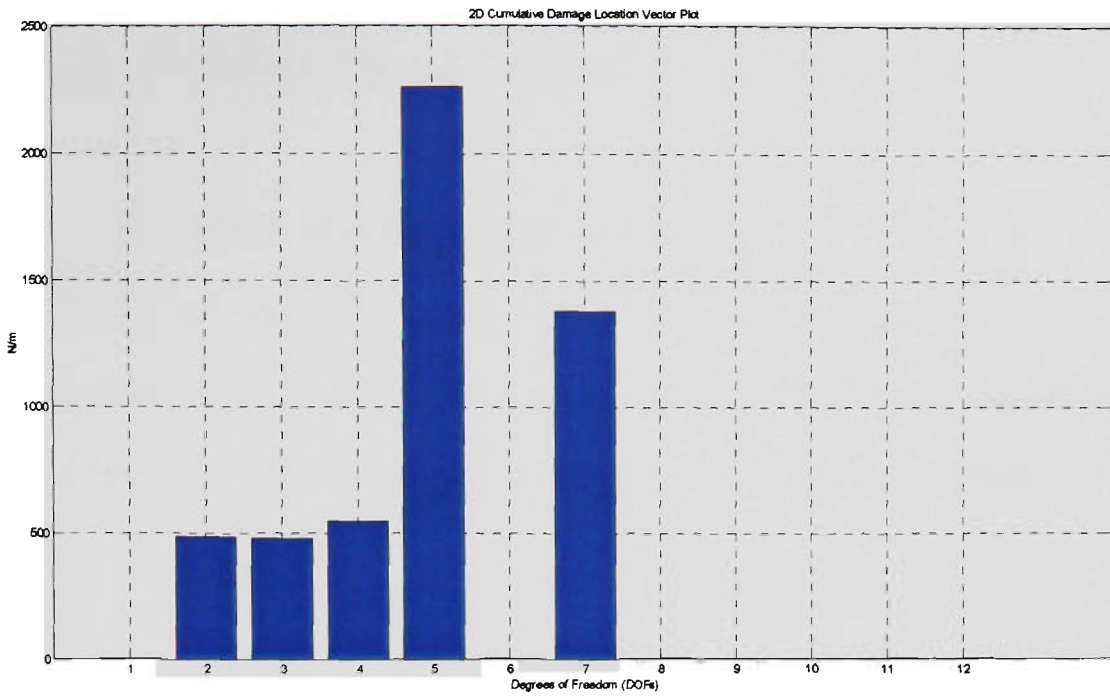
$$\{\bar{\alpha}\}_{uc} = \begin{Bmatrix} 10 \\ 8 \\ 9 \\ 6 \\ 11 \\ 12 \end{Bmatrix}$$

| No. Measured Coordinates                   | 1 | 2 | 3 | 4 | 5 | 6 | 7  | 8 | 9 | 10 | 11 | 12 |
|--|---|---|---|---|---|---|----|---|---|----|----|----|
| Measured Coordinate Randomly Ordered (DOF) | 2 | 4 | 7 | 1 | 3 | 5 | 10 | 8 | 9 | 6  | 11 | 12 |

**Table 3.5: Measured Coordinates Index**



**Figure 3.5a: 3D DLV Plot of the 12 DOFs Mass Spring System with 6 Measured Coordinates and 6 Expanded Coordinates and No Noise Interference**



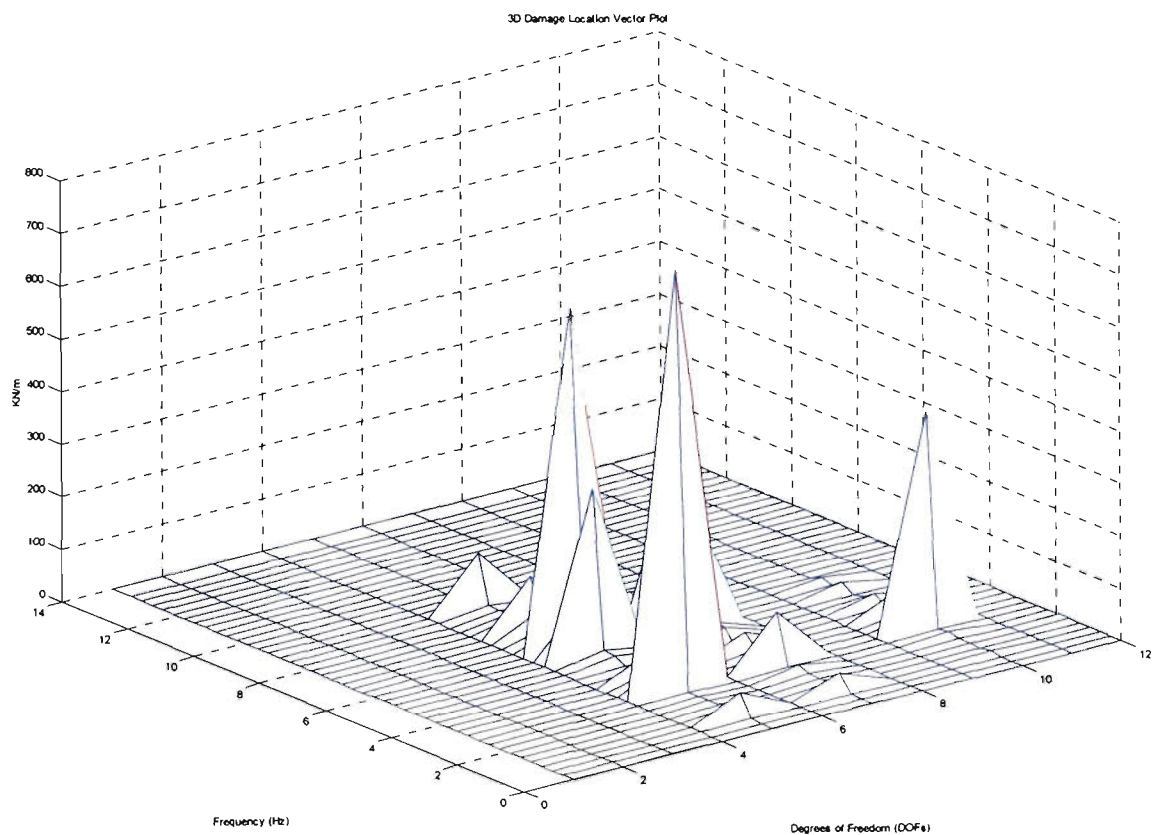
**Figure 3.5b: 2D CDLV Plot of the 12 DOFs Mass Spring System with 6 Measured Coordinates and 6 Expanded Coordinates and No Noise Interference**

Figure 3.5a and Figure 3.5b show the 3D DLV plot and the 2D CDLV plot for the 12 DOFs mass spring system with six measured coordinates and six expanded coordinates and no noise interference respectively. Comparing Figure 3.3a with Figure 3.3b, it can be seen that Figure 3.5a and Figure 3.5b are incorrect. In fact Figure 3.5b suggests that damage may exist at DOF 2, DOF 3, DOF 4, DOF 5 and DOF 7. The initial reaction to this is that the Damage Detection Algorithm did not correctly detect the simulated damage. However on closer inspection, Figure 3.5a show that large peaks occur at DOF 5 and DOF 7. Smaller peak can be seen to occur at DOF 2, DOF 3 and DOF 4. From the previous section it is known that the damage location should in fact lie between DOF 5 and DOF 6. However, since DOF 6 is not a measured coordinate and has not been supplied to the Damage Detection Algorithm, it cannot indicate exactly the location of damage. Hence the next closest available measured DOF to the damage DOF is displayed. Since not all the coordinates have been measured the results obtained cannot be taken as the final and foremost results. The result should be interpreted as giving only an indication of where the damage lies. From Figure 3.5b, the damage can be seen to lie between

DOF 2, DOF 3, DOF 4, DOF 5 and DOF 7. Further measurements should be taken between these DOFs in order to accurately identify the damage locations within the structure.

### 3.3.2 EIGHT MEASURED COORDINATES SUPPLIED

Now let us consider the case in which only 8 measured coordinates are chosen from Table 3.5. Using the previously chosen 6 measured coordinates a further 2 measured coordinates will be selected from Table 3.5. These 2 measured coordinates are DOF no. 10 and DOF no. 8.



**Figure 3.6a: 3D DLV Plot of the 12 DOFs Mass Spring System with 8 Measured Coordinates and 4 Expanded Coordinates and No Noise Interference**

Figure 3.6a and Figure 3.6b show the 3D DLV Plot and the corresponding 2D CDLV plot for the 12 DOFs mass spring system with eight measured coordinates supplied and four expanded coordinates and no noise interference. Comparison with Figure 3.5a and Figure 3.5b show that

the initial damage locations at DOF 2, DOF 3 and DOF 4 no longer exist when two more measured coordinates are supplied. In fact Figure 3.6b, now suggests that damage may lie between DOF 5, DOF 7 and DOF 10. However, since not all the coordinate have been supplied further measurements should be taken between these DOFs in order to accurately identify the damage locations.

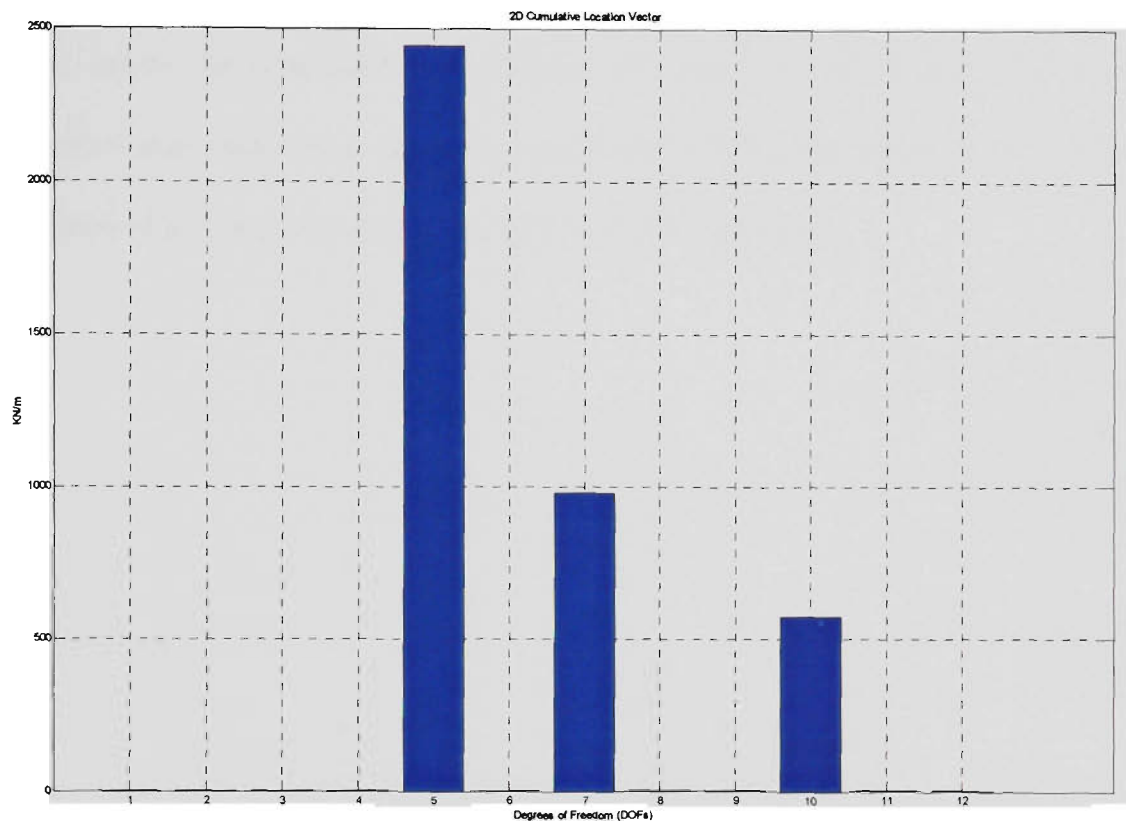


**Figure 3.6b: 2D CDLV Plot of the 12 DOFs Mass Spring System with 8 Measured Coordinates and 4 Expanded Coordinates and No Noise Interference**

### 3.3.3 TEN MEASURED COORDINATES SUPPLIED

Now let us consider the case in which only 10 measured coordinates are chosen from Table 3.5. Using the previously chosen 8 measured coordinates a further 2 measured coordinates will be selected from Table 3.5. These 2 measured coordinates are DOF no. 9 and DOF no. 6.

Figure 3.7a and Figure 3.7b are the corresponding 3D DLV plot and 2D CDLV Plot for the 12DOFs mass spring system with ten measured coordinates supplied and twelve expanded

coordinates and no noise interference. It can be seen that as more measured coordinates are supplied to the Damage Detection Algorithm the location of damage within the structure can be more accurately pinpointed.

Figure 3.7b show that the damage is located within DOF 5 and DOF 6. This corresponds to the original simulated damage locations. However, since there are still some unmeasured coordinates it cannot be concluded that damage only exist at DOF 5 and DOF 6 as further damage locations may exist within the unmeasured part of the mass spring system. However, it is highly unlikely since there are only 2 unsupplied DOFs remaining.

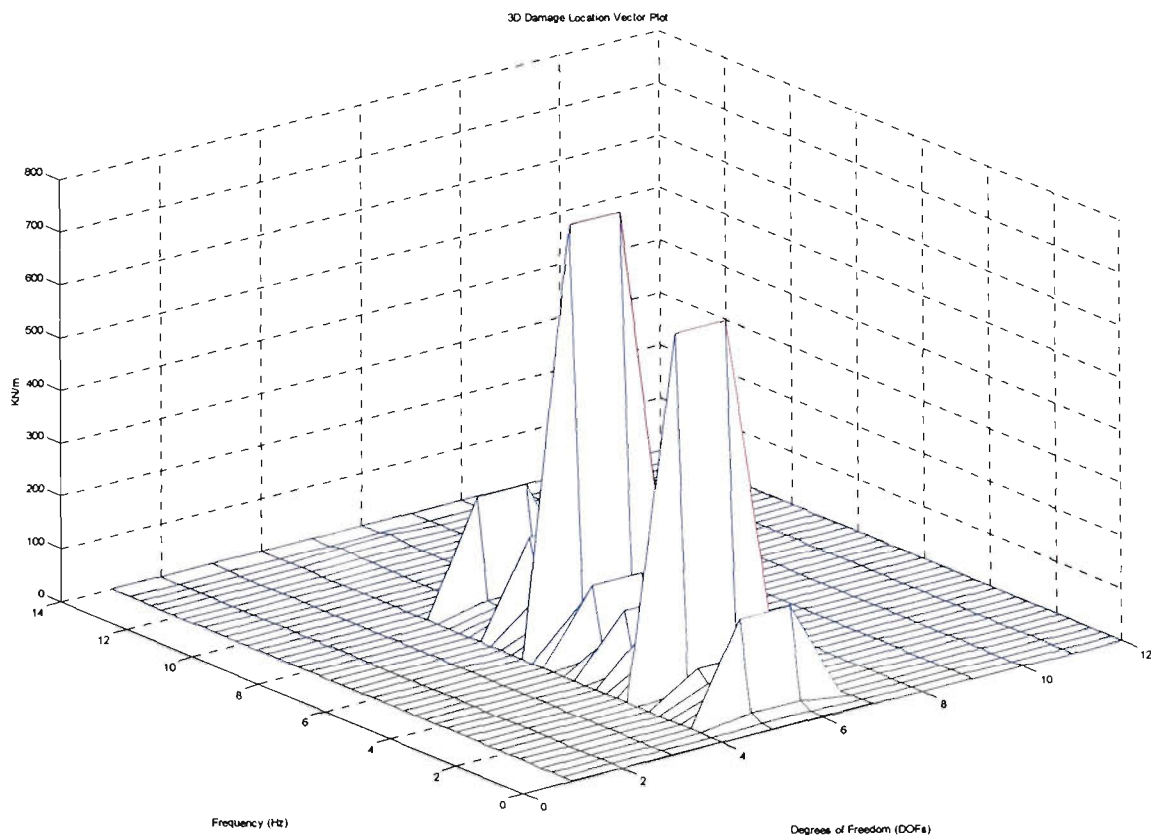


**Figure 3.7a: 3D DLV Plot of the 12 DOFs Mass Spring System with 10 Measured Coordinates and 2 Expanded Coordinate and No Noise Interference**

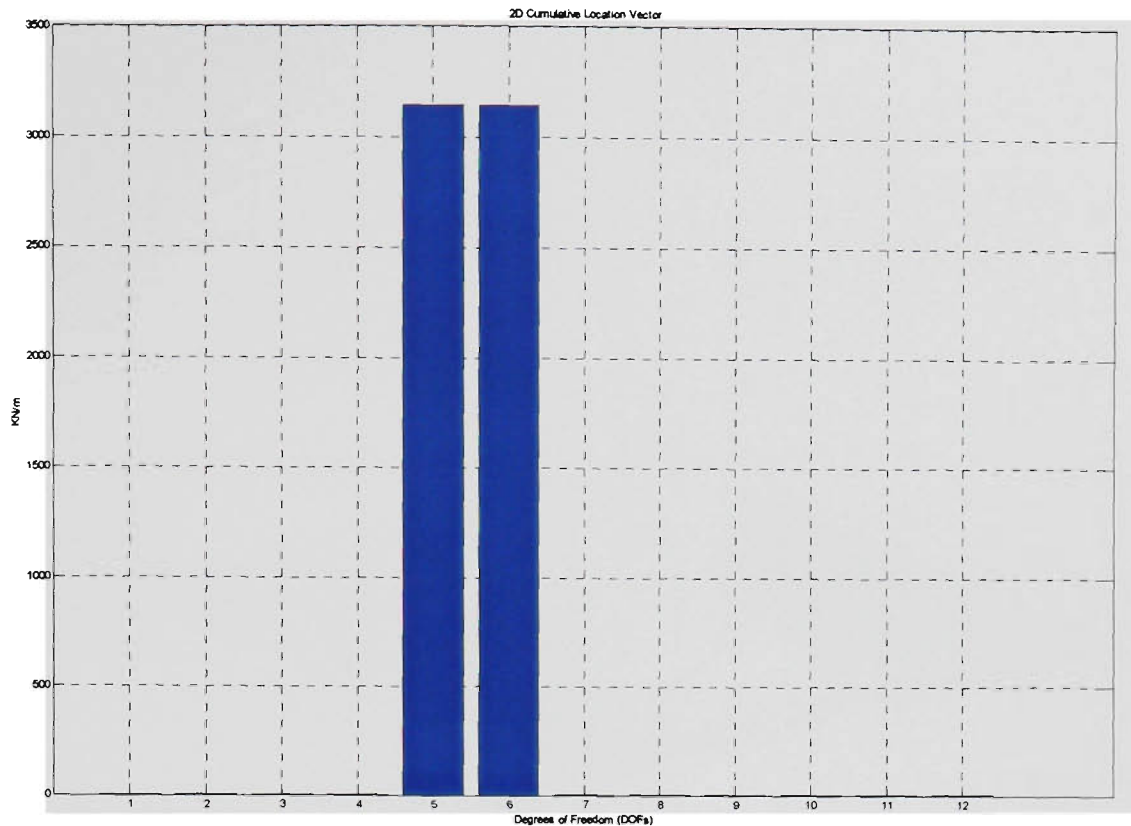


**Figure 3.7b: 2D CDLV Plot of the 12 DOFs Mass Spring System with 10 Measured Coordinates and 2 Expanded Coordinates and No Noise Interference**

### **3.4 DAMAGE DETECTION WITH COORINDATE INCOMPATIBILITY AND WITH 5% NOISE**

The effect of 5% random noise in the data with only ten measured coordinates supplied was also studied. Figure 3.8a and Figure 3.8b show the 3D DLV plot and the 2D CDLV plot for the 12 DOFs mass spring system with ten measured and two expanded coordinates. It can be observed that the effect of the 5% noise did not have a great effect on the results. The results are similar to the previous section, with the exception that the random error now appears on all DOFs. The detected damage location of DOF 5 and DOF 6 can still be observed to possess much larger DLV values than those due to noise. This can be more clearly seen in Figure 3.8b.

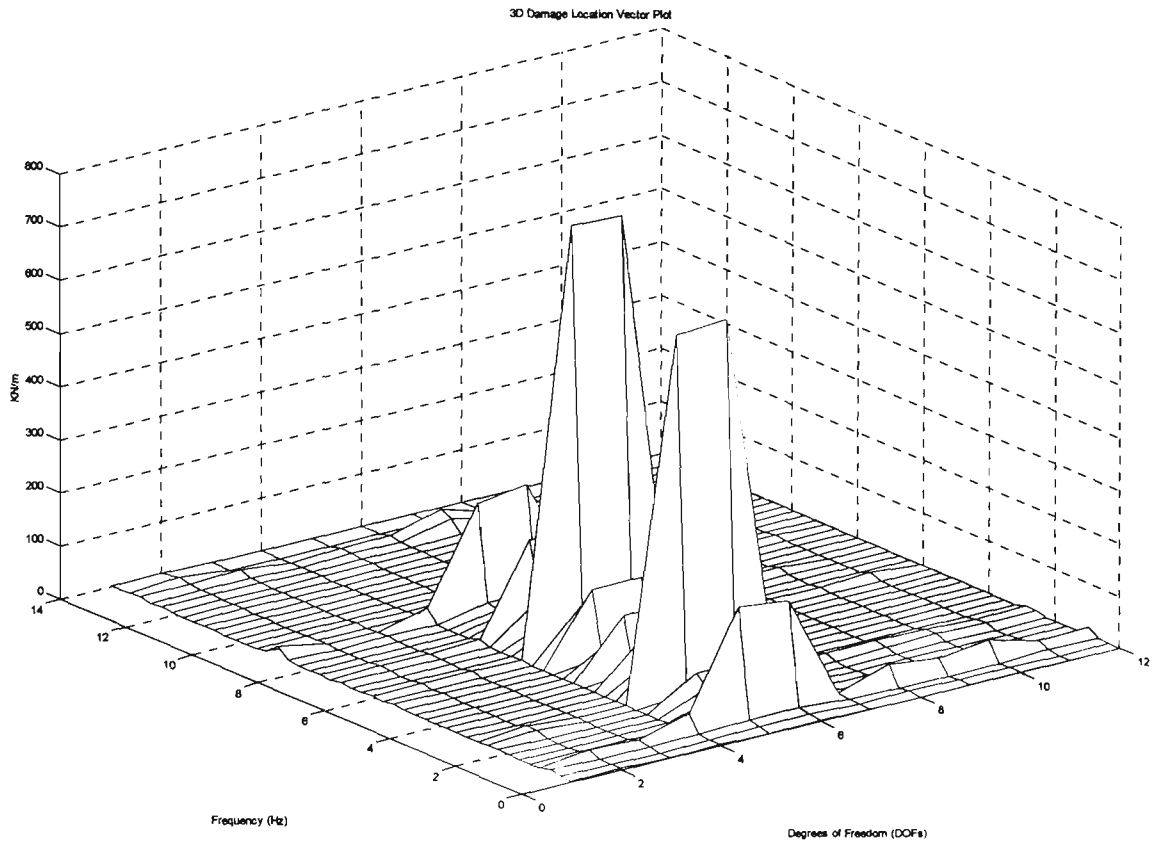


**Figure 3.8a: 3D DLV Plot of the 12 DOFs Mass Spring System with 10 Measured Coordinates and 2 Expanded Coordinate and 5% Noise Interference**

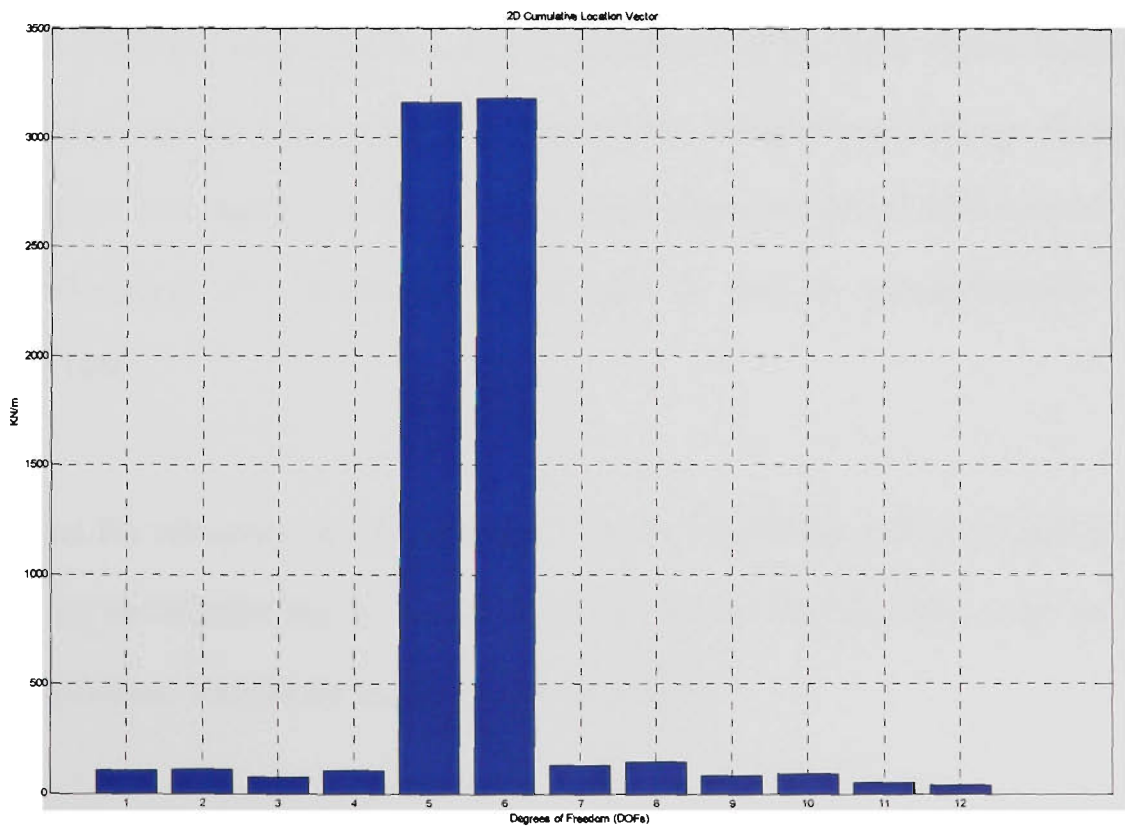


**Figure 3.8b: 2D CDLV Plot of the 12 DOFs Mass Spring System with 10 Measured Coordinates and 2 Expanded Coordinates and 5% Noise Interference**

### 3.5 DISCUSSION

The developed Damage Detection Algorithm works exceptionally well when at least one column or row of the FRF matrix of the structure is supplied. It has been able to successfully detect the location of damage with 5% normalised random errors introduced in the data. For cases that involved coordinate incompatibility, the Damage Detection Algorithm detected additional damage locations than the actual simulated locations when only six randomly selected measured coordinates were supplied to the algorithm. As more measured coordinates are supplied to the Damage Detection Algorithm the location of damage within the structure can be more accurately pinpointed. However, it should be noted that the results obtained when there is a coordinate incompatibility should not be assumed to be entirely accurate since the location of damage can only be accurate to within the spatial resolution of the measured points. In cases where coordinate incompatibility exists, the Damage Detection Algorithm should only be used as a tool to estimate the location of damage within a structure.

The Damage Detection Algorithm is a simple procedure that has been shown to successfully detect simulated damage compared to the Constrained Minimization Damage Quantification (CMDQ) method investigated by Choudhury (1996). However, the CMDQ method involved extensive calculations of various parameters and is not be computationally efficient. (Choudhury, 1996).

To further test the robustness of the Damage Detection Algorithm, various simulated damage scenarios were investigated for the NASA eight bay space truss structure using the Damage Detection Algorithm. Results are shown in the next chapter.

---

# CHAPTER 4

## DAMAGE DETECTION IN

### TRUSS STRUCTURES

The NASA 8 bay truss structure has been the focus of much attention in structural damage detection and has provided a benchmark for testing developed Damaged Detection Algorithms (Doebeling et. al., 1996). Several simulated damage scenarios will be investigated in this chapter to assess the robustness of the developed Damage Detection Algorithm.

The NASA 8 bay truss structure in reality is described by 36 nodes and has 6 DOFs (3 translational and 3 rotational) per node. The structure therefore has a total of 216 DOFs. To simplify the problem, only translational degrees of freedom are considered for the study of this truss structure. This is a valid assumption, as currently there are no accelerometers available that can accurately measure rotational degrees of freedom. Under this assumption the NASA 8 bay truss structure has a total of 108 DOFs. The structure is also grounded at one end, therefore a further 4 nodes may be eliminated from the problem, thus leaving only 96 DOFs.

#### 4.1 DESCRIPTION OF THE STRUCTURE

Figure 4.1 show the node configurations for the NASA 8 bay truss structure (Lim and Kashangaki, 1994). It is important that the same order is maintained for numbering the nodes, as this will allow easy interpretation for damage location in later processes. Figure 4.2 show the NASA 8 bay truss lattice structure for a section.

---

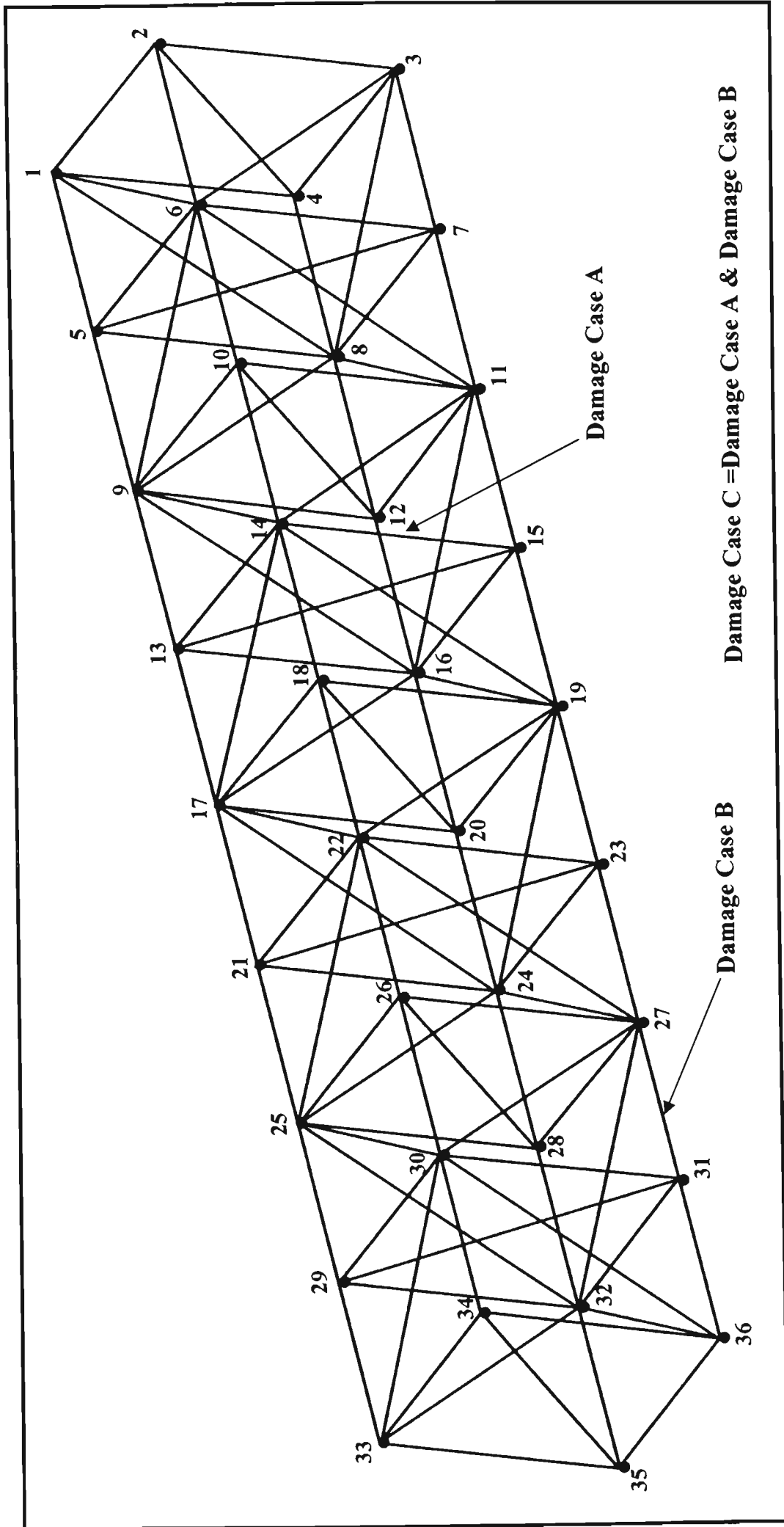


Figure 4.1: NASA Eight Bay Truss Structure

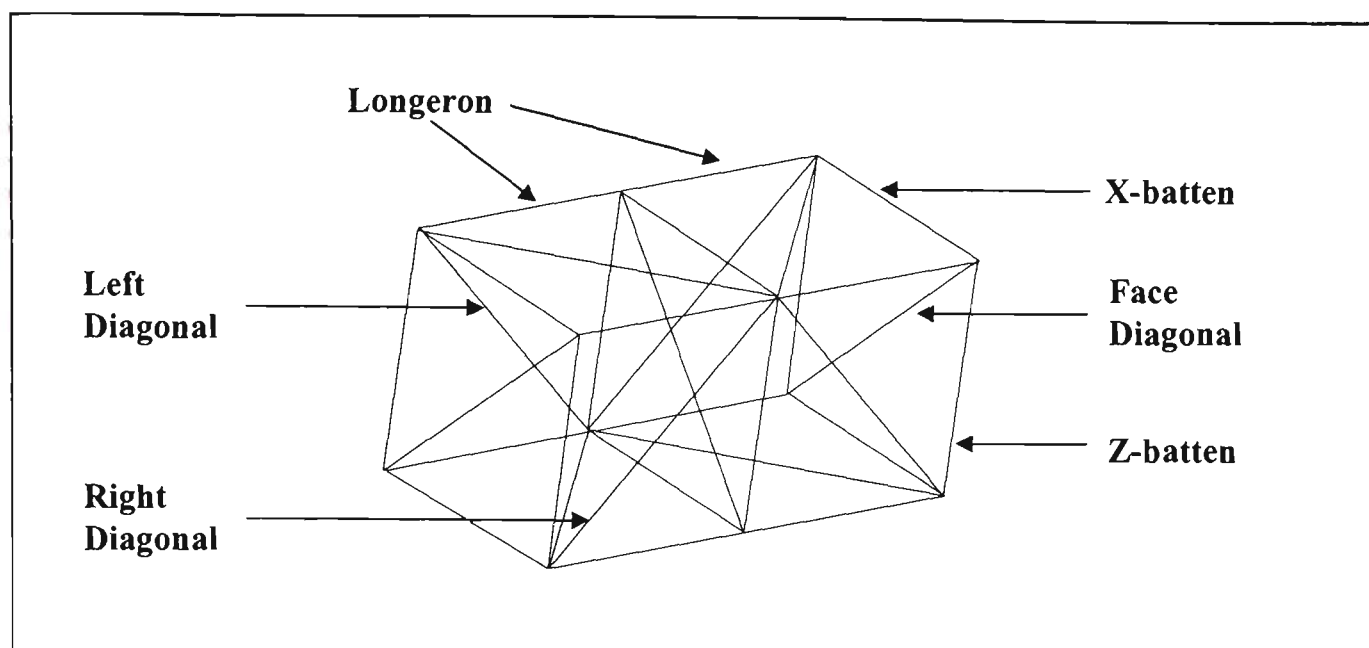


Figure 4.2: Section of Eight Bay Truss Lattice Structure

The mass configuration for the NASA 8 bay truss structure is given in Table 4.1. The masses applied to this truss structure were considered to be concentrated masses on the nodes only. This was achieved by distributing the mass of each longeron and diagonal between each of the nodes. Appendix 2 and Appendix 3 details the exact mass per each of the 36 nodes.

|                | Mass (grams) | Quantity using in 8 Bay Truss | Total Mass for 8 Bay Truss (Kg) |
|----------------|--------------|-------------------------------|---------------------------------|
| Node Ball      | 5.80         | 36                            | 0.2088                          |
| Longeron       | 180          | 68                            | 1.2240                          |
| Diagonal       | 27           | 41                            | 1.107                           |
| Joint Assembly | 7.7          | 218                           | 1.6786                          |
| Triax + Block  | 11.0         | 32                            | 0.3520                          |
| Total          |              |                               | 4.5704                          |

Table 4.1: Mass Configuration

Table 4.2 is a summary of the damage cases that will be introduced to the truss structure. Simulated damage in the truss structure will be considered as a loss in stiffness of a longeron or diagonal member. The damage introduced to the truss structure will firstly begin as a simple simulation where the Young's Modulus of one member will be reduced by 20%. Because the NASA 8 bay truss structure is far more complex than the simple mass spring system, adjusting

the Young's Modulus of the truss element is a simple and efficient way of introducing simulated damage into the structure.

These simulated cases are made on the assumption that it is possible to reduce the stiffness of these members without causing catastrophic failures. Case C involves multiple damage locations.

| Damage Case | Location      | Type          | Nodes         |
|-------------|---------------|---------------|---------------|
| A           | Bay 3         | Z-Batten      | 14 – 15       |
| B           | Bay 7         | Longeron      | 27 – 31       |
| C           | Both of Above | Both of Above | Both of Above |

**Table 4.2: Summary of Damage Cases**

Since the truss structure will be considered as a grounded structure, the DOFs associated with the grounded nodes will not be considered and will be removed. The remaining nodes that are not grounded will be assigned new corresponding DOFs when the grounded DOFs are removed. Table 4.3 below gives the corresponding DOFs numbers, when the grounded DOFs are removed, of the nodes numbers shown in Table 4.2. Since there are 3 DOFs (translational x, y, z) each node will have 3 corresponding DOFs. The first DOF for any node number can be calculated using the following relationship:

$$\text{Corresponding DOF} = [(\text{Node Number} - \text{Number of Grounded Nodes}) \times 3] - 2$$

| Node Number | Corresponding DOFs |
|-------------|--------------------|
| 14          | 28, 29, 30         |
| 15          | 31, 32, 33         |
| 27          | 67, 68, 69         |
| 31          | 79, 80, 81         |

**Table 4.3: Corresponding DOFs for Damage Cases**

## 4.2 CASE OF NON DAMAGED STRUCTURE

The mass and stiffness matrices were first calculated for the NASA 8 bay truss structure via an algorithm written in Matlab™. This algorithm ensured that the mass and stiffness matrices were constructed with the correct size to reflect the real life structure, and also took into account the grounded nodes. A Young's Modulus value of  $210 \times 10^9 \text{ N/m}^2$  and density of  $7850 \text{ kg/m}^3$  was used in the calculations. Table 4.4 show the diagonal stiffness values at each of the DOFs concerned taken from the calculated undamaged stiffness matrix. These values will be used later in this chapter to compare with the adjusted damage stiffness matrix for each different damage case.

| Node Number | DOF No. | Diagonal $[K]_{UD}$ Value at DOF (KN/m) |
|-------------|---------|---|
| 14          | 28      | 3298.1                                  |
|             | 29      | 6596.2                                  |
|             | 30      | 3298.1                                  |
| 15          | 31      | 2615.0                                  |
|             | 32      | 386.4                                   |
|             | 33      | 2615.0                                  |
| 27          | 67      | 3298.1                                  |
|             | 68      | 6596.2                                  |
|             | 69      | 3298.1                                  |
| 31          | 79      | 2615.0                                  |
|             | 80      | 386.4                                   |
|             | 81      | 2615.0                                  |

**Table 4.4: Diagonal Undamage Stiffness Values at DOF Locations**

To verify that the constructed mass and stiffness matrices were indeed correct, the natural frequencies of the structure were also calculated. A frequency range of 0Hz to 400Hz at a resolution of 0.5Hz was used. This range was sufficient to observe the first 10 natural frequencies of the NASA 8 bay truss structure. The results of the natural frequencies were compared with results obtained from ANSYS™, a finite element program.

Table 4.5 show the results of the first 10 natural frequencies for the NASA 8 bay truss structure obtained for Matlab™ compared to results obtained from ANSYS™, where consistent stiffness and mass matrices were used, as so are the matrices developed here. This table clearly demonstrates that very small differences exist between the results obtained from Matlab™ and the results obtained from ANSYS™. This suggests that the theoretically constructed mass and stiffness matrices are a representative of the real life structure. It can also be seen that as the frequency increases the percentage of errors becomes larger. However, since this study is only concerned with the first few frequency modes, increases in errors at higher frequency modes can be neglected.

| Natural Frequency Mode Numbers | Matlab™ (Hz) | ANSYS™ (Hz) | % Error from ANSYS™ |
|--------------------------------|--------------|-------------|---------------------|
| 1                              | 11.69        | 11.778      | 0.75                |
| 2                              | 12.13        | 12.221      | 0.74                |
| 3                              | 40.88        | 41.260      | 0.92                |
| 4                              | 55.90        | 56.071      | 0.30                |
| 5                              | 60.37        | 60.498      | 0.21                |
| 6                              | 97.80        | 100.15      | 2.35                |
| 7                              | 121.42       | 122.29      | 0.71                |
| 8                              | 122.41       | 124.31      | 1.53                |
| 9                              | 131.86       | 133.42      | 1.17                |
| 10                             | 184.33       | 189.51      | 2.73                |

**Table 4.5: Comparison of Natural Frequencies between Matlab™ and ANSYS™ for Undamage Case**

Receptance frequency response function (FRF) for the NASA 8 bay truss structure was also calculated using Matlab™. Shown in Figure 4.3 is the corresponding receptance FRF plot for  $\alpha(1, 1)$  of the undamage NASA 8 bay truss structure. Where  $\alpha(1, 1)$  in this case corresponds to obtaining the receptance FRF data from an accelerometer that is fixed at node no.5 and the structure is also excited at the same node. This is commonly referred to as a point FRF measurement. It also must be noted that  $\alpha(1, 1)$  corresponds to node no.5 for the truss structure only, because the DOFs of the grounded nodes have been removed.

Only point FRF measurements exhibit anti-resonance behaviour between two resonances (Ewins, 1984). This may be used as a simple check to confirm that the resultant FRF exhibits behaviour that is consistent with a point FRF measurement. These peaks can be clearly seen in Figure 4.3 and confirms that it is indeed a point FRF measurement.

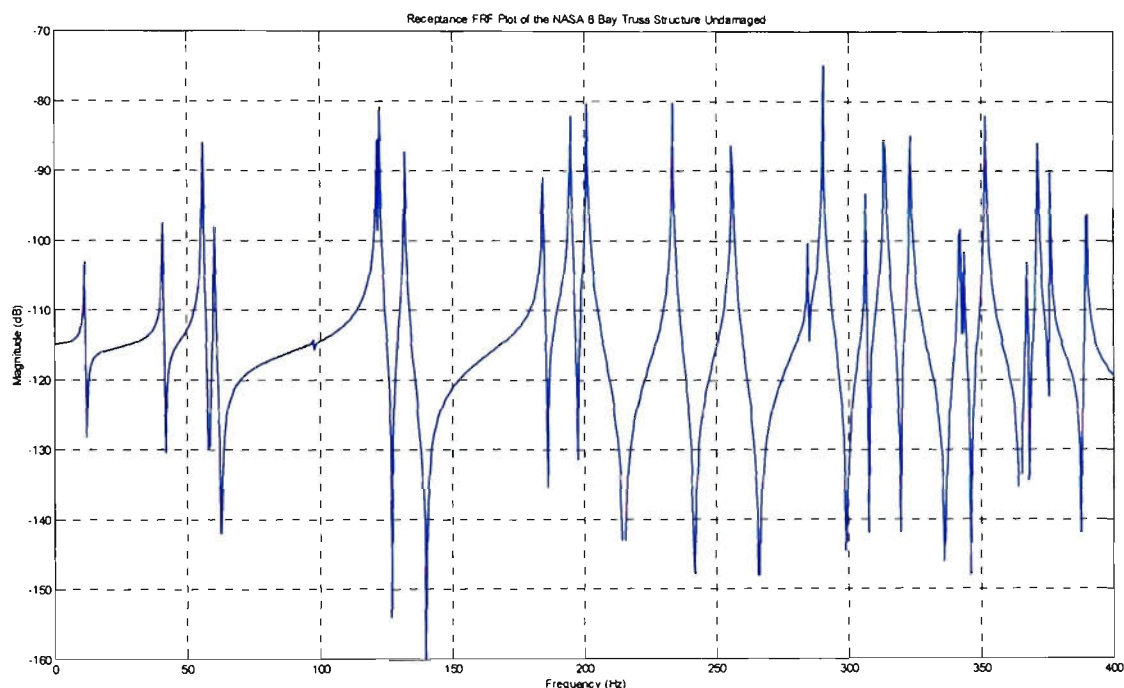


**Figure 4.3: Receptance FRF Plot of  $\alpha(1, 1)$  for Undamage Case**

As a check the Damage Detection Algorithm was firstly tested on the NASA 8 bay truss structure without any damage being introduced to the structure. Figure 4.4a and Figure 4.4b are the corresponding 3D DLV plot and 2D CDLV plot respectively, produced from the algorithm. As expected, these plots do not show any peaks whatsoever, which leads to the conclusion that the structure is free from damage.

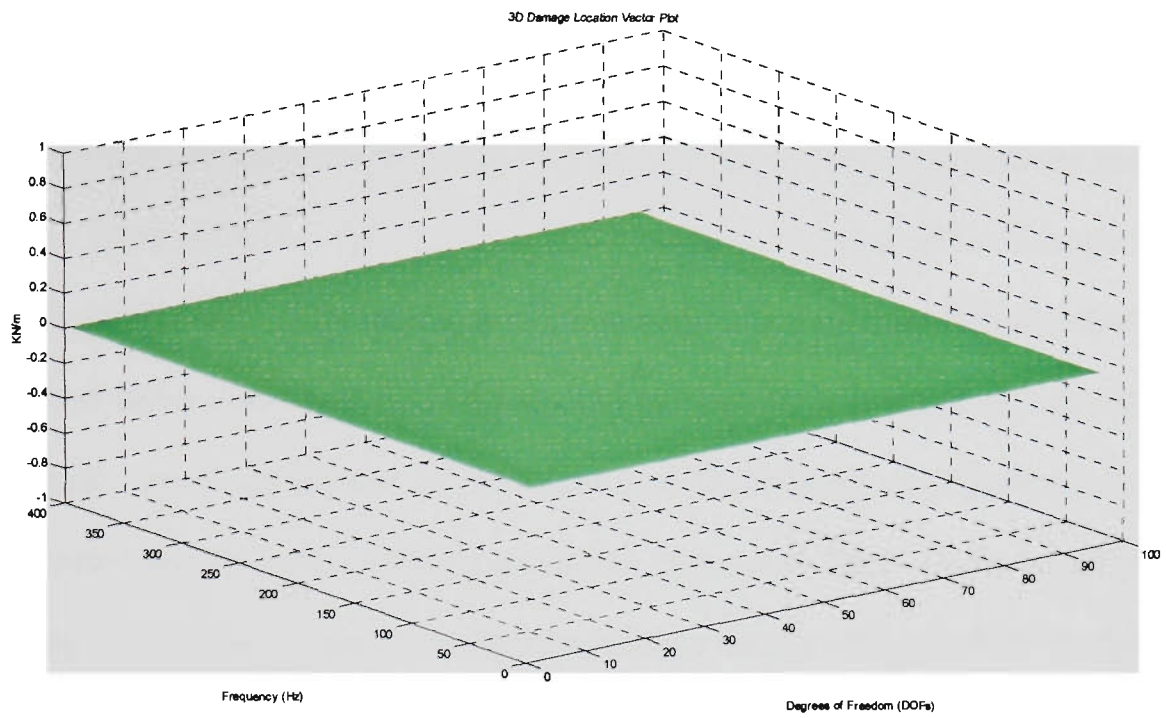


**Figure 4.4a: 3D DLV Plot for Undamage Case without Coordinate Incompatibility nor noise**

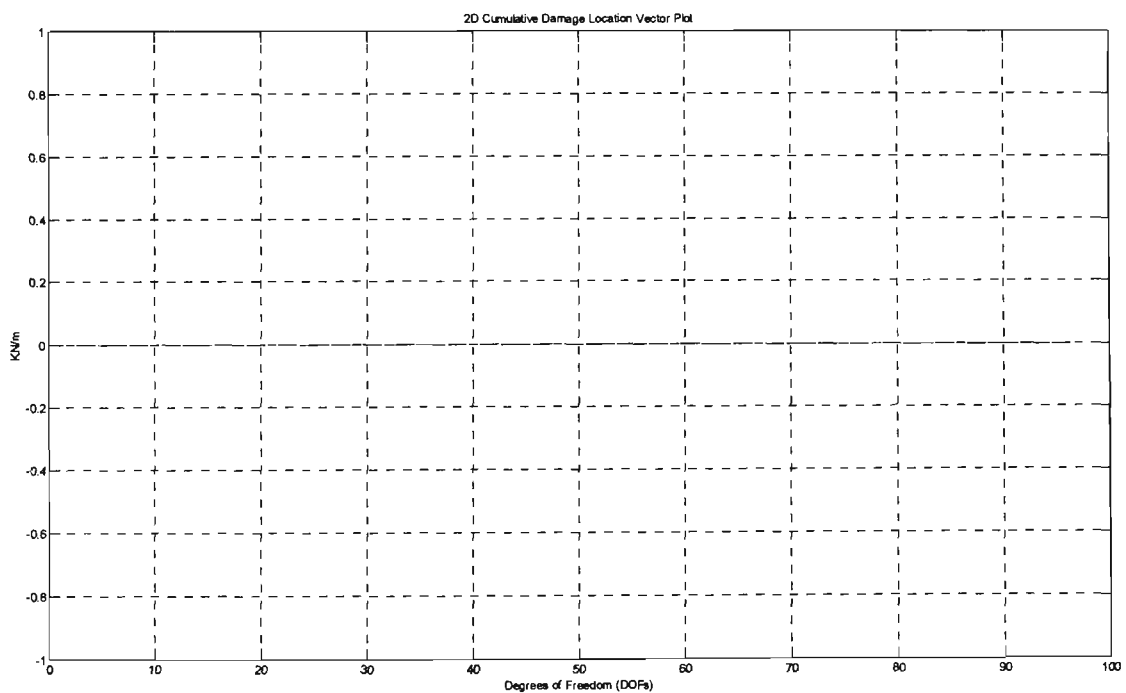


**Figure 4.4b: 2D CDLV Plot for Undamage Case without Coordinate Incompatibility nor noise**

### 4.3 DAMAGE CASES

#### 4.3.1 DAMAGE CASE A

In Damage Case A, simulated damage was introduced to the Z-batten link between node no. 14 and node no. 15 as shown in Figure 4.1. This is simulated by reducing the Young's Modulus corresponding to that link to  $168e9$  N/m, which represents a reduction by 20% and assuming that damage did not affect the mass of the structure. The corresponding damaged stiffness matrix was then calculated. Initial comparison for the diagonal of the undamaged stiffness matrix with the newly calculated stiffness matrix for Damage Case A is shown in Table 4.6. A reduction of 20% in the Young's Modulus was seen to reduce the stiffness corresponding to DOF no. 30 of node no. 14 by a stiffness of 386.4 KN/m or approximately 11.72% reduction from the original undamaged stiffness and accordingly to DOF no. 33 of node no. 15 by a stiffness of 386.4 KN/m or approximately 14.77% reduction from the original undamage stiffness.

| Node No. | DOF No. | Diagonal [K] <sub>UD</sub><br>Value at DOF<br>(KN/m) | Diagonal [K] <sub>D</sub><br>Value at DOF<br>(KN/m) | $\Delta K$ Value at<br>DOF (KN/m) |
|----------|---------|--|---|-----------------------------------|
| 14       | 28      | 3298.1   | 3298.1  | 0                                 |
|          | 29      | 6596.2   | 6596.2  | 0                                 |
|          | 30      | 3298.1   | 2911.7  | 386.4                             |
| 15       | 31      | 2615.0   | 2615.0  | 0                                 |
|          | 32      | 386.4  | 386.4   | 0                                 |
|          | 33      | 2615.0   | 2228.6  | 386.4                             |

**Table 4.6: Comparison of the Change in Stiffness (Delta K) Values for Damage Case A**

Following similar procedures in the previous section, natural frequencies were calculated from Matlab™ and compared with natural frequencies from ANSYS™ for this Damage Case A as shown in Table 4.7. The mass matrix used in the natural frequencies calculations via Matlab™ was the original mass matrix obtained from the undamaged structure.

Comparison of the natural frequencies from the calculated mathematical model to that of the FE model show that there are negligible differences between the two models. This suggests that the stiffness matrix corresponding to Damage Case A calculated by the Matlab™ algorithm is acceptably accurate.

| Natural Frequency Mode Number | Matlab™ (Hz) | ANSYS™ (Hz) | % Error from ANSYS™ |
|-------------------------------|--------------|-------------|---------------------|
| 1                             | 11.69        | 11.778      | 0.75                |
| 2                             | 12.13        | 12.221      | 0.74                |
| 3                             | 40.88        | 41.260      | 0.92                |
| 4                             | 55.90        | 56.070      | 0.30                |
| 5                             | 60.37        | 60.496      | 0.21                |
| 6                             | 97.78        | 100.13      | 2.35                |
| 7                             | 121.40       | 122.27      | 0.71                |
| 8                             | 122.41       | 124.30      | 1.52                |
| 9                             | 131.84       | 133.41      | 1.18                |
| 10                            | 184.33       | 189.50      | 2.73                |

**Table 4.7: Comparison of Natural Frequencies between Matlab™ and ANSYS™ for Damage Case A**

Receptance FRFs for the NASA 8 bay space truss were also calculated using Matlab™. Shown in Figure 4.5 is the receptance FRF plot for  $\alpha(1, 1)$  of the NASA eight bay truss structure for before and after Damage Case A was introduced. It can be barely observed that the effects of Damage Case A caused a shift in some of the peaks compared to the original undamaged receptance FRF trace, but nothing can be said about the location and severity of damage from this plot.

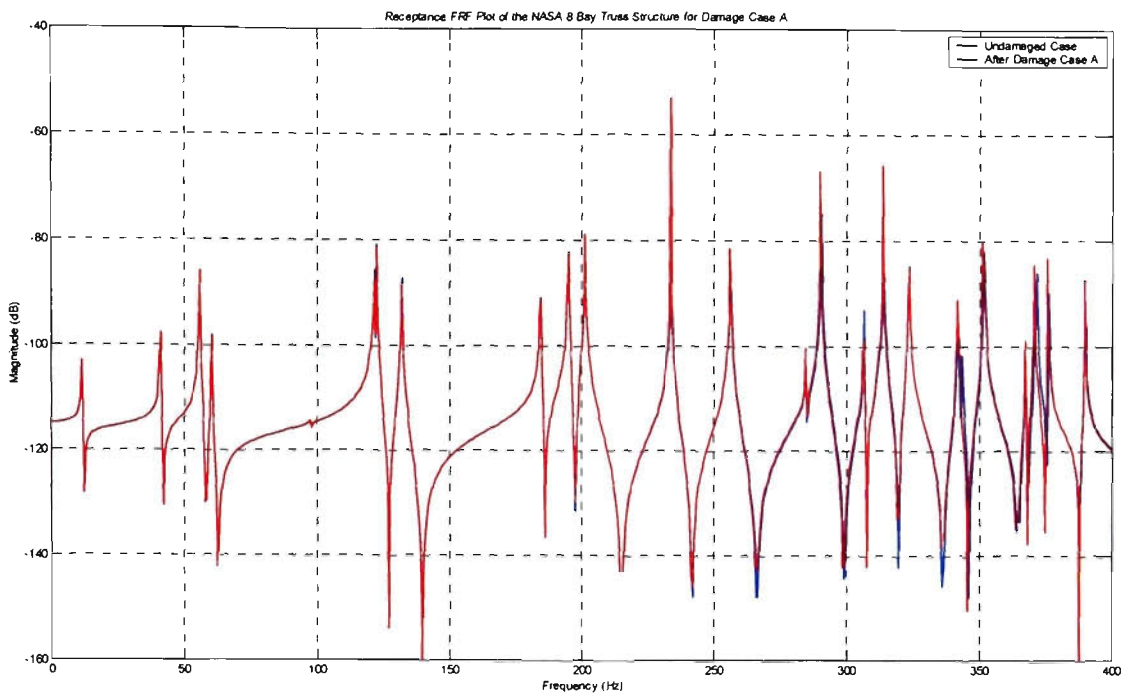


Figure 4.5: Receptance FRF Plot of  $\alpha(1, 1)$  for Damage Case A

### 4.3.2 DAMAGE CASE B

In Damage Case B, simulated damage was introduced to the longeron link between node no. 27 and node no. 31 as shown in Figure 4.1. Similar to Damage Case A, this is simulated by reducing the Young's Modulus corresponding to that longeron link to  $168 \times 10^9$  N/m, which represents a reduction by 20%. The corresponding damaged structure stiffness matrix was then calculated. Comparison of the diagonal of the undamaged stiffness matrix with the newly calculated stiffness matrix for Damage Case B is shown in Table 4.8. A reduction of 20% in the Young's Modulus was seen to reduce the stiffness corresponding to DOF no. 68 of node no. 27 by a stiffness of 368.4 KN/m or approximately 5.86% reduction from the original undamaged stiffness and to DOF no. 80 of node no. 31 by a stiffness of 368.4 KN/m or approximately 10% reduction from the original undamaged stiffness.

| Node No. | DOF No. | Diagonal [K] <sub>UD</sub><br>Value at DOF<br>(KN/m) | Diagonal [K] <sub>D</sub><br>Value at DOF<br>(KN/m) | $\Delta K$ Value at<br>DOF (KN/m) |
|----------|---------|--|---|-----------------------------------|
| 27       | 67      | 3298.13  | 3298.13   | 0                                 |
|          | 68      | 6596.26  | 6209.86   | 368.40                            |
|          | 69      | 3298.13  | 3298.13   | 0                                 |
| 31       | 79      | 2615.06  | 2615.06   | 0                                 |
|          | 80      | 3864.00  | 3477.60   | 368.40                            |
|          | 81      | 2615.06  | 2615.06   | 0                                 |

**Table 4.8: Comparison of the Change in Stiffness (Delta K) Values for Damage Case B**

Following similar procedures to the previous section, natural frequencies were calculated in Matlab™ and compared with natural frequencies from ANSYS™ and these are presented in Table 4.9. Again there are negligible differences between the two sets of natural frequencies.

| Natural Frequency<br>Mode Number | Matlab™ (Hz) | ANSYS™ (Hz) | % Error from<br>ANSYS™ |
|----------------------------------|--------------|-------------|------------------------|
| 1                                | 11.69        | 11.78       | 0.76                   |
| 2                                | 12.13        | 12.22       | 0.74                   |
| 3                                | 40.88        | 41.26       | 0.92                   |
| 4                                | 55.90        | 56.07       | 0.30                   |
| 5                                | 60.32        | 60.45       | 0.22                   |
| 6                                | 97.74        | 100.09      | 2.34                   |
| 7                                | 121.42       | 122.29      | 0.71                   |
| 8                                | 122.41       | 124.31      | 1.53                   |
| 9                                | 131.43       | 132.99      | 1.17                   |
| 10                               | 184.33       | 189.50      | 2.73                   |

**Table 4.9: Comparison of Natural Frequencies between Matlab™ and ANSYS™ for Damage Case B**

Receptance FRFs for the NASA 8 bay space truss were also calculated using Matlab™. Shown in Figure 4.6 below is the receptance FRF plot for  $\alpha(1, 1)$  of the NASA eight bay space truss structure before and after Damage Case B. Again, there is a small shift observed in some of the peaks.

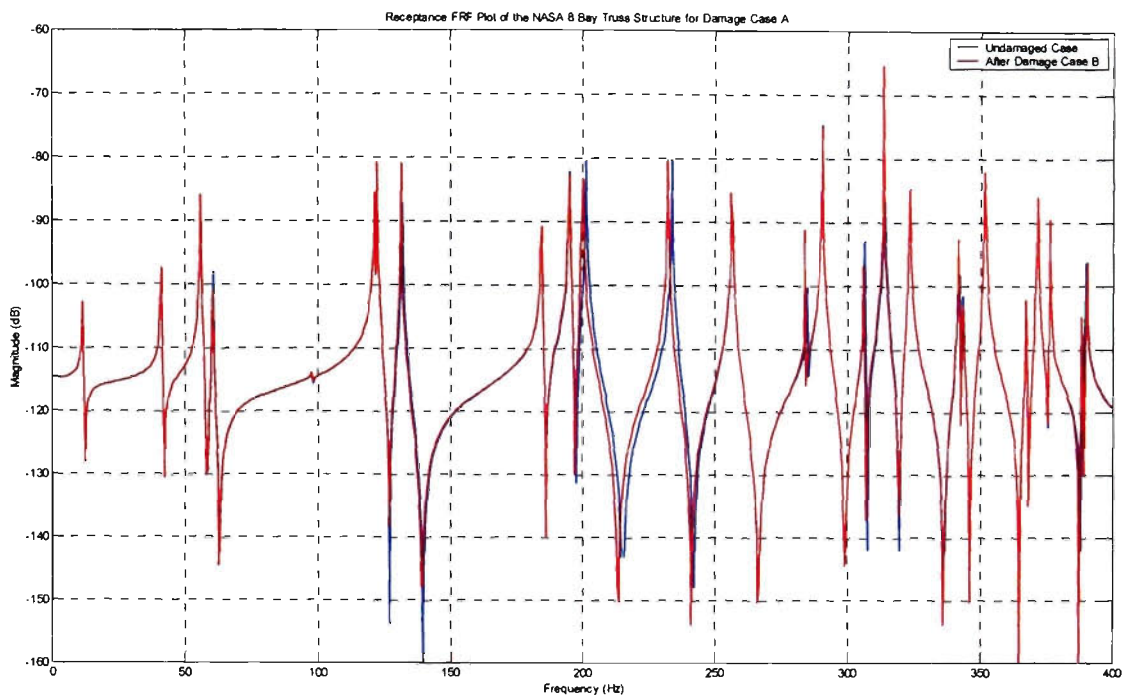


Figure 4.6: Receptance FRF Plot of  $\alpha(1, 1)$  for Damage Case B

### 4.3.3 DAMAGE CASE C

To further verify the developed Damage Detection Algorithm, a simulation involving multiple damage locations was introduced to the truss structure. Damage Case C is the cumulation of Damage Case A and Damage Case B as shown in Table 4.2. For changes in the diagonal stiffness matrix for Damage Case C, Table 4.6 and Table 4.8, which correspond to Damage Case A and Damage Case B respectively should be used. Natural Frequencies were then calculated from Matlab™ and also compared with natural frequencies from ANSYS™. Shown in Table 4.10 are the natural frequencies of the truss structure with the damage introduced at the location specified as Damage Case C. Comparison of the natural frequencies from that of the calculated mathematical model to that of the FE model show that there is negligible difference between corresponding frequencies.

| Natural Frequency Mode Numbers | Matlab™ (Hz) | ANSYS™ (Hz) | % Error from ANSYS™ |
|--------------------------------|--------------|-------------|---------------------|
| 1                              | 11.69        | 11.78       | 0.76                |
| 2                              | 12.13        | 12.22       | 0.74                |
| 3                              | 40.88        | 41.26       | 0.92                |
| 4                              | 55.90        | 56.07       | 0.30                |
| 5                              | 60.32        | 60.45       | 0.22                |
| 6                              | 97.72        | 100.07      | 2.35                |
| 7                              | 121.40       | 122.27      | 0.71                |
| 8                              | 122.41       | 124.30      | 1.52                |
| 9                              | 131.41       | 132.97      | 1.17                |
| 10                             | 184.33       | 189.49      | 2.72                |

**Table 4.10: Comparison of Natural Frequencies between Matlab™ and ANSYS™ for Damage Case C**

Receptance FRFs for the NASA 8 bay space truss structure were also calculated using Matlab™. Shown in Figure 4.7 is the receptance FRF plot at  $\alpha(1, 1)$  of the NASA 8 bay space truss structure for before and after Damage Case C. It is again observed that damage causes a shift in some of the peaks. This shift causes these peaks to occur at lower frequencies compared to the undamaged receptance FRF, but it is only a qualitative indication that some damage has been inflicted.

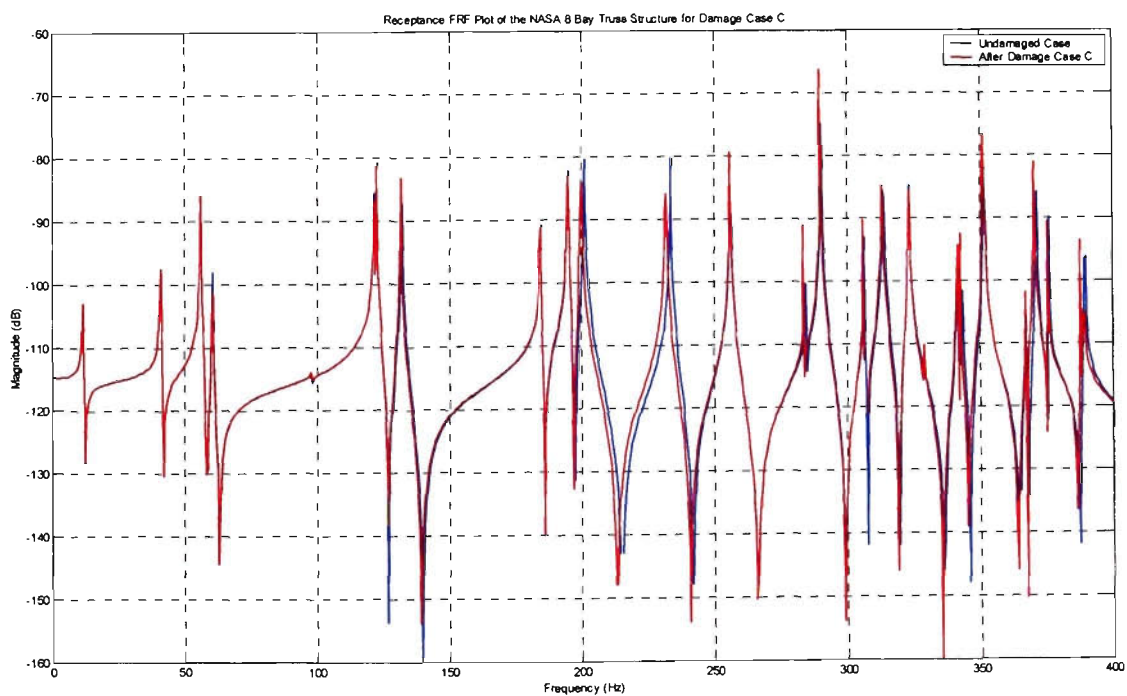
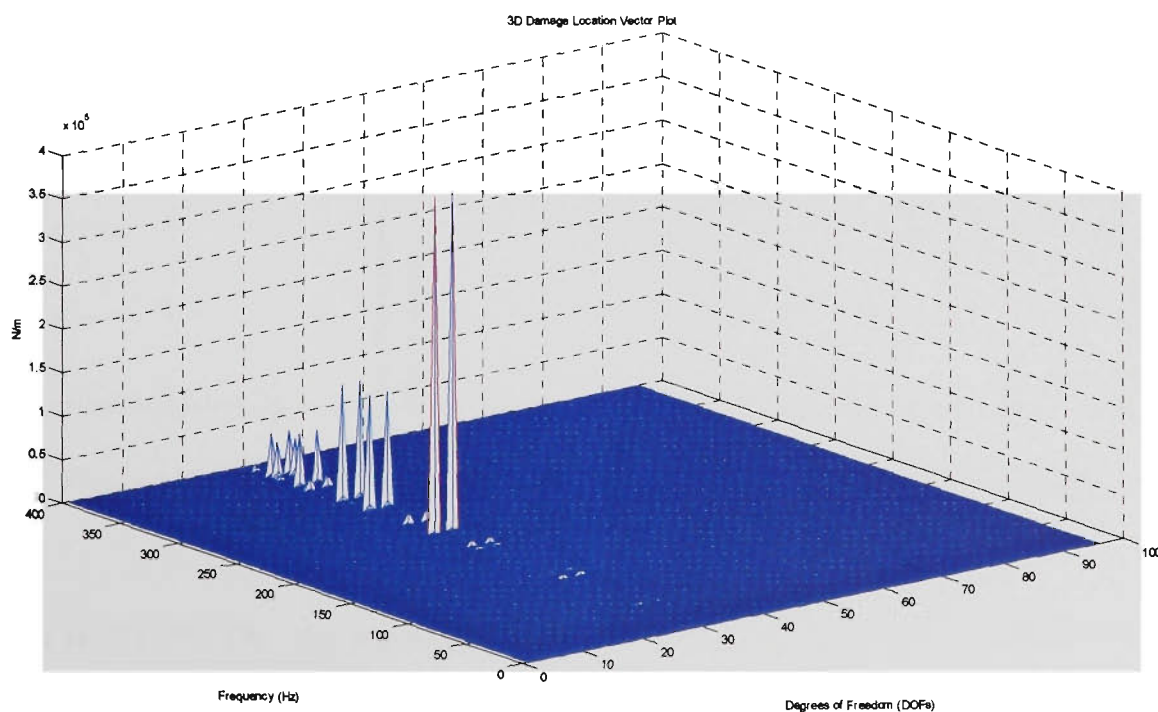


**Figure 4.7: Receptance FRF Plot of  $\alpha(1, 1)$  for Damage Case C**

#### 4.4 DAMAGE DETECTION WITHOUT COORDINATE INCOMPATIBILITY AND NO NOISE

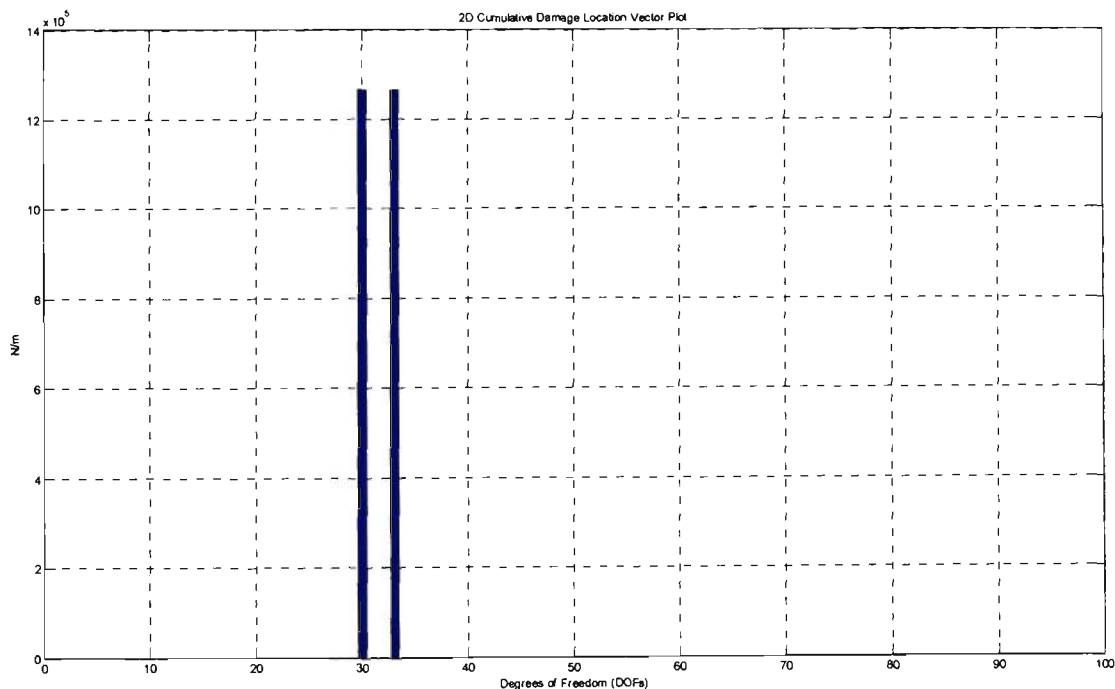
The Damage Detection Algorithm was then applied to the three Damage Cases without any coordinate incompatibility and no noise interference. The frequency range of these plots was from 0Hz – 400Hz with a frequency resolution of 0.5Hz.

Figure 4.8a below is the 3D Damage Location Vector plot for Damage Case A. From Figure 4.8a peaks can be seen to occur at various frequencies and are contained between DOF 20 and DOF 40. It may be difficult to see but many of the larger dominant peaks occur between DOF 20 and DOF 40, and the magnitude of the largest peak can be estimated to be approximately 350 KN/m. This estimate corresponds to the amount of stiffness that was reduced from the Z-batten link, which from Table 4.6 was exactly 386.4 KN/m. It may be difficult to see the actual DOFs in this 3D DLV Plot due to the amount of information it contains, however it is possible to utilise this 3D DLV plot in conjunction with the corresponding 2D CDLV plot to locate and estimate the damage extent. It also must be noted that due to computational constraints, the full natural frequency spectrum of the whole truss structure has not been plotted.



**Figure 4.8a: 3D DLV Plot for Damage Case A without Coordinate Incompatibility nor Noise**

Figure 4.8b is the corresponding 2D CDLV plot for Damage Case A. Here it can be clearly seen that the damage is associated with DOF 30 and DOF 33. This confirms the location of the damage since the original damage was introduced between node no. 14 (DOFs: 28, 29, 30) and node no. 15 (DOFs: 31, 32, 33). The Damage Detection Algorithm successfully located the simulated damage within the structure and no other damage was located. It is also interesting to note that the introduced simulated damage was observed to affect only the translational Z component at the point of damage. It must be noted that the magnitude in the 2D CDLV plot is a cumulation of the magnitude at various frequencies for each of the DOFs. This cumulative value can not be interpreted to be anything meaningful, since this cumulative magnitude depends on the frequency resolution. If a finer frequency resolution is used then the cumulative magnitude will be greater since there will be more magnitude per frequency resolution to be added.



**Figure 4.8b: 2D CDLV Plot for Damage Case A without Coordinate Incompatibility nor Noise**

Figure 4.9a is the 3D Damage Location Vector Plot for Damage Case B without coordinate incompatibility and no noise interference. From Figure 4.9a peaks can be seen to occur at various frequencies and are contained between DOF 60 and DOF 80. It may be difficult to see,

but the magnitude of the damage is approximately 350 KN/m, which corresponds to the amount of stiffness that was reduced from the longeron link. It may be also difficult to see the actual DOFs where the damage occurs due to the amount of information that it contains, hence the 2D Cumulative Damage Location Vector plot should be consulted.

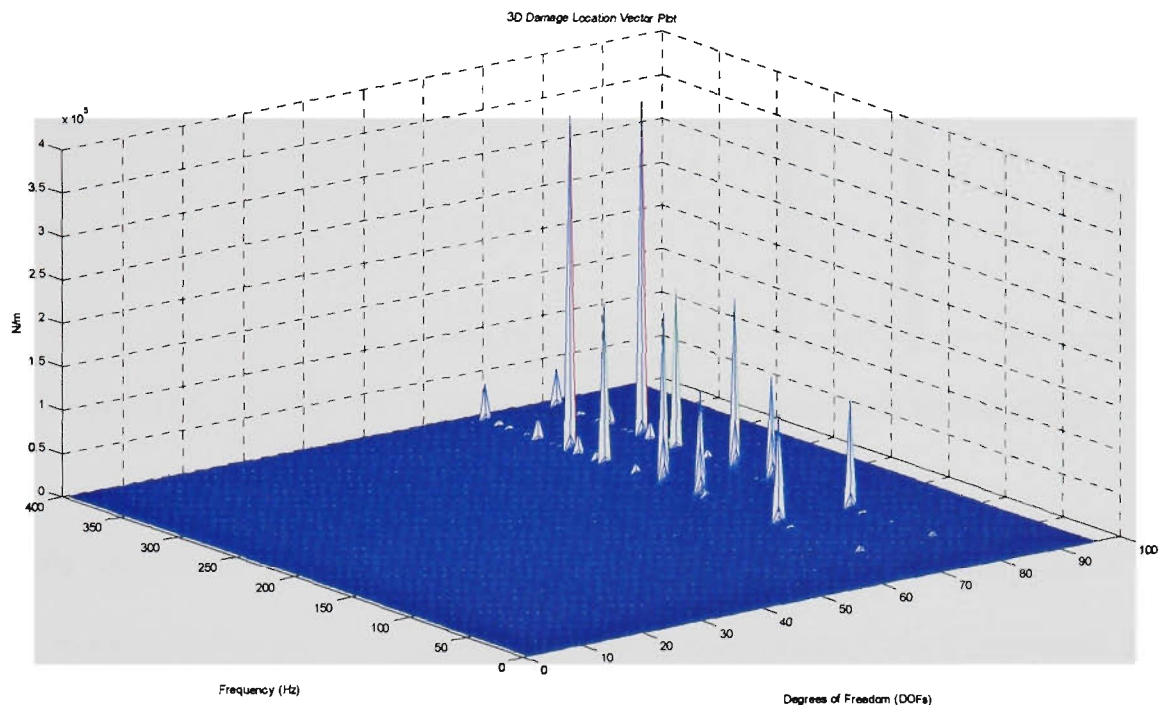


**Figure 4.9a: 3D DLV Plot for Damage Case B without Coordinate Incompatibility nor Noise**

Figure 4.9b is the corresponding 2D CDLV plot for Damage Case B without coordinate incompatibility and no noise interference. Here it can be clearly seen that the damage is associated with DOF 68 and DOF 80. This confirms the location of the damage to exist between node no. 27 (DOFs: 67, 68, 69) and node no. 31 (DOFs: 79, 80, 81). It is interesting to note that the introduced simulated damage for this Longeron link was observed to affect only the translational Y component at the point of damage. Again the Damage Detection Algorithm successfully detected and located the simulated damage within the structure and no other damage was located.

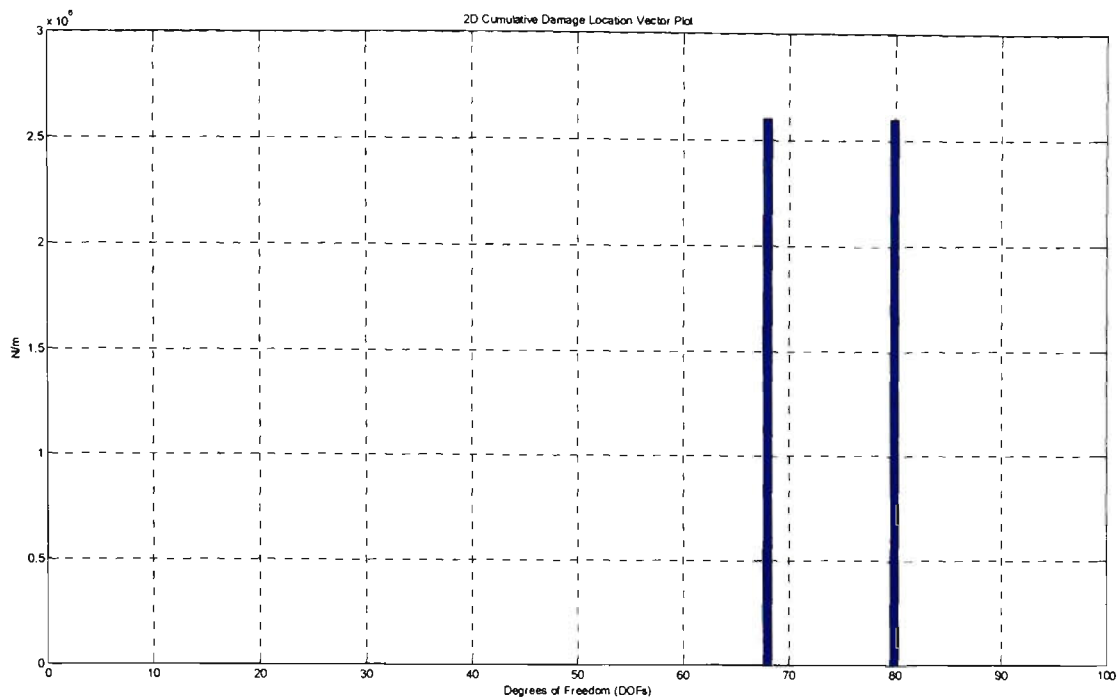
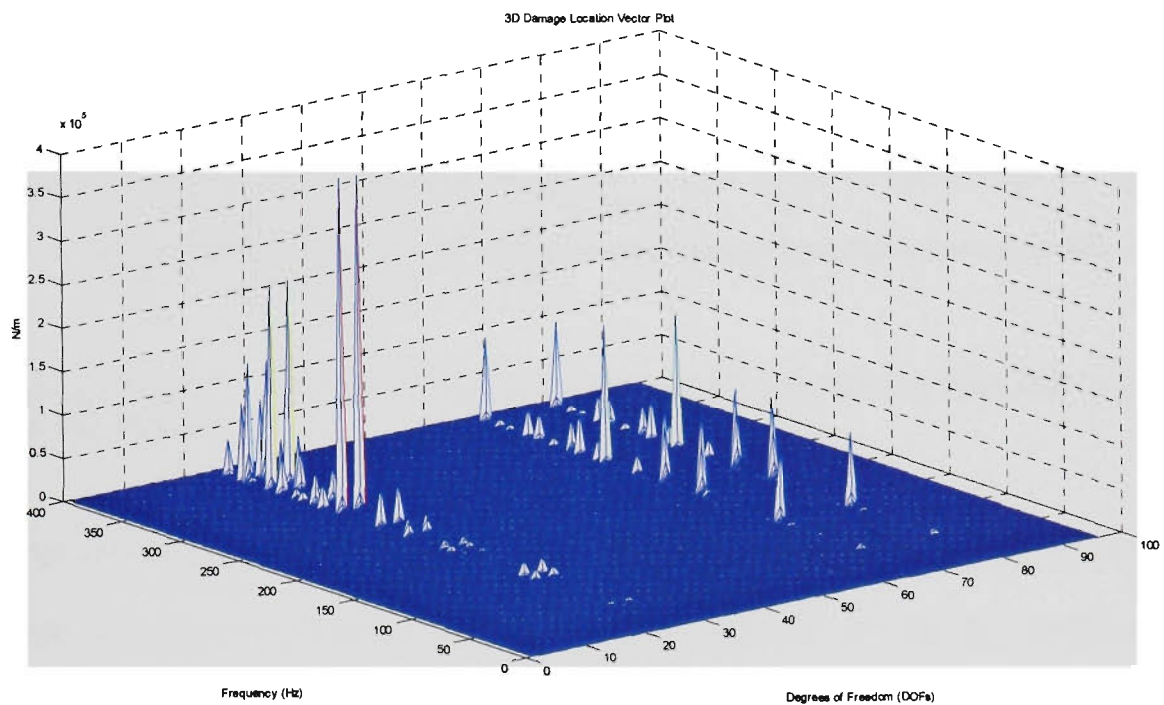


**Figure 4.9b: 2D CDLV Plot for Damage Case B without Coordinate Incompatibility nor Noise**

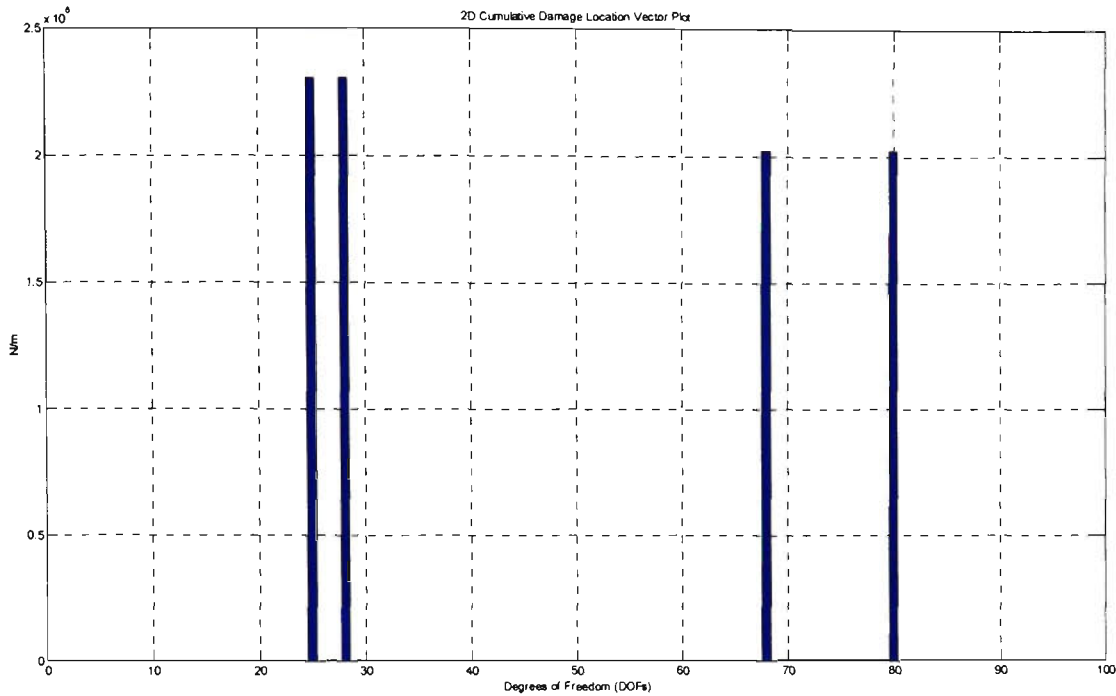
Figure 4.10a shown is the 3D Damage Location Vector plot for Damage Case C without coordinate incompatibility and no noise interference. Since Damage Case C represents simulated damage from both Damage Case A and Damage Case B it can be seen that multiple peaks are present in this plot. These peaks can be seen to occur at various frequencies, but are isolated between DOF 20 and DOF 40 and between DOF 60 and DOF 80. However, due to the amount of information that is contained in this plot it is very difficult to accurately isolate individual DOFs or pinpoint the location of damage on the truss. Again, the 2D CDLV should be consulted in conjunctions with this plot to adequately pinpoint the location of damage.

Figure 4.10b is the corresponding 2D CDLV plot for Damage Case C without coordinate incompatibility and no noise interference. It can be clearly seen that the damage is associated with DOF 30, DOF 33, DOF 69 and DOF 80. These DOFs correspond to node no. 14 (DOFs: 28, 29, 30), node no. 15 (DOFs: 31, 32, 33), node no. 27 (DOFs: 67, 68, 69) and node no. 31 (DOFs: 79, 80, 81). Although the Damage Detection Algorithm successfully located the damage, care must be taken when interpreting the locations of damage in situations where multiple damages occur.

At this point, knowledge of the connectivity within the structure becomes extremely important. Fortunately, for this damage case, the only possible node (of the 'damaged' DOF set) relating to node no. 14 is node no. 15. Therefore, damage exists between node no. 14 and node no. 15, which corresponds to the Z-batten link. Similarly, the only possible node (of the 'damaged' DOF set) relating to node no. 27 is node no. 31, and hence the location of damage is between node no. 27 and node no. 31, which corresponds to the longeron link.



**Figure 4.10a: 3D DLV Plot for Damage Case C without Coordinate Incompatibility nor Noise**



**Figure 4.10b: 2D CDLV Plot for Damage Case B without Coordinate Incompatibility nor Noise**

#### **4.5 DAMAGE DETECTION WITHOUT COORDINATE INCOMPATIBILITY AND WITH 5% NOISE**

The Damage Detect Algorithm was successful in detecting the simulated damage in the previous section under the ideal condition without any noise interference. To test the robustness of the Damage Detection Algorithm, 5% random noise interference will now be introduced to the algorithm. This 5% noise interference is chosen to represent measurement errors and environmental interference. Its effectiveness will be assessed on the same damage scenario cases adopted in the previous section. The frequency range of these plots was from 0Hz – 400Hz with a frequency resolution of 0.5Hz.

Figure 4.11a is the 3D Damage Location Vector Plot for Damage Case A without coordinate incompatibility and with 5% random noise interference introduced. The effects of the 5% random noise on the 3D DLV plot can be seen to only affect the whole system within a certain frequency range whilst leaving other frequencies untouched. This 5% random noise does not affect the prominence of the peaks that were previously found in Figure 4.11a.

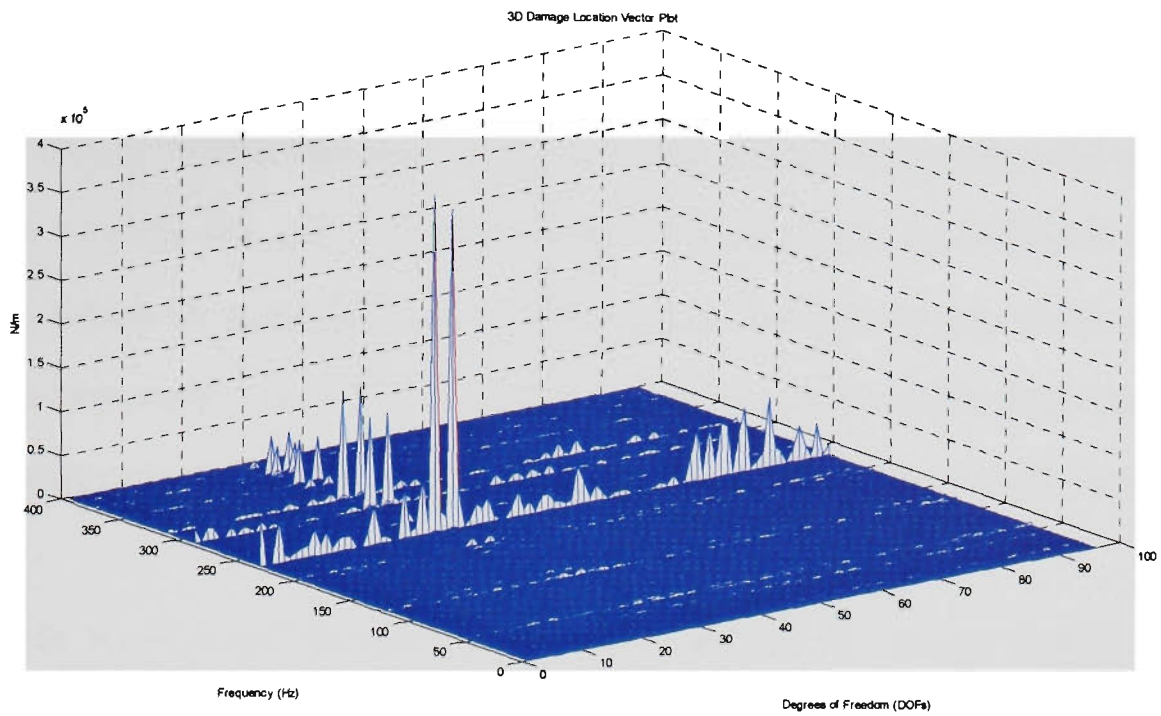


**Figure 4.11a: 3D DLV Plot for Damage Case A without Coordinate Incompatibility (5% Noise)**

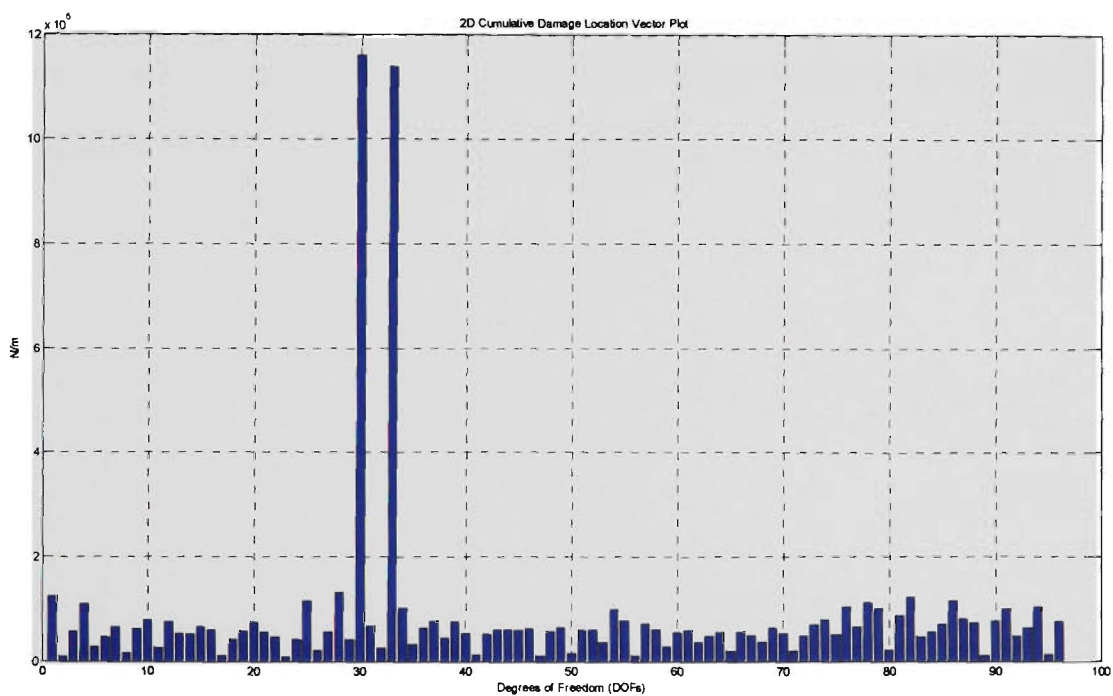
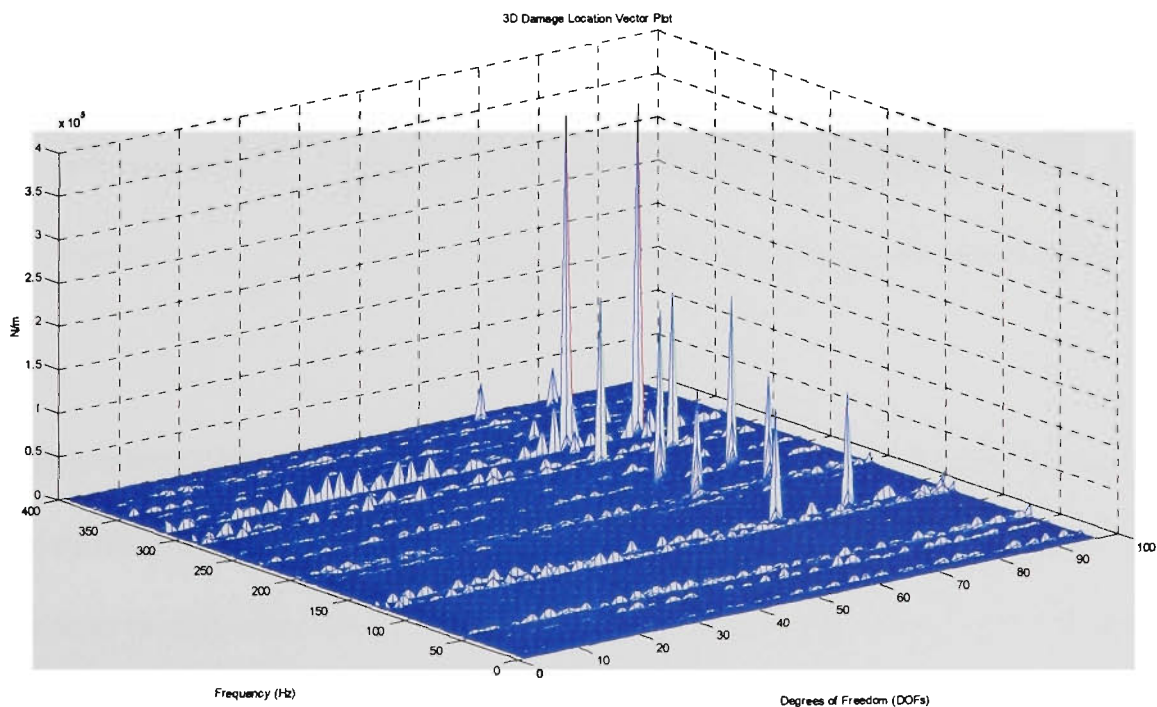


**Figure 4.11b: 2D CDLV Plot for Damage Case A without Coordinate Incompatibility (5% Noise)**

Figure 4.11b is the corresponding 2D CDLV plot for Damage Case A without coordinate incompatibility and with 5% random noise introduced. A comparison between Figures 4.8b and Figure 4.11b show that the effect of 5% randomised noise on the Damage Detection Algorithm was minimal, and the algorithm was still able to successfully detect damage in the same location.

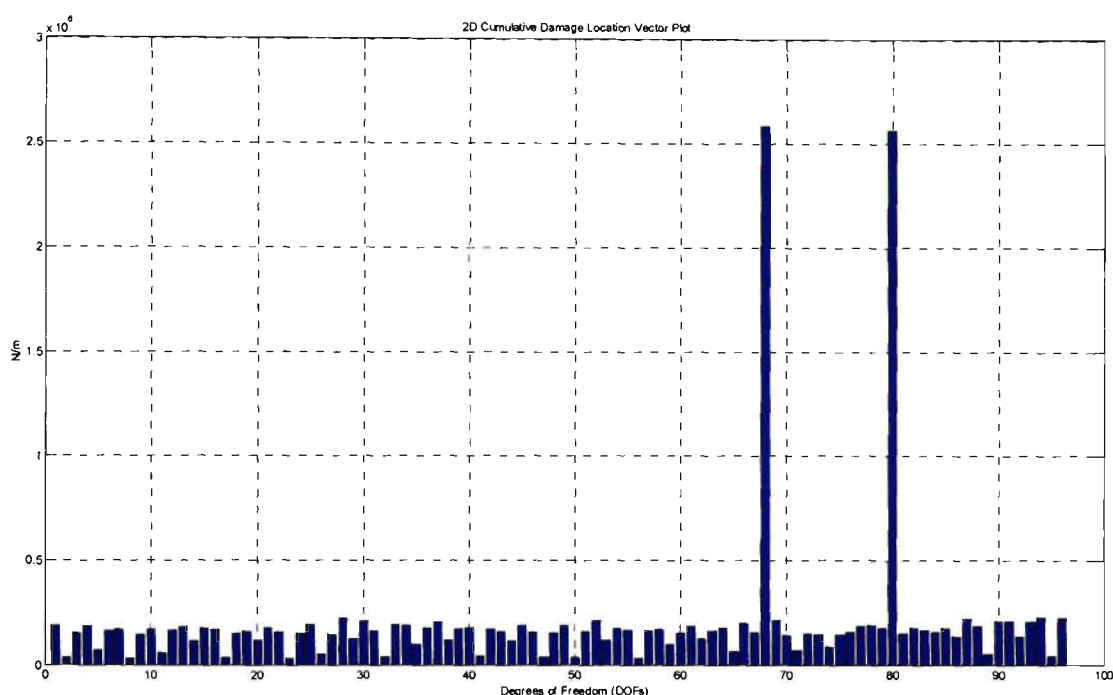
The only effect from the introduction of the random noise was that it affected all DOFs within the structure. When collated cumulatively every DOF had vectors of nonzero value. This was due to the introduced noise influence. It can be clearly seen that these noise peaks are much lower than the peaks that actually contain damage. This is because the DOFs that are truly affected by damage occur only at certain frequencies, while those that are only affected by noise occur at all frequencies. Hence, when collated cumulatively together over the frequency ranges, those that truly contain damage would be much greater than those that are affected by noise only.

Figure 4.12a below is the 3D Damage Location Vector plot for Damage Case B without coordinate incompatibility and 5% random noise interference introduced. The effects of the 5% random noise on the 3D DLV plot can be seen to only affect the whole system within a certain frequency range whilst leaving other frequencies essentially untouched. This 5% random noise does not seem to affect the peaks that were previously shown in Figure 4.13a. The peaks still show up in the same location between DOF 60 and DOF 80.



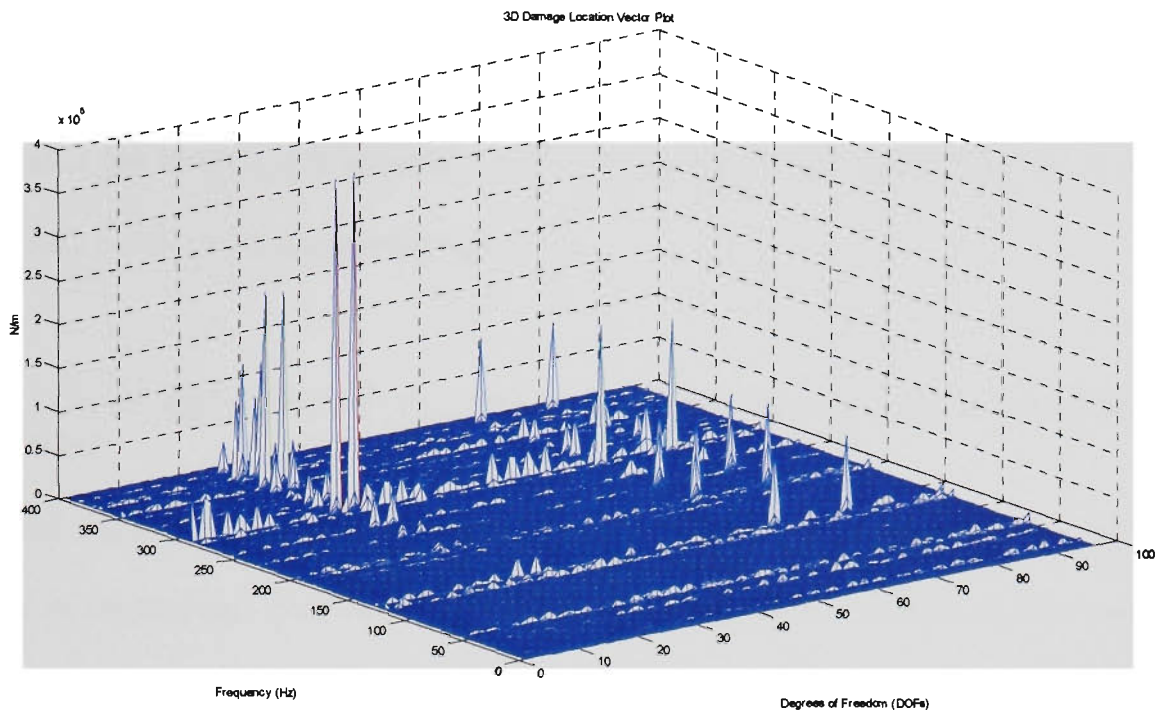
**Figure 4.12a: 3D DLV Plot for Damage Case B without Coordinate Incompatibility (5% Noise)**

Figure 4.12b is the corresponding 2D CDLV plot for Damage Case B without coordinate incompatibility and with 5% random noise interference introduced. A comparison between Figures 4.9b and Figure 4.12b show that the effects of 5% random noise on the Damage Detection Algorithm was minimal, and the algorithm was still able to successfully detect damage in the same location as previously. It can be seen that the introduction of the randomised noise affected all DOFs within the structure. When collated cumulatively every DOF had vectors of nonzero value. With careful observation, it can be clearly seen that these noise peaks are much lower than the peaks that actually contain damage.

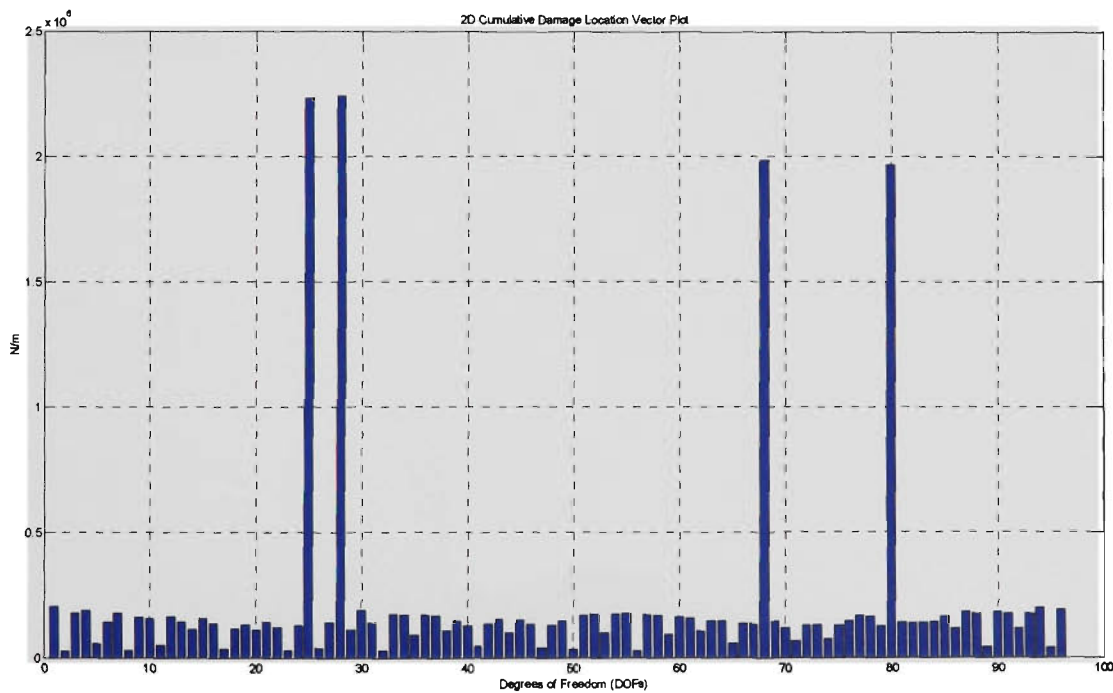


**Figure 4.12b: 2D CDLV Plot for Damage Case B without Coordinate Incompatibility (5% Noise)**

Figure 4.13a is the 3D DLV plot for Damage Case C without coordinate incompatibility and with 5% random noise interference introduced. The effects of the 5% random noise on the 3D DLV plot can be seen to only affect the whole system within certain frequency ranges whilst leaving other frequencies essentially untouched. This 5% random noise does not seem to affect the peaks that were shown in Figure 4.13a. These peaks still show up in the same locations.



**Figure 4.13a: 3D DLV Plot for Damage Case C without Coordinate Incompatibility (5% Noise)**



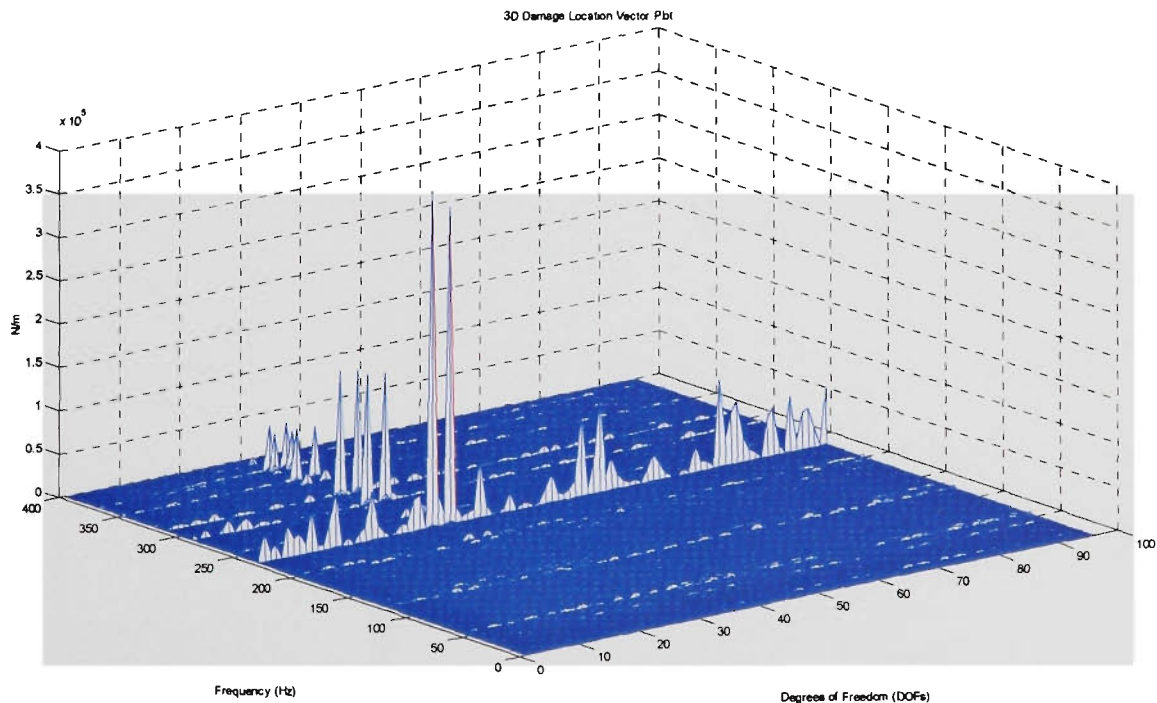
**Figure 4.13b: 2D CDLV Plot for Damage Case C without Coordinate Incompatibility (5% Noise)**

Figure 4.13b is the corresponding 2D CDLV plot for Damage Case C without coordinate incompatibility and with 5% random noise introduced. A comparison between Figure 4.10b and Figure 4.13b show that the effects of the 5% random noise on the Damage Detection Algorithm

was minimal and the algorithm was still able to successfully detect damage in the same locations as previously. The only effects from the introduction of the randomised noise were that it affected all DOFs within the structure. When collated cumulatively every DOF has vectors of nonzero value due to the noise influence. It can be seen that these noise peaks are much lower than the peaks that actually contain damage.

#### 4.6 DAMAGE DETECTION WITH COORDINATE INCOMPATIBILITY AND WITH 5% NOISE

Often in real life it is not possible to measure all the coordinates of a structure. To further test the robustness of the Damage Detection Algorithm only FRF data for 72 DOFs will be supplied for the three previous damage cases. The data for these 72 DOFs were randomly chosen from a possible 96 DOFs. Appendix 4 contains the sequence order for these 72 randomly chosen DOFs. This will require the Damage Detection Algorithm to expand the 24 missing data to match the 96 DOFs found in the undamaged structure.



**Figure 4.14a: 3D DLV Plot for Damage Case A with Coordinate Incompatibility (5% Noise)**

Figure 4.14a show the 3D DLV plot for Damage Case A with 72 measured and 24 expanded coordinates and 5% noise interference introduced. For this scenario only data for 72 DOFs were supplied to the Damage Detection Algorithm, leaving the developed Damage Detection Algorithm to expand the 24 missing data to match the DOFs of the undamaged case using Dynamic Expansion method A as discussed previously in Chapter 2. Again the Damage Detection Algorithm successfully detects the damage and the effect of damage is shown as distinctive peaks on the plot.

Figure 4.14b is the corresponding 2D CDLV plot for Damage Case with 72 measured and 24 expanded DOFs and 5% noise interference. On this plot the location of damage can be distinctively observed to be the dominant peaks over those that are caused by noise interference. The location of damage is DOF 30 and DOF 33 and corresponds to node no. 14 and node no. 15 on the truss structure. This is consistent with the location of damage for Damage Case A. The Damage Detection algorithm was able to successfully detect the simulated damage in this case since the DOFs that contain damage lie within the 72 randomly chosen DOFs.

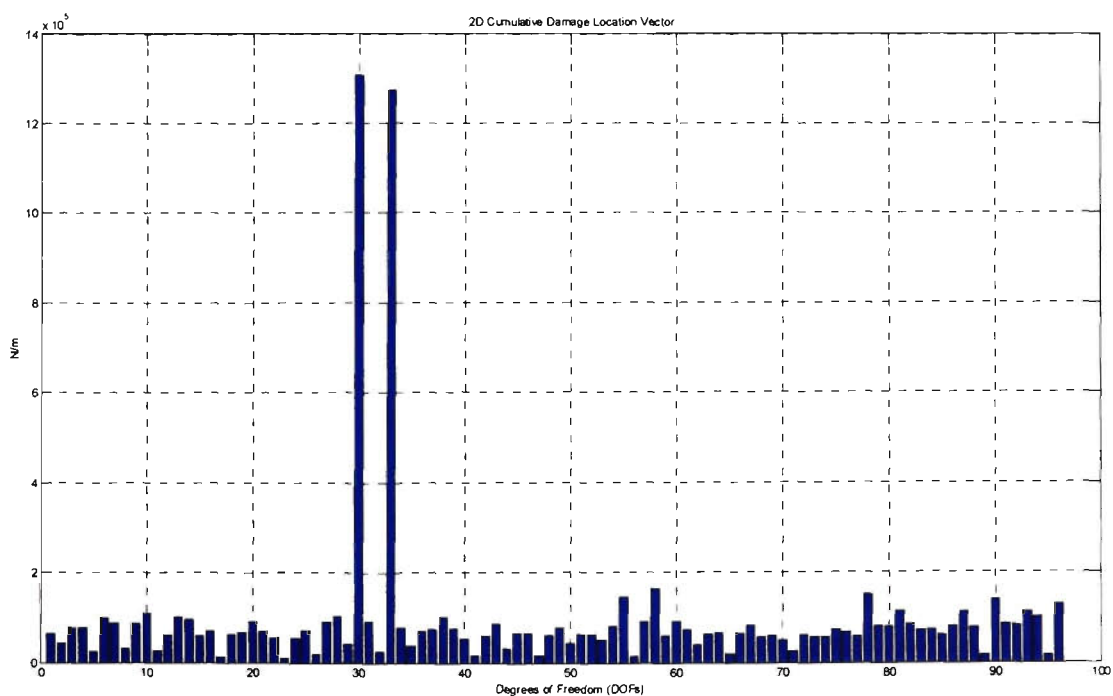
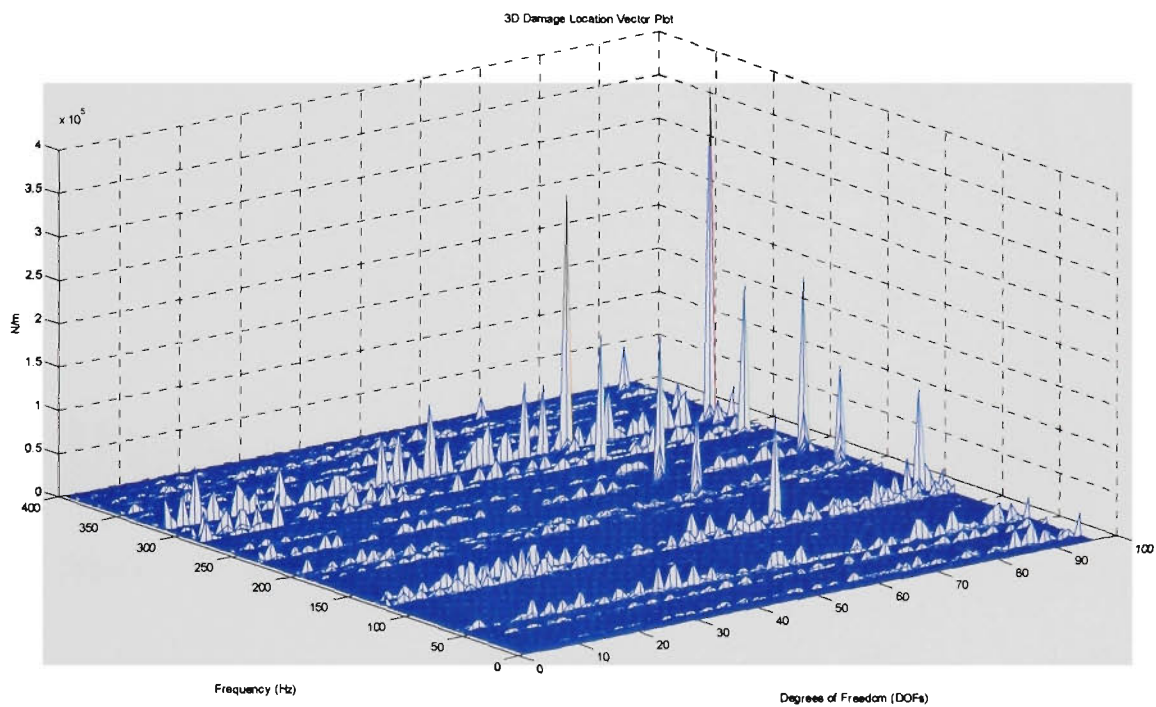


Figure 4.14b: 2D CDLV Plot for Damage Case A with Coordinate Incompatibility (5% Noise)

Figure 4.15a show the 3D DLV plot for Damage Case B with 72 randomly supplied DOFs and 24 expanded DOFs and with 5% noise interference introduced. These peaks can be seen to occur between DOF 60 and DOF 90. Comparison of Figure 4.13a and Figure 4.15a show that the peaks do not occur between the same intervals, and yet both figures are produced for the same Damage Case B. The reason for this is due to the fact that DOF 80 was not supplied in the measured DOFs. So the Damage Detection Algorithm displayed the next available DOFs closest to the damage. This is demonstrated more clearly on the 2D CDLV Plot.



**Figure 4.15a: 3D DLV Plot for Damage Case B with Coordinate Incompatibility (5% Noise)**

Figure 4.15b is the corresponding 2D CDLV Plot for Damage Case B with 72 randomly supplied DOFs and 24 expanded DOFs and with 5% noise interference introduced. Here the location of damage can clearly be seen to occur at DOF 69 and DOF 92. This translates to the damage being located between node no. 27 (DOFs: 67, 68, 69) and node no. 35 (DOFs: 91, 92, 93). However, since there is no direct connectivity between node no. 27 and node no. 35 on the truss structure this would signify an erroneous damage detection. Therefore, results obtained from incomplete supplied data can only be interpreted as an indication of where damage exists. Hence, the

interpretation of Figure 4.15b suggests that damage only exist between node no. 27 and node no. 35 on the truss structure. This correlates to the last two bays in the truss structure. In order to determine the exact location where damage exists, further measurements are required to be made. However not all FRF of DOFs on the structure are required to be supplied, only nodes with DOFs that fall between DOF 69 and DOF 92 are required.

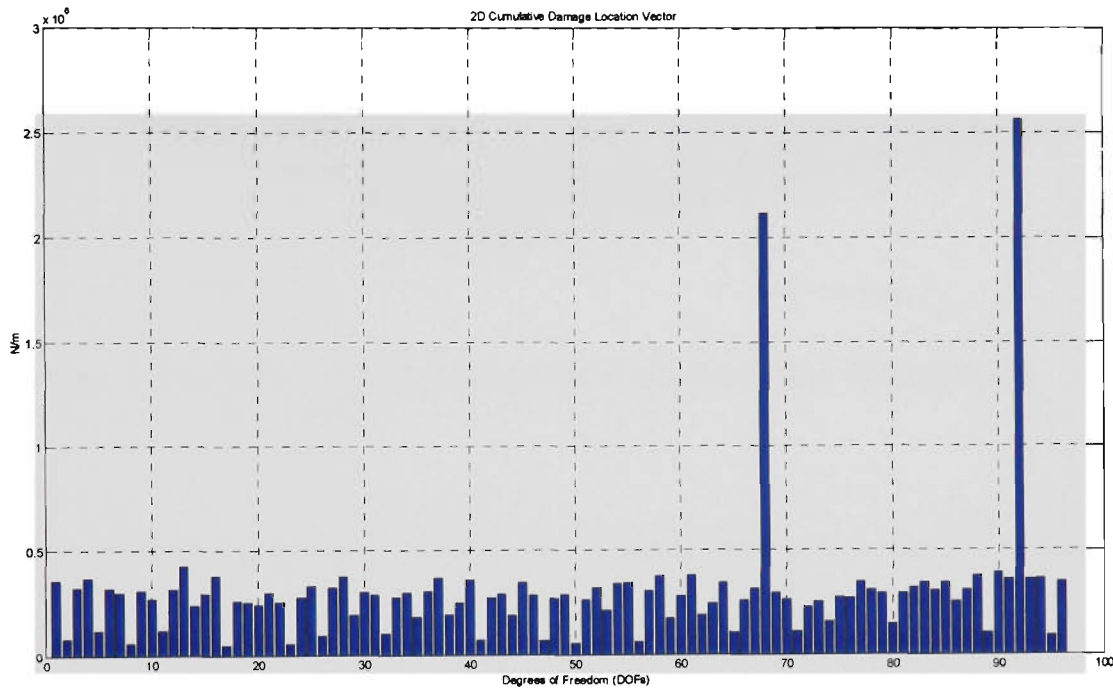


**Figure 4.15b: 2D CDLV Plot for Damage Case B with Coordinate Incompatibility (5% Noise)**

Figure 4.16a is the 3D DLV Plot for Damage Case C with 72 DOFs randomly supplied and 24 expanded DOFs and with 5% noise interference introduced. As expected the Damage Detection Algorithm detected the peaks that were consistent with Damage Case A and DOFs containing peaks that were closest to describing Damage Case B. However since not all the measurements have been supplied care must be taken in interpreting the damage locations. At this point the information on the connectivity of the structure becomes important, as it allows further interpretation.

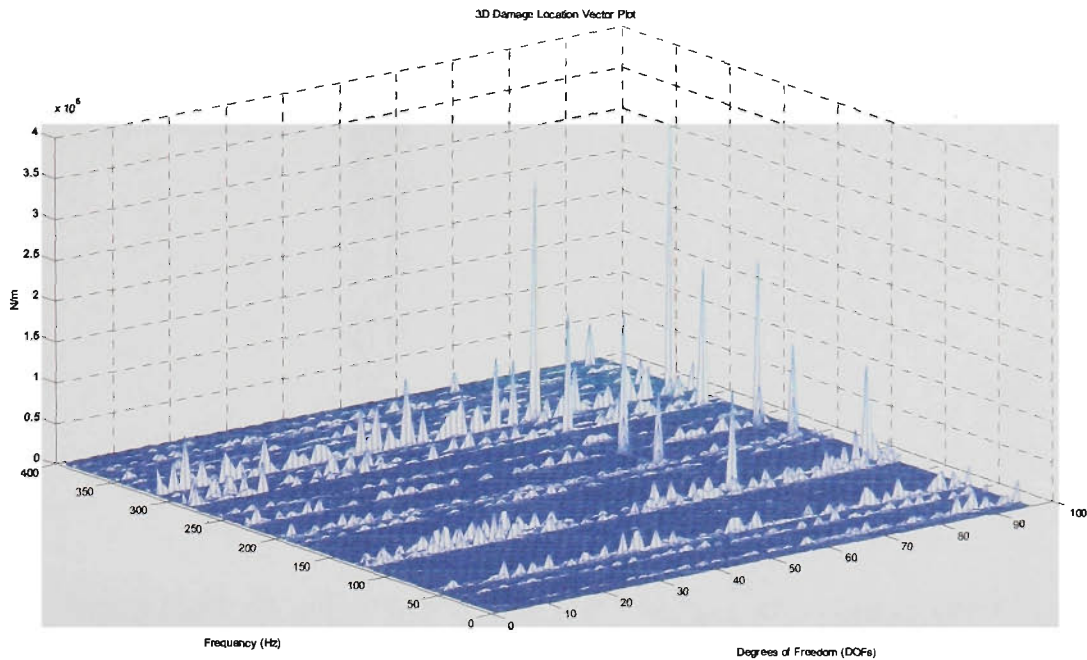


**Figure 4.15a: 3D DLV Plot for Damage Case B with Coordinate Incompatibility (5% Noise)**

Figure 4.15b is the corresponding 2D CDLV Plot for Damage Case B with 72 randomly supplied DOFs and 24 expanded DOFs and with 5% noise interference introduced. Here the location of damage can clearly be seen to occur at DOF 69 and DOF 92. This translates to the damage being located between node no. 27 (DOFs: 67, 68, 69) and node no. 35 (DOFs: 91, 92, 93). However, since there is no direct connectivity between node no. 27 and node no. 35 on the truss structure this would signify an erroneous damage detection. Therefore, results obtained from incomplete supplied data can only be interpreted as an indication of where damage exists. Hence, the interpretation of Figure 4.15b suggests that damage only exists between node no. 27 and node no. 35 on the truss structure. This correlates to the last two bays in the truss structure. In order to determine the exact location where damage exists, further measurements are required to be made. However, not all nodes on the structure are required to be supplied, only nodes with DOFs that fall between DOF 69 and DOF 92 are required.

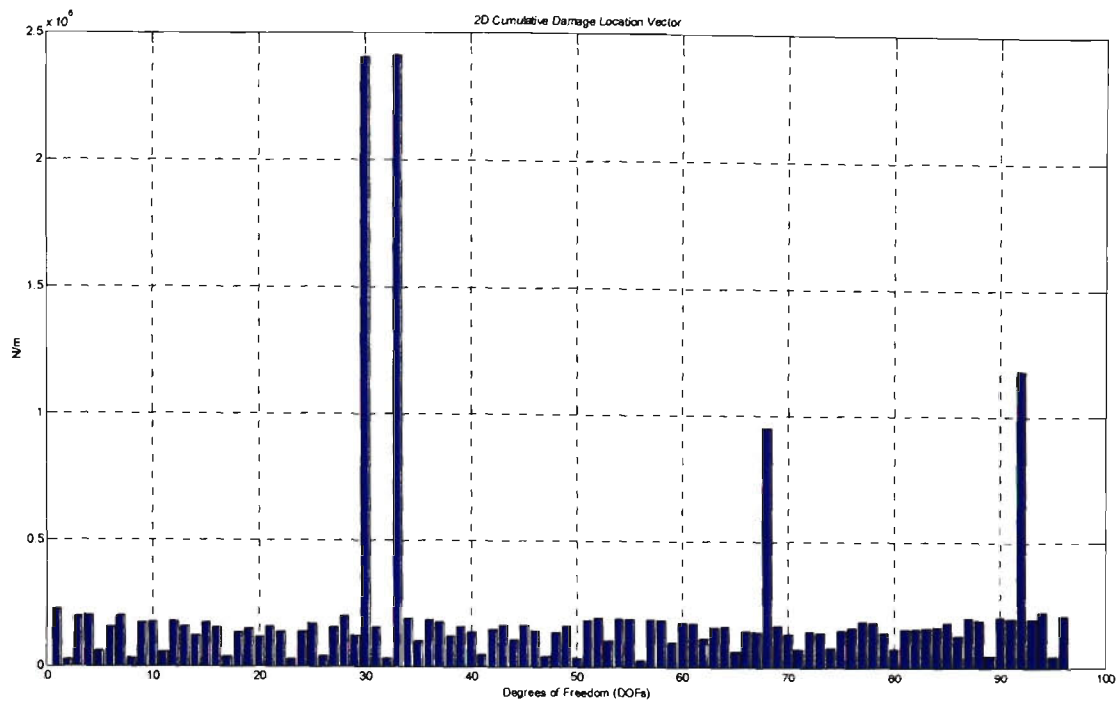


Figure 4.16b: 2D CDLV Plot for Damage Case C with Coordinate Incompatibility (5% Noise)

#### 4.7 DISCUSSION

The developed Damage Detection Algorithm was found to be extremely robust in that it was able to successfully detect simulated damage introduced to the truss structure at various locations. Furthermore, the Damage Detection Algorithm did surprisingly well to detect the simulated damage scenarios considering that the various cases studied only involved changes in stiffness between 10% - 15%. The Damage Detection Algorithm was also subjected to 5% randomised noise and was still able to successfully detect simulated damage. It also was still able to successfully indicate the interval where damage may exist for cases that involved coordinate incompatibility.

Further studies in the next chapter will utilise the Damage Detection Algorithm to study a thin cantilever plate structure under various conditions.

# **CHAPTER 5**

## **DAMAGE DETECTION IN**

### **PLATE STRUCTURES**

While a 3D space truss structure can be easily modelled using finite element philosophy and the mass and stiffness matrices readily calculated, it is relatively difficult to manufacture ball joints and members to satisfy the essential requirements of a 3D space truss structure for experimental studies. Plate structures on the other hand can be easily manufactured. However, the mass and stiffness matrices of a plate element are far more complex than those of a truss structure.

Thin flat plate elements are subjected to both in plane and transverse loads. This chapter will apply the Damage Detection Algorithm presented in Chapter 2 to thin flat plate structures to evaluate the Damage Detection Algorithm.

The aim of this chapter is firstly to formulate the mass and stiffness matrices for a single plate element. This will then be verified using FE. Once this single element has been verified, it will be used to construct plate structures. Damage will then be introduced to various locations on a thin cantilevered plate. The Damage Detection Algorithm will then be used to locate the damage within the cantilevered plate to investigate its performance.

#### **5.1 BASIC THIN PLATE THEORY**

Thin flat plate structures are used in many different applications in engineering, for instance the outer surfaces of aircraft can be considered to be made of thin plates. In finite element modelling

---

(FEM), a simple element can be described by three or four nodes. There are several theories that can be used to describe thin flat plates, the two most common theories being the Discrete Kirchoff's Theory (DKT) and the Mindlin Theory. In this study, the DKT will be used.

The main features of the DKT for thin flat plates are outline below:

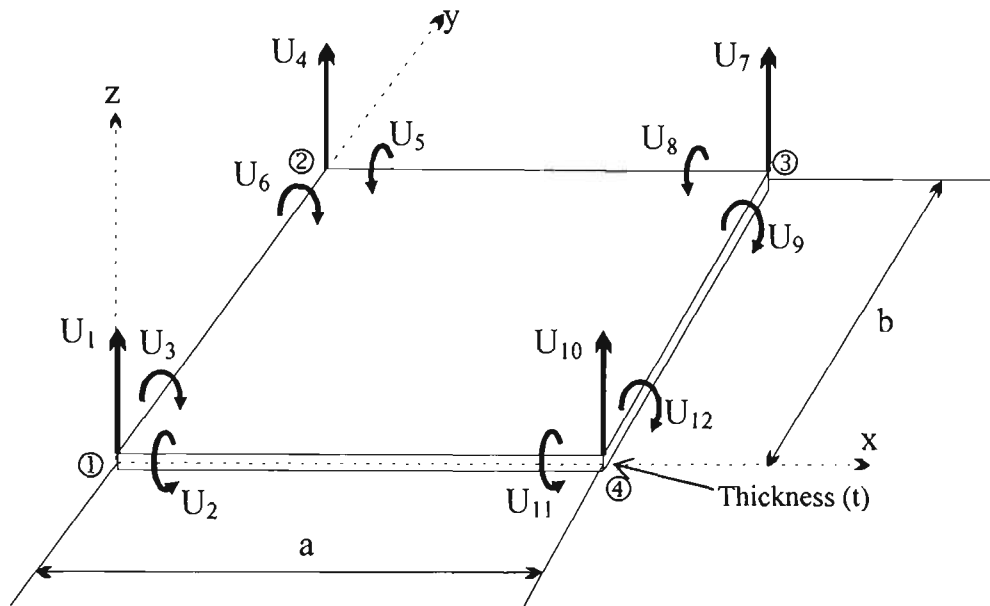


Figure 5.1: A Single Rectangular Thin Flat Plate Element

| Node | Plate Deflection | Rotation in X-Axis | Rotation in Y-Axis |
|------|------------------|--------------------|--------------------|
| 1    | $U_1$            | $U_2$              | $U_3$              |
| 2    | $U_4$            | $U_5$              | $U_6$              |
| 3    | $U_7$            | $U_8$              | $U_9$              |
| 4    | $U_{10}$         | $U_{11}$           | $U_{12}$           |

Table 5.1: DOFs with Respect to Node Numbers for a Single Plate Element

Consider the thin rectangular plate element defined by Figure 5.1. It is a single rectangular element that is defined by width (a), height (b) and thickness (t). The single element is described by 4 nodes each having 3 DOFs. The DOFs with respect to each node number are outlined in Table 5.1. It is important to adopt a convention that can be used for numbering the nodes describing an element. This convention can be either clockwise or anticlockwise. For example,

from Figure 5.1, if the nodes were read starting from node 1 in an anticlockwise manner then the node order would be 1-4-3-2. Similarly, if the nodes were read in a clockwise manner then the node order would be 1-2-3-4. The clockwise convention will be used in this thesis.

The mass and stiffness for the single rectangular flat plate element can be found in Appendix 5, and was derived from first principle by Przemieniecki (1967), (with an error in one element, which has been corrected in this thesis). However, before Przemieniecki's mass and stiffness matrices are used they must first be validated to be correct for our application.

## 5.2 VALIDATION OF MASS AND STIFFNESS MATRICES

There are two different sets of mass and stiffness matrices presented by Przemieniecki (1967) for the rectangular flat plate element, a non-compatible and a compatible one. In the non-compatible case, the mass and stiffness matrices are derived so that the boundary deflections on adjacent plate elements are compatible, whilst rotations of the element edges on common boundaries are not compatible and consequently, discontinuities in the slope exist across the boundaries. For the compatible case, both the deflection and slope compatibility on the adjacent element are ensured. Both cases will be examined to determine the most suitable mass and stiffness matrices that will be required later in this chapter.

Now let's consider an example shown in Figure 5.2, a thin flat plate structure that is made up of 4 smaller plate elements with properties shown. It is described by 9 nodes and for ease of reference it will be referred to as "Plate9" from this point onwards. There are 3 DOFs per node. Here nodes 1, 2 and 3 are the fixed nodes within this structure.

---

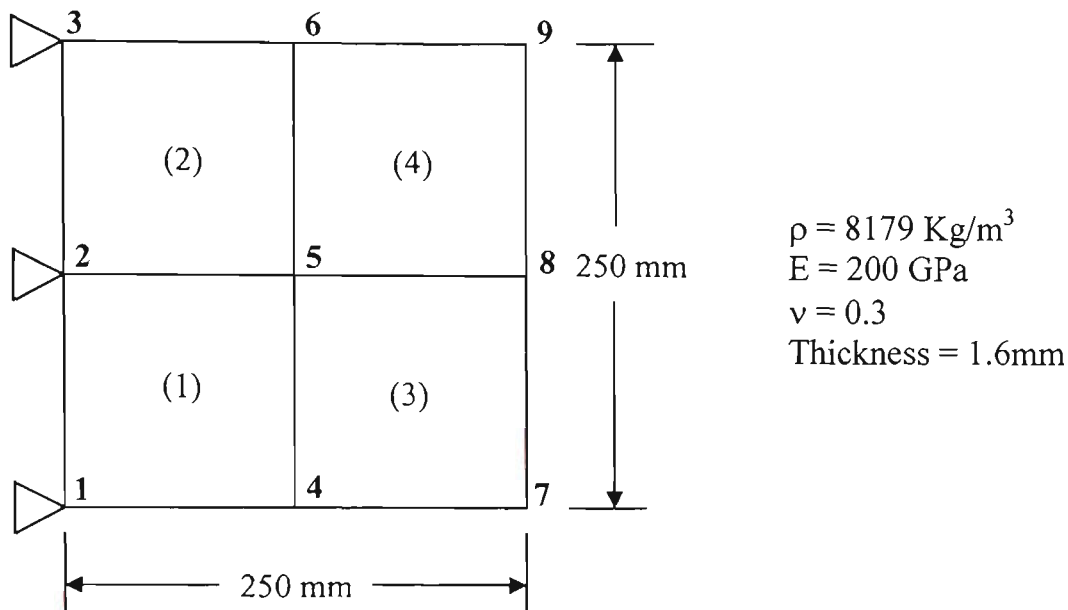


**Figure 5.2: Thin Flat Plate Structure with 4 Smaller Elements also Known as Plate9**

Matlab™ will be used to perform theoretical calculations for the mass and stiffness matrices for both the compatible and non-compatible cases. ANSYS™ finite element software will also be used to analyse this structure. Natural frequencies for the structure will be obtained from the theoretical and finite element analysis. Natural frequencies from the theoretical calculations will be compared to natural frequencies obtained from ANSYS™, in which a more elaborate shell element was used.

### 5.2.1 FINITE ELEMENT ANALYSIS OF PLATE9

The plate is modelled in ANSYS™ using SHELL63 quadrilateral elements and is shown in Figure 5.3. It is described by 4 elements and 9 nodes. The edges between nodes 1, 2 and 3 have their DOFs fixed in all directions. The appropriate masters DOFs were chosen without rotations. The modal analysis option was chosen in ANSYS™ using the reduced option. The first six natural frequencies and mode shapes for the plate were then requested and are shown in Table 5.2.

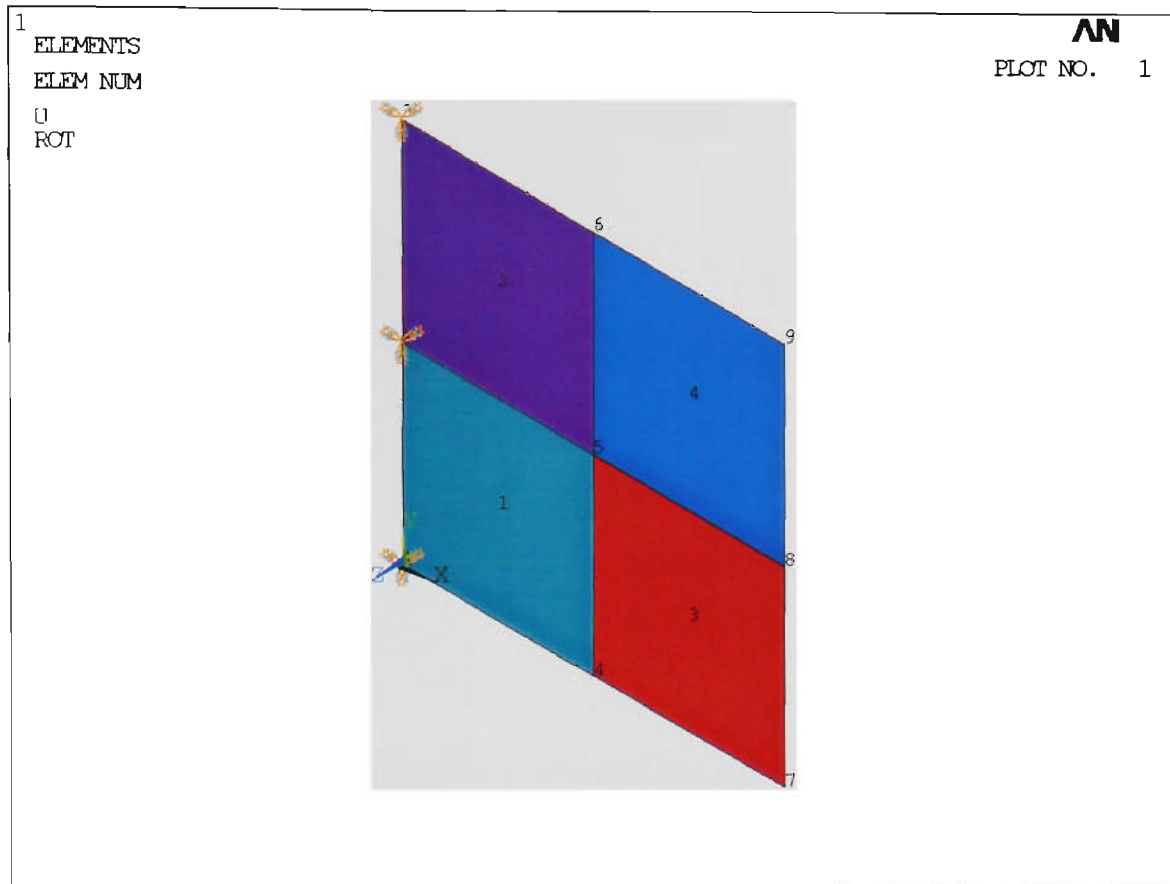


Figure 5.3: The Plate9 Example Modelled in ANSYS™

| Mode Number | Natural Frequency (Hz) | Mode Shape Behaviour                          |
|-------------|------------------------|---|
| 1           | 21.17                  | Bending about Y-axis                          |
| 2           | 52.06                  | Twisting about X-axis                         |
| 3           | 130.25                 | Bending about Y-axis                          |
| 4           | 166.40                 | Bending about X-axis                          |
| 5           | 190.12                 | Twisting about X-axis                         |
| 6           | 334.66                 | Twisting about Y-axis & Twisting about X-axis |

Table 5.2: First Six Natural Frequencies and Mode Shape for Plate9 Example from ANSYS™

Mode shape analysis was also carried out to study the behaviour of the plate. Figure 5.4 shows an isometric view and side view of the first mode shape for the Plate9 example. The first mode shape occurs at approximately 21.17 Hz and the plate can be seen as bending about the Y-axis. The bending mode behaviour experienced by the plate can be better seen in the side view.

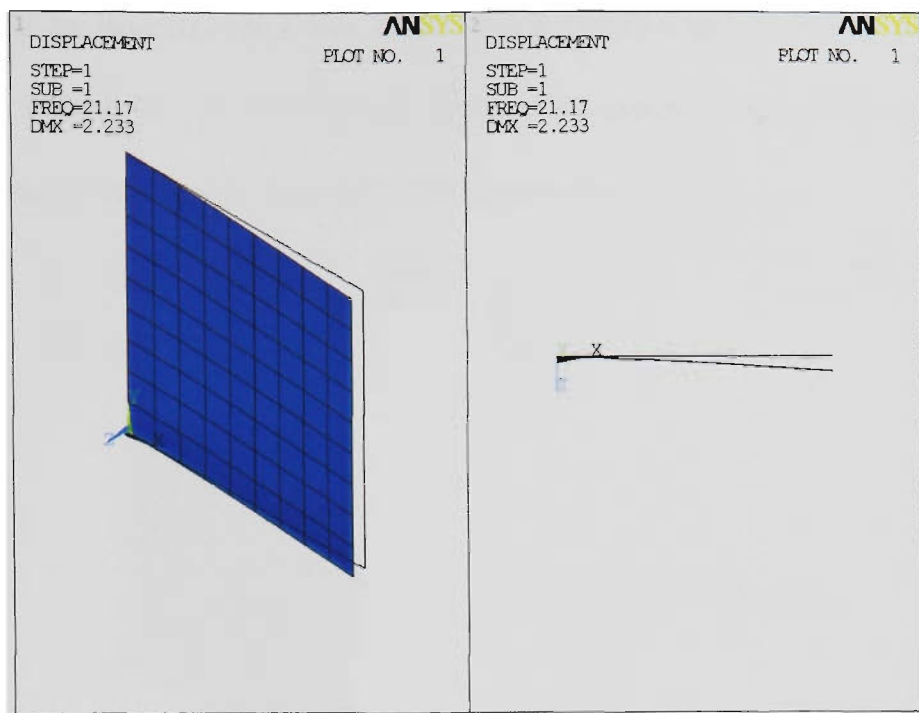


Figure 5.4: Mode Shape No.1 – Isometric and Side View of Plate9 Example

Figure 5.5 shows an isometric and side view of the Plate9 example at 52.06 Hz. This is where the second mode shape occurs. In this mode a twisting behaviour about the X-axis can be observed.

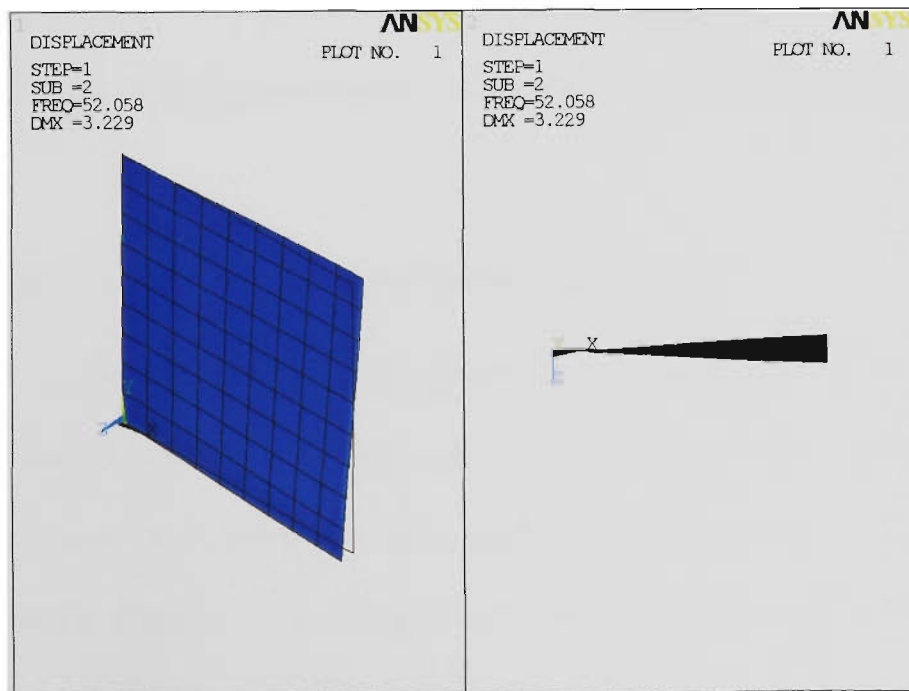


Figure 5.5: Mode Shape No. 2 – Isometric and Side View of Plate9 Example

Figure 5.6 shows an isometric and side view of the Plate9 example in the third mode shape, which occurs at 130.25 Hz. At this frequency the plate seems to be bending principally in the XY-plane. A clearer view can be seen from the corresponding side view.

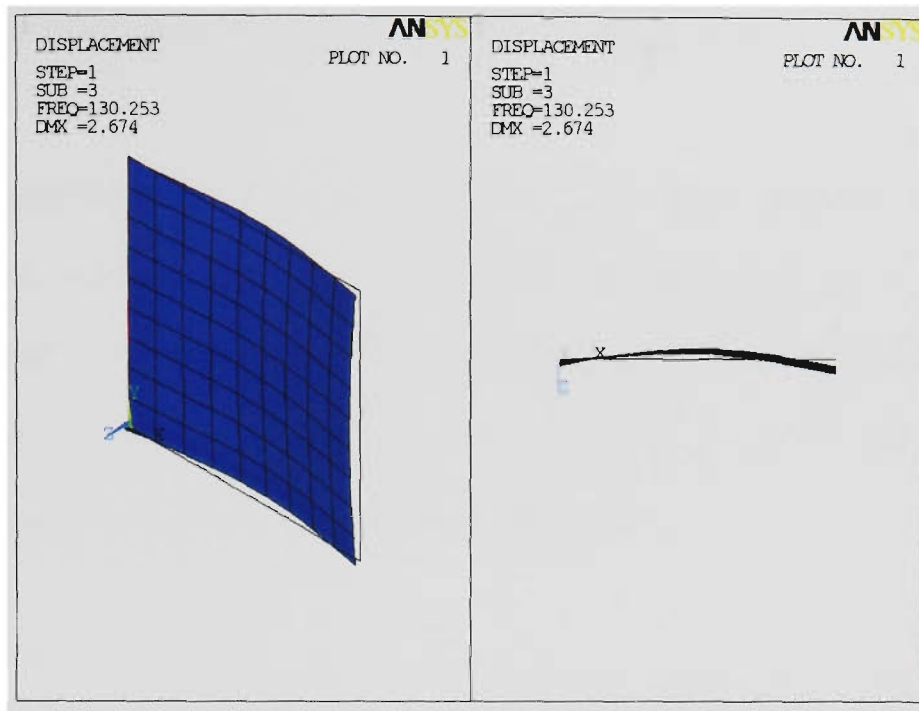


Figure 5.6: Mode shape no. 3 – Isometric and side view of Plate9 example

Only the first three modes of the Plate9 example have been presented. The third mode shape is illustrated here to show the bending behaviour of the plate at modes of higher frequencies.

### 5.2.2 THEORETICAL CALCULATIONS USING MATLAB™

Theoretical calculations using the non-compatible deformation theory for the Plate9 example were conducted using Matlab™. The mass and stiffness matrix used to describe a single plate element can be found in Appendix 5 and Appendix 6 respectively and was derived by Przemieniecki (1967). The mass and stiffness matrix for the Plate9 examples, which consisted of 4 single plate elements, is simply the assembly of the single plate element using simple matrix assembly theory. An algorithm was written in Matlab™ to aid in the matrix assembly process. Upon completion, the algorithm produced a mass and a stiffness matrix that were each 18 x 18 in

size. The reason why each matrix is 18 x 18 in size rather than 27 x 27 in size is due to the fact that node 1, 2 and 3 are grounded in the Plate9 example and hence only the reduced mass and stiffness matrix were found. The first six natural frequencies were also found from an algorithm written in Matlab™ and is shown in Table 5.3 in the next sub section.

Theoretical calculations were also performed for the Plate9 example using the mass and stiffness matrix developed by Przemieniecki (1967) based on compatible deformation theory. The mass and stiffness matrix for a single plate element based on compatible deformation theory can be found in Appendix 7 and Appendix 8 respectively. The first six natural frequencies were also found and are also shown in Table 5.3 in the next sub-section.

### 5.2.3 COMPARISON OF THEORETICAL RESULTS WITH FINITE ELEMENT

Natural frequencies from theoretical results and finite element results are shown in Table 5.3. It can be seen that the non-compatible deformation theory yields a more accurate result than that of the compatible deformation theory. The percentage error associated with using the non-compatible deformation is very low for the first few modes and becomes large from mode four onwards. Hence, for the purpose of this thesis Przemieniecki's non compatible deformation theory for thin plates will be used since the percentage errors for the first few modes are quite small.

| Mode No. | ANSYS™<br>(Hz) | Non-<br>Compatible<br>Theory (Hz) | % Error<br>from<br>ANSYS™ | Compatible<br>Theory (Hz) | % Error<br>from<br>ANSYS™ |
|----------|----------------|-----------------------------------|---------------------------|---------------------------|---------------------------|
| 1        | 21.17          | 21.08                             | 0.43                      | 13.99                     | 33.92                     |
| 2        | 52.06          | 52.13                             | 0.13                      | 62.98                     | 20.98                     |
| 3        | 130.25         | 132.72                            | 1.89                      | 132.03                    | 1.35                      |
| 4        | 166.40         | 160.49                            | 3.55                      | 171.30                    | 2.95                      |
| 5        | 190.12         | 184.31                            | 3.06                      | 198.00                    | 4.14                      |
| 6        | 334.66         | 329.68                            | 1.49                      | 345.18                    | 3.14                      |

Table 5.3: Comparison of Results for Non-Compatible and Compatible Theories against ANSYS™

### 5.3 SIMULATION OF DAMAGE

There are many different ways damage can occur in a structure such as a cantilever plate. Consider a cantilever plate that is fixed at one edge and is modelled by several equally spaced smaller elements. There are several different types of ways damage can be simulated on this cantilever:

1. A cut along the element boundary between two nodes in a plate. The effects of simulating such a cut can be approximated as crack propagation in a real life structure, and is shown in Figure 5.7a. Depending on the length and location of the cut, two or more elements may be affected.
2. One element in a plate. The effects of simulating such damage can be seen to affect all the surrounding elements as shown in Figure 5.7b.
3. A small cut in the centre of one element. The effect of simulating such damage is shown in Figure 5.7c and can be assumed to affect only the nodes related to that element and no other surrounding elements.
4. At the point where the cantilever plate is fixed. The effects of simulating such damage would cause the boundary conditions to change and is shown in Figure 5.7d.

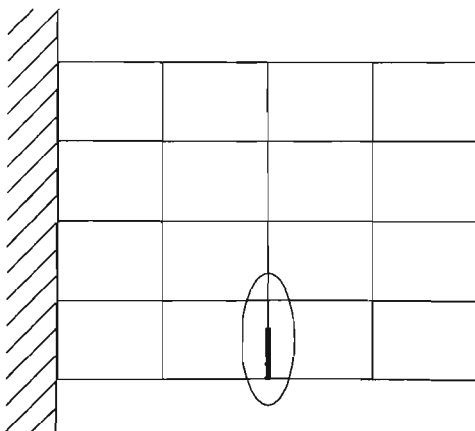


Figure 5.7a: Damage between Nodes

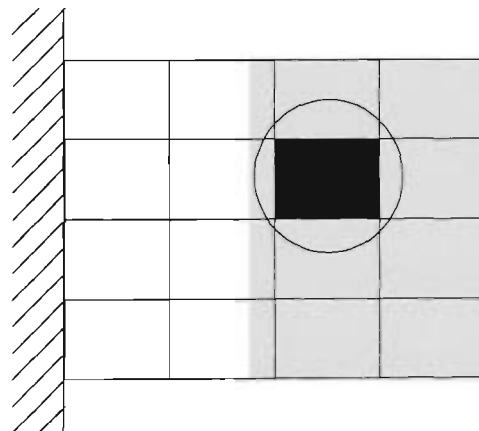
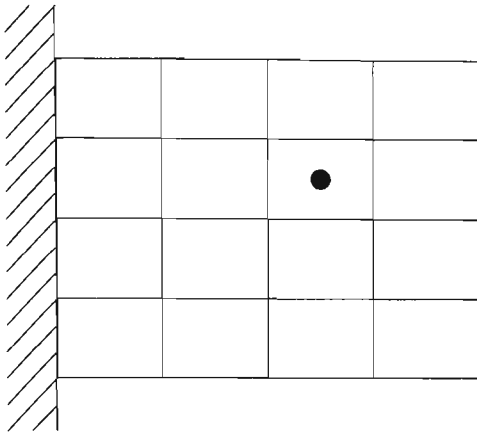
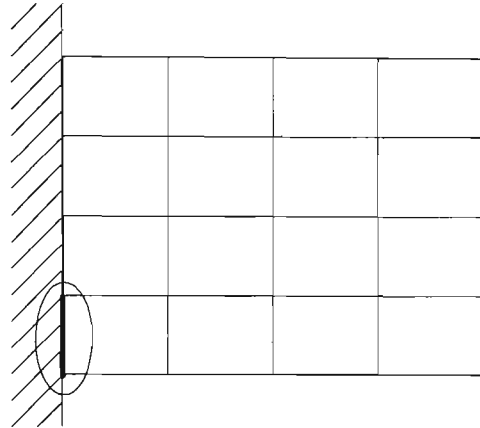


Figure 5.7b: Damage of One Whole Element



**Figure 5.7c: Partial Damage of One Element Affecting Only the Nodes**



**Figure 5.7d: Damage at the Fixing Point**

In this thesis damage is isolated to one element and only affects the nodes associated with that element. This does not suggest that multiple damages can not occur within the plate. In the theoretical analysis, reducing the modulus of elasticity is one way to simulate this type of damage, since each element in the elementary matrix is calculated separately. In the experimental analysis which will be covered in the next chapter, drilling a hole in the centre or a longitudinal cut of the desired element can simulate these simple types of damage.

#### 5.4 DESCRIPTION OF THE PLATE STRUCTURE

The element and node configuration for the thin cantilever plate that will be studied is shown in Figure 5.8. As defined previously, it is important that an order is maintained with the numbering of the nodes and elements as this will allow easy interpretation later on. The thickness of the plate is 3.0mm with a density of  $8179 \text{ Kg/m}^3$  and a Young's Modulus of 200 GPa. The plate is cantilevered along one end (i.e. grounded), with nodes no. 1, 2, 3 and 4 as the grounding points. The overall dimension of the plate is 0.3m x 0.6m. The dimension for each square element is 0.1m x 0.1m. As it has 28 nodes this plate shall be referred to as "Plate28" throughout this thesis.



Figure 5.8a: Nodes and Elements Configuration for Plate28 Example

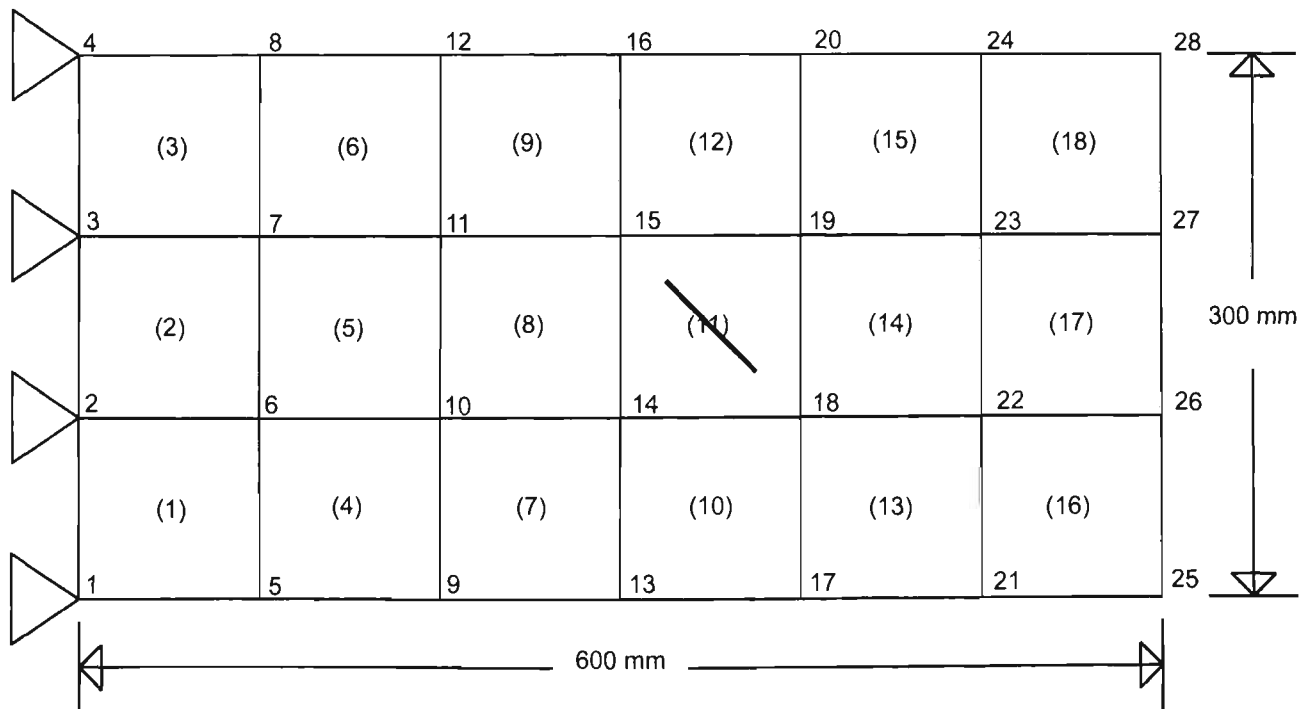


Figure 5.8b: Nodes and Elements Configuration for Plate28 Example Illustrating Damage Case A

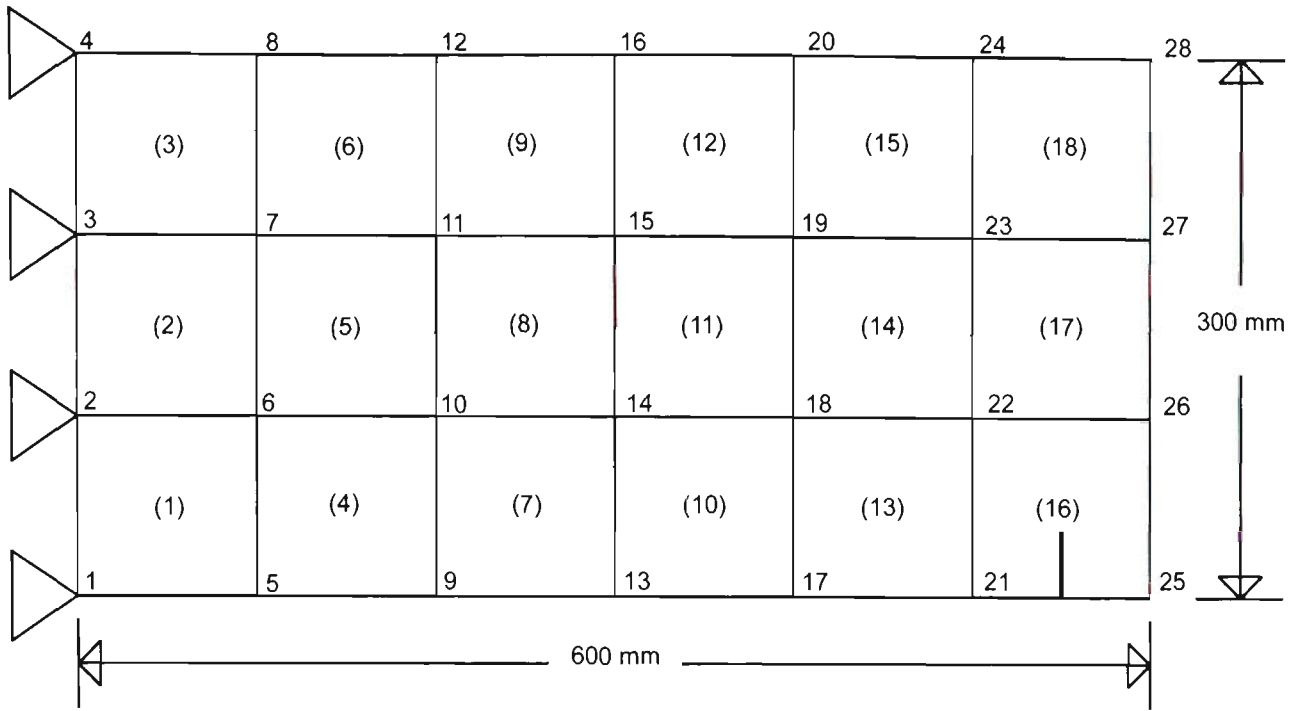


Figure 5.8c: Nodes and Elements Configuration for Plate28 Example Illustrating Damage Case B

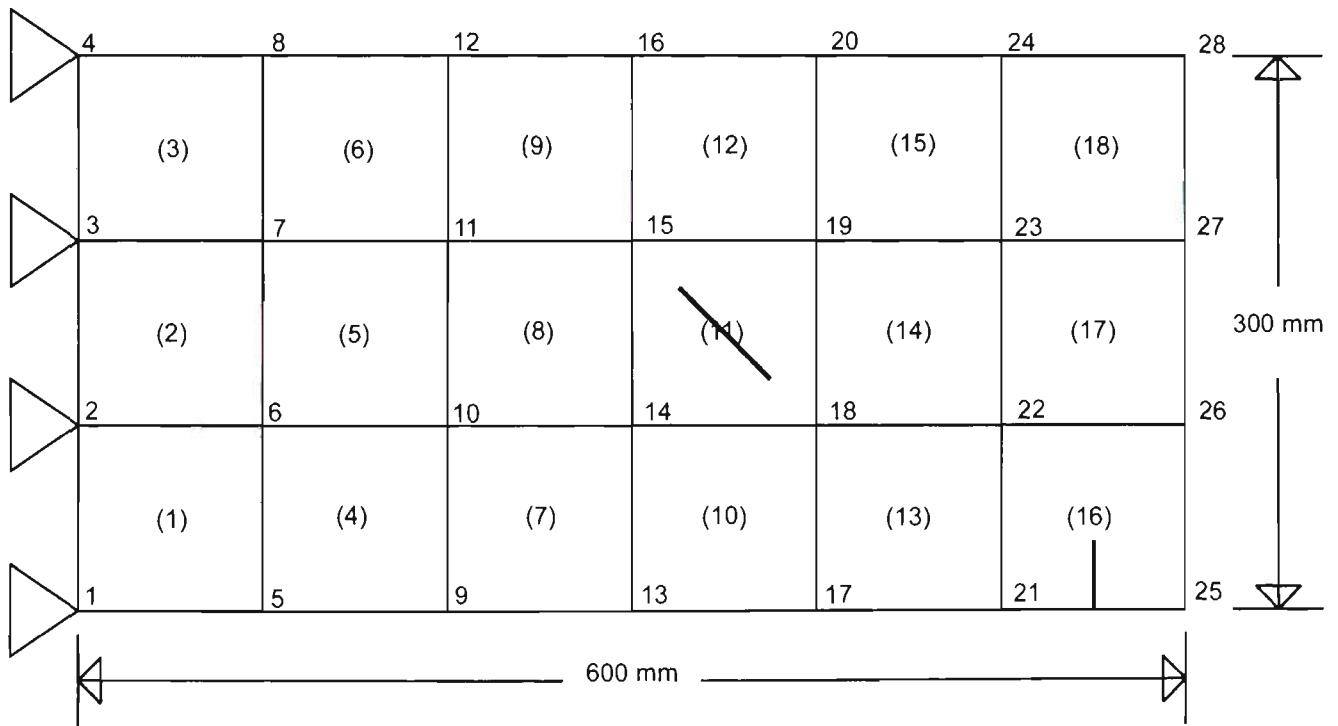


Figure 5.8d: Nodes and Elements Configuration for Plate28 Example Illustrating Damage Case C

Table 5.4 is a summary of the damage cases that will be introduced to the Plate28 structure as illustrated by Figures 5.8b, 5.8c and 5.8d. Simulated damage is considered as a loss in stiffness and any damage will be isolated to the four nodes that describe the damaged element. As mentioned in the previous chapter, it is difficult to manipulate the stiffness matrix directly due to the complexities of such a large matrix. It is however possible to simulate a loss in stiffness by reducing the Young's Modulus associated with the damage element. A reduction of 40% in the Young's Modulus has been found to be adequate in this thesis. Although a reduction of 40% in the Young's Modulus seems large, it will be shown later in this chapter that such a reduction is only equivalent to a loss in stiffness of approximately 10%. A loss in stiffness of approximately 10% is large enough to be considered as damage, while not causing the structure to become unstable, but small enough to test the sensitivity of the developed Damage Detection Algorithm. Again any change in mass due to the change in stiffness can be considered to be negligible. Damage will be introduced progressively to the thin cantilever plate structure, starting with damage to a single element only and then moving to a simulation of multiple damage at two elements.

| Damage Case | Location       | Nodes Effected | Type of Damage                             |
|-------------|----------------|----------------|--|
| A           | Element No. 11 | 14, 15, 18, 19 | Fracture in the centre of the plate        |
| B           | Element No. 16 | 21, 22, 25, 26 | Crack propagation at the edge of the plate |
| C           | Both of above  | Both of Above  | All of Above                               |

**Table 5.4: Summary of Simulated Damage Cases for Plate28 Example**

Since the thin plate structure is cantilevered, the DOFs associated with the grounded nodes are not considered. Therefore, the remaining nodes that are not grounded will have renumbered DOFs. Table 5.5 gives an outline of the corresponding DOFs numbers when the grounded DOFs are removed for node numbers showed in Table 5.3.

| Node Number | Corresponding DOFs<br>(X, Y, Z) |
|-------------|---------------------------------|
| 14          | 28, 29, 30                      |
| 15          | 31, 32, 33                      |
| 18          | 40, 41, 42                      |
| 19          | 43, 44, 45                      |
| 21          | 49, 50, 51                      |
| 22          | 52, 53, 54                      |
| 25          | 61, 62, 63                      |
| 26          | 64, 65, 66                      |

**Table 5.5: Corresponding DOFs for Damage Cases**

### 5.5 UNDAMAGED CASE

The mass and stiffness matrices were first calculated for the cantilever plate based on Prezemieniecki's non compatible deformation theory in Matlab™. The Matlab™ algorithm ensures that the constructed mass and stiffness matrices were assembled to the correct size to reflect the real life structure and also accounted for the grounded nodes. To verify that the constructed matrices from Matlab™ were indeed correct, the cantilever plate was also modelled with ANSYS™. Table 5.6 shows the results for the first 10 natural frequencies obtained from ANSYS™ and Matlab™. A comparison of the first 10 natural frequencies from the ANSYS™ to that of Matlab™ shows that the differences between the natural frequencies of the two models are very small. This suggests that the constructed mass and stiffness matrices from the algorithm are acceptably accurate.

Table 5.7 shows the diagonal stiffness values at each of the DOFs concerned taken from the calculated undamaged stiffness matrix of the cantilever plate. These values will be used later in this chapter to compare with the adjusted damage stiffness matrix for each different damage case.

| Mode Number | ANSYS™<br>Natural<br>Frequency (Hz) | Matlab™<br>Natural<br>Frequency (Hz) | % Error from<br>ANSYS™ |
|-------------|-------------------------------------|--------------------------------------|------------------------|
| 1           | 6.83                                | 6.83                                 | 0.00                   |
| 2           | 29.78                               | 29.40                                | 0.01                   |
| 3           | 42.82                               | 42.84                                | 0.04                   |
| 4           | 98.07                               | 95.79                                | 2.40                   |
| 5           | 120.71                              | 120.90                               | 0.16                   |
| 6           | 187.63                              | 183.33                               | 2.34                   |
| 7           | 190.79                              | 184.97                               | 3.15                   |
| 8           | 239.20                              | 236.37                               | 1.20                   |
| 9           | 258.36                              | 248.81                               | 3.84                   |
| 10          | 318.02                              | 301.08                               | 5.63                   |

**Table 5.6: Comparison of Natural Frequencies between Matlab™ and ANSYS™ for Undamaged Case**

| Node Number | DOF No. | Diagonal [K] <sub>UD</sub> Value<br>at DOF (KN/m) |
|-------------|---------|---|
| Node 14     | 28      | 2088.79   |
|             | 29      | 3.00  |
|             | 30      | 3.00  |
| Node 15     | 31      | 2088.79   |
|             | 32      | 3.00  |
|             | 33      | 3.00  |
| Node 18     | 40      | 2088.79   |
|             | 41      | 3.00  |
|             | 42      | 3.00  |
| Node 19     | 43      | 2088.79   |
|             | 44      | 3.00  |
|             | 45      | 3.00  |
| Node 21     | 49      | 1044.39   |
|             | 50      | 1.50  |
|             | 51      | 1.50  |
| Node 22     | 52      | 2088.79   |
|             | 53      | 3.00  |
|             | 54      | 3.00  |
| Node 25     | 61      | 522.19  |
|             | 62      | 0.75  |
|             | 63      | 0.75  |
| Node 26     | 64      | 1044.39   |
|             | 65      | 1.50  |
|             | 66      | 1.50  |

**Table 5.7: Diagonal Undamaged Stiffness Value at DOF Locations**

Receptance FRF for the thin cantilever plate was also calculated within Matlab™ from the algorithm presented in Chapter 2 that utilised the following equation:

$$[Z(\omega)] = ([K] - \omega^2[M])^{-1} \quad (5.1)$$

Shown in Figure 5.9 is the corresponding receptance FRF plot at  $\alpha(1, 1)$  of the undamaged thin cantilever plate. It must be noted that  $\alpha(1, 1)$  corresponds to node no. 5 for this example, because the DOFs of the grounded nodes have been removed. An inspection of Figure 5.9 shows that the receptance plot exhibits behaviour consistent with a point FRF measurement. The receptance plot also is consistent with structures that are considered to be in the grounded state. It must be noted that only the first 400 Hz of the frequency spectrum have been presented here.

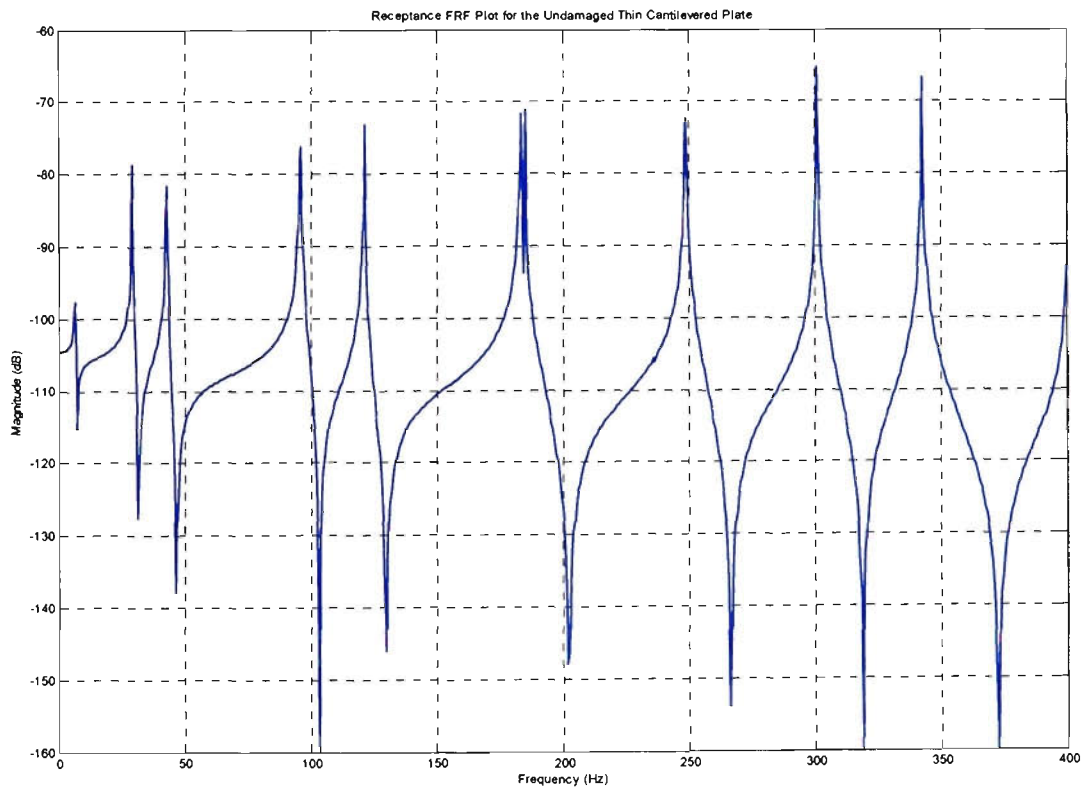


Figure 5.9: Point Receptance Plot at  $\alpha(1, 1)$  for the Undamaged Case

## 5.6 DAMAGE CASE A

In Damage Case A, simulated damage will be introduced to element no. 11 by reducing the Young's Modulus associated with that element by 40%. By doing so, this attempts to simulate the effects of crack propagation. It is assumed that changing the Young's Modulus of element no. 11 only affects the elements of the stiffness matrix associated with this element. The nodes describing element no. 11 are nodes no. 14, 15, 18 and 19.

Table 5.8 is a comparison of the first 10 natural frequencies from ANSYS™ and Matlab™ for Damage Case A. It can be seen that the difference is very small, especially for the first three modes. Therefore, it can be assumed that the algorithm used to calculate the mass and stiffness matrices with for Damage Case A is correct.

| Mode Number | ANSYS™<br>Natural<br>Frequency (Hz) | Matlab™<br>Natural<br>Frequency (Hz) | % Error from<br>ANSYS™ |
|-------------|-------------------------------------|--------------------------------------|------------------------|
| 1           | 6.81                                | 6.80                                 | 0.15                   |
| 2           | 29.42                               | 29.05                                | 0.13                   |
| 3           | 41.85                               | 41.86                                | 0.03                   |
| 4           | 96.89                               | 94.65                                | 2.31                   |
| 5           | 119.46                              | 119.67                               | 0.18                   |
| 6           | 181.23                              | 178.47                               | 1.52                   |
| 7           | 189.21                              | 182.12                               | 3.75                   |
| 8           | 237.06                              | 234.49                               | 1.08                   |
| 9           | 254.92                              | 245.52                               | 3.69                   |
| 10          | 314.82                              | 298.57                               | 5.16                   |

**Table 5.8: Comparison of Natural Frequencies between Matlab™ and ANSYS™ for Damage Case A**

Table 5.9 is a comparison of the first 10 natural frequencies of the Matlab™ results for the Undamaged Case against Damage Case A.

| Mode Number | Natural Frequency (Hz) Undamage | Natural Frequency (Hz) Damage Case A | % Change from Undamage |
|-------------|---------------------------------|--------------------------------------|------------------------|
| 1           | 6.83                            | 6.80                                 | 0.44                   |
| 2           | 29.40                           | 29.05                                | 1.19                   |
| 3           | 42.84                           | 41.86                                | 2.29                   |
| 4           | 95.79                           | 94.65                                | 1.19                   |
| 5           | 120.90                          | 119.67                               | 1.02                   |
| 6           | 183.33                          | 178.47                               | 2.65                   |
| 7           | 184.97                          | 182.12                               | 1.54                   |
| 8           | 236.37                          | 234.49                               | 0.80                   |
| 9           | 248.81                          | 245.52                               | 1.32                   |
| 10          | 301.08                          | 298.57                               | 0.83                   |

Table 5.9: Comparison of Natural Frequencies between Undamage and Damage Case A

A receptance FRF for the cantilever plate was also calculated using Matlab™. Shown in Figure 5.10 is the receptance FRF plot at  $\alpha(1, 1)$  of the cantilever plate before and after Damage Case A. The effect of reducing the Young's Modulus of element no. 11 into the undamaged structure can clearly be seen to cause a negative shift to some of the peaks.

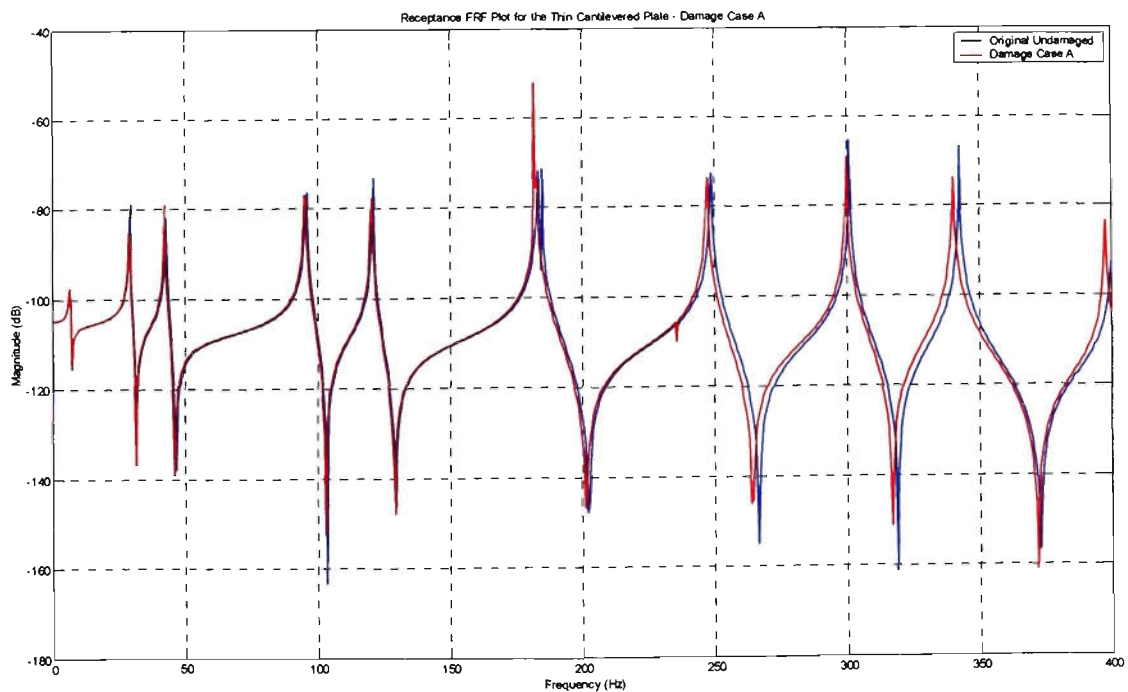
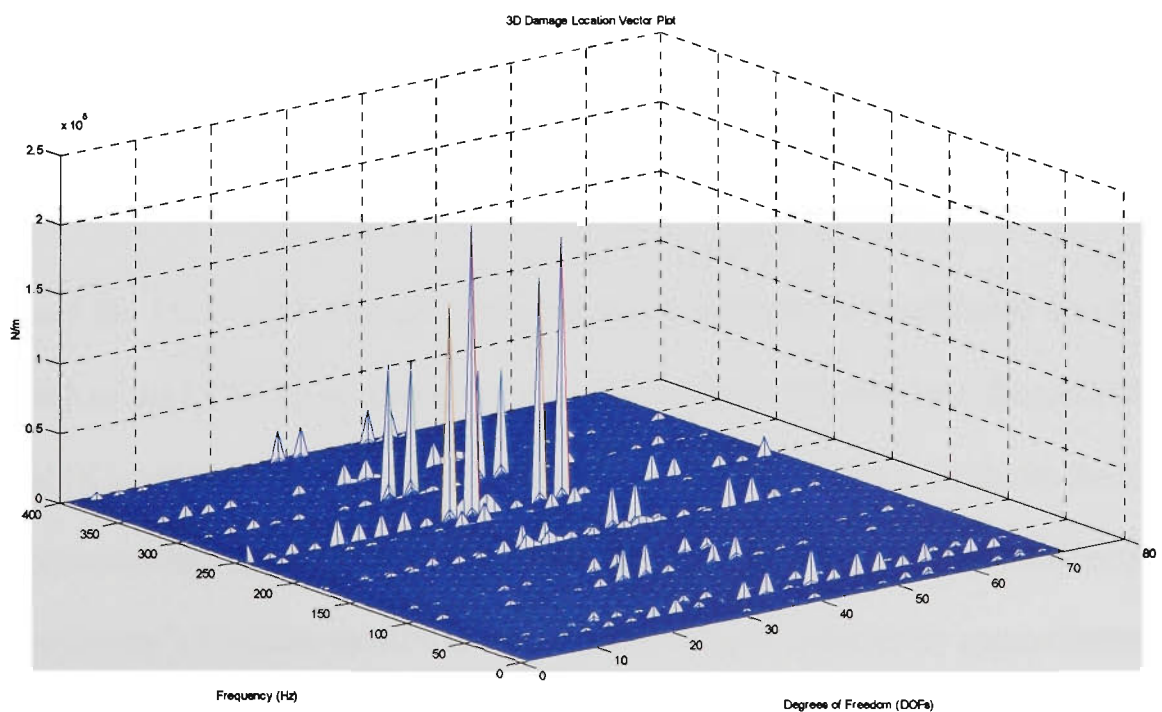


Figure 5.10: Point Receptance Plot at  $\alpha(1, 1)$  for Damage Case A

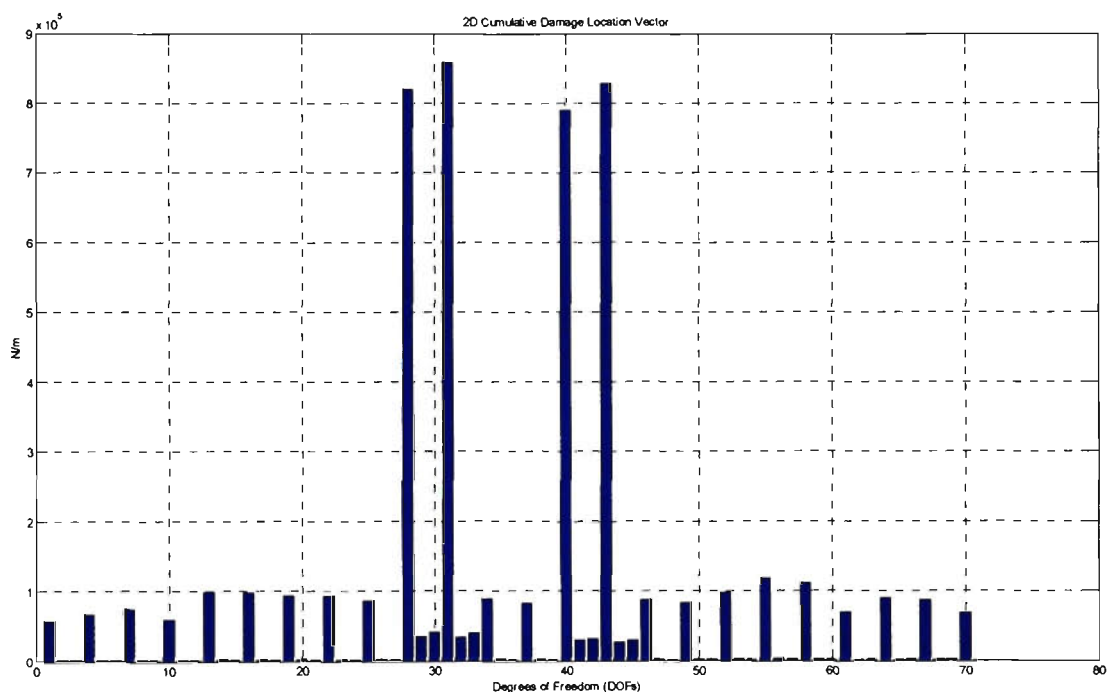
The developed Damage Detection Algorithm was then applied to Damage Case A firstly without coordinate incompatibility. Randomly generated noise interference of approximately 5% was also introduced into the Damage Detection Algorithm.

Figure 5.11a is the corresponding 3D Damage Location Vector Plot for Damage Case A. From Figure 5.11a many scattered peaks can be seen to occur throughout the frequency spectrum. This is the effects of the 5% noise interference. A close observation shows that most of the large peaks occurring throughout the frequency spectrum are contained between DOFs 25 and 45. It may be difficult to see the actual DOFs in this 3D DLV Plot due to the amount of information it contains. Estimation on the extent of damage can also be found on the 3D DLV Plot by reading the vertical axis. The damage extent for Damage Case A from Figure 5.11a can be said to be approximately 200 KN/m. This value can be further quantified once the location of damage has been pinpointed. The location of damage can be seen more clearly on the corresponding 2D CDLV Plot. It must also be noted that due to computational constraints, the full natural frequency spectrum of the cantilever plate has not been plotted.



**Figure 5.11a: 3D DLV Plot for Damage Case A without Coordinate Incompatibility (5% Noise)**

Figure 5.11b is the corresponding 2D CDLV plot for Damage Case A. Here it can be seen that the damage is associated with DOF 28, DOF 33, DOF 40 and DOF 45, since these peaks can be observed to be much larger than the other DOFs. The remaining DOFs which are much smaller than the ones caused by damage are due to noise interference. The corresponding node numbers that are associated with the above DOFs that contain damage are nodes no. 14, 15, 18 and 19. This confirms the location of damage since the original damage was introduced into element no. 11, which is bounded by node no. 14 (DOFs: 28, 29, 30), node no.15 (DOFs: 31, 32, 33), node no. 18 (DOFs: 40, 41, 42) and node no. 19 (DOFs: 43, 44, 45).



**Figure 5.11b: 2D CDLV Plot for Damage Case A without Coordinate Incompatibility (5% Noise)**

Having found the location of damage it is possible to determine a quantitative damage extent value for each of the DOFs by obtaining the change in stiffness  $\Delta K$ , since the diagonal  $[K]_{UD}$  and the diagonal  $[K]_D$  values corresponding to the DOFs are known. Table 5.10 shows the change in stiffness corresponding to each DOF that contains damage. This table also shows the effects of reducing the Young's Modulus by 40% is seen as a reduction in stiffness by approximately 10%.

| Nodes No. | DOFs No. | Diagonal [K] <sub>UD</sub> Value at DOF (KN/m) | Diagonal [K] <sub>D</sub> Value at DOF (KN/m) | Diagonal $\Delta$ [K] Value at DOF (KN/m) | % Change from Undamage |
|-----------|----------|--|---|---|------------------------|
| 14        | 28       | 2088.79  | 1879.91                                       | 208.88                                    | 10%                    |
|           | 29       | 3.00   | 2.70  | 0.30                                      | 10%                    |
|           | 30       | 3.00   | 2.70  | 0.30                                      | 10%                    |
| 15        | 31       | 2088.79  | 1879.91                                       | 208.88                                    | 10%                    |
|           | 32       | 3.00   | 2.70  | 0.30                                      | 10%                    |
|           | 33       | 3.00   | 2.70  | 0.30                                      | 10%                    |
| 18        | 40       | 2088.79  | 1879.91                                       | 208.88                                    | 10%                    |
|           | 41       | 3.00   | 2.70  | 0.30                                      | 10%                    |
|           | 42       | 3.00   | 2.70  | 0.30                                      | 10%                    |
| 19        | 43       | 2088.79  | 1879.91                                       | 208.88                                    | 10%                    |
|           | 44       | 3.00   | 2.70  | 0.30                                      | 10%                    |
|           | 45       | 3.00   | 2.70  | 0.30                                      | 10%                    |

**Table 5.10: Damage Extent Corresponding to DOFs for Damage Case A**

This shows that the developed Damage Detection Algorithm successfully detected the simulated damage and did not find any other damage within the plate. It is also interesting to note that the detected damage was shown to be much larger for translational DOFs than rotational DOFs.

## 5.7 DAMAGE CASE B

In Damage Case B, simulated damage will be introduced to element no. 16 by reducing the Young's Modulus associated with that element by 40% to simulate the effects of a crack propagation occurring at the edge. The nodes describing element no. 16 are nodes no. 21, 22, 25 and 26.

Table 5.11 is a comparison of the first 10 natural frequencies from ANSYS™ and Matlab™ for Damage Case B. It can be seen that for the first few modes the errors are minimal. From this it can be safely assumed that the theoretical calculations for the first few modes are sufficiently accurate.

| Mode Number | ANSYS™ Natural Frequency (Hz) | Matlab™ Natural Frequency (Hz) | % Error from ANSYS™ |
|-------------|-------------------------------|--------------------------------|---------------------|
| 1           | 6.83                          | 6.83                           | 0.00                |
| 2           | 29.70                         | 29.32                          | 1.28                |
| 3           | 42.77                         | 42.79                          | 0.05                |
| 4           | 96.83                         | 94.56                          | 2.34                |
| 5           | 120.13                        | 120.30                         | 0.14                |
| 6           | 185.30                        | 180.69                         | 2.49                |
| 7           | 188.41                        | 182.61                         | 3.08                |
| 8           | 236.71                        | 233.69                         | 1.27                |
| 9           | 256.06                        | 246.62                         | 3.69                |
| 10          | 313.65                        | 296.66                         | 5.42                |

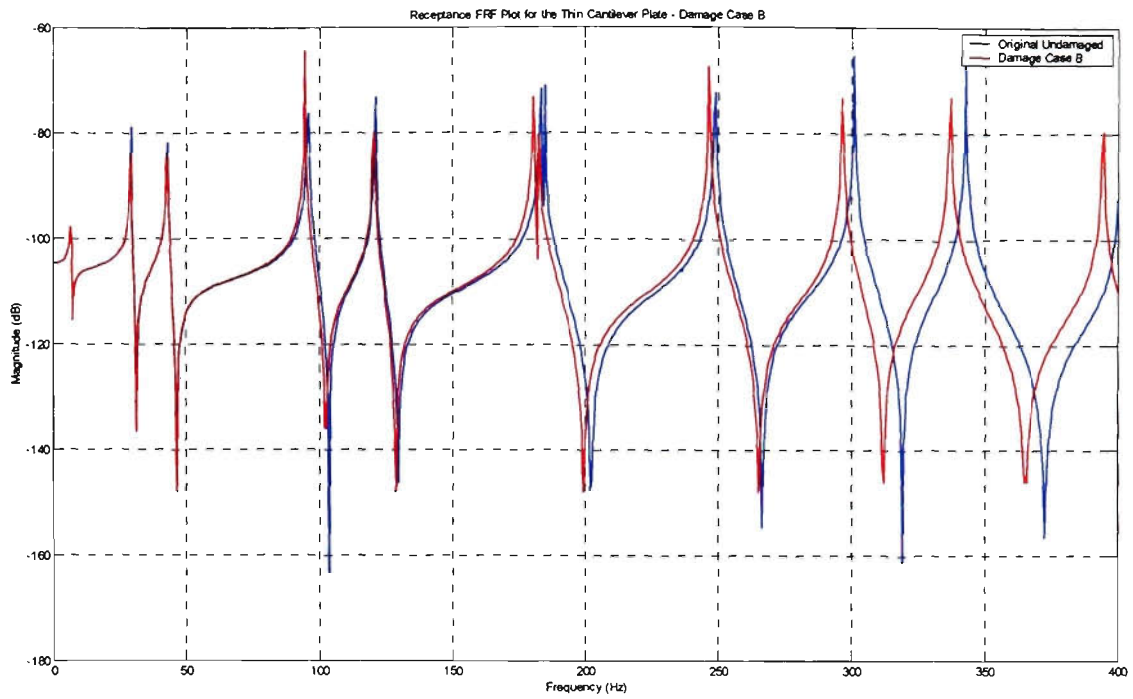
**Table 5.11: Comparison of Natural Frequencies between Matlab™ and ANSYS™ for Damage Case B**

Table 5.12 is a comparison of the first 10 natural frequencies of the Matlab™ results for the Undamaged Case and Damage Case B.

| Mode Number | Natural Frequency (Hz) Undamage Case | Natural Frequency (Hz) Damage Case B | % Change from Undamage Case |
|-------------|--------------------------------------|--------------------------------------|-----------------------------|
| 1           | 6.83                                 | 6.83                                 | 0.00                        |
| 2           | 29.40                                | 29.32                                | 0.27                        |
| 3           | 42.84                                | 42.79                                | 0.12                        |
| 4           | 95.79                                | 94.56                                | 1.28                        |
| 5           | 120.90                               | 120.30                               | 0.49                        |
| 6           | 183.33                               | 180.69                               | 1.44                        |
| 7           | 184.97                               | 182.61                               | 1.28                        |
| 8           | 236.37                               | 233.69                               | 1.13                        |
| 9           | 248.81                               | 246.62                               | 0.88                        |
| 10          | 301.08                               | 296.66                               | 1.47                        |

**Table 5.12: Comparison of Natural Frequencies between Undamage and Damage Case B**

Receptance FRFs for the cantilevered plate for Damage Case B were also calculated. Shown in Figure 5.12 is the receptance FRF plot at  $\alpha(1, 1)$  of the cantilever plate before and after Damage Case B. The effects of introducing Damage Case B into the undamaged structure can be seen to cause some of the peaks to occur at lower frequencies compared to the undamaged receptance FRF.



**Figure 5.12: Point Receptance Plot at  $\alpha(1, 1)$  for Damage Case B**

Figure 5.13a is the corresponding 3D Damage Location Vector Plot for Damage Case B without coordinate incompatibility and with 5% noise interference. From Figure 5.13a peaks can be seen to occur at various frequencies throughout the spectrum. A closer observation shows that a majority of the larger peaks are contained between DOFs 45 – 65. It may be difficult to see the actual DOFs in this 3D DLV due to the amount of information it contains. Estimation on the extent of the damage can be found on the 3D DLV plot by reading the vertical axis. The damage extent for Damage Case A from Figure 5.13a can be said to be approximately 200 KN/m. This value can be further quantified once the location of damage has been pinpointed. The location of damage can be observed more easily on the 2D CDLV plot as shown in Figure 5.13b. Here it can be seen that the damage is associated with DOFs 49, 54, 61 and 66. The corresponding node numbers that are associated with the above DOFs are node no. 21, 22, 25 and 26. This confirms the location of damage, since the original damage was introduced into element no. 16, which is bounded by node no. 21 (DOFs: 49, 50, 51), node no. 22 (DOFs: 52, 53, 54), node no. 25 (DOFs: 61, 62, 63) and node no. 26 (DOFs: 64, 65, 66).

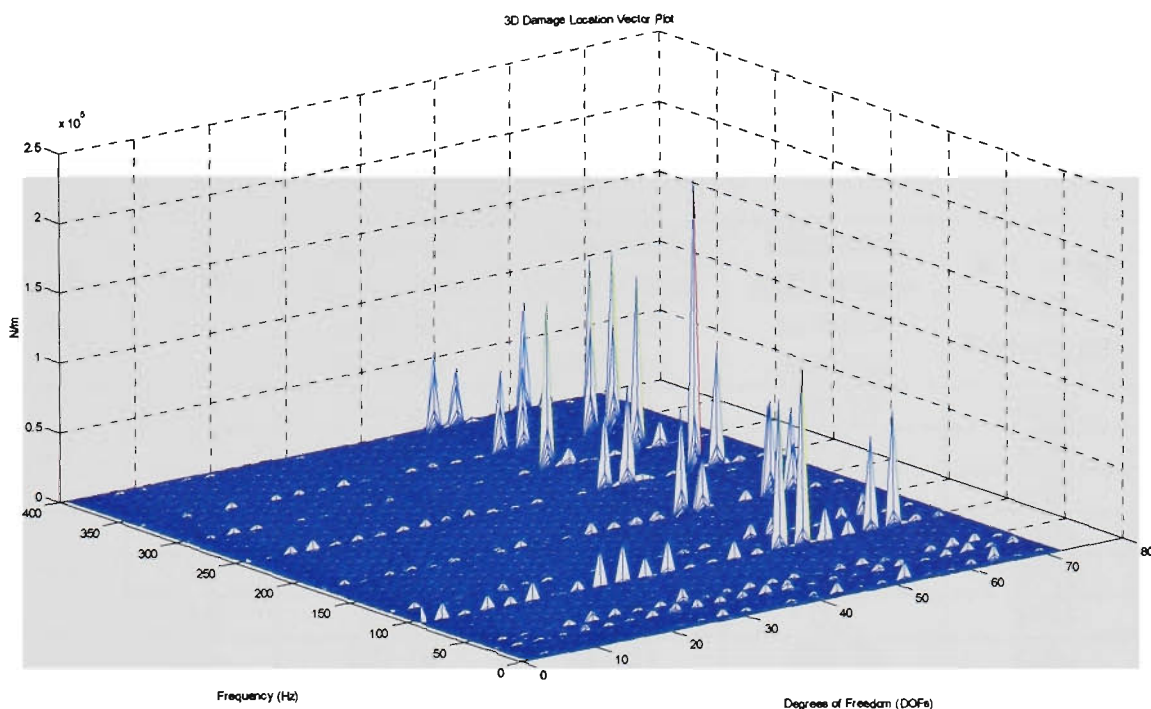


**Figure 5.13a: 3D DLV Plot for Damage Case B without Coordinate Incompatibility (5% Noise)**

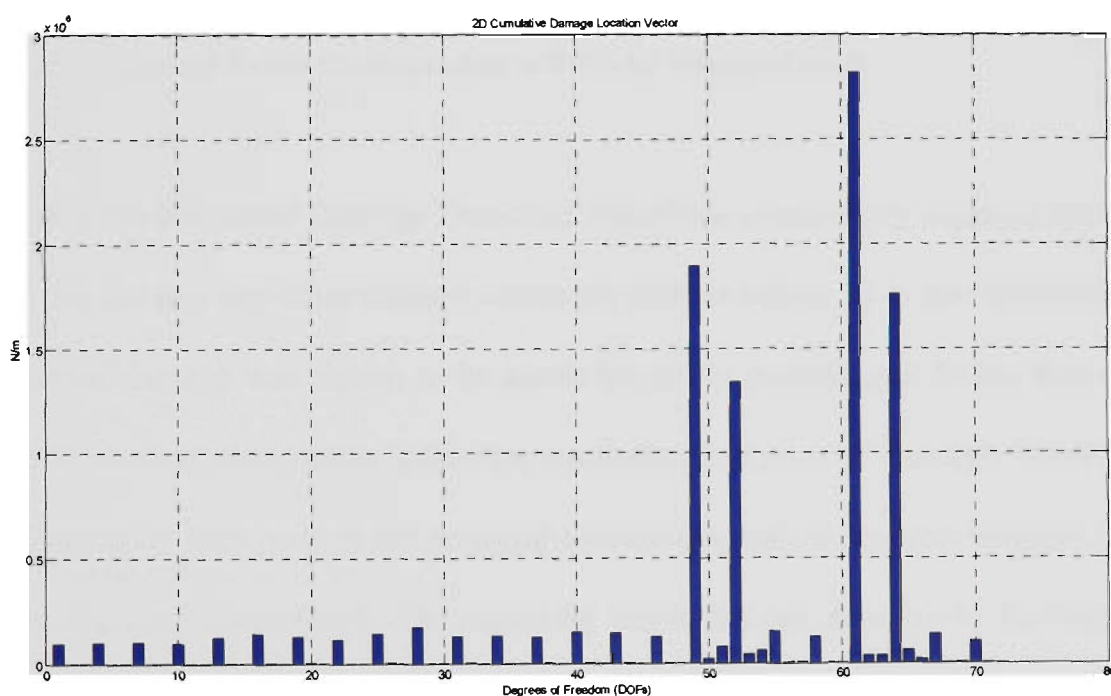


**Figure 5.13b: 2D CDLV Plot for Damage Case B without Coordinate Incompatibility (5% Noise)**

Having found the location of damage it is possible to determine a quantitative damage extent value for each of the DOFs by obtaining the change in stiffness  $\Delta K$ , since the diagonal  $[K]_{UD}$  and the diagonal  $[K]_D$  values corresponding to the DOFs are known. Table 5.13 shows the change in

stiffness corresponding to each DOF that contains damage. This table also shows the effects of reducing the Young's Modulus by 40% is seen as a reduction in stiffness by approximately 10%.

| Nodes No. | DOFs No. | Diagonal $[K]_{UD}$ Value at DOF (KN/m) | Diagonal $[K]_D$ Value at DOF (KN/m) | Diagonal $\Delta[K]$ Value at DOF (KN/m) | % Change from Undamage |
|-----------|----------|---|--------------------------------------|--|------------------------|
| 21        | 49       | 1044.39                                 | 835.51                               | 208.79                                   | 10%                    |
|           | 50       | 1.50                                    | 1.20                                 | 0.3                                      | 10%                    |
|           | 51       | 1.50                                    | 1.20                                 | 0.3                                      | 10%                    |
| 22        | 52       | 2088.79                                 | 1879.12                              | 208.79                                   | 10%                    |
|           | 53       | 3.00                                    | 2.70                                 | 0.3                                      | 10%                    |
|           | 54       | 3.00                                    | 2.70                                 | 0.3                                      | 10%                    |
| 25        | 61       | 522.19                                  | 313.31                               | 208.79                                   | 10%                    |
|           | 62       | 0.75                                    | 0.45                                 | 0.3                                      | 10%                    |
|           | 63       | 0.75                                    | 0.45                                 | 0.3                                      | 10%                    |
| 26        | 64       | 1044.39                                 | 835.51                               | 208.79                                   | 10%                    |
|           | 65       | 1.5                                     | 1.20                                 | 0.3                                      | 10%                    |
|           | 66       | 1.5                                     | 1.20                                 | 0.3                                      | 10%                    |

**Table 5.13: Damage Extent Corresponding to DOFs for Damage Case B**

This shows that the developed Damage Detection Algorithm successfully detected the simulated damage and did not find any other damage within the plate structure. It is also interesting to note that the detected damage was shown to be much larger for translational DOFs than rotational DOFs. An interesting observation is that the translational amount of damage shown in Figure 5.13b experienced by each node is not an equal distribution, taking into consideration the added affects of the 5% noise interference. The reason for this is that the connectivity for various nodes of element no. 16 is different for each node. For example, node no. 21 is an edge node and is connected by nodes on 3 sides compared to node no. 25 which is a corner node and is only connected by 2 nodes.

### 5.8 DAMAGE CASE C

To further verify that the robustness of the developed Damage Detection Algorithm, multiple damage scenarios will be introduced to the plate structure. Damage Case C is the combination of damage simulated on the plate from Damage Case A and Damage Case B, simultaneously, that simulates crack propagation at multiple locations.

Table 5.14 is a comparison of the first 10 natural frequencies from ANSYS™ and Matlab™ for Damage Case C. It can be seen that the difference is very small, especially for the first three modes.

| Mode Number | ANSYS™ Natural Frequency (Hz) | Matlab™ Natural Frequency (Hz) | % Error from ANSYS™ |
|-------------|-------------------------------|--------------------------------|---------------------|
| 1           | 6.81                          | 6.80                           | 0.15                |
| 2           | 29.33                         | 28.97                          | 1.23                |
| 3           | 41.80                         | 41.81                          | 0.02                |
| 4           | 95.67                         | 93.45                          | 2.32                |
| 5           | 118.92                        | 119.11                         | 0.16                |
| 6           | 179.10                        | 176.26                         | 1.59                |
| 7           | 186.80                        | 179.54                         | 3.89                |
| 8           | 234.57                        | 231.70                         | 1.22                |
| 9           | 252.45                        | 243.16                         | 3.68                |
| 10          | 310.62                        | 294.30                         | 5.25                |

**Table 5.14: Comparison of Natural Frequencies between Matlab™ and ANSYS™ for Damage Case C**

Table 5.15 is a comparison of the first 10 natural frequencies of the Matlab™ results between the Undamaged Case and Damage Case C.

| Mode Number | Natural Frequency (Hz) Undamage Case | Natural Frequency (Hz) Damage Case C | % Change from Undamage Case |
|-------------|--------------------------------------|--------------------------------------|-----------------------------|
| 1           | 6.83                                 | 6.80                                 | 0.44                        |
| 2           | 29.40                                | 28.97                                | 1.46                        |
| 3           | 42.84                                | 41.81                                | 2.40                        |
| 4           | 95.79                                | 93.45                                | 2.44                        |
| 5           | 120.90                               | 119.11                               | 1.48                        |
| 6           | 183.33                               | 176.26                               | 3.86                        |
| 7           | 184.97                               | 179.54                               | 2.93                        |
| 8           | 236.37                               | 231.70                               | 1.98                        |
| 9           | 248.81                               | 243.16                               | 2.27                        |
| 10          | 301.08                               | 294.30                               | 2.25                        |

Table 5.15: Comparison of Natural Frequencies between Undamage and Damage Case C

Receptance FRFs for the cantilevered plate were also calculated using Matlab™. Shown in Figure 5.14 is the receptance FRF plot for location (1, 1) of the cantilever plate before and after Damage Case C. It can be seen that the frequency shifts in some of the peaks are much larger than previous shifts observed in either Damage Case A or Damage Case B.

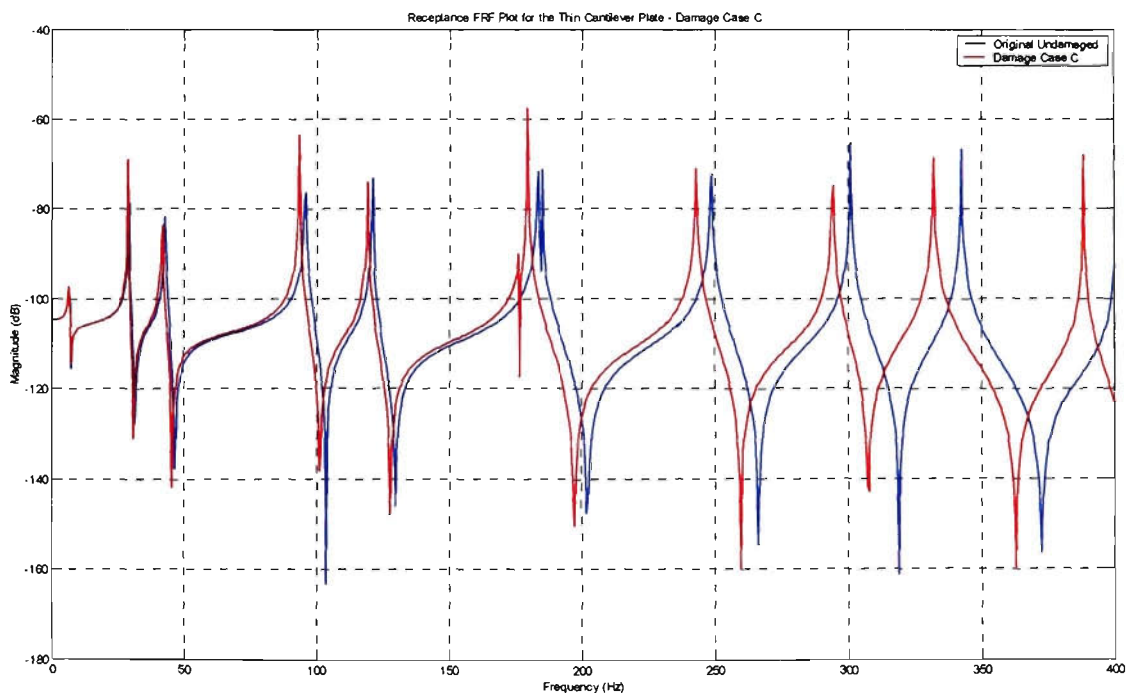
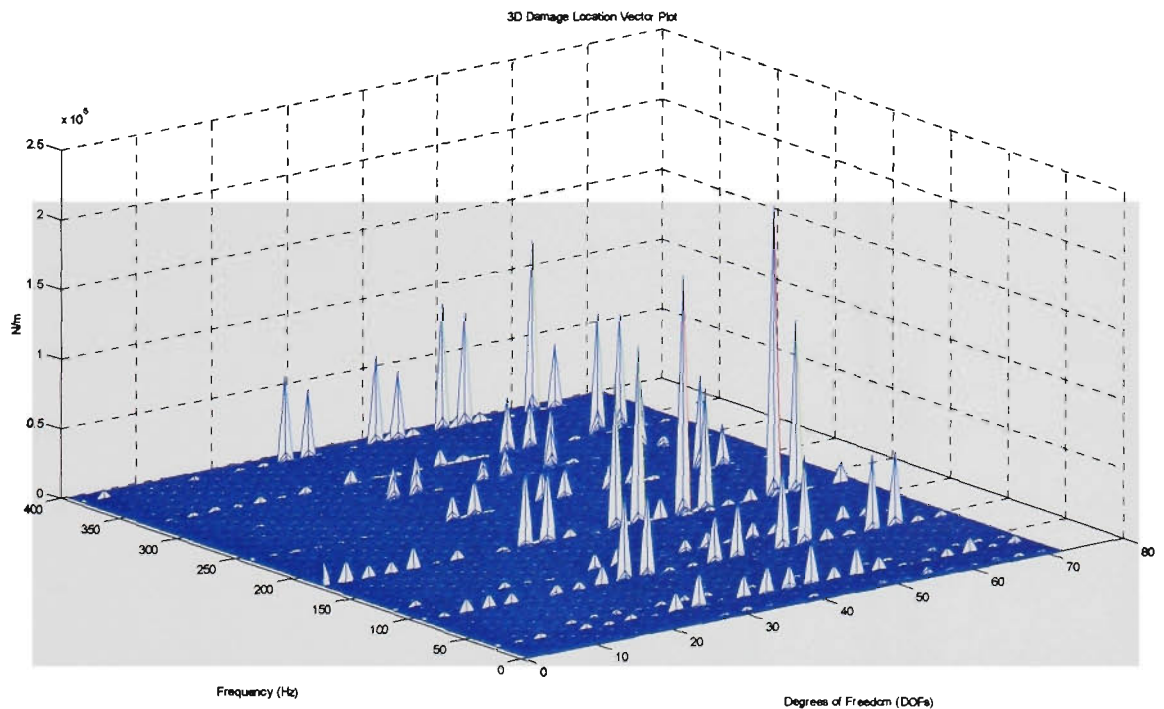


Figure 5.14: Point Receptance Plot at  $\alpha(1, 1)$  for Damage Case C

Figure 5.15a is the corresponding 3D Damage Location Vector Plot for Damage Case C. From Figure 5.15a peaks can be seen to occur at various frequencies. However, it can be observed that

the larger dominant peaks occur between DOFs 25 – 65, which is consistent with the locations found in Damage Case A and Damage Case B.



**Figure 5.15a: 3D DLV Plot for Damage Case C without Coordinate Incompatibility (5% Noise)**

Figure 5.15b is the corresponding 3D CDLV plot for Damage Case C. Here it can be seen that the damage is associated with DOFs 28, 33, 40, 43, 49, 54, 61 and 64, since these peaks are much greater than the rest of the peaks which are due to the 5% noise interference. The corresponding node numbers that are associated with the above DOFs are nodes no. 14, 15, 18, 19, 21, 22, 25, and 26. Although the Damage Detection Algorithm successfully located the damage, care must be taken to interpret the location of damage in situations where multiple damage occur. At this point the connectivity within the structure becomes extremely important. Fortunately, through the process of elimination, it is possible to isolate each individual damage location. For instance, in Damage Case C, it is known that four nodes shall describe each element. Interpretation of the results shows that damage is present in 8 nodes. This suggests that there are only two locations in the plate structure that is damaged. Through the process of elimination it can be seen that only element no. 11 is bounded by node no. 14 (DOFs: 28, 29, 30), node no. 15 (DOFs: 31, 32, 33),

node no. 18 (DOFs: 40, 41, 42) and node no. 19 (DOFs: 43, 44, 45). Likewise, only element no. 16 is bounded by node no. 21 (DOFs: 49, 50, 51), node no. 22 (DOFs: 52, 53, 54), node no. 25 (DOFs: 61, 62, 63) and node no. 26 (DOFs: 64, 65, 66).

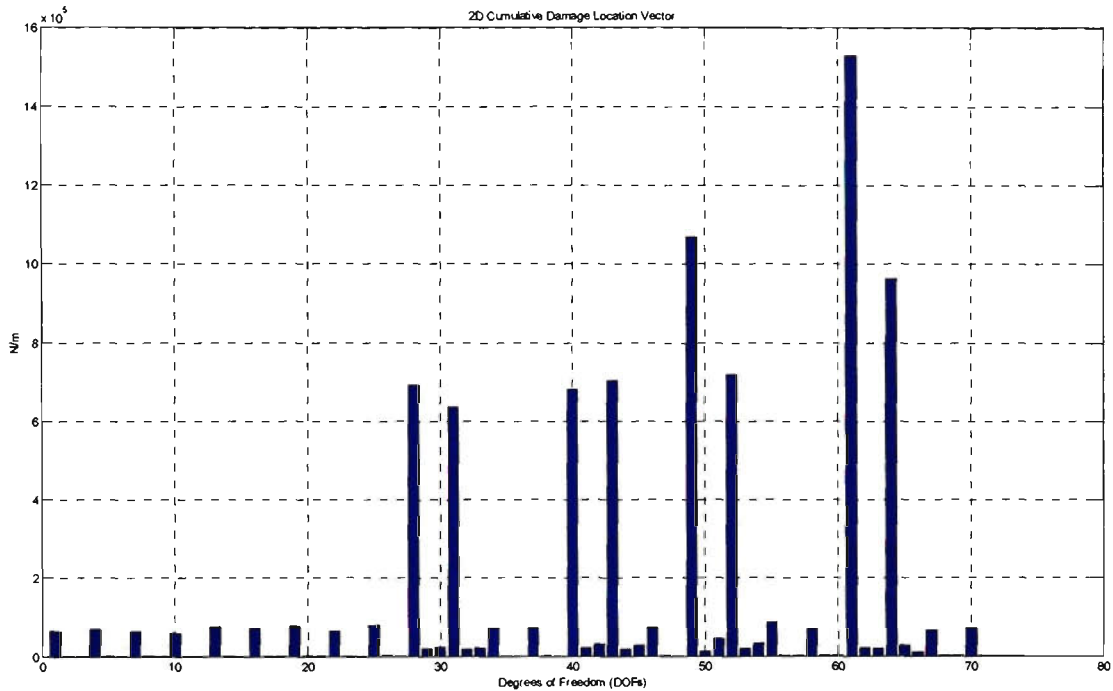


Figure 5.15b: 2D CDLV Plot for Damage Case C without Coordinate Incompatibility (5% Noise)

## 5.9 COORDINATE INCOMPATIBILITY

First only 48 DOFs out of a possible 72 DOFs will be supplied to the Damage Detection Algorithm. This would require the Damage Detection Algorithm to utilise the Dynamic Expansion method A (D.E. A), as discussed in Chapter 2, to expand the 24 missing DOFs to match the 72 DOFs found in the undamaged analytical model. The 48 DOFs that were supplied into the Damage Detection Algorithm were chosen randomly from the 72 DOFs available. See Appendix 9 for the list of the randomly chosen DOFs.

For simplicity, Damage Case A scenario from the previous section will be used in this section. A coordinate incompatibility study will only be applied to Damage Case A for this section, since Damage Case B and Damage Case C would lead to essentially the same conclusion. As with

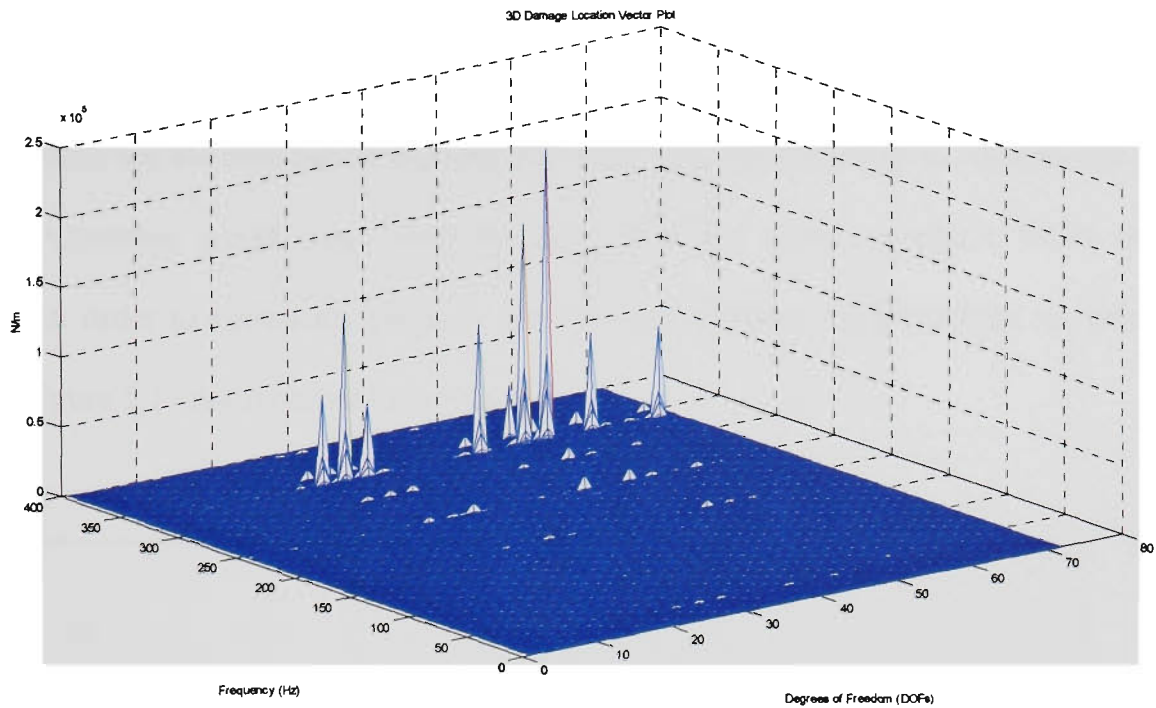
previous studies, noise of 5% will also be introduced to the algorithm at the same time as coordinate incompatibility.

Figure 5.16a is the corresponding 3D DLV Plot for Damage Case A when only 48 DOFs from a possible 72 DOFs were supplied to the Damage Detection Algorithm. Since not all the coordinates have been supplied to the Damage Detection Algorithm, the location of damage can not be predicted with certainty. However it is possible to utilise the Damage Detection Algorithm to determine an approximate area of damage. Once this approximate area of damage has been located, further measurements within this area may aid in pinpointing the location of damage. Once the location of damage has been pinpointed accurately then a quantitative value may be determined for the damage using the same procedures as shown in the previous section.

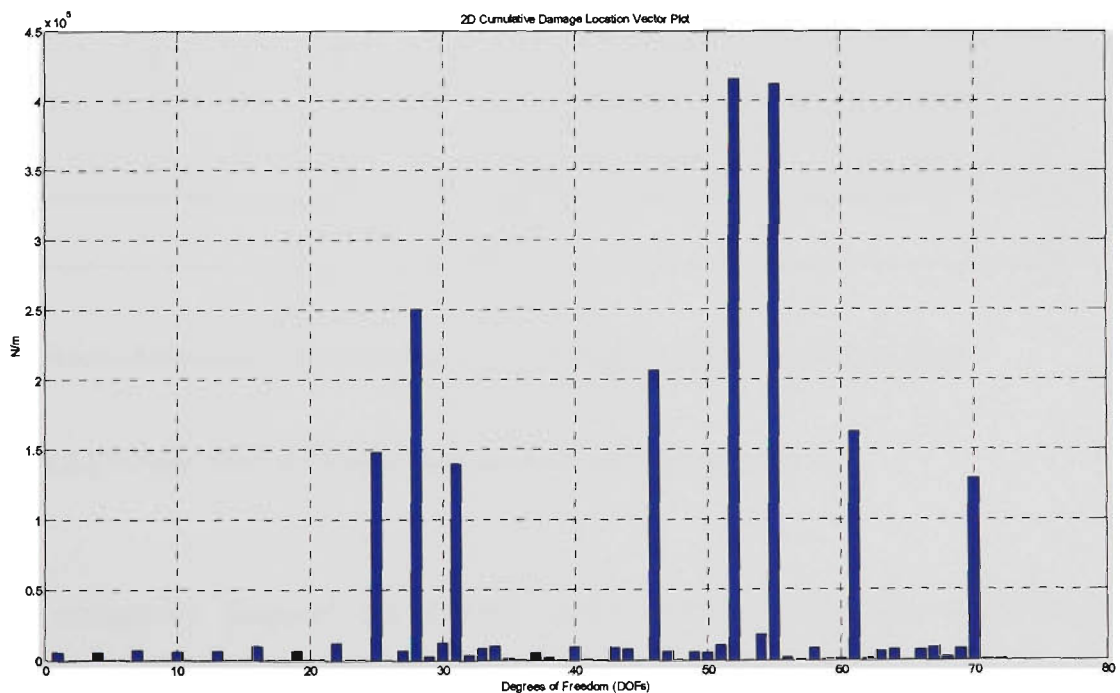
It must be noted that unlike the previous section, in cases where coordinate incompatibility exists, the vertical axis of the 3D DLV plot may not necessarily indicate the damage extent within the structure.

Figure 5.16b is the corresponding 2D CDLV Plot for Damage Case A with 48 DOFs supplied and 24 expanded DOFs. Here the location of damage can be seen to occur at DOFs 25, 28, 31, 36, 52, 55, 61 and 70. This translates to the damage being associated with nodes no. 13 (DOFs: 26, 26, 27), node no. 14 (DOFs: 28, 29, 30), node no. 15 (DOFs: 31, 32, 33), node no. 20 (DOFs: 46, 47, 48), node no. 22 (DOFs: 52, 53, 54), node 23 (DOFs: 55, 56, 57) node no. 25 (DOFs: 61, 62, 63) and node no. 28 (DOFs: 70, 71, 72). It should be noted that damage for the cantilever plate is considered as damage to the element rather than to a node.

---



**Figure 5.16a: 3D DLV Plot for Damage Case A with 48 Measured Coordinates and 24 Expanded Coordinates (5% Noise)**



**Figure 5.16b: 2D CDLV for Damage Case A with 48 Measured Coordinates and 24 Expanded Coordinates (5% Noise)**

Recall that for Damage Case A, only element no. 11 is the damaged element. The initial conclusion would suggest that the Damage Detection Algorithm did not detect the damage accurately. However, if the location of these nodes were examined on the cantilever plate as

shown in Figure 5.17, it can be seen that the nodes mapped out an area where the damage may be located and that element no. 11 lies within this area. The reason why it was not possible to accurately pinpoint the damage to element no. 11 at this present stage is because the Damage Detection Algorithm could only detect the damage to the closest available DOFs that were supplied. In order to accurately pinpoint the damaged element, DOFs within the shaded area shown in Figure 5.17 are required to be supplied.

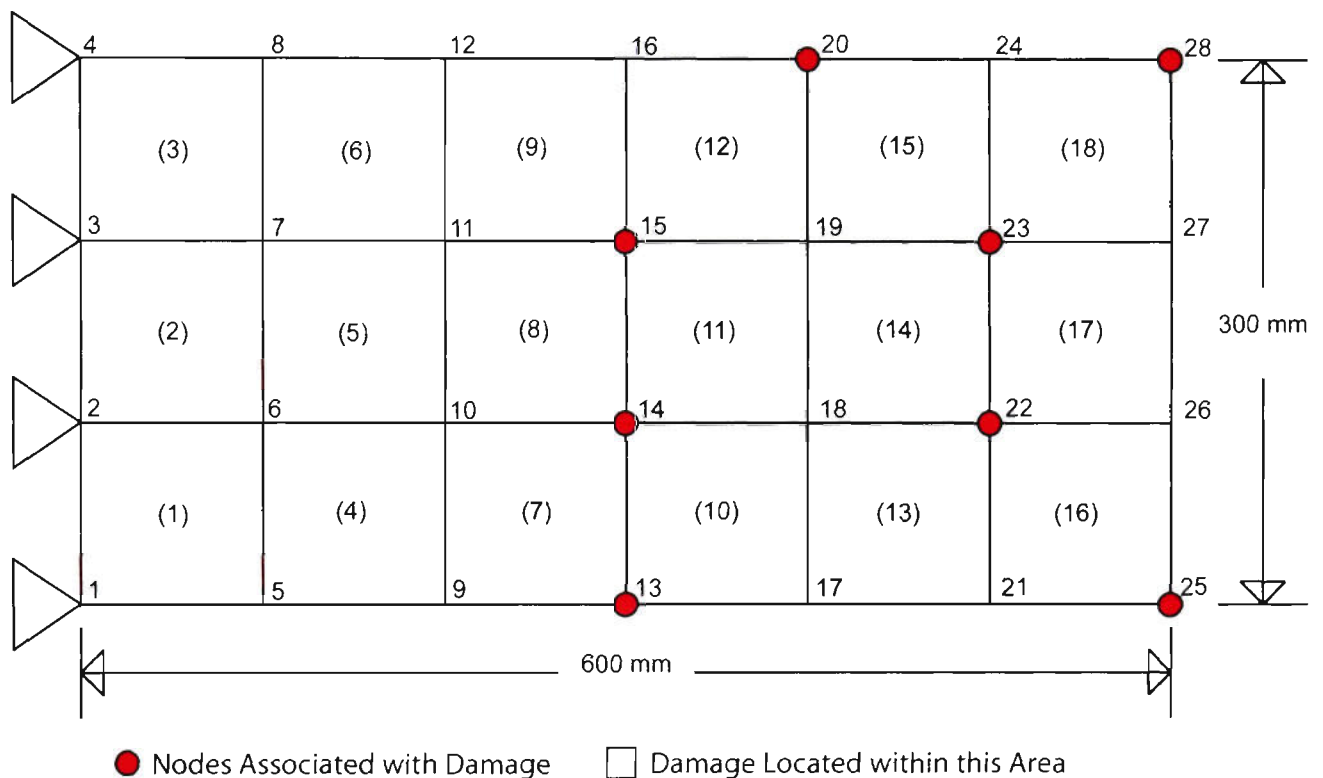


**Figure 5.17: Node Map of Possible Damage Area for Damage Case A**

In order to accurately pinpoint the damage further DOFs within the identified area were subsequently supplied to the Damage Detection Algorithm. Figure 5.18a is the corresponding 3D DLV Plot for Damage Case A when 12 more DOFs, totalling 60 DOFs out of 72 DOFs were supplied to the Damage Detection Algorithm.

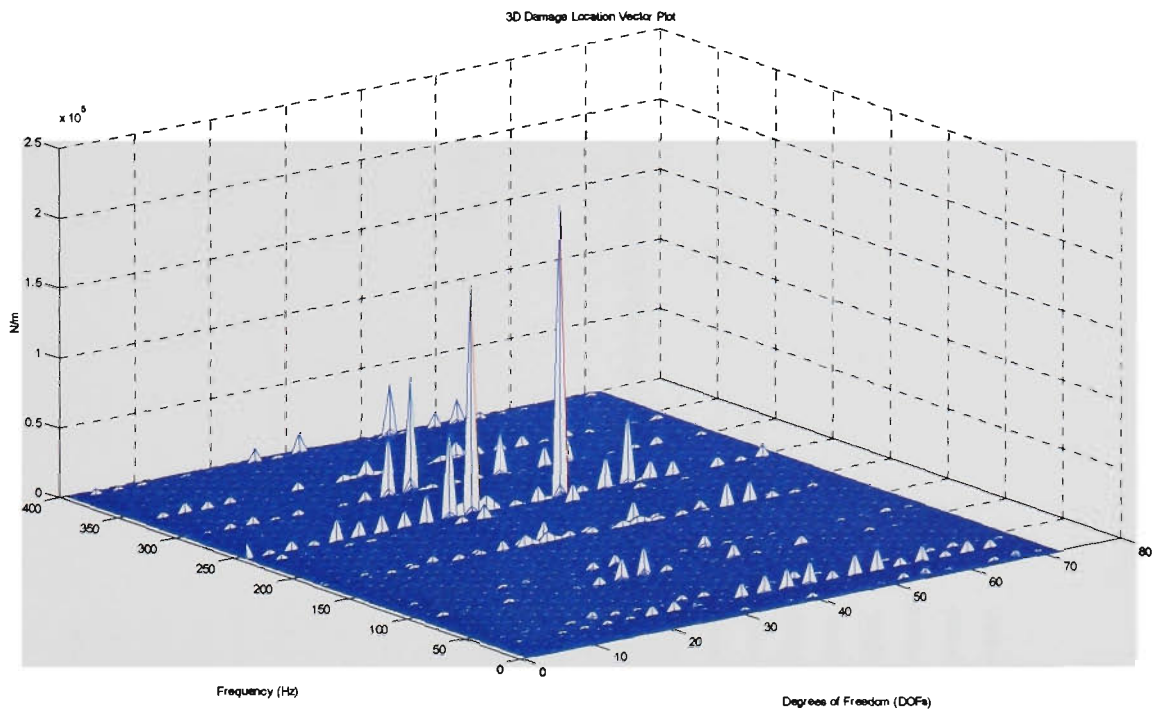


**Figure 5.18a: 3D DLV Plot for Damage Case A with 60 Measured Coordinates and 12 Expanded Coordinates (5% Noise)**

Figure 5.18b is the corresponding 2D CDLV plot for Damage Case B with 60 DOFs supplied and 12 expanded DOFs. Here the location of damage can be seen to occur at DOFs 28, 31, 43 and 52 whose peaks are clearly dominate over the smaller peaks that are due to noise. This translates to the damage being associated with node no. 14 (DOFs: 28, 29, 30), node no. 15 (DOFs: 31, 32, 33), node no. 19 (DOFs: 43, 44, 45) and node no. 22 (DOFs: 52, 53, 55). If these nodes were examined onto the cantilever plate as shown in Figure 5.19, they map out an area on the plate where damage may exist. Since not all the coordinates have been supplied, it is still not possible to determine the exact location of damage. However comparison of Figure 5.17 and Figure 5.19, shows that the area of damage is furthered refined when more DOFs for the cantilever plate are supplied to the Damage Detection Algorithm. It can be seen that in order to improve the resolution of the location of damage, all the DOFs that lie within the shaded area of Figure 5.19 must be supplied to the Damage Detection Algorithm.

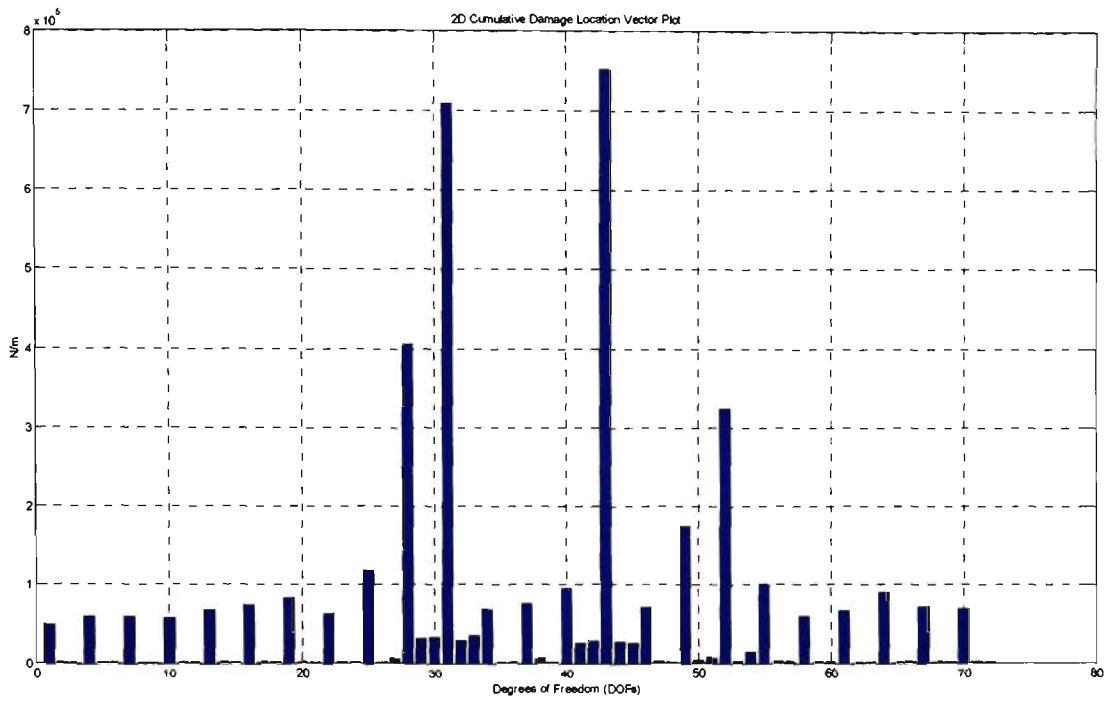


Figure 5.18b: 2D CDLV Plot for Damage Case A with 60 Measured Coordinates and 12 Expanded Coordinates (5% Noise)

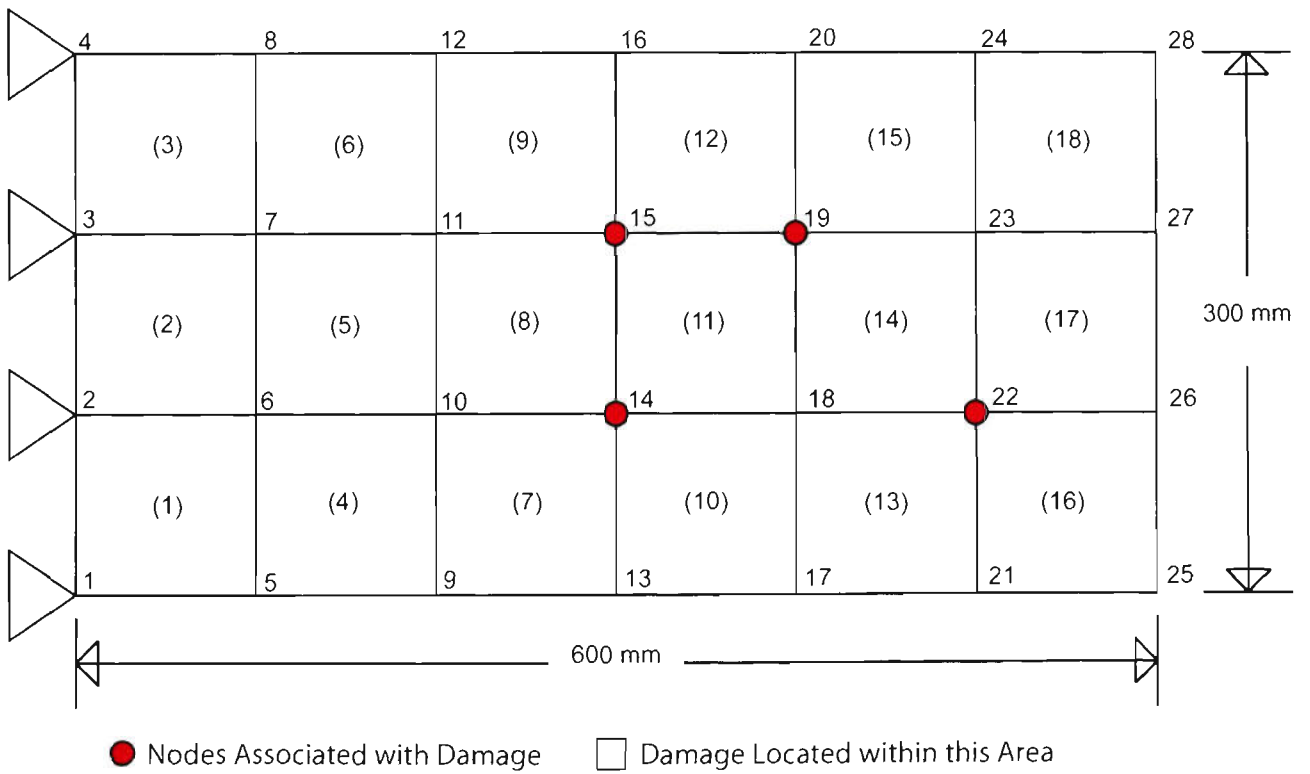


Figure 5.19: Node Map of Possible Damage Area

## 5.10 DISCUSSION

In this Chapter the Damage Detection Algorithm was found to be robust and demonstrated that it could be used as a tool to locate damage within a thin flat plate structure. Furthermore, the Damage Detection Algorithm was also able to give estimation on the extent of damage present once the location was found. It was also shown that the algorithm was capable of detecting damage for multiple simulated damages with 5% simulated noise interference.

For the case where coordinate incompatibility exists, the Damage Detection Algorithm demonstrated that it could be used as a tool to firstly determine a broad area of damage within the structure. Once an area of damage has been identified on the structure, further refinements to pinpoint the damage can be effected if more FRF data in the area are available.

A real cantilever plate will be studied in the next chapter. An experimental FRF will be obtained from a cantilever plate from vibration testing. Damage will be introduced to the cantilever plate and the ability of the Damage Detection Algorithm to detect this damage will be assessed.

---

# **CHAPTER 6**

## **EXPERIMENTAL STUDIES: DAMAGE DETECTION IN A CANTILEVER PLATE**

The aim of this chapter is to utilise the Damage Detection Algorithm that has been studied in the previous chapters and apply it to a real structure using experimental FRFs which will be obtained from non destructive vibration tests. Physical damage will be introduced to the cantilever plate and the performance of the Damage Detection Algorithm will be assessed.

The dimension of the physical test piece has been chosen to match the dimension of the Plate28 example from the previous chapter. This will enable a comparison to be made between the results previously obtained from simulated damage to experimental results obtained in this chapter. First basic concepts from experimental modal analysis are briefly presented.

### **6.1 BASIC MODAL ANALYSIS**

The basic experimental setup required in order to obtain FRF data is simple and consists of three main items:

1. Transducers
  2. Excitation mechanism
  3. Frequency Analyser
-

### 6.1.1 TRANSDUCERS

Transducers are used to measure the parameters of interest in modal testing. There are a wide variety of transducers available, the most common being the “Force Transducer” and the “Accelerometer”. These transducers consist of a piezoelectric element which exhibits an electrical charge across its end face when subjected to mechanical stresses. With the appropriate design, a piezoelectric element may be incorporated into devices that may induce a stress proportional to the physical quantity to be measured such as force or acceleration.

It is important that the transducer such as an accelerometer is attached correctly to the test structure and that the correct method of fixation is chosen for the desired frequency response range of the test structure, as limitations in frequency response ranges exist for each method (Ewins, 1984) and are shown in Figure 6.1. It is also important that when attaching the transducer to the test structure that the selected method does not dramatically change the local stiffness or mass of the structure. The simplest and easiest method to attach a transducer (of small relative mass) to the test structure is to use a thin layer of wax which acts as a weak adhesive. This method will be used for experiments in this chapter.

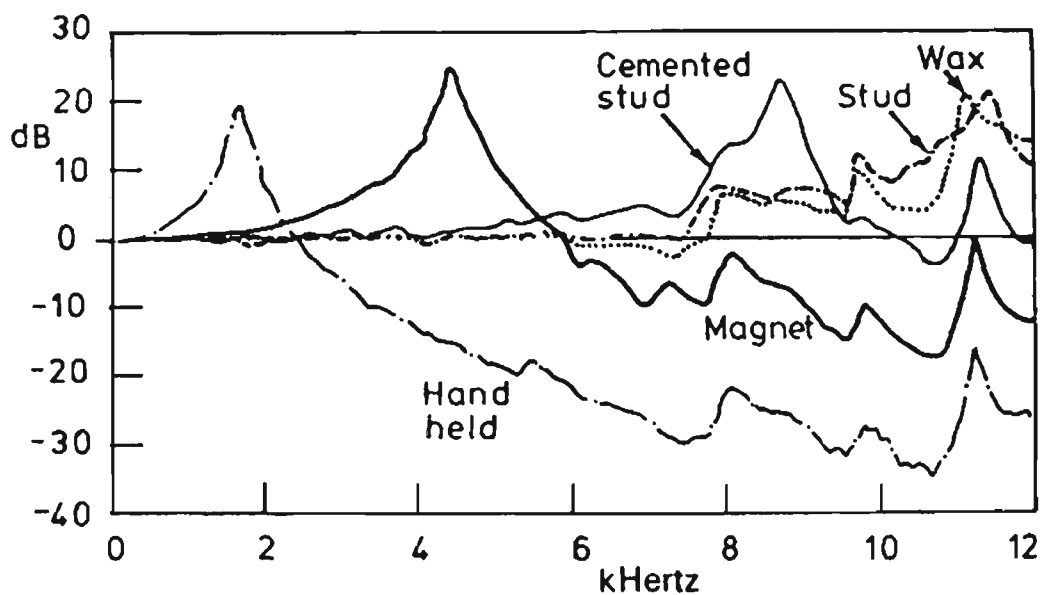


Figure 6.1: Limitation of Frequency Response Range (extracted from Ewins, 1984)

### 6.1.2 EXCITATION MECHANISM

The excitation mechanism is important in modal testing as it is used to introduce vibration into the test structure through a controlled excitation. The hammer excitor is a simple way to introduce excitation into a test structure. The hammer consists of a handle with an impactor as the head. For this reason the hammer excitor is often referred to as an “Impact Hammer”. This impactor head can be fitted with different types of tips so that different frequency ranges and force levels may be achieved for testing of different structures. The impactor head also incorporates a force transducer, which records the force felt by the impactor.

The operator who controls the velocity of the impact on the test structure determines the magnitude of the force. One of the difficulties associated with using the impact hammer is the ability to ensure that consistent impact force is applied to the test structure. The location on the test structure where the contact of the impact hammer is to occur is also important. Ensuring that the impact is always normal to the test surface would result in greater accuracy and repeatability. At the same time, multiple impacts should be avoided, that is to say that one impact should only occur at any one time and the reverberation of the impact hammer should not make contact with the test structure during this period.

### 6.1.3 FREQUENCY ANALYSER

The purpose of the analyser is to record and process the signal reported by the transducer. This signal is transmitted to the analyser in analogue format and is converted to a digital signal by the analyser.

---

## 6.2 EXPERIMENTAL SETUP

The experimental setup shown in Figure 6.2 that was used to obtain FRF data from the cantilever plate in this chapter consisted of the following equipment:

1. Miniature Accelerometer (Type 4393 Bruel & Kjaer)
2. Instrumental Hammer (PCB 086B03)
3. Nexus Conditional Amplifier
4. Power Unit (PCB 480D06)
5. Oscilloscope
6. Dual Channel Signal Analyser (Bruel & Kjaer 2032)
7. Personal Computer

A single direction miniature accelerometer (Type 4393 Bruel & Kjaer) with a mass of 2.3g was used to measure the response of the test structure. Its calibration chart can be found in Appendix 10. Attention was given to the selection of this accelerometer. Incorrect selection may inadvertently change the overall test piece.

This miniature accelerometer with a sensitivity of  $0.314 \text{ pc/ms}^{-2}$  was connected to the Nexus Conditional Amplifier, which amplified the response signal to a suitable level before the signal was fed into Channel B of the Signal Analyser. A gain of  $10\text{mV/ms}^{-2}$  was also set on the Nexus Conditional Amplifier. Additionally, the response signal from the miniature accelerometer was also fed into an oscilloscope. The purpose of this was to observe the real time response from the miniature accelerometer.

An instrumented hammer that incorporated a force transducer with a plastic tip was used to excite the experimental test piece. The sensitivity of the force transducers of this hammer is

---

2.10mV/N and was connected to a power unit with a gain of 100mV/ms<sup>-2</sup>. The signal output from the power unit was connected to channel A of the Dual Channel Analyser and was also fed into an oscilloscope to monitor the real time responses.

The output of the Dual Channel Analyser was connected to a personal computer via the GPIB port on the Dual Channel Analyser. By connecting the Dual Channel Analyser to a personal computer, this allows the FRFs to be stored, since the Dual Channel Analyser is not capable of storing more than one FRF trace at any one time. Appendix 11 details the setting used on the Dual Channel Analyser.

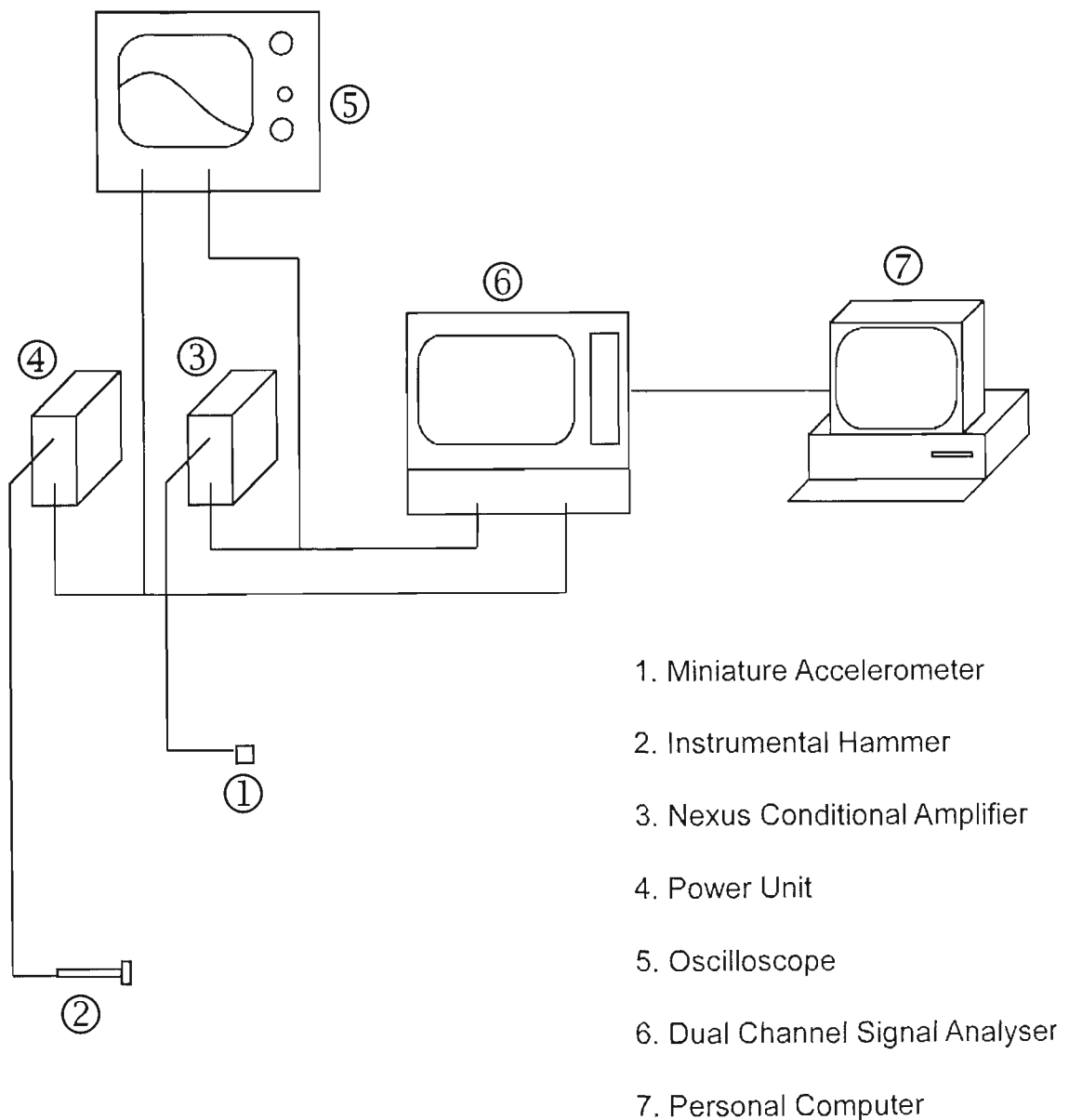


Figure 6.2: Sketch of Experimental Setup

### 6.3 EXPERIMENTAL TEST PIECE

The test structure is a thin cantilever plate with similar properties of the Plate28 structure studied in the previous chapter. The cantilever plate structure is a thin galvanised steel plate with dimension 700mm x 300mm x 3mm and is larger than the defined working area to allow for fixation. It is assumed that the galvanised steel has a Young's Modulus (E) of 200 GPa, Poisson's Ratio ( $\nu$ ) of 0.3 and density ( $\rho$ ) of 8179 kg/m<sup>3</sup>.

Using a felt tip pen, a grid of squares the size of 100mm x 100mm was marked out on the surface of the cantilever plate. Nodes were also marked at each intersection of the grid. This resulted in 28 nodes and 18 square elements over the cantilevered portion as shown in Figure 6.3. With the plate under such a configuration the full length of the plate was not fully utilised. This was deliberately done so that there was adequate amount of space left over on one side so that this could be used to ground the plate. The test piece was clamped between two solid steel bars and then fixed on a large tri-angular steel frame using several G-Clamps.

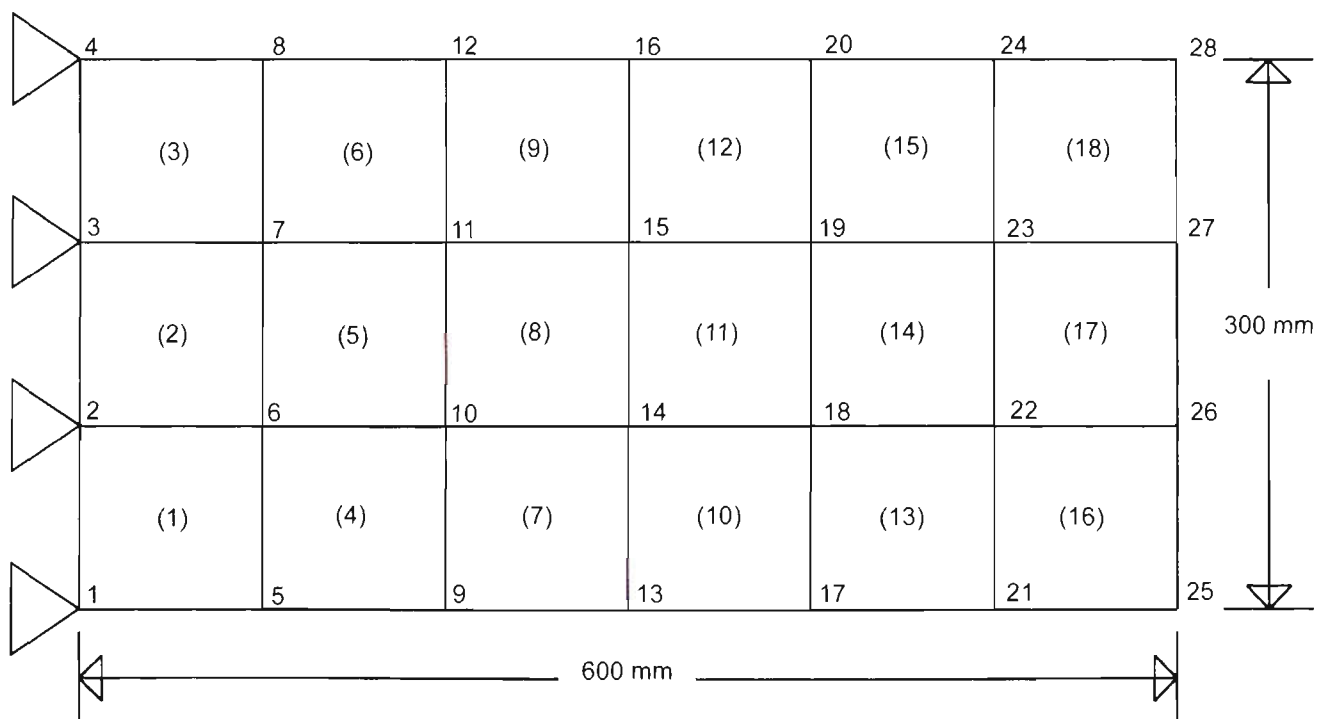


Figure 6.3: Experimental Test Piece

In reality this thin cantilever plate is described by 28 nodes and had 6 DOFs (3 translational and 3 rotational) per node. This experimental structure therefore has a total of 168 DOFs. To simplify the problem, only translation degrees of freedom are considered for the study of this structure. This is justified, as the rotational degrees of freedom can not be practically measured with the same degree of accuracy as translational DOF. Under this assumption, the thin cantilever plate has a total of 84 DOFs. Since this thin cantilever plate is to be grounded at one end, therefore a further 4 nodes may be eliminated, thus leaving only 72 DOFs.

#### 6.4 CALIBRATION

It is critical that before any data is obtained that equipment calibration is performed to ensure that all equipment is functioning correctly. Ewins, (1984) suggests that a simple and easy technique of calibrating can be done by using a known mass. Calibration can be done by freely suspending this known mass and attaching the accelerometer to be used for measurement onto this mass. A hammer should then be used to excite the mass. The overall sensitivity of the equipment can be calibrated by measuring the ratio of response to force of this mass. From this simple structure, the overall result expected is a constant magnitude over the frequency range.

The mass that was used weighed 9.328 kg and was suspended from a free-free structure as shown in Figure 6.4.

For this particular mass the calibration is given by;

$$m\ddot{X} = F$$

$$\text{or, } 20\log_{10}\left(\frac{\ddot{X}}{F}\right) = 20\log_{10}\left(\frac{1}{m}\right) = 20\log_{10}\left(\frac{1}{9.328}\right) = -19.4 \text{ dB}$$

Where  $m = 9.328 \text{ kg}$



**Figure 6.4 Free-Free Known Mass Structure**

Therefore, for a known mass of 9.328 kg the expected accelerance FRF results obtained by the Bruel & Kjaer analyser should show a constant magnitude of -19.4 dB across a range of frequency. Averages of five measurements were obtained for the calibration run.

Initial measurements resulted in a recorded magnitude of -18.4 dB. This was not the value that was expected for the mass that was used. The setup was adjusted until the desired result was achieved (Ewins, 1984). The advantage of such type of calibration is that it is relatively simple to perform and ensures that the complete measurement setup is calibrated in one process, rather than having to calibrate each individual piece of equipment.

The sensitivity of the miniature accelerometer Bruel & Kjaer Type 4393 was adjusted from  $0.314\text{pc/ms}^{-2}$  to  $0.354\text{pc/ms}^{-2}$ . By adjusting the sensitivity of the miniature accelerometer the correct dB value of -19.4 dB was eventually achieved and is shown in Figure 6.5.

Figure 6.5 shows the accelerance FRF plot obtained for the calibration of the known mass after adjustments were made to the equipment to produce the correct theoretical desired dB as indicated by the dotted line in Figure 6.5. It can also be seen that the accelerance FRF plot decreases in dB as the frequency increases or rather it can be observed that the pulse is decaying. This is consistent with experimental results. The coherence plot for the corresponding accelerance FRF plot has also been provided. It can be seen that the coherence is extremely good, in that most values are close to one or unity. This suggests that the FRF data obtained corresponding to this coherence plot is fairly free from noise. However it can not be concluded that the FRF data is free from errors. It can be observed that the calibration curve is extremely good over most of the range of frequency studied, while between 5 Hz – 40 Hz, the error is of order 5%. Poor FRF data at this frequency range could be caused by the existence of rotational DOFs at the point of fixation causing inadequate grounding of the structure. Despite efforts to adequately ground the structure, it was not possible to eliminate this problem.

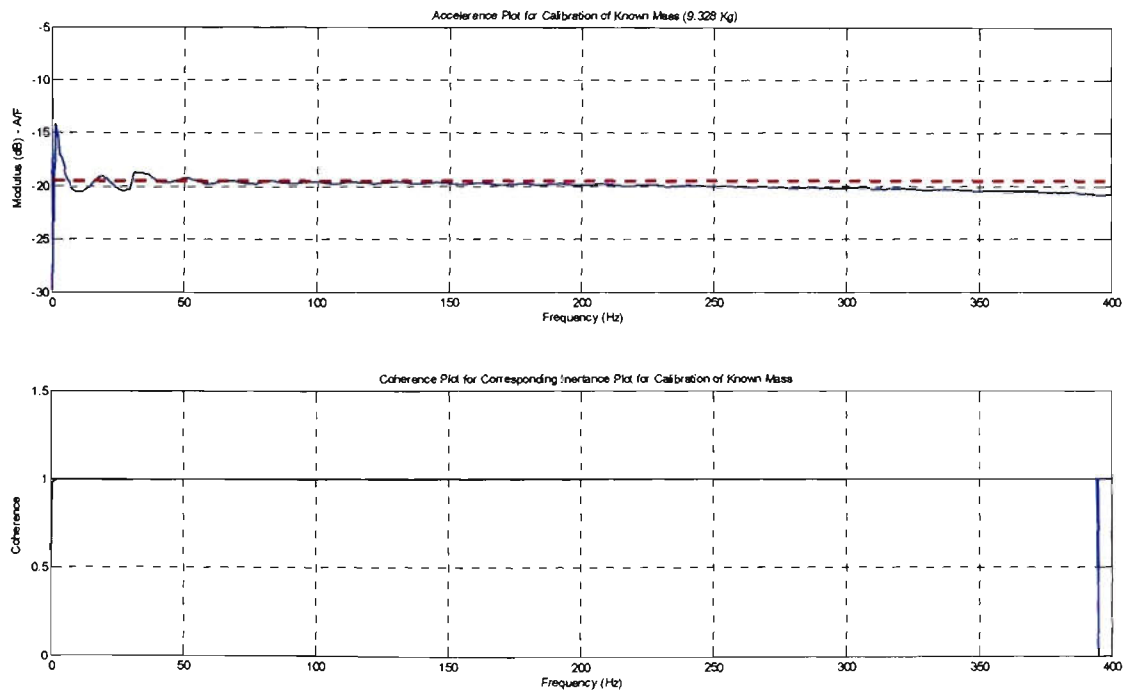


Figure 6.5: Accelerance and Coherence Plot for Calibration of Known Mass

## 6.5 STRUCTURE SETUP

As the plate is fixed at one end i.e. tested in grounded conditions, the test structure will not exhibit any rigid bound modes. In theory, it is relatively simple to ground a test structure, however in practice it is very difficult to provide a sufficiently rigid foundation on which the test structure may be grounded. A common procedure is to measure the mobility of the rigid foundation itself over a frequency range to establish that the foundation has a much lower mobility than the corresponding levels of the test structure at the point of fixation. If this is satisfied then the test structure can be said to be sufficiently grounded.

However it is important to note that it may often not be very easy to fully ground a structure, as most often there may be some rotational degrees of freedom existing at the point of fixation. These rotational degrees of freedom may be very difficult to detect or measure.

## 6.6 SIMULATION OF DAMAGE

Similar damage cases used in Section 5.4 will be introduced to the experimental test piece (Table 5.4 and Table 5.5). Controlled damage will be firstly introduced to a single element on the cantilever plate by a small cut across the element. Since it is desired to firstly study the different damage cases individually before multiple damage scenarios are considered, two identical cantilever plates have been used.

## 6.7 OBTAINING EXPERIMENTAL FREQUENCY RESPONSE FUNCTION DATA

Experimental FRFs data will be obtained for at least one row or column of the FRF matrix of the structure. For example, in the case of Plate28, which is described by 72 DOFs, the minimum FRFs data required without considering coordinate incompatibility is 72 experimental FRF data traces. Having said this, it is not sufficient to supply 72 experimental FRF data traces in random

---

order. Some order is required when obtaining the experimental FRF, which will satisfy the needs of one row or column. Through reciprocity, it is easier to obtain a column of FRF data rather than a row of FRF data. Since, in order to obtain a column of FRF data one must have the accelerometer fixed on one location while the excitation location cycles through all the nodal locations. This is easier to realise than to obtain a row of FRFs data where the excitation location remains fixed and the accelerometer location moves through all the nodal locations.

### **6.8 ICATS & CIRCLE FIT METHOD**

The Bruel & Kjaer Frequency Analyser is used in the experimental setup to acquire the experimental FRF. However, the analysis of the experimental FRF data will be done using a modal analysis software, "ICATS" (Imperial College Analysis and Testing Software). ICATS is a combination of several utilities that caters for specific applications within the modal analysis field. The MODACQ component within ICATS is used to transfer the experimental FRF data captured by the Bruel & Kjaer Frequency Analyser to the PC. This data is stored in an ASCII format.

The circle fit analysis method relies on the fact that the Nyquist plot of the frequency response function properties produces circle like curves at the vicinity of a resonance in the FRF data. A proof can be found in Ewins (1984).

Within the ICATS program the circle fit analysis method can be invoked by running the MODENT module of ICATS. This MODENT module allows the operator to analyse the obtained FRF experimental data using different analysis methods.

---

## 6.9 UNDAMAGED CASE



**Figure 6.6** Experimental Setup of Plate28 without Damage

Figure 6.6 shows the experimental setup for the undamaged cantilever plate. The experimental plate is clamped between two solid steel bars and fixed to a much larger steel frame by several G-Clamps. It is assumed that this steel frame is fully grounded. Although theoretically, grounding a structure is trivial, in reality this was found to be extremely difficult to ensure that all the rotational DOFs were grounded at the point of fixation. One method to ensure that no rotational DOFs exist at the fixing point is to obtain preliminary FRFs at or near the grounded nodes. In

Figure 6.6, the accelerometer is attached to node no. 10 of the plate. A magnetic swivel arm was used to ensure that the cabling of the accelerometer did not interfere with the vibration of the cantilever plate during impact.

The Circle Fit Method was used to analyse and detect the mode shapes and natural frequencies of the FRF data that were obtained from non-destructive impact testing of the undamaged cantilever plate. Figure 6.7 shows the point FRF data corresponding to location (1, 1) which correlates to node no. 5 since all previous (lower numbered) nodes have been grounded. Natural frequencies were also obtained from ICATS and these are presented in Table 6.1. It can be seen from Figure 6.7 that this is indeed a point FRF data since it only contains well defined resonance and anti-resonance. It can be seen that ICATS detect only 11 out of 12 natural frequencies shown in Table 6.1. The frequency of 6.83 Hz is missed because of experimental limitation.

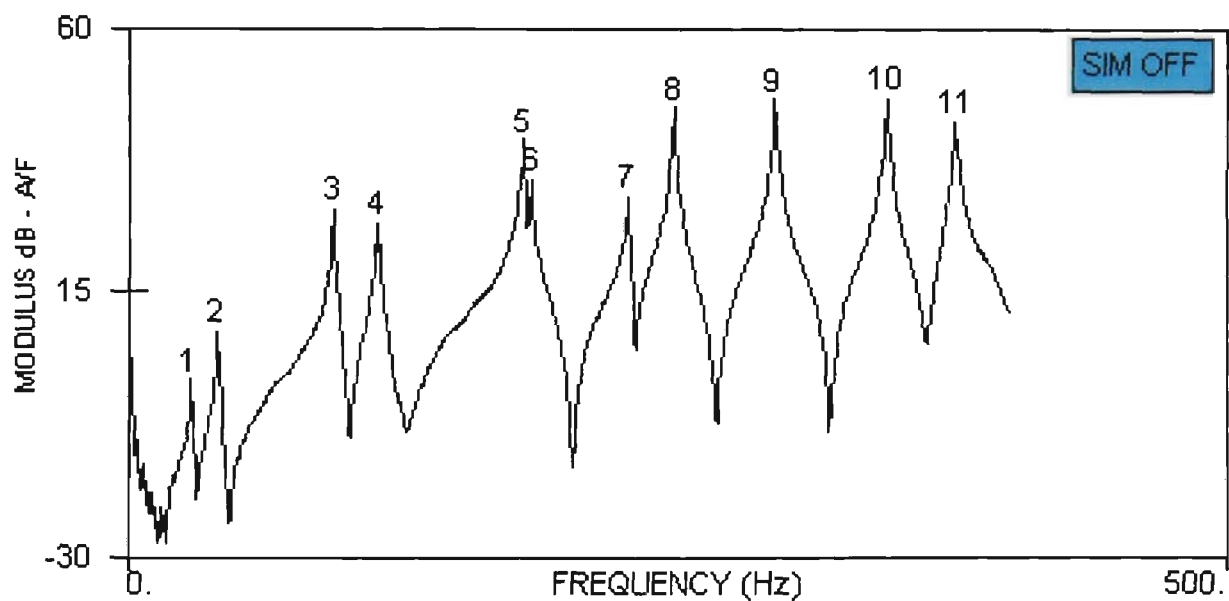


Figure 6.7: ICATS Identification of Mode Shapes

From Table 6.1, it can be seen that the modes and natural frequencies correlated closely with the natural frequencies obtained from Matlab and ANSYS. It must also be noted that the first mode shape and corresponding natural frequency could not be obtained.

| Modes No. | Matlab (Hz) | ANSYS (Hz) | Experimental (Hz) |
|-----------|-------------|------------|-------------------|
| 1         | 6.83        | 6.83       | Unobtainable      |
| 2         | 29.40       | 29.78      | 29.50             |
| 3         | 42.84       | 42.82      | 41.50             |
| 4         | 95.79       | 98.07      | 95.50             |
| 5         | 120.90      | 120.71     | 113.50            |
| 6         | 183.33      | 187.63     | 182.00            |
| 7         | 184.97      | 190.79     | 185.50            |
| 8         | 236.37      | 239.20     | 229.50            |
| 9         | 248.81      | 258.36     | 249.50            |
| 10        | 301.08      | 318.02     | 298.00            |

**Table 6.1: Comparison of Natural Frequencies for the Cantilever Plate Undamage**

Figure 6.8 shows the comparison of the experimental receptance FRF plot obtained from the undamaged cantilever plate against theoretical calculations from the previous chapter. It can be seen that at low frequencies both the experimental and theoretical receptances are fairly similar. It also must be noted that the experimental receptance trace at the initial zero frequency does not exhibit stiffness like characteristics as presented in modal analysis theories. This does not suggest that the experimental results obtained are incorrect or that modal analysis is incorrect, but is due to the erroneous results obtained at the initial zero frequency.

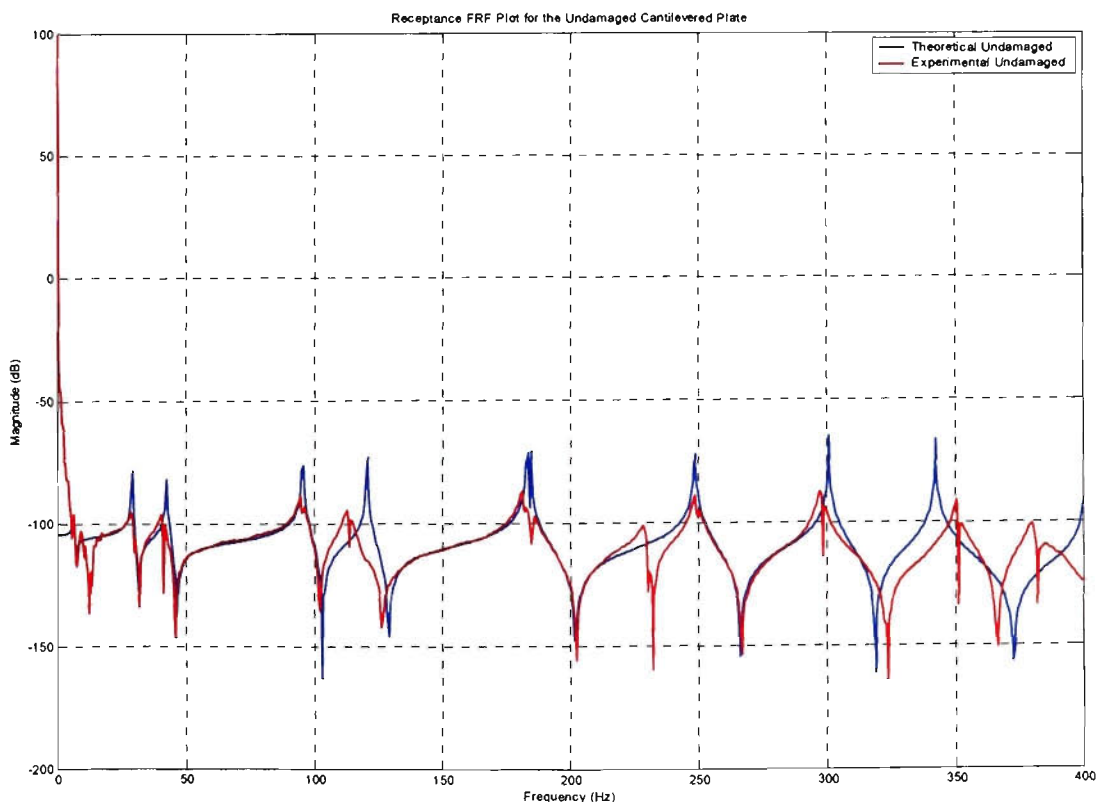


**Figure 6.8: Comparison of Experimental against Theoretical Receptance FRF at  $\alpha(1, 1)$  for the Undamaged Cantilever Plate**

First the effect of noise is investigated by inputting into the DLV algorithm the experimental signals due to noise only by using only the undamaged structure. Figure 6.9a is the corresponding 3D Damage Location Vector plot for the Undamaged Case between the frequency ranges of 50Hz – 200Hz with a frequency resolution of 0.5Hz. The Damage Detection Algorithm was applied to this frequency range so that it would be possible to avoid the erroneous experimental results obtained at the beginning frequencies closest to zero hertz.

From Figure 6.9a peaks can be seen to occur in all DOFs and this would suggest that all DOFs within the cantilever plate contained damage. Reading from the vertical axis the maximum change in stiffness [ $\Delta K$ ] can be estimated to be approximately 60N/m. Using Matlab™ it is possible to investigate further into the DLV to determine the exact location and magnitude of where the maximum change in stiffness occurs. The magnitude of the stiffness peak was found to be 64N/m and occurred at DOF 1. From the undamaged stiffness matrix, the original stiffness magnitude at DOF 1 is approximately 1.044MN/m. Comparison between the stiffness magnitudes obtained from the DLV with the original magnitude shows that the percentage of change from the original stiffness value to be approximately 0.006%. This suggests that the effect of noise was not significant.

Figure 6.9b is the corresponding 2D CDLV plot for the Undamaged Case which shows the effect of noise. In this plot extremely large peaks can be seen to occur. However closer inspections shows that the scale on the vertical axis is extremely small compared to later plots. It can be seen that the effect of noise is small and present in most DOFs, relatively more dominant for deflection DOFs compared to rotational DOFs.

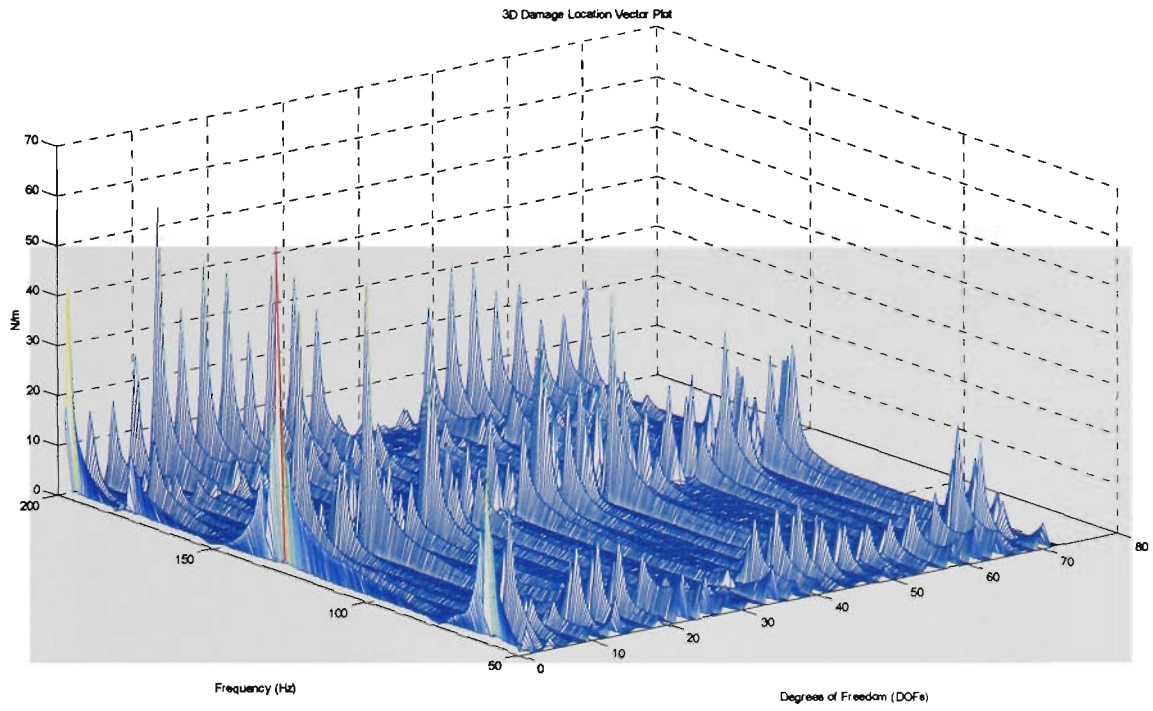


Figure 6.9a: 3D DLV Plot for Undamaged Case

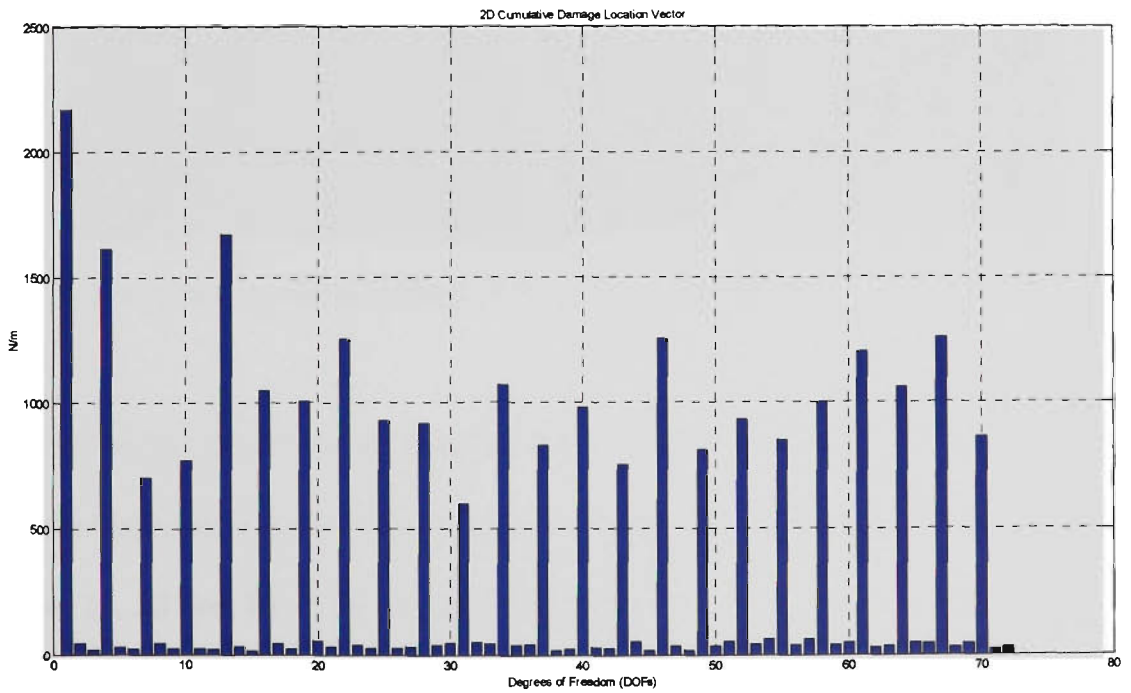


Figure 6.9b: 2D CDLV Plot for Undamaged Case

### 6.10 DAMAGE CASE A



**Figure 6.10: Experimental Setup of Plate28 for Damage Case A**

Figure 6.10 shows the experimental setup for the cantilever plate for Damage Case A. Physical damage was introduced to the cantilever plate as a diagonal cut across element no. 11, affecting nodes no. 14, 15, 18 and 19. This cut can clearly be seen in Figure 6.9. It is assumed that this diagonal cut does not change the mass of the cantilever plate significantly and thus it can be assumed that there is no change in the mass of the structure.

Once the experimental plate was securely fixed to the large steel frame structure, FRFs data traces were obtained by systematically impacting each node at any one time with the impact hammer. An average of five FRFs data traces were taken for each node.

Table 6.2 is a comparison of natural frequencies obtained from theoretical analysis in the previous chapter compared with real experimental FRF data for Damage case A. It can be seen that the experimental data correlate closely with the theoretical analysis.

| Modes No. | Matlab (Hz) | ANSYS (Hz) | Experimental (Hz) |
|-----------|-------------|------------|-------------------|
| 1         | 6.79        | 6.80       | Unobtainable      |
| 2         | 28.95       | 29.32      | 28.50             |
| 3         | 41.55       | 41.56      | 40.50             |
| 4         | 94.33       | 96.55      | 92.50             |
| 5         | 119.30      | 119.08     | 113.00            |
| 6         | 176.44      | 179.31     | 179.00            |
| 7         | 181.78      | 188.75     | 182.50            |
| 8         | 233.96      | 236.41     | 227.00            |
| 9         | 244.52      | 253.92     | 247.50            |
| 10        | 297.87      | 313.89     | 293.00            |

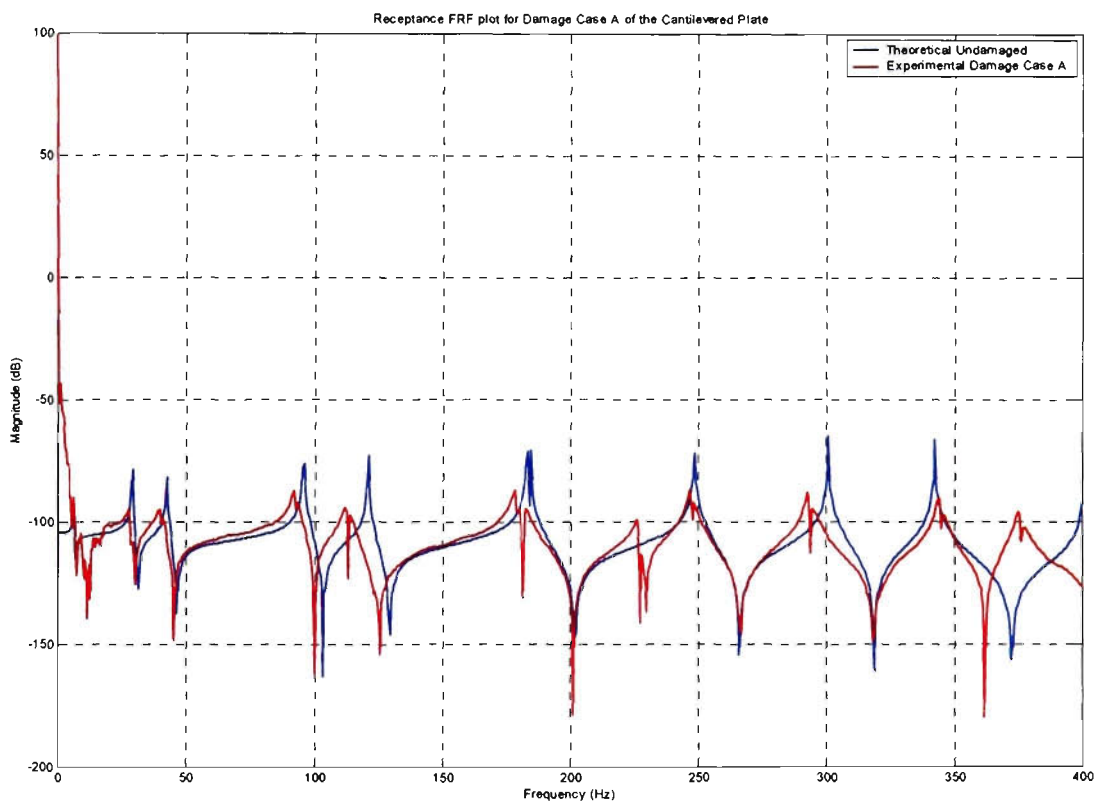
Table 6.2: Natural Frequency of the Cantilever Plate Obtained from Experiment for Damage Case A

Table 6.3, is a comparison of natural frequencies between the experimental undamaged data and the experimental data obtained from Damage Case A. A percentage change between 0.44% - 3.39% from the undamaged cantilever plate can be seen at various natural frequencies.

| Modes No. | Experimental Undamage (Hz) | Experimental Damage Case A (Hz) | Change from Experimental Undamage (%) |
|-----------|----------------------------|---------------------------------|---------------------------------------|
| 1         | Unobtainable               | Unobtainable                    | NA                                    |
| 2         | 29.50                      | 28.50                           | 3.39                                  |
| 3         | 41.50                      | 40.50                           | 2.41                                  |
| 4         | 95.50                      | 92.50                           | 3.14                                  |
| 5         | 113.50                     | 113.00                          | 0.44                                  |
| 6         | 182.00                     | 179.00                          | 1.65                                  |
| 7         | 185.50                     | 182.50                          | 1.62                                  |
| 8         | 229.50                     | 227.00                          | 1.09                                  |
| 9         | 249.50                     | 247.50                          | 0.80                                  |
| 10        | 298.00                     | 293.00                          | 1.68                                  |

Table 6.3: Change from Experimental Undamaged Natural Frequency for Damage Case A

Figure 6.11 is a comparison of the receptance FRF plots of the theoretical undamaged structure against Damage Case A for  $\alpha(1, 1)$ , where  $\alpha(1, 1)$  in this example corresponds to node no. 5 since all nodes with smaller numeral orders have been grounded. With the introduction of damage, the receptance FRF plot can be seen to shift towards the lower frequencies ranges compared to the original undamaged receptance FRF plot. Also it can be seen that the peaks on the experimental receptance FRF plot are not as sharp and defined as the theoretical receptance FRF plot. This is possibility due to noise, numerical errors, structural damping and numerical damping (Ewins, 1984).



**Figure 6.11: Comparison of Experimental against Theoretical Receptance FRF at  $\alpha(1, 1)$  for Damage Case A.**

Figure 6.12a is the corresponding 3D Damage Location Vector plot for Damage Case A between the frequency range of 50Hz – 200Hz with a frequency resolution of 0.5Hz. It must be noted that a frequency resolution of 0.5Hz was chosen so that it would match the frequency resolution of the Bruel & Kjaer frequency analysers. By applying the Damage Detection Algorithm within

this range it was possible to avoid the erroneous experimental results obtained at the beginning frequencies closest to zero hertz.

From Figure 6.12a peaks can be seen to occur between DOF 25 and DOF 55. This suggests that the damage would lie between these DOFs. It should also be noted that since the peaks between DOF 25 and DOF 55 are quite large, smaller peaks due to noise that are existent in other DOFs may not show up clearly.

Reading from the vertical axis the maximum change in stiffness  $[\Delta K]$  can be estimated to be approximately 40000N/m. Using Matlab™ it is possible to investigate further into the DLV to determine the exact location and magnitude of where the maximum changes in stiffness occurs. The maximum magnitude of the stiffness peak was found to be 43088.45N/m and occurred at DOF 43. This represents the largest change in value of elements of the stiffness matrix of approximately 2% from the original undamaged stiffness matrix. This is quiet reasonable as the cut is very small compared to the element surface area. Table 6.4 shows the relative percentage changes from the original stiffness matrix for the DOFs identified in Figure 6.12b. These values are ranked in accordance with maximum magnitude observed from the DLV.

Figure 6.12b is the corresponding 2D CDLV plot for Damage Case A. Here it can be seen that the damage is associated with quite a few DOFs. However the four most predominant DOFs are DOF 28, DOF 31, DOF 40 and DOF 43. These predominant DOFs correspond to element no. 11 and clearly suggest that damage is present at this location. Having taken into account the DOFs that correspond to element no. 11, this leaves approximately 8 DOFs that have a much lesser magnitude than the four predominant DOFs. These DOFs of lower magnitude require some interpretation.

---

| Rank | DOF | Diagonal<br>[K] <sub>UD</sub> at<br>DOF<br>Location<br>N/m | [ΔK] at<br>DOF<br>Location<br>N/m | % Change<br>in Stiffness |
|------|-----|--|-----------------------------------|--------------------------|
| 1    | 43  | 2088791.21   | 43088.45                          | 2.06                     |
| 2    | 40  | 2088791.21   | 39833.78                          | 1.91                     |
| 3    | 28  | 2088791.21   | 32198.13                          | 1.54                     |
| 4    | 31  | 2088791.21   | 29421.32                          | 1.41                     |
| 5    | 16  | 2088791.21   | 11828.22                          | 0.57                     |
| 6    | 19  | 2088791.21   | 11641.64                          | 0.56                     |
| 7    | 46  | 1044395.60   | 10640.49                          | 1.02                     |
| 8    | 55  | 2088791.21   | 10172.46                          | 0.49                     |
| 9    | 34  | 1044395.60   | 10017.76                          | 0.96                     |
| 10   | 25  | 1044395.60   | 9910.17                           | 0.95                     |
| 11   | 52  | 2088791.21   | 9606.97                           | 0.46                     |
| 12   | 37  | 1044395.60   | 8904.05                           | 0.85                     |

**Table 6.4: Change in Stiffness for Damage Case A**

Table 6.5 summarises the remaining smaller magnitude DOFs produced by the 2D CDLV plot in relation to their corresponding node numbers. The corresponding node numbers of the eight smaller magnitude DOFs were then mapped onto the cantilever plate for analysis.

| DOFs No. | Corresponding Node No. |
|----------|------------------------|
| 16       | 10                     |
| 19       | 11                     |
| 25       | 13                     |
| 34       | 16                     |
| 37       | 17                     |
| 46       | 20                     |
| 52       | 22                     |
| 55       | 23                     |

**Table 6.5: Summary of Lower Magnitude DOFs for Damage Case A**

Figure 6.13 shows the experimental test structure with the nodes of the lower magnitude DOFs highlighted in relation to the damage element no. 11. It is interesting to see that the nodes corresponding to the lower magnitude DOFs corresponds to elements that surround the identified

damage element no. 11. This can be interpreted as either smaller damage exists at each of the elements described by the nodes relating to the lower magnitude DOFs or that the damage from element no. 11 is sufficient enough to affect the stiffness in all the surrounding element, thus the appearance of the cross formation. The latter, explanation seems to be more plausible. This also suggests that the initial assumption that a small cut in the centre of an element only affects the stiffness of that element is in fact incorrect.

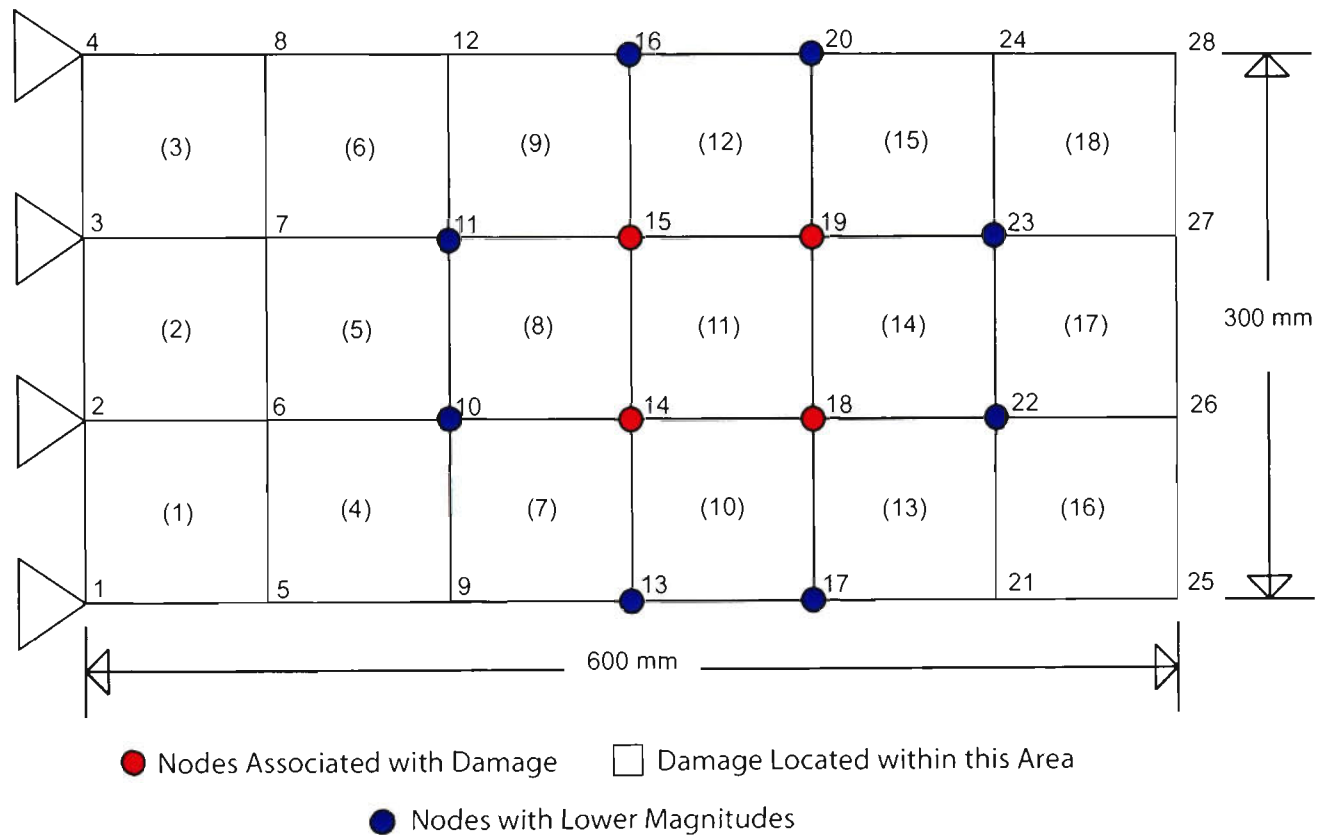
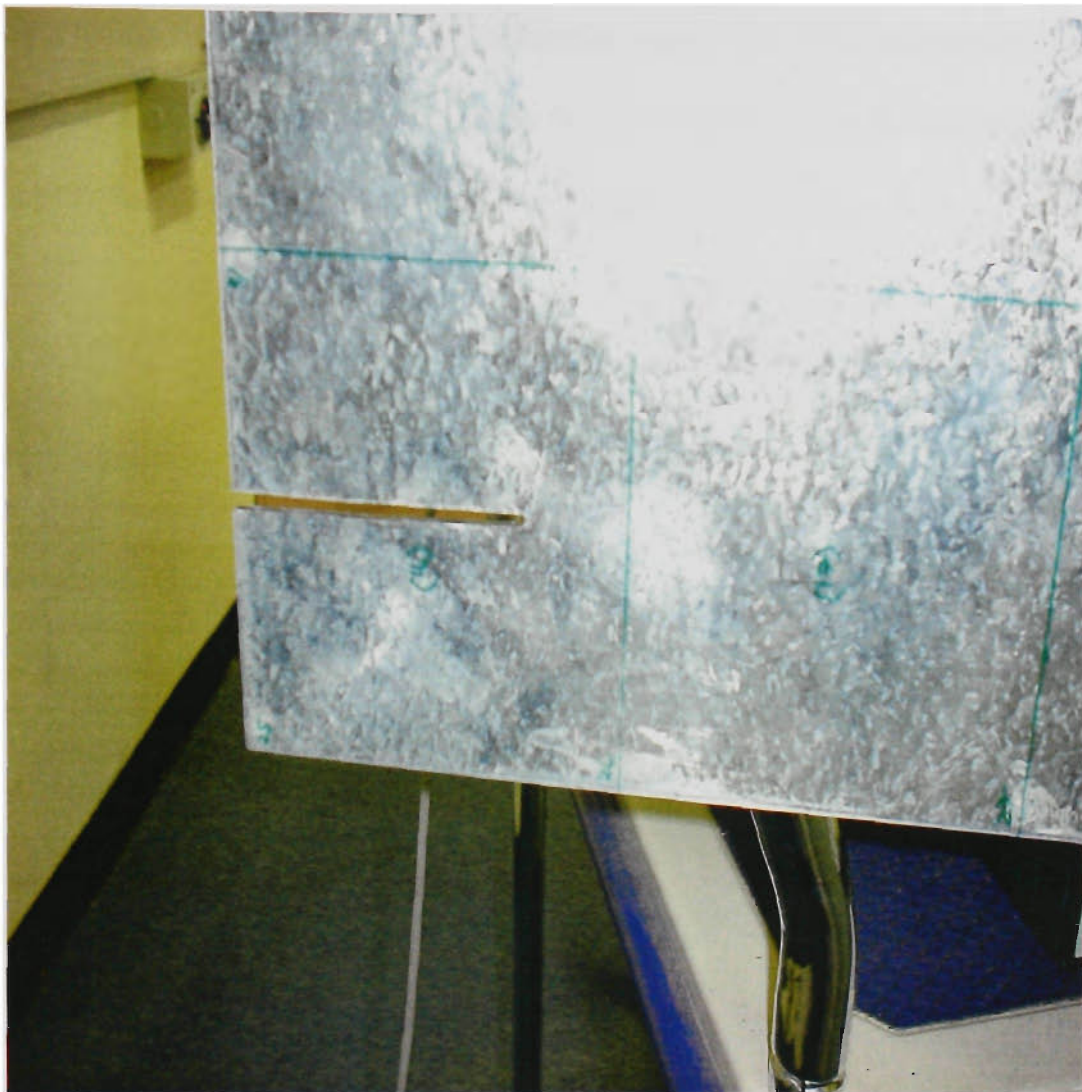


Figure 6.13: Configuration of Lower Magnitude DOFs for Damage Case A

### 6.11 DAMAGE CASE B

Figure 6.14 shows the damage introduced for Damage Case B: Physical damage was introduced to a new equivalent galvanised cantilever plate and can be clearly seen as a straight horizontal cut across element no. 16, affecting nodes no. 21, 22, 25 and 26. This experimental plate was then securely fixed to the large steel frame structure and FRFs data traces were then systematically obtained at each nodal point.



**Figure 6.14: Experimental Setup for Plate28 for Damage Case B**

Table 6.6 is a comparison of natural frequencies obtained from theoretical analysis in the previous chapter against real experimental FRF data for Damage Case B. It can be seen that the experimental natural frequencies correlate closely with the theoretical analysis.

| Modes No. | Matlab (Hz) | ANSYS (Hz) | Experimental (Hz) |
|-----------|-------------|------------|-------------------|
| 1         | 6.83        | 6.83       | Unobtainable      |
| 2         | 29.30       | 29.67      | 29.50             |
| 3         | 42.27       | 42.75      | 41.00             |
| 4         | 94.13       | 96.42      | 93.50             |
| 5         | 120.06      | 119.91     | 112.00            |
| 6         | 179.73      | 184.36     | 172.00            |
| 7         | 181.62      | 187.58     | 185.50            |
| 8         | 232.66      | 235.76     | 222.50            |
| 9         | 245.58      | 255.04     | 242.50            |
| 10        | 294.77      | 311.78     | 272.50            |

**Table 6.6: Natural Frequency of the Cantilever Plate Obtained from Experiment for Damage Case B**

Table 6.7 is a comparison between the experimental undamaged data and the experimental data obtained from Damage Case B. A percentage change between 0% - 8.5% from the undamaged cantilever plate can be seen at various natural frequencies.

| Modes No. | Experimental Undamage (Hz) | Experimental Damage Case B (Hz) | Change from Experimental Undamage (%) |
|-----------|----------------------------|---------------------------------|---------------------------------------|
| 1         | Unobtainable               | Unobtainable                    | NA                                    |
| 2         | 29.50                      | 29.50                           | 0.00                                  |
| 3         | 41.50                      | 41.00                           | 1.20                                  |
| 4         | 95.50                      | 93.50                           | 2.09                                  |
| 5         | 113.50                     | 112.00                          | 1.32                                  |
| 6         | 182.00                     | 172.00                          | 5.49                                  |
| 7         | 185.50                     | 185.50                          | 0.00                                  |
| 8         | 229.50                     | 222.50                          | 3.05                                  |
| 9         | 249.50                     | 242.50                          | 2.80                                  |
| 10        | 298.00                     | 272.50                          | 8.56                                  |

Table 6.7: Change from Experimental Undamage Natural Frequency for Damage Case B

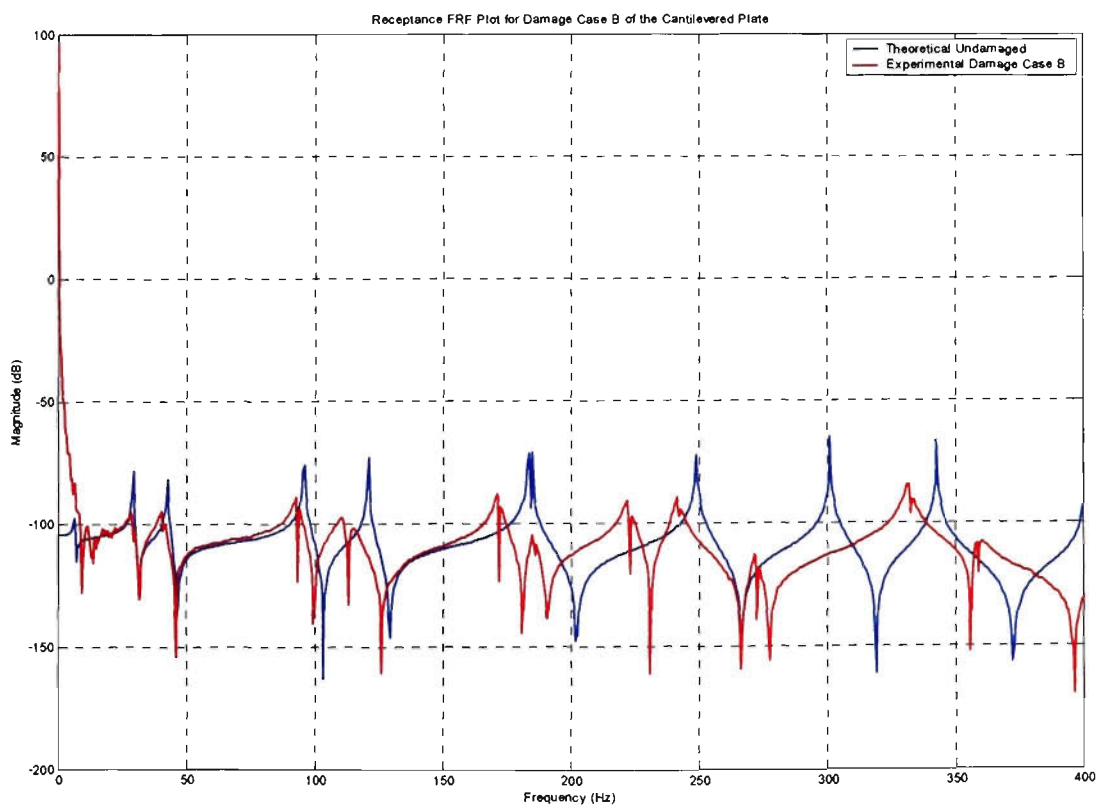


Figure 6.15: Comparison of Experimental against Theoretical Receptance FRF at  $\alpha(1, 1)$  for Damage Case B.

Figure 6.15 is a comparison of the receptance FRF plot of the theoretical Undamaged Case against the receptance FRF plot of Damage Case B for  $\alpha(1, 1)$ , where  $\alpha(1, 1)$  for this example corresponds to node no. 5 and is the same location as in Damage Case A. The effect of introducing the simulated Damage Case B can be seen to affect the higher end of the frequency trace while leaving the lower end of the frequency trace unchanged.

Figure 6.16a is the corresponding 3D Damage Location Vector plot for Damage Case B between the frequencies of 50Hz – 200Hz with a frequency resolution of 0.5Hz. By applying the Damage Detection Algorithm within this range it was possible to avoid the erroneous experimental results obtained at the beginning frequencies close to zero hertz.

From Figure 6.16a peaks can be seen to occur between DOF 35 and DOF 55. This suggests that the damage would lie between these DOFs. It should also be noted that since the peaks between DOF 35 and DOF 55 are quite large, smaller peaks that are existent in other DOFs may not show up clearly.

Reading from the vertical axis the maximum change in stiffness  $[\Delta K]$  can be estimated to be approximately 50000N/m. Using Matlab™ it is possible to investigate further into the DLV to determine the exact location and magnitude of where the maximum change in stiffness occurs. The magnitude of the maximum stiffness peak was found to be DOF 61 with a stiffness of 50770.28N/m. This represented a change in stiffness from the original undamaged stiffness matrix of approximately 9.72%. This suggested that the cut introduced on the cantilever plate as controlled damage causes approximately 9.72% in stiffness change to elements of the stiffness matrix of the plate structure. Table 6.8 shows the relative percentage changes from the original

---

stiffness matrix for the DOFs identified in Figure 6.16b. These values are ranked in accordance with maximum magnitude observed from the DLV.

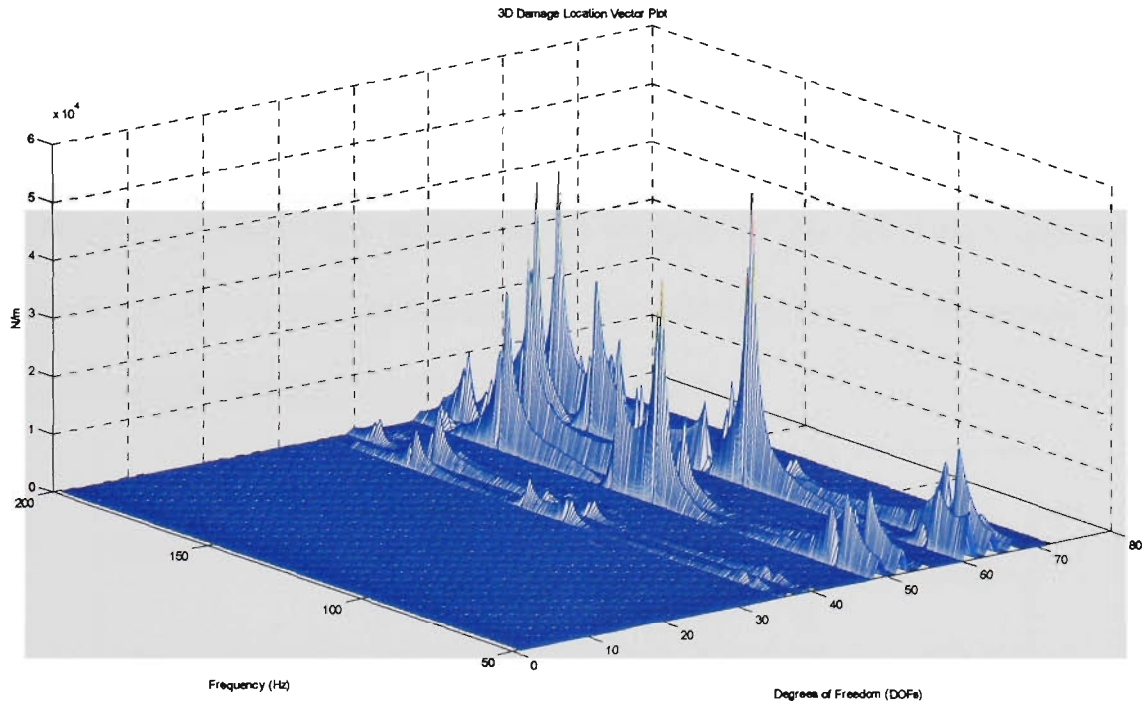


Figure 6.16a: 3D DLV Plot for Damage Case B

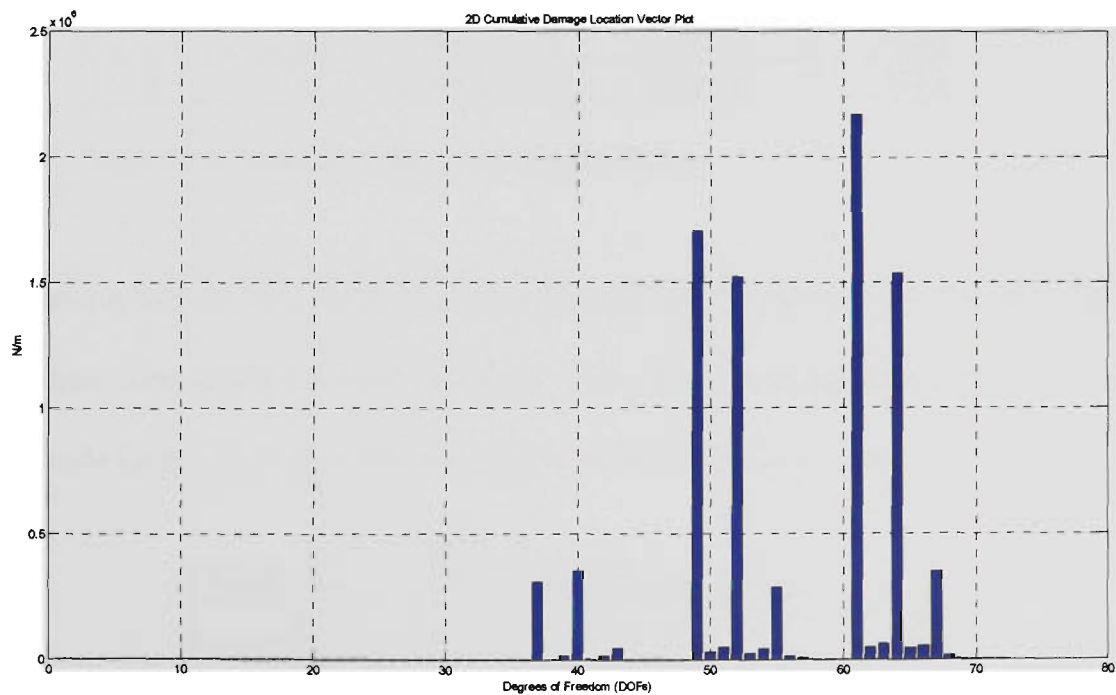


Figure 6.16b: 2D CDLV Plot for Damage Case B

Figure 6.16b is the corresponding 2D CDLV plot for Damage Case B. Here the DOFs that are associated with damage can clearly be seen. It also can clearly be seen that there are quite a few DOFs that show an indication of damage. However, one can see that there are at least 4 predominant DOFs whose magnitudes are larger than the rest of the DOFs. These predominant DOFs are DOF 49, 52, 61 and 64. These DOFs correspond to node nos. 21, 22, 25 and 26, which describes element no. 16 and clearly suggest that damage is present at this location. Having taken into account the DOFs that correspond to element no. 16, this leaves approximately 4 DOFs that have a much lower magnitude than the four DOFs that describe element no. 16. These lower magnitude DOFs have been summarised in Table 6.8.

| Rank | DOF | Diagonal<br>[K] <sub>UD</sub> at<br>DOF<br>Location<br>N/m | [ΔK] at<br>DOF<br>Location<br>N/m | % Change<br>in Stiffness |
|------|-----|--|-----------------------------------|--------------------------|
| 1    | 61  | 522197.80  | 50770.28                          | 9.72                     |
| 2    | 64  | 1044395.60   | 41252.25                          | 3.95                     |
| 3    | 49  | 1044395.60   | 38724.14                          | 3.71                     |
| 4    | 52  | 2088791.21   | 32462.55                          | 1.55                     |
| 5    | 40  | 2088791.21   | 9475.50                           | 0.45                     |
| 6    | 67  | 1044395.60   | 7895.62                           | 0.76                     |
| 7    | 55  | 2088791.21   | 6851.95                           | 0.33                     |
| 8    | 37  | 1044395.60   | 6705.59                           | 0.64                     |

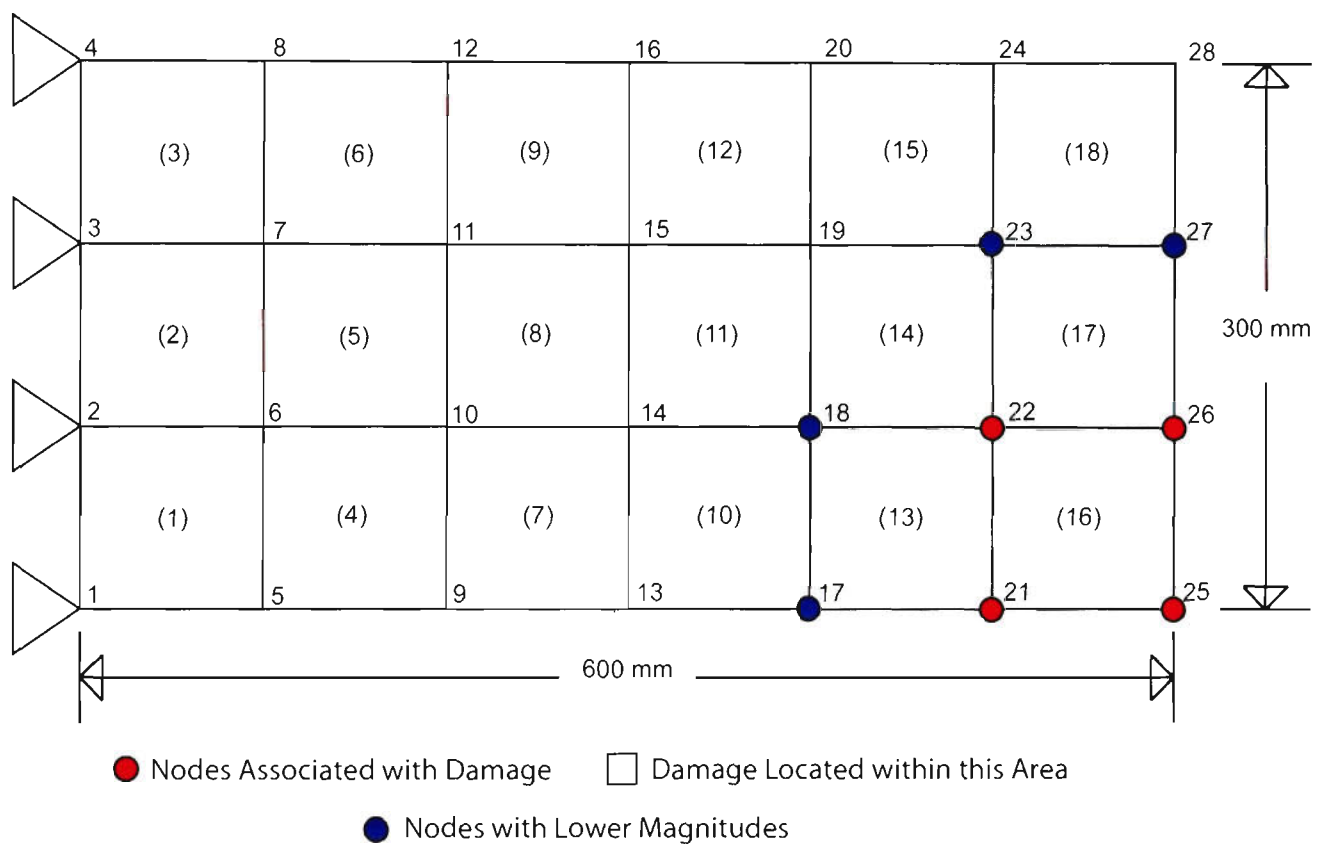
**Table 6.8: Change in Stiffness for Damage Case B**

Table 6.9 summarises the remaining lower magnitude DOFs produced by the 2D CDLV plot in relation to their corresponding node numbers. The corresponding node numbers of the four lower magnitude DOFs were then mapped on the cantilever plate for analysis.

| DOFs No. | Corresponding Node No. |
|----------|------------------------|
| 37       | 17                     |
| 40       | 18                     |
| 55       | 23                     |
| 67       | 27                     |

**Table 6.9: Summary of Lower Magnitude DOFs for Damage Case B**

Figure 6.17 is the experimental test structure with the nodes of the lower magnitude DOFs plotted in relation to damage element no. 16. It is interesting to see that the nodes of the lower magnitude DOFs correspond to elements that surround the identified damage element no. 16. This can be interpreted as either damage exists at each element described by these lower magnitude DOFs or that the damage from element no. 16 is sufficient enough to also affect the stiffness of the surrounding elements. The latter explanation seems to be more plausible.



**Figure 6.17: Configuration of Lower Magnitude DOFs for Damage Case B**

## 6.12 DAMAGE CASE C

Figure 6.18 shows the experimental setup for Damage Case C. Damage Case C attempts to simulate multiple damage locations within the cantilever plate. Once again, a diagonal cut similar to Damage Case A was introduced to element no. 11 and a horizontal cut similar to

Damage Case B was introduced to element no. 16 of the experimental cantilever plate and can clearly be seen in Figure 6.18.



**Figure 6.18: Experimental Setup for Damage Case C**

The experimental plate was then securely fixed to the large steel frame and FRFs data traces were obtained by systematically impacting each node at any one time with the impact hammer. Although only one column of FRFs data was required, three sets of FRFs data were obtained for different locations of the accelerometer which were node no. 5, node no. 10 and node no. 19.

These nodal locations were chosen randomly. An average of five FRF data traces were taken for each node location.

Table 6.10 is a comparison of natural frequencies obtained from theoretical analysis in the previous chapter compared with real experimental FRF data for Damage Case C. It can be seen that the experimental data correlates closely with the theoretical analysis.

| Modes No. | Matlab (Hz) | ANSYS (Hz) | Experimental (Hz) |
|-----------|-------------|------------|-------------------|
| 1         | 6.79        | 6.80       | Unobtainable      |
| 2         | 28.84       | 29.20      | 28.50             |
| 3         | 41.49       | 41.49      | 40.50             |
| 4         | 92.73       | 94.94      | 91.00             |
| 5         | 118.53      | 118.35     | 112.00            |
| 6         | 173.41      | 176.40     | 168.50            |
| 7         | 178.22      | 185.49     | 182.00            |
| 8         | 230.07      | 233.00     | 238.00            |
| 9         | 240.97      | 250.29     | 269.00            |
| 10        | 291.81      | 307.95     | 328.50            |

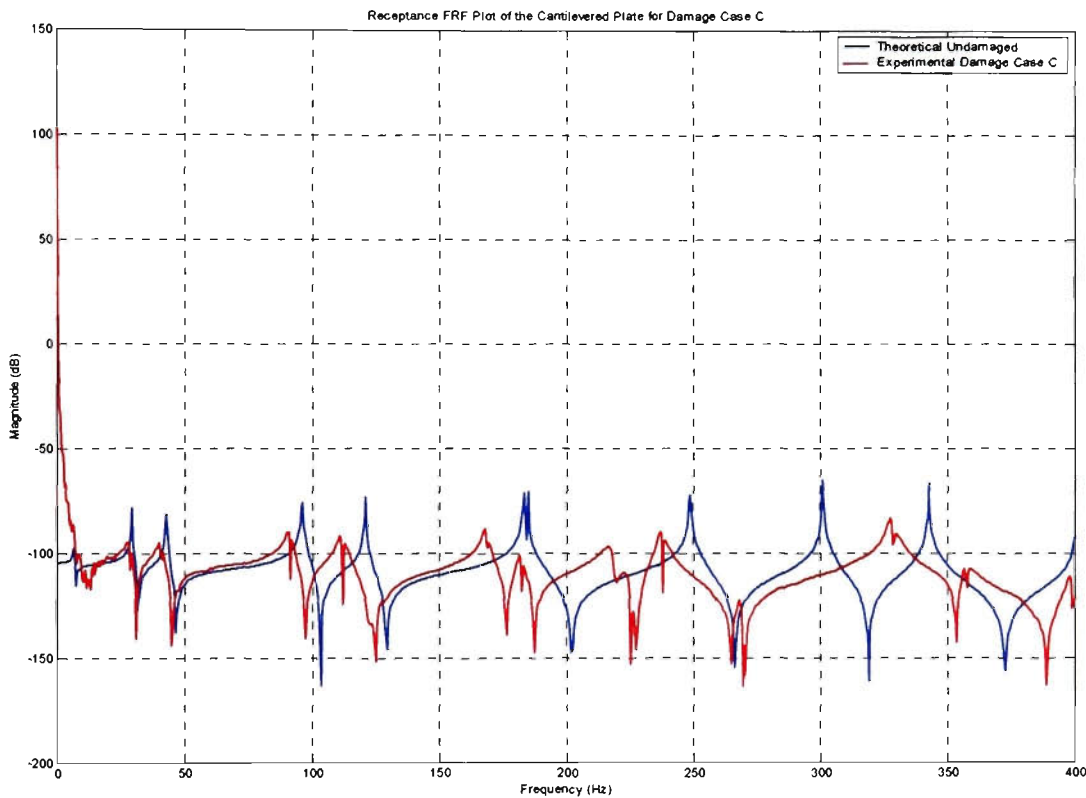
**Table 6.10: Natural Frequency of the Cantilever Plate Obtained from Experiment for Damage Case C**

Table 6.11 is a comparison between the experimental undamaged data and the experimental data obtained from Damage Case C. A percentage change between 1.3% - 10.3% from the undamaged cantilever plate can be seen at various natural frequencies.

| Modes No. | Experimental Undamage (Hz) | Experimental Damage Case C (Hz) | Change from Experimental Undamage (%) |
|-----------|----------------------------|---------------------------------|---------------------------------------|
| 1         | Unobtainable               | Unobtainable                    | NA                                    |
| 2         | 29.50                      | 28.50                           | 3.39                                  |
| 3         | 41.50                      | 40.50                           | 2.41                                  |
| 4         | 95.50                      | 91.00                           | 4.71                                  |
| 5         | 113.50                     | 112.00                          | 1.32                                  |
| 6         | 182.00                     | 168.50                          | 7.42                                  |
| 7         | 185.50                     | 182.00                          | 1.89                                  |
| 8         | 229.50                     | 238.00                          | 3.70                                  |
| 9         | 249.50                     | 269.00                          | 7.82                                  |
| 10        | 298.00                     | 328.50                          | 10.23                                 |

**Table 6.11: Change from Experimental Undamage Natural Frequency for Damage Case C**

Figure 6.19 is a comparison of the receptance FRF plot of the theoretical Undamaged Case against Damage Case C for  $\alpha(1, 1)$ , where  $\alpha(1, 1)$  for this case is still node no. 5 and is the same location as in all previous damage scenarios. It can be seen that the combination of multiple damage location has caused the frequency shifts to be much greater as shown in Table 6.11 and Figure 6.19.



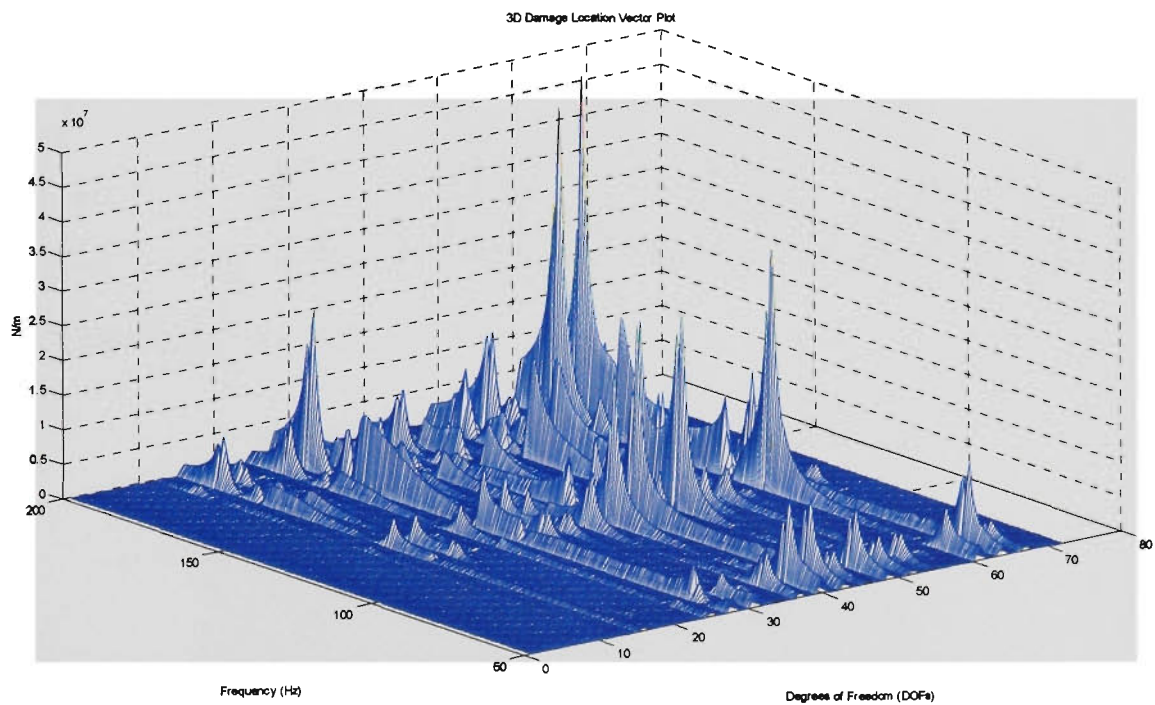
**Figure 6.19: Comparison of Experimental against Theoretical Receptance FRF at  $\alpha(1, 1)$  for Damage Case C**

Figure 6.20a is the corresponding 3D Damage Location Vector plot for Damage Case C between the frequencies of 50Hz – 200Hz with a frequency resolution of 0.5Hz. By applying the Damage Detection Algorithm within this range it was possible to avoid the erroneous experimental results obtained at the beginning frequencies closest to zero hertz.

From Figure 6.20a peaks can be seen to occur between DOF 25 and DOF 65. This suggests that damage would lie between these DOFs. Since the node connectivity has been preserved and the

DOFs are in relation to each node, it is possible to conclude from the 3D Damage Location Vector plot that more than one damage location exists due to such a broad range.

Reading from the vertical axis the maximum magnitude corresponding to the change in stiffness  $[\Delta K]$  can be estimated to be approximately 50000N/m. Using Matlab™ it is possible to investigate further into the DLV to determine the exact location and magnitude of where the maximum change in stiffness occurs. The magnitude of the change in stiffness was found to be 46863.71N/m and occurred at DOF 61. The change in stiffness at DOF 61 from the original is approximately 8.97%.



**Figure 6.20a: 3D DLV Plot for Damage Case C**

Figure 6.20b is the corresponding 2D CDLV plot for Damage Case C. Here it is evident that multiple damage location may exist within this structure. Care is required for analysis of multiple damage locations. The easiest and simplest method to analyse this 2D CDLV plot is to firstly rank the DOFs from highest value to lowest value as shown in Table 6.12. The first seven values have been identified as possible damage locations since their values are much greater than

the rest of the DOFs. Table 6.12 also shows the corresponding node numbers in relation to the DOFs. Once the highest and lowest DOFs have been ranked and their node numbers identified, it is just a simple case of mapping these damage locations to the experimental test piece. This is shown in Figure 6.21.

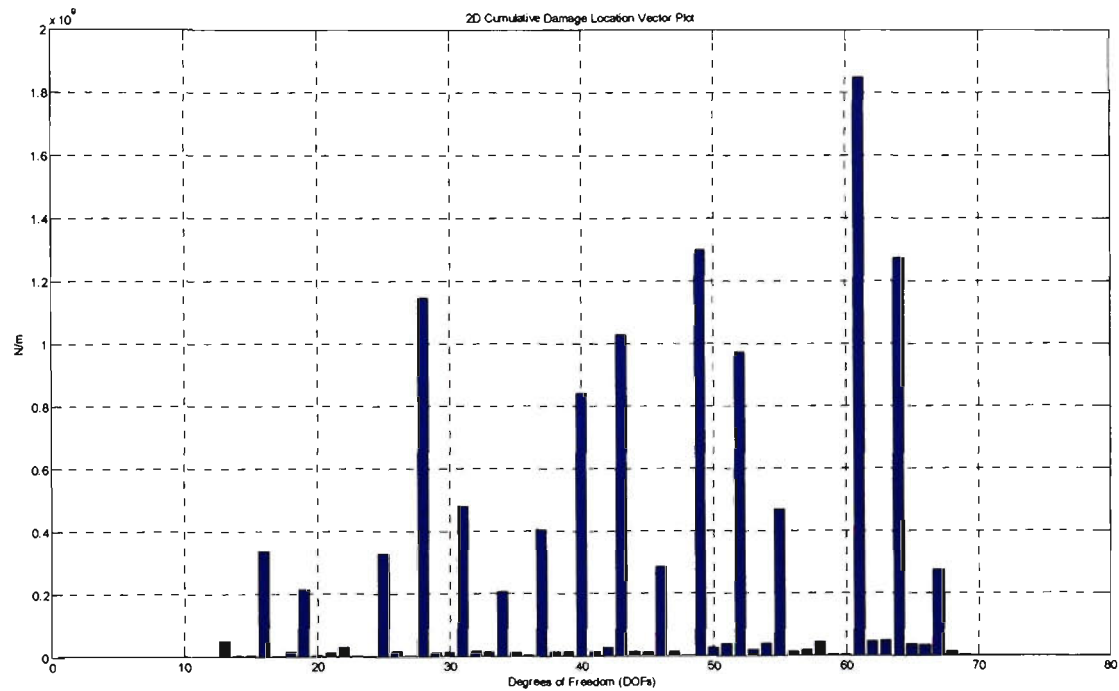


Figure 6.20b: 2D CDLV Plot for Damage Case C

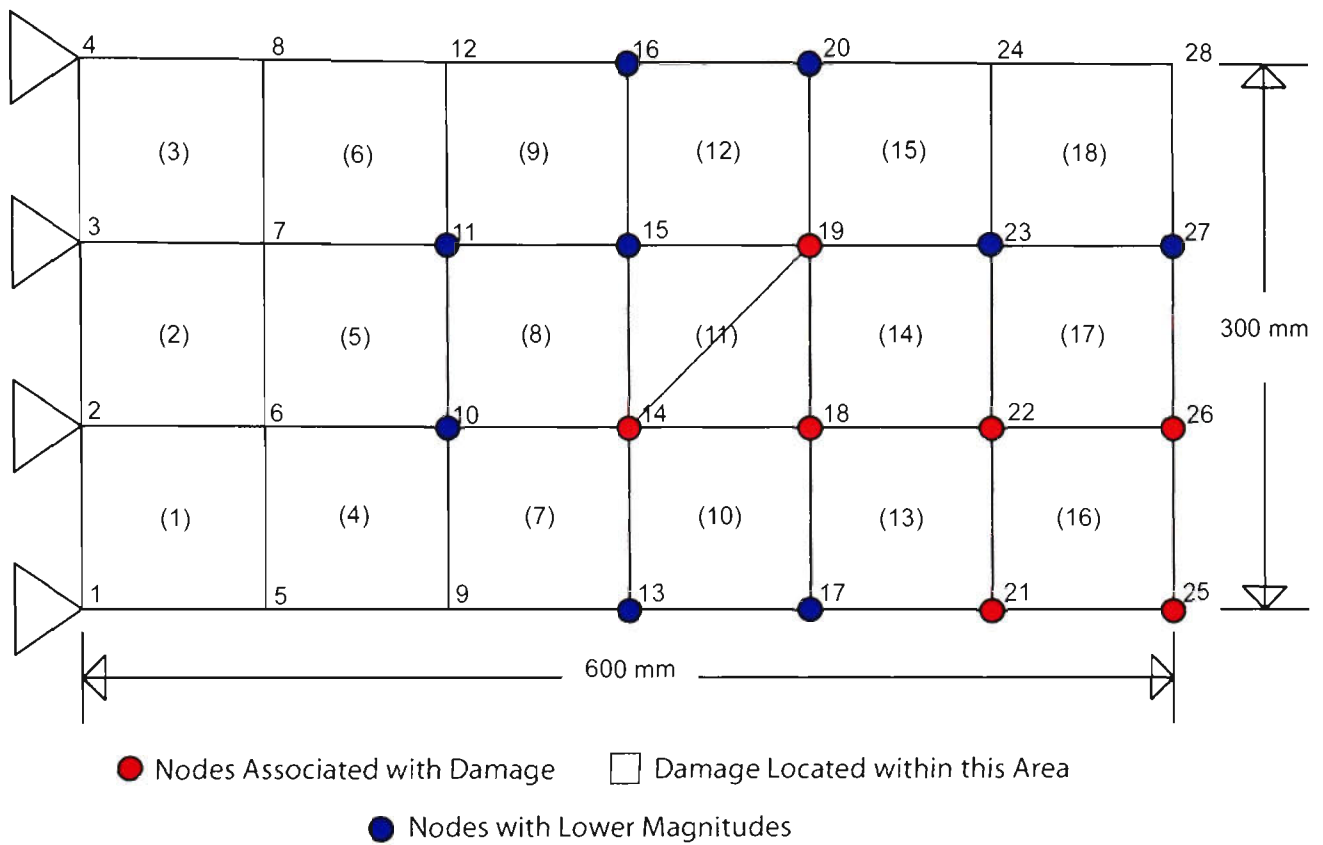
| Rank No. | DOFs No. | Corresponding Node No. |
|----------|----------|------------------------|
| 1        | 61       | 25                     |
| 2        | 49       | 21                     |
| 3        | 64       | 26                     |
| 4        | 28       | 14                     |
| 5        | 43       | 19                     |
| 6        | 52       | 22                     |
| 7        | 40       | 18                     |
| 8        | 31       | 15                     |
| 9        | 55       | 23                     |
| 10       | 37       | 17                     |
| 11       | 16       | 10                     |
| 12       | 25       | 13                     |
| 13       | 46       | 20                     |
| 14       | 67       | 27                     |
| 15       | 19       | 11                     |
| 16       | 34       | 16                     |

Table 6.12: Rank of DOFs from the 2D CDLV Plot for Damage Case C

Figure 6.21 is the experimental cantilever plate with the DOFs from the 2D CDLV for Damage Case C mapped. The first 7 DOFs that have been identified as damage locations have been mapped in red and the remaining DOFs have been mapped in blue. With the DOFs so mapped, Figure 6.21 clearly shows that damage exists at element no. 16. It can also be said that damage co-exist at element no. 11, even though only 3 of the DOFs have been identified, since it was previously assumed that damage would affect all found nodes of an element.

Inspection of Figure 6.21 shows that element no. 14 may also contain damage. However, on closer inspection and interpretation, it can be concluded with certainty that element no. 14 does not contain any damage. This is because the magnitude of the DOFs describing element no. 14 from Table 6.10 can be seen to be ranked 5<sup>th</sup>, 6<sup>th</sup> and 7<sup>th</sup>. If element no. 14 indeed does contain damage then it is expected that the magnitude of the DOFs describing element no. 14 to be much larger, since some nodes are shared with element no. 11 and element no. 16 which both contain damage. Therefore the magnitude of the overall shared DOFs would be much larger since damage would have an effect on each of the shared DOFs.

The lower magnitude DOFs are mapped in blue on Figure 6.19 and can be observed to follow similar behaviour as noted in Damage Case A and Damage Case B. It should also be noted that the Damage Detection Algorithm detected the simulated damages in the cantilever plate successfully and did not detect any other damage that was not implanted. It should also be noted that no damage was detected for element no. 1, 2 and 3 as expected.



**Figure 6.21: Configuration of Lower Magnitude DOFs for Damage Case C**

### 6.13 DISCUSSION

The developed damage detection was found to be extremely robust in detecting the simulated damage in a real structure for single damage scenarios. The Damage Detection Algorithm was also successful in detecting multiple damage locations, however care should be exercised in interpreting the results produced from the Damage Detection Algorithm. It must be noted that it was difficult to utilise the full FRF data spectrum due to the erroneous results obtained at the initial frequency closest to zero hertz. Hence only data from 50Hz – 200Hz at a frequency resolution of 0.5Hz was used in this section of the thesis.

# CHAPTER 7

## CONCLUSIONS

The main aim of this thesis was to investigate the performance of a damage detection method called “Damage Detection Algorithm”, which utilises measured FRF data to locate the existence of damage in a structure.

The DDA was firstly tested using simulated FRF data on a simple 12 DOF mass spring system. It was found to be extremely efficient for cases where there is no coordinate incompatibility. DDA is able to locate simulated damage even when 5% simulated normalised random noise was introduced into the simulated FRF data. For cases where there is coordinate incompatibility DDA is still able to detect the simulated damage within the mass spring system, however it can only locate damage to the extent of elements defined by measured constraints. It requires further data within this area to pinpoint damage. (Chapter 3, Section 3.3)

The DDA was found to be successful in locating the damage within the NASA eight bay space truss structure. Again, DDA proved to be extremely robust, in that it is able to detect successfully the location of the simulated damage even with 5% simulated normalised random noise introduced to the simulated FRF data. It is also able to accurately detect the damage location for multiple damages. For cases that involved coordinate incompatibility DDA is able to indicate successfully the area where damage may exist and these locations were consistent with the location of simulated damage. (Chapter 4, Section 4.6, Figure 4.16 and Figure 4.16b).

---

The developed Damage Detection Algorithm was found to be capable of locating simulated damage within a thin flat plate structure including multiple damages. (Chapter 5, Section 5.8, Figure 5.15a and Figure 5.15b)

The DDA also proved to be capable of detecting real damage from a plate structure using measured FRFs data, for single and multiple damage locations. (Chapter 6, Section 6.12, Figure 6.20a, Figure 6.20b and Figure 6.21)

In order to make DDA applicable to a general engineering structure the following areas need further studies:

- A better measure of the amount of damage in a structure
  - The smallest amount of damage that can be detected by DDA.
  - The number of multiple damage locations that can be detected by DDA.
  - To study the effects of gradually increasing the amount of noise interference until the Damage Detection Algorithm ceases to detect damage.
  - To study the effects of different extents of coordinate incompatibility and of different types of DOFs incompatibility on the success of DDA.
-

- 
- To study the effects of varying the frequency resolution of the FRF data on the performance of DDA, with the objective of finding the optimum frequency resolution and the optimum frequency.
  - To study the effects of non-linearity on DDA.
  - To study the performance of DDA on more complex hybrid structures consisting of truss, beam, plate and shell elements with damping.
  - To integrate all steps of the algorithm including numerical processing and graphical display into a compact program that will allow users to easily interpret the results.
-

- Baruch M. and Bar Itzhack I. Y.**, “Optimal Weighted Orthogonalisation of Measured Modes”, 1978, AIAA Journal, Vol. 16, No. 4, pp. 346 – 351.
- Berman A. and Flannelly W. G.**, “Theory of Incomplete Models of Dynamic Structures”, 1971, AIAA Journal, Vol. 9, No. 8, pp. 1481 – 1487.
- Berman A. and Nagy E. J.**, “Improvement of a Large Analytical Model Using Test Data”, 1983, AIAA Journal, Vol. 21, No. 8, pp. 1168 – 1173.
- Brock J. E.**, “Optimal Matrices Describing Linear Systems”, 1968, AIAA Journal, Vol. 6, No. 7, pp. 1292 – 1296.
- Cawley P. and Adams R. D.**, “The Location of Defects in Structures from Measurement of Natural Frequencies”, 1979, Journal of Strain Analysis, Vol. 14, No. 2, pp. 49 – 57.
- Chen J. C. and Garba J. A.**, “On-Orbit Damage Assessment for Large Space Structures”, 1988, AIAA Journal, Vol. 26, No. 9, pp. 1119 – 1126.
- Choudhury A. R.**, “Damage Detection of Truss Structures Using Measured Frequency Response Function Data”, 1996, Ph. D Thesis, Department of Mechanical Engineering, Victoria University of Technology, Melbourne, Australia.
- Choudhury A. R. and He J.**, “Identification of Analytical Model Error Using Incomplete Measured Frequency Response Function Data”, 1993, Proceedings of the Asia-Pacific Vibration Conference, Japan, pp. 667 – 682.
-

**Doebling S. W., Hemez F. M., Paterson L. D. and Farhat C.**, “Improved Damage Location Accuracy Using Strain Energy-Based Mode Selection Criteria”, 1997, AIAA Journal, Vol. 35, No. 4, pp. 693 – 699.

**Doebling, S. W., Farrar, C. R., Prime, M. B., and Shevitz, D. W.**, “Damage Identification and Health Monitoring of Structural and Mechanical Systems from Changes in Their Vibration Characteristics: A Literature Review”, 1996, Los Alamos National Laboratory, New Mexico, USA.

**Ewins D. J.**, “Modal Analysis: Theory and Practice”, 1984, Research Studies Press. Hertfordshire, England.

**Friswell M. I., Penny J. E. T. and Wilson D. A. L.**, “Using Vibration Data and Statistical Measures to Locate Damage In Structures”, 1994, Modal Analysis: The International Journal of Analytical and Experimental Modal Analysis, Vol. 9, No. 4, pp. 239 – 254.

**Guyan R. J.**, “Reduction of Stiffness and Mass Matrices”, 1965, AIAA Journal, Vol. 3, No. 2, pp. 380 – 385.

**Haug E. J. and Choi K. K.**, “Structural Design Sensitivity Analysis with Generalised Global Stiffness and Mass Matrices”, 1984, AIAA Journal, Vol. 22, No.9, pp. 1229 – 1303.

**Kabe A. M.**, “Stiffness Matrix Adjustment Using Mode Data”, AIAA Journal, Vol. 23, No. 9, pp. 1431 – 1436.

---

**Kaouk M.**, “Structural Damage Assessment and Finite Element Model Refinement Using Measured Modal Data”, 1993, Department of Aerospace Engineering, Mechanics and Engineering Science, University of Florida, USA.

**Kidder R. L.**, “Reduction of Structural Frequency Equations”, 1973, AIAA Journal, Vol. 11, No. 6, pp. 892.

**Krammer D. C.**, “Optimum Approximation for Residual Stiffness in Linear System Identification”, 1988, AIAA Journal, Vol. 26, No. 1, pp. 104 – 112.

**Lieven N. A. J. and Ewins D. J.**, “Spatial Correlation of Mode Shape, the Coordinate Modal Assurance Criterion (COMAC)”, 1998, Proceedings of the 6<sup>th</sup> International Modal Analysis Conference, Kissimmee, Florida, pp. 690 – 695.

**Lieven N. A. J and Ewins D. J.**, “Expansion of Modal Data for Correlation”, 1990, Proceedings of the 8<sup>th</sup> International Modal Analysis Conference, pp. 605 – 609.

**Lim T. W.**, “Structural Damage Detection Using Modal Test Data”, 1991, AIAA Journal, Vol. 29, No. 12, pp. 2271 – 2274.

**Lim T. W. and Kashangaki T. A. L.**, “Structural Damage Detection of Space Truss Structure Using Best Achievable Eigenvectors”, 1994, AIAA Journal, Vol. 32, No. 5, pp. 1049 – 1057.

---

**O'Callahan J., Avitable P. and Riemer R.**, "System Equivalent Reduction Expansion Process (SEREP)", 1989, Proceedings of the 7<sup>th</sup> International Modal Analysis Conference, Las Vegas, Nevada, pp. 29 – 37.

**Przemieniecki J. S.**, "Theory of Matrix Structural Analysis", 1967, McGraw-Hill, New York, USA.

**Rodden W. P.**, "A Method for Deriving Structural Influence Coefficients from Ground Vibration Test", 1967, AIAA Journal, Vol. 5. No. 5, pp. 991 – 1000.

**Tran D. and He J.**, "Structural Damage Detection in a Simple Cantilever Plate", 1998, Proceedings of the 16<sup>th</sup> International Modal Analysis Conference, Santa Barbara, CA, USA, pp. 369 – 374.

**Tran D., He J., and Choudhury A. R.**, "Damage Detection of Truss Structures Using Measured FRF data", 1997, Proceedings of the 15<sup>th</sup> International Modal Analysis Conference, Orlando, USA, pp. 961 – 967.

**Zimmerman D. C., Abdalla M. and Grigoriadis K. M.**, "Enhanced Damage Detection Using Linear Matrix Inequalities", 1998, Proceedings of the 16<sup>th</sup> International Modal Analysis Conference, Santa Barbara, CA, USA, pp. 144 – 150.

**Zimmerman D. C. and Kauok M.**, "Structural Damage Detection Using a Minimum Rank Update Theory", 1994, Journal of Vibration and Acoustics, Vol. 116, pp. 222 – 231.

---

**APPENDIX 1: DAMAGE DETECTION ALGORITHM WRITTEN IN MATLAB™**

```

%Damage Detection Program V1.0
%For Problems with and without Coordinate Incompatibility
%Incorporating Kidders Expansion Method, which rearranges the mass and
%stiffness matrix as per points for which measurement have been taken.
%The matrix is then expanded and arranged back to original order.
%Random Errors have been implemented
%M-File Name=DAMAGEDETECT.m
%Last Updated=10/08/2002
%Files Required By this Program
% *.USM <= Undamaged Stiffness Matrix File in the form of ASCII delimited
% *.DSM <= Damaged Stiffness Matrix File in the form of ASCII delimited
% *.MAS <= Mass Matrix File in the form of ASCII delimited
% *.AIM <= Measured Coordinates File in the form of ASCII delimited
% SORT.M <= Matlab file required for Matrix Sorting/Manipulation
% INSN.M <= Matlab file generating random numbers
%%%%%%%%%%%%%%%%%%%%%%%%%%%%%%%%%%%%%%%%%%%%%%%%%%%%%%%%%%%%%%%%%%%%%%%%
clear all;
format long;

%Input
NN=input('Please enter the number of nodes (DOFs) :');
if NN <= 0
    error('DOFs must be greater than 0')
end
NCOOR=input('Please enter the number of measured coordinates : ');
if NCOOR <= 0
    error('Number of Measured Coordinates must be greater than 0')
elseif NCOOR > NN
    error('Number of Measured Coordinates cannot be greater than Number of DOFs')
end
NFREQ1=input('Please enter the first frequency (Hz) :');
if NFREQ1 < 0
    error('Initial frequency must be greater 0')
end
NFREQ2=input('Please enter the last frequency (Hz) :');
if NFREQ2 <= NFREQ1
    error('Last frequency must be larger than first frequency');
end
FREQRES=input('Please enter the Frequency Resolution (Delta F) :');
if FREQRES <= 0
    error('Frequency Resolution must be greater than 0');
end
ERR=input('Please enter the amount of random error to include (%) :');
if ERR < 0
    error('Random errors must be greater or equal to 0%')
elseif ERR > 100
    error('Random errors cannot be greater than 100%')
end
%RECEPT=input('Please enter the node number to obtain RAW FRF trace :');
RECEPT=1;

%Calculating Number of Points Required
NPOINTS=(NFREQ2-NFREQ1)/FREQRES)+1;

>Loading the Undamaged Stiffness Matrix
STIFFU1=input('Please enter the Undamaged Stiffness Matrix filename (*.USM) :','s');
STIFFU=DLMREAD(STIFFU1);
clear STIFFU1;

```

```
%Loading the Damaged Stiffness Matrix
STIFFD1=input('Please enter the Damaged Stiffness Matrix filename (*.DSM) : ','s');
STIFFD=DLMREAD(STIFFD1);
clear STIFFD1;

%Loading the Mass Matrix
MASS1=input('Please enter the Mass Matrix filename (*.MAS) : ','s');
MASS=DLMREAD(MASS1);
clear MASS1;

%Writing ModeShapes
a=modal(MASS,STIFFU);
b=modal(MASS,STIFFD);
for i=1:NN;
    fid=fopen('MODESHAPE.TXT','A');
    fprintf(fid,'%d %6.2f %6.2f\n',i,b(1,i),a(1,i));
    fclose(fid);
end
```

---

**APPENDIX 2: EQUIVALENT CONCENTRATED NODAL MASS THE NASA 8  
BAY TRUSS STRUCTURE**

| Nodes Per Similar Mass Configuration For the NASA 8-Bay Truss Structure |          |          |           |           |           |
|---|----------|----------|-----------|-----------|-----------|
| 77.1 (g)  | 88.1 (g) | 98.3 (g) | 104.8 (g) | 109.3 (g) | 168.4 (g) |
| Node 2  | Node 34  | Node 1   | Node 5    | Node 33   | Node 6    |
| Node 4  | Node 36  | Node 3   | Node 7    | Node 35   | Node 8    |
|   |          |          | Node 10   |           | Node 9    |
|   |          |          | Node 12   |           | Node 11   |
|   |          |          | Node 13   |           | Node 14   |
|   |          |          | Node 15   |           | Node 16   |
|   |          |          | Node 18   |           | Node 17   |
|   |          |          | Node 20   |           | Node 19   |
|   |          |          | Node 21   |           | Node 22   |
|   |          |          | Node 23   |           | Node 24   |
|   |          |          | Node 26   |           | Node 25   |
|   |          |          | Node 28   |           | Node 27   |
|   |          |          | Node 29   |           | Node 30   |
|   |          |          | Node 31   |           | Node 32   |

### APPENDIX 3: MASS CALCULATION PER NODE FOR THE NASA 8 BAY TRUSS STRUCTURE

| <b>NODE 1</b>      |                                   |        |
|--------------------|-----------------------------------|--------|
| 1 x Node Ball      | 5.8 g                             | 5.8 g  |
| 3 x Longeron       | $\frac{3 \times 18 \text{ g}}{2}$ | 27 g   |
| 2 x Diagonal       | $\frac{2 \times 27 \text{ g}}{2}$ | 27 g   |
| 5 x Joint Assembly | 5 x 7.7 g                         | 38.5 g |
| 0 x Triax + Block  | 0                                 | 0      |
|                    | Total                             | 98.3 g |

| <b>NODE 2</b>      |                                   |        |
|--------------------|-----------------------------------|--------|
| 1 x Node Ball      | 5.8 g                             | 5.8 g  |
| 3 x Longeron       | $\frac{3 \times 18 \text{ g}}{2}$ | 27 g   |
| 1 x Diagonal       | $\frac{1 \times 27 \text{ g}}{2}$ | 13.5 g |
| 4 x Joint Assembly | 4 x 7.7 g                         | 30.8 g |
| 0 x Triax + Block  | 0                                 | 0      |
|                    | Total                             | 77.1 g |

| <b>NODE 5</b>      |                                   |         |
|--------------------|-----------------------------------|---------|
| 1 x Node Ball      | 5.8 g                             | 5.8 g   |
| 4 x Longeron       | $\frac{4 \times 18 \text{ g}}{2}$ | 36 g    |
| 1 x Diagonal       | $\frac{1 \times 27 \text{ g}}{2}$ | 13.5 g  |
| 5 x Joint Assembly | 5 x 7.7 g                         | 38.5 g  |
| 1 x Triax + Block  | 1 x 11 g                          | 11 g    |
|                    | Total                             | 104.8 g |

| <b>NODE 6</b>      |                                   |         |
|--------------------|-----------------------------------|---------|
| 1 x Node Ball      | 5.8 g                             | 5.8 g   |
| 4 x Longeron       | $\frac{4 \times 18 \text{ g}}{2}$ | 36 g    |
| 4 x Diagonal       | $\frac{4 \times 27 \text{ g}}{2}$ | 54 g    |
| 8 x Joint Assembly | 8 x 7.7 g                         | 61.6 g  |
| 1 x Triax + Block  | 1 x 11 g                          | 11 g    |
|                    | Total                             | 168.4 g |

| <b>NODE 33</b>     |                                   |         |
|--------------------|-----------------------------------|---------|
| 1 x Node Ball      | 5.8 g                             | 5.8 g   |
| 3 x Longeron       | $\frac{3 \times 18 \text{ g}}{2}$ | 27 g    |
| 2 x Diagonal       | $\frac{2 \times 27 \text{ g}}{2}$ | 27 g    |
| 5 x Joint Assembly | 5 x 7.7 g                         | 38.5 g  |
| 1 x Triax + Block  | 1 x 11 g                          | 11 g    |
|                    | Total                             | 109.3 g |

| <b>NODE 34</b>     |                                   |        |
|--------------------|-----------------------------------|--------|
| 1 x Node Ball      | 5.8 g                             | 5.8 g  |
| 3 x Longeron       | $\frac{3 \times 18 \text{ g}}{2}$ | 27 g   |
| 1 x Diagonal       | $\frac{1 \times 27 \text{ g}}{2}$ | 13.5 g |
| 4 x Joint Assembly | 4 x 7.7 g                         | 30.8 g |
| 1 x Triax + Block  | 1 x 11 g                          | 11 g   |
|                    | Total                             | 88.1 g |

**APPENDIX 4: DOFS RANDOM MEASUREMENT ORDER FOR THE NASA 8 BAY TRUSS STRUCTURE**

| Measurement No. | DOF No. | Measurement No. | DOF No. | Measurement No. | DOF No. |
|-----------------|---------|-----------------|---------|-----------------|---------|
| 1               | 96      | 33              | 15      | 65              | 92      |
| 2               | 25      | 34              | 27      | 66              | 71      |
| 3               | 11      | 35              | 46      | 67              | 65      |
| 4               | 12      | 36              | 47      | 68              | 19      |
| 5               | 18      | 37              | 68      | 69              | 2       |
| 6               | 1       | 38              | 89      | 70              | 20      |
| 7               | 10      | 39              | 90      | 71              | 41      |
| 8               | 21      | 40              | 70      | 72              | 49      |
| 9               | 34      | 41              | 69      | 73              | 39      |
| 10              | 56      | 42              | 50      | 74              | 42      |
| 11              | 78      | 43              | 62      | 75              | 36      |
| 12              | 32      | 44              | 61      | 76              | 43      |
| 13              | 35      | 45              | 52      | 77              | 26      |
| 14              | 44      | 46              | 83      | 78              | 37      |
| 15              | 86      | 47              | 82      | 79              | 24      |
| 16              | 77      | 48              | 93      | 80              | 40      |
| 17              | 5       | 49              | 23      | 81              | 53      |
| 18              | 63      | 50              | 13      | 82              | 84      |
| 19              | 73      | 51              | 16      | 83              | 74      |
| 20              | 94      | 52              | 8       | 84              | 81      |
| 21              | 95      | 53              | 29      | 85              | 64      |
| 22              | 85      | 54              | 9       | 86              | 57      |
| 23              | 30      | 55              | 6       | 87              | 67      |
| 24              | 38      | 56              | 31      | 88              | 80      |
| 25              | 59      | 57              | 33      | 89              | 91      |
| 26              | 60      | 58              | 66      | 90              | 75      |
| 27              | 51      | 59              | 7       | 91              | 79      |
| 28              | 72      | 60              | 54      | 92              | 58      |
| 29              | 22      | 61              | 54      | 93              | 48      |
| 30              | 3       | 62              | 45      | 94              | 17      |
| 31              | 4       | 63              | 88      | 95              | 28      |
| 32              | 14      | 64              | 87      | 96              | 76      |

Please note that all DOFs have been included in the sequence. If 72 DOFs are to be supplied, then only the random DOFs corresponding to the first 72 measurement numbers should be used.

**APPENDIX 5: MASS MATRIX FOR PLATE STRUCTURES – NON COMPATIBLE THEORY (SINGLE ELEMENT)**

|    | 1   | 2   | 3   | 4   | 5   | 6   | 7   | 8   | 9   | 10  | 11  | 12 |
|----|-----|-----|-----|-----|-----|-----|-----|-----|-----|-----|-----|----|
| 1  | MA  |     |     |     |     |     |     |     |     |     |     |    |
| 2  | MD  | MB  |     |     |     |     |     |     |     |     |     |    |
| 3  | ME  | MF  | MC  |     |     |     |     |     |     |     |     |    |
| 4  | MG  | MH  | MI  | MA  |     |     |     |     |     |     |     |    |
| 5  | -MH | MJ  | MK  | -MD | MB  |     |     |     |     |     |     |    |
| 6  | MI  | -MK | ML  | ME  | -MF | MC  |     |     |     |     |     |    |
| 7  | MM  | MN  | MO  | MG  | MP  | MQ  | MA  |     |     |     |     |    |
| 8  | -MN | MR  | MS  | MP  | MT  | MK  | -MD | MB  |     |     |     |    |
| 9  | -MO | MS  | MU  | -MQ | -MK | MV  | -ME | MF  | MC  |     |     |    |
| 10 | MG  | -MP | MQ  | MM  | -MN | MO  | MG  | -MH | -MI | MA  |     |    |
| 11 | -MP | MT  | -MK | MN  | MR  | -MS | MH  | MJ  | MK  | MD  | MB  |    |
| 12 | -MQ | MK  | MV  | -MO | MS  | MU  | -MI | -MK | ML  | -ME | -MF | MC |

Symmetric

All values to be multiplied by  $\left(\frac{\rho t a b}{176400}\right)$

Where  $\rho$  = density,  $t$  = thickness,  $a$  = length,  $b$  = width

$$MA = 24178$$

$$ML = 280a^2$$

$$MB = 560b^2$$

$$MM = 2758$$

$$MC = 560a^2$$

$$MN = -812a$$

$$MD = 3227b$$

$$MO = -812a$$

$$ME = -3227a$$

$$MP = -1393b$$

$$MF = -441ab$$

$$MQ = -1918a$$

$$MG = 8582$$

$$MR = -210b^2$$

$$MH = 1918b$$

$$MS = 196ab$$

$$MI = -1393a$$

$$MT = 280b^2$$

$$MJ = -420b^2$$

$$MU = -210a^2$$

$$MK = 294ab$$

$$MV = -420a^2$$



$$SA = 4(\beta^2 + \beta^{-2}) + \frac{1}{5}(14 - 4\nu)$$

$$SO = -2(2\beta^2 - \beta^2) - \frac{1}{5}(14 - 4\nu)$$

$$SB = \left[ 2\beta^{-2} + \frac{1}{5}(1 + 4\nu) \right] b$$

$$SP = \left[ -\beta^{-2} + \frac{1}{5}(1 + 4\nu) \right] b$$

$$SC = \left[ \frac{4}{3}\beta^{-2} + \frac{4}{15}(1 - \nu) \right] b^2$$

$$SQ = \left[ 2\beta^2 + \frac{1}{5}(1 - \nu) \right] a$$

$$SD = -\left[ 2\beta^2 + \frac{1}{5}(1 + 4\nu) \right] a$$

$$SR = \left[ \frac{1}{3}\beta^{-2} + \frac{1}{15}(1 - \nu) \right] b^2$$

$$SE = -\nu ab$$

$$SS = \left[ \frac{2}{3}\beta^{-2} - \frac{4}{15}(1 - \nu) \right] b^2$$

$$SF = \left[ \frac{4}{3}\beta^2 + \frac{4}{15}(1 - \nu) \right] a^2$$

$$ST = \left[ \frac{1}{3}\beta^2 + \frac{1}{15}(1 - \nu) \right] a^2$$

$$SG = 2(\beta^2 - 2\beta^{-2}) + \frac{1}{5}(14 - 4\nu)$$

$$SU = \left[ \frac{2}{3}\beta^2 - \frac{1}{15}(1 - \nu) \right] a^2$$

$$SH = -\left[ 2\beta^{-2} + \frac{1}{5}(1 - \nu) \right] b$$

$$SI = \left[ -\beta^2 + \frac{1}{5}(1 + 4\nu) \right] a$$

$$SJ = \left[ \frac{2}{3}\beta^{-2} - \frac{1}{15}(1 - \nu) \right] b^2$$

$$SK = \left[ \frac{2}{3}\beta^2 - \frac{4}{15}(1 - \nu) \right] a^2$$

$$SL = -2(\beta^2 + \beta^{-2}) + \frac{1}{5}(14 - 4\nu)$$

$$SM = \left[ -\beta^{-2} + \frac{1}{5}(1 - \nu) \right] b$$

$$SN = \left[ \beta^2 - \frac{1}{5}(1 - \nu) \right] a$$

### APPENDIX 7: MASS MATRIX FOR PLATE STRUCTURES – COMPATIBLE THEORY (SINGLE ELEMENT)

|    | 1   | 2   | 3   | 4   | 5   | 6   | 7   | 8   | 9   | 10  | 11  | 12 |
|----|-----|-----|-----|-----|-----|-----|-----|-----|-----|-----|-----|----|
| 1  | MA  |     |     |     |     |     |     |     |     |     |     |    |
| 2  | MB  | MC  |     |     |     |     |     |     |     |     |     |    |
| 3  | MD  | ME  | MF  |     |     |     |     |     |     |     |     |    |
| 4  | MG  | MH  | MI  | MA  |     |     |     |     |     |     |     |    |
| 5  | -MH | MJ  | MK  | -MB | MC  |     |     |     |     |     |     |    |
| 6  | MI  | -MK | ML  | MD  | -ME | MF  |     |     |     |     |     |    |
| 7  | MM  | MN  | MO  | MG  | MP  | MQ  | MA  |     |     |     |     |    |
| 8  | -MN | MR  | MS  | MP  | MT  | MK  | -MB | MC  |     |     |     |    |
| 9  | -MO | MS  | MU  | -MQ | -MK | MV  | -MD | ME  | MF  |     |     |    |
| 10 | MG  | -MP | MQ  | MM  | -MN | MO  | MG  | -MH | -MI | MA  |     |    |
| 11 | -MP | MT  | -MK | MN  | MR  | -MS | MH  | MJ  | MK  | MB  | MC  |    |
| 12 | -MQ | MK  | MV  | -MO | -MS | MU  | -MI | -MK | ML  | -MD | -ME | MF |

Symmetric

All values to be multiplied by  $\left(\frac{ptab}{176400}\right)$

Where  $\rho$  = density,  $t$  = thickness,  $a$  = length,  $b$  = width

$$MA = 24336$$

$$ML = 216a^2$$

$$MB = 3432b$$

$$MM = 2916$$

$$MC = 624b^2$$

$$MN = 702b$$

$$MD = -3432a$$

$$MO = -702a$$

$$ME = -484ab$$

$$MP = -1188b$$

$$MF = 624a^2$$

$$MQ = -2028a$$

$$MG = 8424$$

$$MR = -162b^2$$

$$MH = 2028b$$

$$MS = 169ab$$

$$MI = -1188a$$

$$MT = 216b^2$$

$$MJ = -468b^2$$

$$MU = -162a^2$$

$$MK = 286ab$$

$$MV = -486a^2$$



$$SA = \frac{156}{35}(\beta^2 + \beta^{-2}) + \frac{72}{25}$$

$$SO = \left[ \frac{27}{35}\beta^2 + \frac{13}{35}\beta^{-2} - \frac{6}{25} \right] a$$

$$SB = \left[ \frac{22}{35}\beta^2 + \frac{78}{35}\beta^{-2} + \frac{6}{25}(1 + 5\nu) \right] b$$

$$SP = -\frac{156}{35}\beta^2 + \frac{54}{35}\beta^{-2} - \frac{72}{25}$$

$$SC = \left[ \frac{4}{35}\beta^2 + \frac{52}{35}\beta^{-2} + \frac{8}{25} \right] b^2$$

$$SQ = \left[ \frac{22}{35}\beta^2 - \frac{27}{35}\beta^{-2} + \frac{6}{25}(1 + 5\nu) \right] b$$

$$SD = -\left[ \frac{78}{35}\beta^2 + \frac{22}{35}\beta^{-2} + \frac{6}{25}(1 + 5\nu) \right] a$$

$$SR = \left[ \frac{78}{35}\beta^2 - \frac{13}{35}\beta^{-2} + \frac{6}{25}(1 + 5\nu) \right] a$$

$$SE = -\left[ \frac{11}{35}(\beta^2 + \beta^{-2}) + \frac{1}{50}(1 + 60\nu) \right] ab$$

$$SS = \left[ \frac{3}{35}\beta^2 + \frac{9}{35}\beta^{-2} + \frac{2}{25} \right] b^2$$

$$SF = \left[ \frac{52}{35}\beta^2 + \frac{4}{35}\beta^{-2} + \frac{8}{25} \right] a^2$$

$$ST = \left[ \frac{13}{70}(\beta^2 + \beta^{-2}) - \frac{1}{50} \right] ab$$

$$SG = \frac{54}{35}\beta^2 - \frac{156}{35}\beta^{-2} - \frac{72}{25}$$

$$SU = \left[ -\frac{4}{35}\beta^2 + \frac{18}{35}\beta^{-2} - \frac{8}{25} \right] b^2$$

$$SH = \left[ \frac{13}{35}\beta^2 - \frac{78}{35}\beta^{-2} - \frac{6}{25} \right] b$$

$$SV = \left[ -\frac{11}{35}\beta^2 + \frac{13}{70}\beta^{-2} - \frac{1}{50}(1 + 5\nu) \right] ab$$

$$SI = \left[ -\frac{27}{35}\beta^2 + \frac{22}{35}\beta^{-2} + \frac{6}{25}(1 + 5\nu) \right] a$$

$$SW = \left[ \frac{9}{35}\beta^2 + \frac{3}{35}\beta^{-2} + \frac{2}{25} \right] a^2$$

$$SJ = \left[ -\frac{3}{35}\beta^2 + \frac{26}{35}\beta^{-2} - \frac{2}{25} \right] b^2$$

$$SX = \left[ \frac{26}{35}\beta^2 - \frac{3}{35}\beta^{-2} - \frac{2}{25} \right] a^2$$

$$SK = \left[ \frac{13}{70}\beta^2 - \frac{11}{35}\beta^{-2} - \frac{1}{50}(1 + 5\nu) \right] ab$$

$$SL = \left[ \frac{18}{35}\beta^2 - \frac{4}{35}\beta^{-2} - \frac{8}{25} \right] a^2$$

$$SM = -\frac{54}{35}(\beta^2 + \beta^{-2}) + \frac{72}{25}$$

$$SN = \left[ -\frac{13}{35}\beta^2 - \frac{27}{35}\beta^{-2} + \frac{6}{25} \right] b$$

**APPENDIX 9: DOFS RANDOM MEASUREMENT ORDER FOR THE  
CANTILEVERED PLATE STRUCTURE**

| <b>Measurement No.</b> | <b>DOF No.</b> | <b>Measurement No.</b> | <b>DOF No.</b> | <b>Measurement No.</b> | <b>DOF No.</b> |
|------------------------|----------------|------------------------|----------------|------------------------|----------------|
| 1                      | 25             | 25                     | 28             | 49                     | 45             |
| 2                      | 11             | 26                     | 27             | 50                     | 71             |
| 3                      | 12             | 27                     | 46             | 51                     | 65             |
| 4                      | 18             | 28                     | 47             | 52                     | 19             |
| 5                      | 1              | 29                     | 68             | 53                     | 2              |
| 6                      | 10             | 30                     | 70             | 54                     | 20             |
| 7                      | 21             | 31                     | 69             | 55                     | 41             |
| 8                      | 34             | 32                     | 50             | 56                     | 49             |
| 9                      | 56             | 33                     | 62             | 57                     | 39             |
| 10                     | 32             | 34                     | 61             | 58                     | 42             |
| 11                     | 35             | 35                     | 52             | 59                     | 36             |
| 12                     | 44             | 36                     | 23             | 60                     | 43             |
| 13                     | 5              | 37                     | 13             | 61                     | 26             |
| 14                     | 63             | 38                     | 16             | 62                     | 37             |
| 15                     | 30             | 39                     | 8              | 63                     | 24             |
| 16                     | 38             | 40                     | 29             | 64                     | 40             |
| 17                     | 59             | 41                     | 9              | 65                     | 53             |
| 18                     | 60             | 42                     | 6              | 66                     | 64             |
| 19                     | 51             | 43                     | 31             | 67                     | 57             |
| 20                     | 72             | 44                     | 33             | 68                     | 67             |
| 21                     | 22             | 45                     | 66             | 69                     | 58             |
| 22                     | 3              | 46                     | 7              | 70                     | 48             |
| 23                     | 4              | 47                     | 55             | 71                     | 17             |
| 24                     | 14             | 48                     | 54             | 72                     | 15             |

Please note that all DOFs have been included in the sequence. If 48 DOFs are to be supplied, then only the random DOFs corresponding to the first 48 measurement numbers should be used.

APPENDIX 10: CALIBRATION CHART FOR ACCELEROMETER

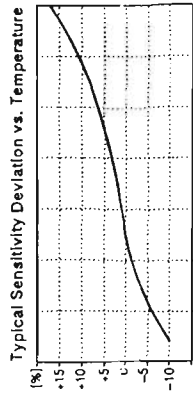
Miniature Accelerometer Type 4393

Serial No.: 2066511

**Environmental:**  
 Temperature Range: -74 to +250°C (-100 to +482°F)  
 Temp. Transient Sensitivity (3 Hz LLF): 5 ms<sup>-1/2</sup>·C  
 Magn. Sensitivity (50Hz): 30 ms<sup>-1/2</sup>T  
 Acoustic Sensitivity (154 dB SPL, 2 - 100 Hz): 0.04 ms<sup>-2</sup>/ $\mu$ F  
 Max. Non-destructive Shock: 250 kms<sup>-2</sup> peak  
 Humidity: Welded, Sealed  
 Base Strain Sensitivity (at 250  $\mu$ e in base plane): 0.005 ms<sup>-2</sup>/ $\mu$ e

**Physical:**  
 Case Material: Titanium, ASTM Grade 2  
 Sensing Element: Piezoelectric, Type PZ 23  
 Construction: Delta Shear  
 Weight: 2.4 gram excl. cable  
 Mounting Thread: M3  
 Mounting Surface Flatness: <3  $\mu$ m  
 Mounting Torque (Recommended): 0.6 Nm  
 Max. 1.0 Nm, Min. 0.3 Nm  
 Seismic Mass: 0.67 gram  
 Center of Gravity of Seismic Mass: 7.1 mm above mounting surface on central axis  
 Center of Gravity of Accelerometer: 5.4 mm above mounting surface

**Mounting Technique:**  
 Examine the mounting surface for cleanliness and smoothness. If necessary, machine surface as per drawing of recommended mounting surface. Fasten the accelerometer using an M3 stud. Take care not to exceed the max. recommended mounting torque and that the stud does not bottom in the mounting hole. A thin film of oil or grease on the mounting surface improves the mounting stiffness. For other types of mounting see Brüel & Kjær Piezoelectric Accelerometers and Vibration Preamplifiers' handbook.



Specifications obtained in accordance with ANSI S2.11-1969 Miniature Accelerometer 4393.

All values are typical at 25°C (77°F) unless measurement uncertainty is specified.

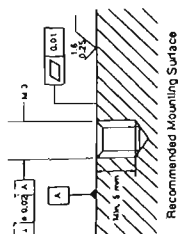
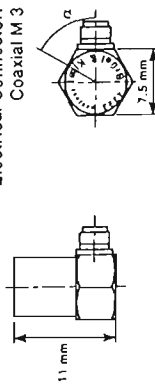
Date 25 Jun 1998 Operator ST



Brüel & Kjær

Acceleration Range:  
 Max. operational shock ( $\pm$  peak): 250 kms<sup>-2</sup>  
 Max. continuous sinusoidal: 50 kms<sup>-2</sup>  
 Capacitance of Transducer: 590 pF  
 Capacitance of cable A0 0038: 110 pF  
 Insulation Resistance (room temp.): >20 GOhm

Electrical Connector: Coaxial M 3



Calibration Chart for Miniature Accelerometer Type 4393

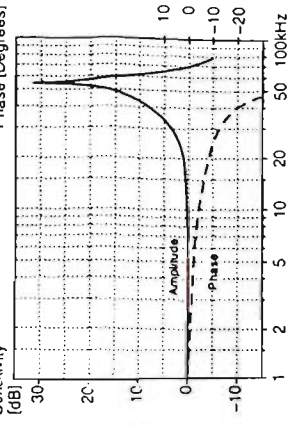
Serial No.: 2066511  
 Reference Sensitivity\* 0.3140 pC/ms<sup>-2</sup>  
 or 3.079 pC/g  
 at 159.2 Hz ( $\omega = 1000$  s<sup>-1</sup>) and 24 °C  
 Upper Frequency Limit (+10%): 16.5 kHz  
 Mounted Resonance Frequency: 55 kHz  
 Undamped Natural Frequency: 85 kHz  
 Transverse Sensitivity: Maximum (at 30 Hz, 100 ms<sup>-2</sup>): 0.9 %  
 Angle of minimum,  $\alpha$ : (see drawing) 1.35 °  
 Transverse Resonance Frequency: 18 kHz

Polarity is positive on the centre of the connector for an acceleration directed from the mounting surface into the body of the accelerometer.

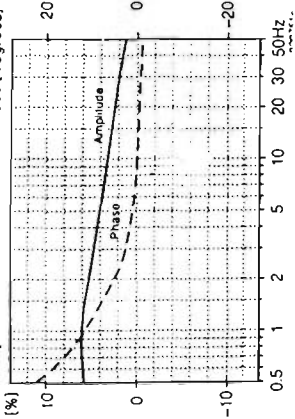
\*This calibration is traceable to the National Institute of Standards and Technology, USA and Physikalisch-Technische Bundesanstalt, Germany.

The expanded uncertainty of this measurement is 1.3 % at 2  $\sigma$  (i.e. expanded uncertainty using a coverage factor of 2).

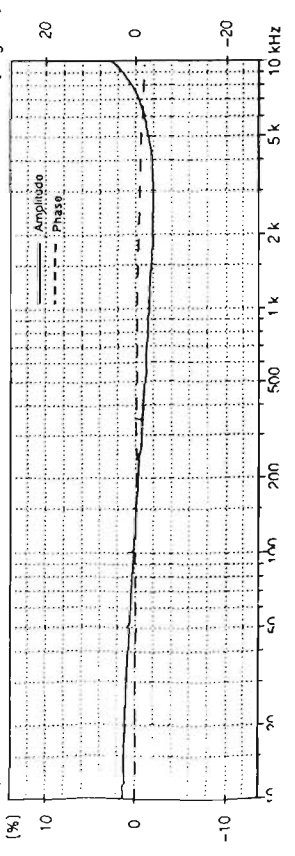
Typical High Frequency Response  
 Incl. Brüel & Kjær Measuring Amplifier Type 2525 (UFL: off)  
 Sensitivity\*\* (dB)  
 Phase (Degrees)



Typical Low Frequency Response  
 Incl. Brüel & Kjær Preamplifier Type 2525 (LFL: off)  
 Sensitivity\*\* (dB)  
 Phase (Degrees)



Individual Frequency Response  
 Sensitivity\*\* (dB)  
 Phase (Degrees)



**APPENDIX 11: BRUEL & KJAER DUAL FREQUENCY ANALYSER SETTINGS (2032)**

Measurement: Dual Spectrum Averaging, zero pad

Trigger: CH. A + Slope Level -0.10 Max Input

Delay: Trig -> A: - 19.53ms CH.A -> B: 0.00ms

Averaging: Lin 5

Freq. Span: 400Hz  $\Delta f$ :0.5Hz T=1s  $\Delta t$ =488 $\mu$ s

Weight CH.A: Transient Shift: 3.90ms Length:42.48ms  
Weight CH.B: Exponential Shift: 0ms Length: 150.87ms

CH.A 6V +3Hz Dir Filt: 6.4kHz 20mV/N  
CH.B 6V +3Hz Dir Filt: 6.4kHz 31.6mV/m/s<sup>2</sup>

